Flow and transport in electrochromatography

Dissertation

zur Erlangung des akademischen Grades

**doctor rerum naturalium
(Dr. rer. nat.)**

von: Dipl.-Ing. (FH) Ivo Nischang

geb. am: 17.03.1980

in: Haldensleben

genehmigt durch die Fakultät für Verfahrens- und Systemtechnik
der Otto-von-Guericke-Universität Magdeburg

Gutachter: Prof. Dr. Ulrich Tallarek

                    Prof. Dr. Andreas Seidel-Morgenstern

eingereicht am: 05.06.2007

Promotionskolloquium am: 29.08.2007

Acknowledgement

I am very grateful to

- Professor Ulrich Tallarek for generally supervising of my work and related scientific discussions to deepen specific scientific understanding,
- Professor Andreas Seidel-Morgenstern for the possibility of conducting research at the Max-Planck-Institute in Magdeburg and ensure critical financial support,
- Dr. Guofang Chen (Dalian Institute of Chemical Physics) for excellent experimental cooperation regarding some of the chromatographic studies, Katja Spannmann to approach pharmaceutical target molecules and
- Dr. Erdmann Rapp as a great lab colleague during my time here in Magdeburg.

Finally I would like to dedicate this work to my parents for always supporting me in my life and dedications, my wonderful to nieces, Vivien and Pia, who always cheered me up of believing in the good things in life and showing me continuity of thinking and visions in a never resting world of dynamics and change.

Zusammenfassung

Die Dissertation „Flow and transport in electrochromatography" beschäftigt sich mit den in flüssigchromatographischen Trennverfahren auftretenden elektrostatischen und elektrokinetischen Stofftransporteigenschaften. Der erste Teil der Dissertation befasst sich nach einer generellen Einführung in die Flussfelddynamik mit der Elektrohydrodynamik in gepackten Betten, insbesondere im Hinblick auf die axiale hydrodynamische Dispersion in der Kapillarelektrochromatographie (KEC). Im zweiten Teil werden die für analytische Anwendungen wichtigen Elektromigrationscharakteristika und die daraus resultierende Retentionsdynamik geladener Analyten untersucht.

Kapitel 1 beschäftigt sich mit einer phänomenologischen Betrachtung der Elektrohydrodynamik in der KEC mit gepackten Betten als stationärer Phase. Im Besonderen wird die Morphologie der gepackten Betten hinsichtlich einer Ungleichverteilung des lokalen und makroskopischen elektroosmotischen Flusses (EOF) als auch die erreichbare Trennleistung diskutiert. Es wird herausgestellt, dass die Porenraummorphologie gepackter Betten, aber auch monolithischer Strukturen eine Strömungsungleichverteilung des lokalen und makroskopischen EOF verursachen. Diese Ungleichverteilung steht in Kontrast zum pfropfenförmigen Flussprofil in einer offenen homogenen Kapillare. Sie wird durch eine Variation der lokalen elektrischen Feldstärke in der Packung bedingt, welche aus der sich ständig verengenden und erweiternden interpartikulären bzw. interskelettären Porenraummorphologie resultiert. Weiterhin werden Wandeffekte elektrokinetischer und geometrischer Natur diskutiert, die sich insbesondere bei kleinen Verhältnissen von Säulen- zu-Partikel-Durchmessern bemerkbar machen. Ausgehend von diesen theoretischen und auch experimentellen Betrachtungen werden die sich durch den hierarchisch strukturierten Porenraum des Festbettes ergebenden Stofftransporteigenschaften experimentell charakterisiert und diskutiert.

Das Hauptaugenmerk dieser Arbeit liegt auf der Untersuchung und Aufklärung von Stofftransportphänomenen im intrapartikulären bzw. intraskelettären Porenraum stationärer Trennphasen. Obwohl der Durchmesser der Mesoporen (Mesoporen sind Poren in der Größe von 2-50 nm) in Partikeln oder im Skelett von Monolithen in derselben Größenordnung wie die elektrische Doppelschicht (räumliche Dimensionen von 1-100 nm) der geladenen Porenoberflächen liegt, kann in Abhängigkeit vom Ausmaß dieser Doppelschichtüberlappung ein intrapartikulärer EOF induziert werden. Die Auswirkungen dieses EOF auf die axiale Dispersion in der KEC hängen sehr stark von der Größe der mesoporösen Domänen des Festbettes als auch von der Doppelschichtüberlappung auf Porenniveau ab. Das Phänomen der elektroosmotischen Perfusion führt zu einem erhöhten Stofftransport im Mesoporenraum (weit über die generelle Diffusionslimitierung bei hydraulichem Fluss durch das Festbett hinaus) und reduziert damit drastisch die axiale Dispersion. Gleichzeitig kann dieser intrapartikuläre Porenraum aus der Sicht geladener Spezies eine beträchtliche elektrische Potentialbarriere aufweisen, die sich in einem erheblichen Überschuss an mobilen Gegenionen manifestiert. Klassisch wird diese Anreicherung im elektrochemischen Gleichgewicht durch das sogenannte Donnan-Potential beschrieben. Dieses Potential hat seinen Ursprung in der Tendenz der

ionischen Spezies existierende Konzentrationsunterschiede zwischen Porenräumen unterschiedlicher Dimensionen (und damit auch Ladungsselektivität) auszugleichen. Der Überschuss der Gegenionen wird durch dieses Potential im intraskelettären/intrapartikulären Porenraum (ladungsselektiv) gehalten und Koionen daran gehindert diesen Porenraum zu permeieren. Der Verteilungskoeffizient ionischer Spezies zwischen den quasi nicht ladungsselektiven (Makroporen) und ladungsselektiven (Mesoporen) Kompartmenten wird durch die Ionenpermselektivität bestimmt. Diese Ionenpermselektivität hängt von der Ionenstärke der mobilen Phase (Dimensionen der elektrischen Doppelschicht), der Oberflächenladungsdichte in den ionenpermselektiven Poren (die das Potentialniveau bestimmt) und auch den Wertigkeiten der ko- und gegenionischen Komponenten im System ab. Durch Anlegen eines (externen) elektrischen Feldes über ein solches poröses Material mit lokalen permselektiven Transporteigenschaften (bevorzugter Transport einer Spezies) kommt es zum Phänomen der Konzentrationspolarisation in der angrenzenden Elektrolytlösung. Sie ist verbunden mit der Ausbildung von Konzentrationsgradienten in der angrenzenden Elektrolytlösung, verursacht durch elektrischen Strom normal zu diesen ionenpermselektiven Grenzflächen und hat ihre Ursache in der Transportdiskriminierung ko- und gegenionischer Spezies. Die Konzentrationspolarisation wird eingehend in Kapitel 2 diskutiert.

Nach einem Überblick und einer Zusammenfassung relevanter Studien zur Konzentrationspolarisation (zum größten Teil bekannt aus den Membranwissenschaften, z.B. der Elektrodialyse) wird in Kapitel 3 die grundsätzliche Abhängigkeit des EOF und hydrodynamischer Dispersion in der KEC untersucht und dargelegt. Diese Untersuchungen schließen gepackte Betten mesoporöser Partikel mit unterschiedlicher Größe der Mesoporen, nichtporöse Partikel, als auch kontinuierliche monolithische Strukturen mit einem mesoporösen Skelett ein. Die nichtporösen Partikel wurden als Referenzmaterial verwendet, um die durch den hierarchisch strukturierten Aufbau des gepackten Bettes mit porösen Partikeln beobachteten Phänomene zu verifizieren. Bereits durch einfache chromatographische Experimente konnte in Betten bestehend aus porösen Partikeln ein Koionenausschluss vom intrapartikulären Porenraum durch verminderte effektive Verweilzeiten koionischer, nichtretardierter (keine Wechselwirkung im klassisch chromatographischen Sinne) Komponenten indiziert werden. Die Verweilzeit konnte durch die Ionenstärke der mobilen Phase und damit durch die Einstellung der Doppelschichtüberlappung auf intrapartikulärem Porenniveau gezielt gesteuert werden, d.h. vom Ausmass der elektrischen Doppelschichtüberlappung werden intraskelettäre/intrapartikuläre effektive Porositäten (Permeationsvolumen), die von geladenen koionischen Molekülen wahrgenommen werden, moduliert. Dieser einstellbare, lokal ladungsselektive Transport in der Flüssigchromatographie bildet in der KEC die Grundlage für Konzentrationspolarisationsphänomene. Die im weiteren untersuchten Konzentrationspolarisationsphänomene werden durch Ausbildung konvektiver Diffusionsgrenzschichten mit reduzierter und angereicherter Elektrolytkonzentration an den anodischen und kathodischen (kationenselektiven) Grenzflächen zwischen Makro- und Mesoporenraum charakterisiert. Konzentrationspolarisation hat ihre Ursache im durch das elektrische Feld induzierten gekoppelten Masse-Ladungstransport normal zu den ladungsselektiven Grenzflächen und hat deutliche Konsequenzen für die elektroosmotische Flussfelddynamik. Insbesondere die Zone stark reduzierter Ionenkonzentration an der anodischen Grenzfläche eines kationenselektiven

Partikels ist von großer Bedeutung, da Stofftransport hier diffusionslimitiert ist. Dieser Diffusionsstrom durch die abgereicherte Zone hat einen Maximalwert (Diffusionsgrenzstrom). Gleichzeitig hängt aber der Transport der Gegenionen im Partikel (oder mesoporösen ionenpermselektiven Skelett von Monolithen) durch gleichgerichtete Elektroosmose und Elektrophorese annähernd linear vom Feld ab. Diese unterschiedlichen Abhängigkeiten des lokalen Transportes sind die Ursache für die Ausbildung einer sekundären elektrischen Doppelschicht mit mobiler gegenionischer Raumladung in der abgereicherten Konzentrationspolarisationszone. Diese wird ab einer kritischen elektrischen Feldstärke induziert, bei der der intrapartikuläre ladungsselektive Transport mobiler Gegenionen den Transport der Gegenionen durch die Diffusionsgrenzschicht übersteigt. Die dort lokal induzierte gegenionische Raumladung (in Form einer so genannten sekundären elektrischen Doppelschicht) führt durch Wechselwirkung mit der lokalen tangentialen Feldkomponente zu einem nichtlinearen EOF im interpartikulären oder interskelettären Porenraum. Dieser nichtlineare EOF wird durch nichtlineare mittlere Geschwindigkeiten im gepackten Bett bzw. in Monolithen und damit einhergehend starker lokaler und tangential zur gekrümmten Oberfläche auftretender Geschwindigkeitskomponenten charakterisiert. Diese erhöhen die laterale Dispersion auf Porenniveau und reduzieren damit die axiale Zonenverbreiterung. Der Unterschied in der Porenraummorphologie gepackter Betten und monolithischer Strukturen beeinflusst die Intensität der Konzentrationspolarisation und des nichtlinearen EOF, was in der vorliegenden Arbeit mittels chromatographischer Feldstudien unter Verwendung neutraler Analyten einhergehend mit Dispersionsstudien gezeigt und diskutiert wird. Die Konzentrationspolarisation wird als ein Schlüsselphänomen in der KEC identifiziert, sie beeinflusst deutlich das nichtlineare EOF Verhalten und kann phänomenologisch mit der elektroosmotischen Perfusion, die in Kapitel 1 diskutiert und auch in Kapitel 3 experimentell und phänomenologisch berücksichtigt wird, in Einklang gebracht werden.

Die Ergebnisse in Kapitel 3 werden in Kapitel 4 durch (quantitative) konfokale Fluoreszenzmikroskopie untermauert, indem die Abhängigkeit des intrapartikulären/intraskelettären Koionenausschlusses (Donnanausschluss) und der Gegenionenanreicherung (Donnananreicherung) und der damit verbundenen Konzentrationspolarisation bei Überlagerung externer elektrischer Felder systematisch von der Ionenstärke der mobilen Phase und der elektrischen Feldstärke visualisiert und quantitativ analysiert wird. Durch diese Untersuchungen werden weitreichende Konsequenzen des Phänomens der Konzentrationspolarisation für chromatographische Anwendungen verdeutlicht. Systematische Studien von Einzelpartikeln (wie in Kapitel 2 angesprochen, erläutert und charakterisiert) bis hin zu multipartikulären Systemen zeigen (wie sie in Kapitel 3 chromatographisch hinsichtlich nichtlinearer EOF-Dynamik charakterisiert wurden), dass es sich um ein eher generelles als spezielles Phänomen an ionenpermselektiven Grenzflächen handelt, wie sie in der Ionenaustauschchromatographie, als auch teilweise in der Umkehrphasenchromatographie mit gepackten Betten und monolithischen Strukturen beobachtet werden können. Während die meisten experimentellen Untersuchungen von Konzentrationspolarisationsphänomenen mit Membranen durchgeführt wurden, wie sie zum Beispiel in der Elektrodialyse Anwendung finden, war es immer schwierig, den Stofftransport innerhalb der Membran zu visualisieren. Im Wesentlichen indizieren die in dieser Arbeit gezeigten Studien eine Erhöhung des intrapartikulären Transportes von gegenionischen (Fluoreszenz-) Molekülen bei

Erhöhung des elektrischen Feldes. Diese Erhöhung des intrapartikulären Transportes beruht auf einer erhöhten Stromdichte durch das Partikel mit erhöhtem elektrischen Feld. Der Transport der zunächst intrapartikulär/intraskelettär dominiert ist, da genügend Gegenionen durch die Diffusionsgrenzschicht nachtransportiert werden können um diesem Strom zu genügen, schwenkt bei weiterer Erhöhung des elektrischen Feldes zum durch die Diffusionsgrenzschicht dominierten Transport um. Die elektrischen Feldstärken, bei denen limitierende Stoffstromdichten (Diffusionsgrenzstrom) lokal im gepackten Bett auftreten wurden bestimmt. In enger Korrelation mit der beobachteten Elektrohydrodynamik charakterisieren sie die Ausbildung einer sekundären elektrischen Doppelschicht in der abgereicherten Konzentrationspolarisationszone (sowohl in monolithischen Strukturen als auch gepackten Betten). Es kommt dabei zu einer An- und Abreicherung ionischer Spezies lokal an den anodischen und kathodischen Grenzflächen mesoporöser Partikel im gepackten Bett oder lokal an den permselektiven Grenzflächen in Monolithen, bei der der Transport gegenionischer Moleküle im System durch den intrapartikulären/intraskelettären Transport mobiler Gegenionen bestimmt wird. Die zunächst lineare Ab- und Zunahme der Elektrolytkonzentration in den Konzentrationspolarisationszonen in Abhängikeit von der elektrischen Feldstärke, gefolgt von einem asymptotischen Verlauf auf einen maximalen bzw. minimalen Wert mit zunehmender elektrischer Felstärke erinnert an die typischen (makroskopisch bestimmten) Strom-Spannungskurven von Ionenaustauschermembranen. Deutliche Konsequenzen des lokalen limitierenden Stofftransportverhaltens ergeben sich hier für die Entwicklung einer nichtlinearen Elektrohydrodynamik (verbunden mit der Ausbildung einer sekundären elektrischen Doppelschicht), und damit einer Abhängigkeit des EOF vom Durchmesser der Partikel des gepackten Bettes, einer Abhängigkeit die dem klassischen linearen Modell von Helmholtz-Smoluchowski (lineare Elektroosmose verbunden mit der Raumladung in der primären elektrischen Doppelschicht) völlig fremd ist. Diese Abhängigkeit bildet den direkten Anknüpfungspunkt an Kapitel 3, mit dem Unterschied, das hier auftretende Wechselwirkungsmechanismen der ausgebildeten Konzentrationspolarisationszonen benachbarter Partikel („Multiparticle effects") in partikulären Betten, aufgrund räumlicher Nähe, untersucht werden. Sie führen lokal zu einer Auslöschung an- und abgereicherter Konzentrationspolarisationszonen, da ihre räumliche Ausdehnung deutlich größer als die Ausdehnung der primären elektrischen Doppelschicht ist. Die resultierende komplexe Wechselwirkung benachbarter Konzentrationspolarisationszonen wird durch die Morphologie des gepackten Bettes bestimmt, was zu einer abgeschwächten, lokal effektiven Konzentrationspolarisation führt und damit erst bei deutlich höheren Feldstärken limitierend wirkt, als für ein einzelnes Partikel. Weiterhin wird gezeigt, das elektroosmotische Mobilitäten in gepackten Betten und elektrophoretische Mobilitäten betreffender Partikel in verdünnten Suspensionen trotz Berücksichtigung der Tortuosität nicht quantitativ verglichen werden können, obwohl Elektrophorese eigentlich ein integrales Charakteristikum der Elektroosmose ist. Im Gegensatz zu den diskreten partikulären Systemen durchziehen die Konzentrationspolarisationszonen axial ausgedehnte monolithische Strukturen wie ein Spinnennetz und sind weniger diskret. Sowohl für partikuläre als auch monolithische Strukturen konnten die Visualisierungsergebnisse quantitativ mit der makroskopisch beobachteten Elektrohydrodynamik korreliert werden, das heißt in beiden Fällen, das lineare Elektroosmose mit Erreichen eines lokalen limitierenden Stofftransportverhaltens (Diffusionsgrenzstrom) sukzessive in ein nichtlineares Verhalten

übergeht und bei weiterer Erhöhung des Feldes eine deutliche Nichtlinearität (die von den charakteristischen axialen Längendimensionen als auch der Morphologie des Makroporenraumes abhängt) zeigt. Anwendungen der nichtlinearen Flussfelddynamik bei gleichzeitig reduzierter axialer Dispersion ergeben sich insbesondere für die Mikrofluidik (z.B. Mikropumpen), die Ausnutzung für Anreicherungseffekte (Konzentrationspolarisation als „Extraktor" positiv oder negativ geladener Moleküle) und gerade auch für hocheffiziente elektrokinetische Trennungen in miniaturisierten Chipstrukturen (Kapitel 3).

In Kapitel 5 wird das Migrationsverhalten und das resultierende Retentionsverhalten geladener Analyten in der KEC untersucht. In dieser Arbeit kann erstmalig durch direkte Korrelation makroskopischer Retentionsdaten mit mikroskopischen Studien auf Partikelebene in identischen chromatographischen Systemen ein deutlicher mechanistischer Unterschied für die Retentionsdynamik geladener gegenüber ungeladener Analyten in Abhängigkeit vom elektrischen Feld gezeigt werden. Für diese Experimente wurden zunächst einfach geladene, kleine und pharmazeutisch relevante Substanzen herangezogen. Die Konzentrationspolarisationszonen, die sich an der Grenzfläche zwischen interpartikulärem und intrapartikulärem Porenraum in Abhängigkeit vom angelegten elektrischen Feld und der Ionenstärke der mobilen Phase ausbilden, reflektieren dabei direkte Änderungen in der Analytretention. Dabei beeinflussen sie geladene nicht aber neutrale Analyten während des Transportes zum, im und vom Partikel. Die Intensität dieser Zonen (welche konvektive Diffusionsgrenzschichten darstellen) hängt direkt ab vom angelegten elektrischen Feld als auch von der Ladungsselektivität zur entsprechenden intrapartikulären bzw. intraskelettären Phasengrenze was eingehend in Kapitel 4 untersucht wurde. Durch entsprechende Komplementärexperimente in gepackten Betten bestehend aus hinreichend großporigen Partikeln (zeigen bedingt Konzentrationspolarisationsphänomene, siehe Kapitel 3) als auch nichtporösen Partikeln (zeigen keine Konzentrationspolarisationsphänomene, siehe Kapitel 3) konnte die generelle Abhängigkeit des Retentionsfaktors geladener Analyten von der Feldstärke unter typischen elektrochromatographischen Bedingungen bestätigt werden. In hinreichend großen Poren ist die elektrische Doppelschichtüberlappung marginal und die Ionenverteilungen im interpartikulären und intrapartikulären Porenraum sind vergleichbar, Konzentrationspolarisationsphänomene sind damit abwesend. Bei nichtporösen Partikeln fehlt dieser intrapartikuläre Porenraum und damit auch die entsprechenden Konzentrationspolarisationsphänomene, folglich zeigen die geladenen Analyten keine feldstärkeabhängige Retention. Generell führt der gekoppelte Masse Ladungstransport bei erhöhtem elektrischem Feld zu einer Verschiebung des Retentionsfensters kleiner einfach geladener Analyten zu höheren Retentionszeiten, was mit einer Erhöhung ihrer Transportintensität durch den intrapartikulären Porenraum (und damit auch der abgereicherten Konzentrationspolarisationszone) zu erklären ist und auch visualisiert werden konnte.

Ferner wird in Kapitel 5 mit der elektrochromatographischen Trennung von Peptidgemischen gezeigt, dass der Retentionsfaktor geladener Analyten in der KEC nicht vom Masse zu Ladungsverhältnis (und damit ihrer elektrophoretischen Mobilität) abhängt, sondern im Wesentlichen von deren Ladungszahl. Die in der Bioanalytik häufig auftretenden komplexen Moleküle zeigen ein breites Spektrum von

Masse-zu- Ladungs- Verhältnissen, was die Kapillarelektrophorese zu einer geeigneten Trennmethode macht. Elektrophoretische Mobilitäten, das heißt Migration im makroskopischen Feldgradienten können hinreichend genau durch entsprechende Masse- zu- Ladungs- Verhältnisse korreliert werden. Der Vorteil des Einsatzes von partikulären Betten führt aufgrund zusätzlich auftretender adsorptiver Wechselwirkungen neben höherer Kapazitäten (aufgrund der vergrößerten Oberfläche) im Wesentlichen zu höheren Selektivitäten, was aus der Ionenaustauschchromatographie bekannt ist. Im Zuge des gekoppelten Masse-Ladungs-Transportes des Hintergrundelektrolyten werden die Verteilungsgleichgewichte der Peptide lokal auf Partikelebene im gepackten Bett und damit auch die makroskopisch beobachtete Retention in Abhängigkeit vom elektrischen Feld signifikant moduliert. Wichtig ist bei ihrem Transport ihre Transportzahl (weitaus gebräuchlicher in der Membranwissenschaft als in der Chromatographie) gegenionischer Komponenten in diesen lokal ionenpermselektiven Systemen. Die effektive Transportzahl gegenionischer Komponenten (Hintergrundelektrolyt) als auch analytisch relevanter Spezies (Peptide mit variabler Ladungszahl) hängt in einem komplexen Zusammenhang von der Stromdichte durch das Partikel ab. Wie zuvor in Kapitel 4 gezeigt, schwenkt das System generell von membran- bzw. intrapartikulär bestimmten Transport zum durch die Grenzschicht dominierten Transport um. Damit ändern sich die effektiven Transportzahlen der Analyten mit sich ändernder Stromdichte durch das Partikel. Diese Transportzahlen hängen von den Diffusionskoeffizienten, der Ladungszahl, als auch ihren Konzentrationen ab. Im intrapartikulär bestimmten Transportregime (d.h. die Transporteigenschaften werden nicht durch die abgereicherte Konzentrationspolarisationzone bestimmt) sind sie durchaus verschieden als im durch die Grenzschicht dominierten Regime, d.h. hier wird intrapartikulärer Transport durch die Transporteigenschaften der abgereicherten Konzentrationspolarisationzone bestimmt. Augrund der unterschiedlichen Molekulargewichte (Diffusionskonstanten), als auch Konzentrationen (intrapartikulär als auch in der abgereicherten Zone) bilden sie den Schlüssel für das gesamte Retentionsverhalten in der KEC. Das ist gleichzusetzen mit der Einstellung von Verteilungsgleichgewichten auf Partikelebene im gepackten Bett. Damit wird in Abhängigkeit von der Ladungszahl der Peptide, die generell im Wettkampf um ihren Stromtransport mit dem Hintergrundelektrolyten stehen, ihr Anteil an diesem Strom mit Erhöhung des elektrischen Feldes sukzessive kleiner oder größer und damit werden sie bei erhöhter Stromdichte zunehmend weniger oder mehr durch die Diffusionsgrenzschicht und damit folglich auch intrapartikulären Kompartmente transportiert. Ihre Retentionsfenster verschieben sich mit dem elektrischen Feld zu kleineren oder grösseren Zeiten. Die Abhängigkeit dieser Modulation von der Ladungszahl der Peptide wurde mit der Untersuchung bei unterschiedlichen pH-Werten (Verringerung ihrer Ladung) konsistent gezeigt. Diese Experimente haben gezeigt, dass bei höher geladenen Peptiden ihre Retention mit dem elektrischen Feld sukzessive abnimmt and bei Verringerung ihrer Ladung ihre Retention sukzessive zunimmt. Das kann nur mit ihrer effektiven Transportzahl erklärt werden, allerdings immer im Bezug auf die gegenionische Komponente des Hintergrundelektrolyten. Damit weiterhin wichtig ist die durch diese Arbeit gewonnene Erkenntnis, dass Selektivität, wie oft angenommen, nicht nur von entsprechenden elektrophoretischen Mobilitäten der Analyten in freier Lösung (wie in der Elektrophorese) und von chromatographischer Retention an der Phasengrenze (wie in der Flüssigchromatographie), sondern auch von der Transportintensität (und damit auch dem elektrischen Feld) in den

Konzentrationspolarisationszonen und mesoporösen Kompartmenten abhängig ist. Der fundamentale Unterschied ist, dass die übliche Masse- zu- Ladungs- Korrelation wie in der reinen Elektrophorese hier nicht ausreicht, um den elektrokinetischen Anteil an der Trennung zu erklären. Es wird gezeigt, dass für unterschiedliche Analyten mit vergleichbarer Ladungszahl, ihre Retentionsabhängigkeit auch von ihrem Molekulargewicht abhängt. Damit wird in Abhängigkeit vom Feld die Selektivität der Trennung sich grundsätzlich ähnlich verhaltender Peptide signifikant verändert.

Es wird gezeigt, dass die Retentionsfenster geladener Analyten in Abhängigkeit vom Feld signifikant verschoben werden, was in erster Linie auf ihre Ladungszahl zurückgeführt wurde. Neutrale Analyten partizipieren in keinerlei Ladungsbilanzen, sie werden nur durch die elektroosmotische Flussfelddynamik und chromatographische unspezifische Verteilungsgleichgewichte beeinflusst und zeigen damit eine vergleichbare Retention wie in der konventionellen Flüssigchromatographie. Durch Einstellung der Nettoladung der untersuchten Peptide konnte auch gezeigt werden, dass das der Fall ist wenn sie gegen den Wert Null strebt und damit auch ihre Retention zunehmend feldstärkeunabhängig wird.

Im Allgemeinen lässt sich sagen, dass die in dieser Arbeit gesammelten Ergebnisse die Anatomie der KEC darstellen und wesentliche Fortschritte bezüglich des mechanistischen Verständnisses der Flussfelddynamik (insbesondere Konzentrationspolarisation und elektroosmotischer Perfusion) als auch der Retentionsdynamik geladener Analyten beinhalten und konzentriert sich dabei auf die wesentlichsten physikalisch-chemischen Eigenschaften analytisch relevanter Spezies und der verwendeten Trennsysteme. Nach den Resultaten dieser Arbeit ist die elektroosmotische Perfusion eher als ein Spezialfall in der KEC zu begreifen. Sie erhöht zwar den intrapartikulären Stofftransport und verringert damit die axiale Bandenverbreiterung (hauptsächlich für neutrale Analyten), spielt aber für das Retentionsverhalten und die Dispersion geladener Analyten eine untergeordnetere Rolle.

Table of content

Introduction

The devised transport of a mobile phase and complex sample mixtures through high and low surface area materials induced by an externally applied electrical field plays a central role in analytical, technological, and environmental processes, including the dewatering of waste sludge and soil remediation, capillary electrophoresis, or electrochromatographic separations in particulate and monolithic fixed beds, as well as micro-chip devices [1-7]. Transport is primarily achieved via electromigration of ions (background electrolyte), electrophoresis (charged analyte molecules or particles), and electroosmosis (bulk liquid) driven by the shear stress concentrated in the electrical double layer (EDL) at charged solid-liquid interfaces [1]. The local and macroscopic behaviour and long-time average magnitude, stability, and uniformity of electroosmotic flow (EOF) in porous media are related to the physicochemical nature of the surface, the pore space morphology, and properties of the liquid electrolyte [8-22]. A detailed analysis of these parameters has a fundamental importance as it guides performance and design strategies of an electrokinetic process with respect to diffusive-convective transport schemes.

This immediately addresses fundamental aspects of capillary electrochromatography (CEC) as a rapidly emerging technique, which was proposed to add a new dimension to separation science [3]. Bulk hydrodynamic flow is achieved by electroosmosis, employing stationary phases usually developed for liquid chromatography (LC). In a very simple way CEC is often described as a hybrid technique between capillary zone electrophoresis (CZE) and LC. From an analytical point of view CEC has not yet overcome its typical "infancy problems", even though one can recognize an increasing number of applications. The reasons are found in relatively early anticipations, regarding EOF velocity profile through more complex porous media (usually borrowed from an open tube as in CZE) and theoretical assumptions for achieving differential migration (by simply synthesizing retention by chromatographic and electrophoretic formalism) [3].

However, for neutral and ion-suppressed analytes a possible benefit may arise from increased efficiencies often obtained with EOF instead of pressure-driven flow through porous media [1, 2, 23]. In addition method transfer from LC to CEC may be straightforward for neutral analytes and no descrepancies between retention in both modes have been observed [24]. Nevertheless an increase in the complexity of the method clearly means that an increase of robustness and applications (e.g. in pharmaceutical industry) can only be realized by understanding the fundamental basis for not only generating flow but also achieving differential migration for charged analytes. Most of the target molecules in bio-analytical and pharmaceutical applications are charged in nature. Until now retention modeling of charged target molecules has not been capable of showing agreement with experiment and the models in CEC are not predictive at all [25, 26].

Unless the physical basis for such a disagreement is known it surely leads to reduction of robustness and reliability, one of the worst drawbacks for any analytical technique. Starting with this critical

appraisal the present thesis covers electrohydrodynamical (flow) aspects in CEC, as well as transport aspects for charged analytes. Even though they may be seen as separate issues, it is subsequently shown that they rely on the same basic phenomena.

This thesis is structured as follows. Chapter 1 starts with a state-of-the-art review on "Fluid dynamics in capillary and chip electrochromatography" and is concerned with the phenomenological fluid dynamics in high-surface-area random porous media as stationary phase in CEC. Specifically, the pore space morphology of packed beds is analyzed with respect to the nonuniformity of local and macroscopic EOF, as well as the achievable separation efficiency. Due to the hierarchical structure of the pore space in packed beds which are characterized by discrete intraparticle mesoporous and interparticle macroporous spatial domains a finite and often significant perfusive EOF is realized in these materials. The electroosmotic perfusion through packed beds of porous particles proceeds with a significantly higher intraparticle (electroosmotic) permeability and, thus, it contributes to a substantial reduction of velocity inequalities between the inter- and intraparticle flow patterns. Concerning the electroosmotic permeability of packed capillaries the perfusive EOF has shown to offer a superior dispersion characteristics (compared to PDF employed in LC) [27]. At the same time it has long remained unrecognized that the intraparticle pore space in packed beds or the porous skeleton of meso- and/or microporous monoliths comprise ion-permselective (that is, charge-selective) regions due to local EDL overlap which actually prevails over a wide range of experimental conditions in CEC and also LC [21, 22]. This directly leads to the flow and transport issues investigated in the present thesis.

It starts in Chapter 2 with a phenomenological interrelation between electrical field driven ion-transport in electrolyte systems containing ion-permselective porous membranes, separating completely adjacent electrolyte solutions, and electrolyte systems containing discrete ion-permselective porous particles. The comprehensive view on "Concentration polarization effects in porous media" addresses key properties of porous media in CEC with a co-existence of bulk, quasi-electroneutral macroporous regions and the mesoporous compartments which are ion-permselective (due to EDL overlap). They cause different transport numbers for co-ionic and counter-ionic species, e.g., background electrolyte components, or the analytes in electrochromatographic separations. This chapter is crucial for the subsequent elucidation of the "Electrohydrodynamics in hierarchically structured monolithic and particulate fixed beds" from the more chromatographic point of view in Chapter 3. Subsequently in this thesis the dynamics of ion-permselective transport properties in fixed beds of porous adsorbent particles and monoliths is approached by employing quantitative confocal laser scanning microscopy to elucidate charge transport relations from a more physicochemical point of view in Chapter 4. The "Confocal laser scanning microscopy study of electrical-field-induced concentration polarization at curved ion-permselective interfaces" is a crucial basis for the second main part of the present thesis reflected in Chapter 5, which focuses on "Retention dynamics of charged analytes in electrochromatography". It resolves the quest of controlling and understanding the whole separation technique.

References

[1]   Probstein, R. F., *Physicochemical Hydrodynamics*, John Wiley & Sons, New York 1994.

[2]   Tsuda, T. (Ed.), *Electric Field Applications in Chromatography, Industrial and Chemical Processes*, VCH, Weinheim 1995.

[3]   Deyl, Z., Svec, F. (Eds.), *Capillary Electrochromatography*, Journal of Chromatography Library, Vol. 62, Elsevier, Amsterdam 2001.

[4]   Delgado, A. V. (Ed.), *Interfacial Electrokinetics and Electrophoresis*, Marcel Dekker, New York 2002.

[5]   Throckmorton, D. J., Shepodd, T. J., Singh, A. K., *Anal. Chem.* 2002, *74*, 784-789.

[6]   Jemere, A. B., Oleschuk, R. D., Harrison, D. J., *Electrophoresis* 2003, *24*, 3018-3025.

[7]   Broyles, B. S., Jacobson, S. C., Ramsey, J. M., *Anal. Chem.* 2003, *75*, 2761-2767.

[8]   Saksena, S., Zydney, A. L., *J. Membr. Sci.* 1995, *105*, 203-215.

[9]   Eykholt, G. R., *J. Hazard. Mater.* 1997, *55*, 171-186.

[10]   Dittmann, M. M., Rozing, G. P., *J. Microcolumn Sep.* 1997, *9*, 399-408.

[11]   Choudhary, G., Horváth, Cs., *J. Chromatogr. A* 1997, *781*, 161-183.

[12]   Erickson, D., Li, D., *Langmuir* 2002, *18*, 1883-1892.

[13]   Jiskra, J., Jiang, T., Claessens, H. A., Cramers, C. A., *J. Microcolumn Sep.* 2000, *12*, 530-540.

[14]   Gaš, B., Kenndler, E., *Electrophoresis* 2000, *21*, 3888-3897.

[15]   Banholczer, A., Pyell, U., *J. Chromatogr. A* 2000, *869*, 363-374.

[16]   Tanigawa, T., Nakagawa, T., Kimata, K., Nagayama, H., Hosoya, K., Tanaka, N., *J. Chromatogr. A* 2000, *887*, 299-305.

[17]   Bohinc, K., Kralj-Iglič, V., Iglič, A., *Electrochim. Acta* 2001, *46*, 3033-3040.

[18]   Sounart, T. L., Baygents, J. C., *Colloids Surf. A* 2001, *195*, 59-75.

[19]   Pačes, M., Kosek, J., Marek, M., Tallarek, U., Seidel-Morgenstern, A., *Electrophoresis* 2003, *24*, 380-389.

[20]   Nischang, I., Tallarek, U., *Electrophoresis* 2004, *25*, 2935-2945.

[21]   Tallarek, U., Leinweber, F. C., Nischang, I., *Electrophoresis* 2005, *26*, 391-404.

[22]   Nischang, I., Chen, G., Tallarek, U., *J. Chromatogr. A* 2006, *1109*, 32-50.

[23]   Colon, L. A., Reynolds, K. J., Alicea-Maldonado, R., Fermier, A. M., *Electrophoresis* 1997, *18*, 2162-2174.

[24]   Zhang, Y. K., Shi, W., Zhang, L. H., Zou, H. F., *J. Chromatogr. A* 1998, *802*, 59-71.

[25]   Valette, J. C., Demesmay, C., Rocca, J. L., Verdon, E., *Chromatographia* 2005, *62*, 393-399.

[26]   Nischang, I.; Spannmann, K.; Tallarek, U., *Anal. Chem.* 2006, *78*, 3601-3608.

[27]   Nischang, I., Tallarek, U., *Electrophoresis* 2007, *28*, 611-626.

1 Fluid dynamics in capillary and chip electrochromatography

1.1 Introduction

Capillary and chip electrochromatography (EC) is a relatively novel microseparation technique which has recently attracted massive interest on the academic research level. Many applications have been demonstrated both in capillary and chip EC, revealing the separation potential of this technique for a broad range of analytes including peptides and proteins, enantiomers, pollutants, and pharmaceuticals [1-13]. Several reviews have focused on practical implications and stationary phase designs using packed beds and monoliths [14-17], as well as on the coupling to mass spectrometry [18]. Besides applications and technological efforts, a central issue for efficiency in EC of, e.g., bioanalytical or pharmaceutical target molecules is the analysis and optimization of the underlying velocity field and an understanding of associated hydrodynamic dispersion.

The flow pattern of a fluid undergoing slow, laminar flow in a packed bed of particles or a monolith depends on the morphology (topology and geometry) of the pore space [19, 20]. The existence of a point-to-point difference in velocity is a fundamental property of the flow field under most general conditions [21]. Besides the inherent structural heterogeneity of the porous medium, also the actual physical origin(s) of the flow influence correlation times and lengths which characterize velocity fluctuations in the mobile phase. In contrast to nano-LC employing PDF, capillary and chip EC utilizes EOF for transporting bulk liquid and analytes through the interconnected pore space of capillary columns or non-cylindrical channels in lab-on-a-chip devices. These are either packed with small adsorbent particles or may contain monolithic structures.

Ideal EOF in a single homogeneous capillary is characterized by a flat, i.e., plug-like velocity profile at distances from the surface that are on the order of the EDL thickness which is usually estimated by the Debye screening length (λ_D) [20]:

$$\lambda_D = \left(\frac{\varepsilon_0 \varepsilon_r RT}{F^2 \sum_i z_i^2 c_{i,\infty}} \right)^{1/2} , \qquad (1.1)$$

where ε_0 and ε_r are the permittivity of vacuum and relative permittivity of the bulk solution, respectively. R is the gas constant, T the absolute temperature, and F Faraday's constant, z_i is the valency of ionic species i and $c_{i,\infty}$ its concentration in bulk electroneutral solution. EOF is generated by interaction of the local tangential component of the applied electrical field with net volume charge in the fluid side part of the EDL. In the thin-EDL-limit, meaning in this context (unpacked capillary) that the EDL thickness is much smaller than the capillary radius, both the cross-sectional velocity profile and magnitude of the EOF become independent of the capillary diameter [22]. Due to high separation efficiencies that have been obtained with electrokinetically driven fluid flows through open (unpacked) capillaries [23], as well as

packed beds [24-26], any factor which influences zone dispersion under these electrokinetic and (electro)hydrodynamic conditions should be characterized and become controllable, in principle. The local and macroscopic velocity profile of the EOF and its stability have a large impact on improving the performance, but also the reproducibility and robustness of EC systems.

Because of its utmost importance and relatively little attention it has received in the past compared to applications of EC, this chapter is concerned with the EOF velocity field in packed beds and monoliths. It is structured as follows. We first discuss pore-scale EOF in the relatively large (compared to the EDL thickness) interparticle pores of packed beds of nonporous, that is impermeable and nonconducting particles considered as "packed-bed-analogon" to EOF through a single homogeneous capillary and address a general microscopic nonuniformity of the local EOF velocity profile in porous media with inherently nonuniform shape of the flow channels. Then, we analyze macroscopic EOF heterogeneities in packed beds caused by the presence of confining walls, in particular, the dependence on a mismatch of ζ-potentials at the wall of the confining channel or capillary and the particles external surface (electrokinetic wall effect), but also on radial porosity fluctuations with a focus on low column-to-particle diameter ratios (geometrical wall effect) below 25, being typical for EC systems. Subsequently, we consider EOF through packed beds of porous (permeable, conducting) particles.

1.2   Pore-scale electroosmotic flow in packed beds of nonporous particles

Starting from a macroscopic point of view the EOF velocity averaged over the column cross-section may be characterized by the electrical conductivity ratio which becomes accessible experimentally via conductivities of a packed column and an identical, but open tube saturated with the same electrolyte solution. It is assumed that the EDL makes a negligible contribution to the total conductivity of the packed bed [27, 28]. The macroscopic model of Overbeek and Wijga [27] has been successfully employed by Zeng et al. [29] for a capillary packed with nonporous (impermeable, nonconducting) particles and was extended to EOF in EC with porous (permeable, conducting) particles [30]. Essentially, these approaches do not contain any valuable information on the local dynamics of EOF in porous media.

A number of theoretical and experimental studies have been reported and used for the investigation of EOF in open channel systems [31-41], as well as packed beds [30, 42-44]. In agreement with experimental results for EOF through a single homogeneous capillary, demonstrating plug-flow behaviour under ideal conditions [45, 46], it was shown by Griffiths and Nilson [31] that longitudinal dispersion coefficients can be orders of magnitude smaller than for PDF. Most of the theoretical approaches used to study EOF in disordered porous media like packed beds are based on a representation of the material as an assembly of individual channels which only allows to find the average velocity. Further, and more important for the dispersion characteristics, it neglects the actual morphology of a material, e.g., the continuously varying pore cross-sections. The nonuniform cross-section of interparticle pores in a packed bed influences the distribution of the local electrical field strength and resulting EOF velocities, which both are uniform in a single homogeneous capillary in the thin-EDL-limit.

In addition, also numerical studies of the EOF problem were mostly performed in open channel systems [47-55]. Until now, direct numerical simulation of EOF in random porous media is a challenging task because of the necessity to resolve, in general, the coupled hydrodynamic, electrostatic, and mass transport problems subjected to the complex geometrical boundary conditions represented by the solid-liquid interface. At the same time, the very different length scales ranging from λ_D of typically 1-100 nm to the characteristic dimension of the whole system (for instance, the capillary diameter) need to be covered. Coelho et al. [56] have developed a numerical solution to the problem of EOF through porous media, in particular, a random array of particles. They used a relatively coarse spatial discretization step to arrive at reasonable computation times. Their model was restricted to the case of a thick EDL and low ζ-potentials (Debye-Hückel approximation). Recent three-dimensional numerical studies carried out by Hlushkou et al. [57, 58] have resolved EOF in regular and random, confined and bulk packings of solid, dielectric (impermeable, nonconducting) spheres under more general conditions, including arbitrary value and distribution of electrokinetic potential at the solid-liquid interface, electrolyte composition, and pore space morphology.

Figure 1.1 demonstrates a fundamental microscopic (interparticle pore-level) nonuniformity of the axial EOF velocity component in a confined sphere packing with a column-to-particle diameter ratio of 10 [57]. The EDL thickness is negligibly thin, in this context, compared to the sphere radius r_p (i.e., $r_p/\lambda_D \gg 1$; thin-EDL-limit). Further, the ζ-potentials of the column wall (ζ_w) and the spheres (ζ_p) are identical. Still, a

nonuniform distribution of the axial EOF velocity exists in the interparticle pore space throughout the packing; velocity profiles are systematically curved over the complete cross-section of an individual pore.
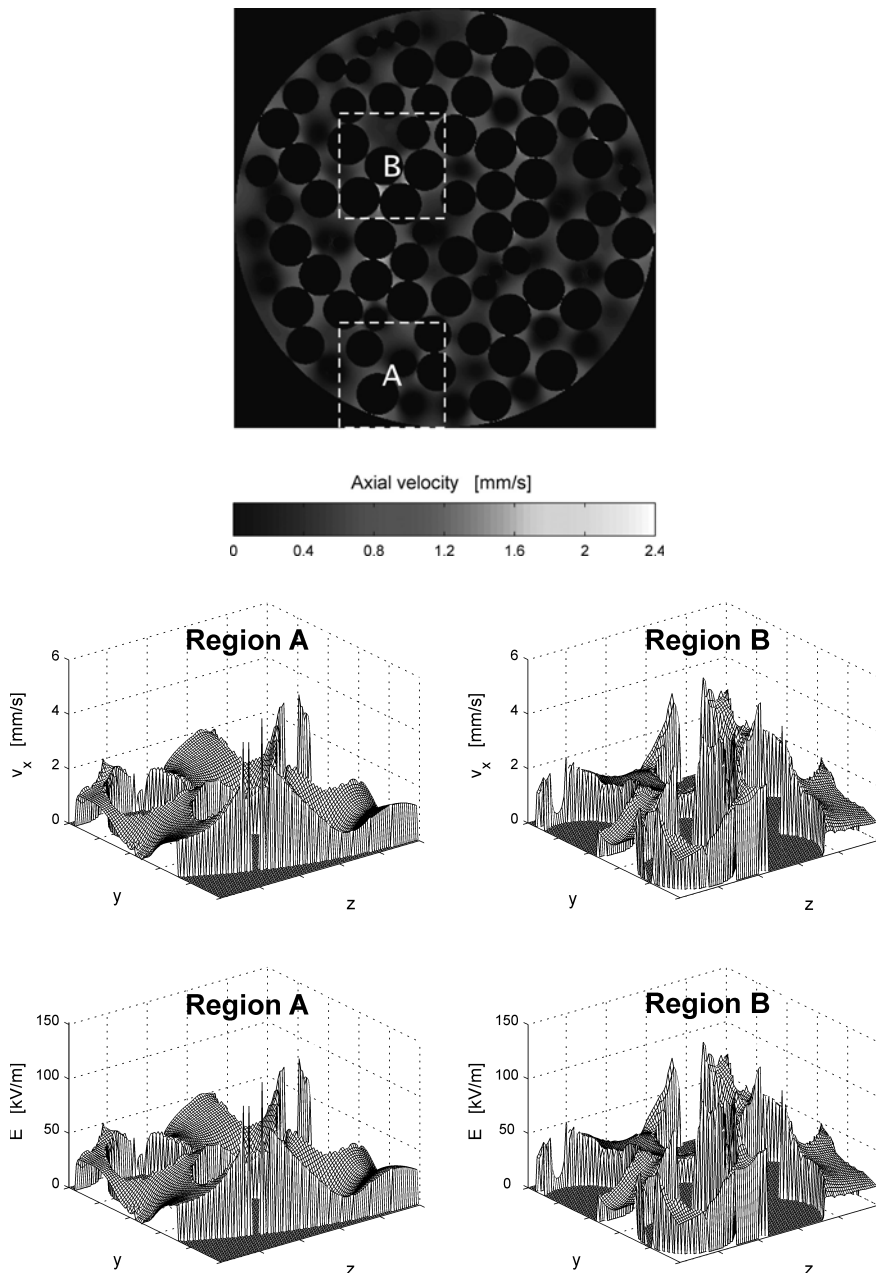

Figure 1.1 Distribution of the axial EOF velocity in a confined packing of monosized solid, dielectric spheres with a column-to-particle diameter ratio of 10. The mobile phase is an aqueous strong electrolyte solution at T = 298 K. ζ-potentials of the column wall (ζ_w) and the particles (ζ_p) are identical, $\zeta_w = \zeta_p = -50$ mV. The applied field strength is $E_{ext} = 50$ kV/m. The profiles of the local axial EOF velocity component v_x (top) and the local electrical field strength E (bottom), here shown for two selected regions of the packing, are nearly identical. The EDL thickness is negligibly thin compared to the sphere radius (thin-EDL-limit). Reproduced with permission from [57]. Copyright 2005 American Chemical Society.

This is illustrated in Figure 1.1 for two regions selected from the packing (regions A and B, respectively). The nonuniform distribution of EOF velocities in a packed bed of solid, dielectric spheres originates in a nonuniformity of the local electrical field strength and should be interpreted in the context of an expected

similitude for the electrical field and EOF velocity field in the thin-EDL-limit [32, 33]. This similarity is seen in Figure 1.1, demonstrating that the distributions of local electrical field strength and EOF velocity are nearly identical.

In other words, the inherent variations in channel cross-sectional area or shape result in a nonuniform distribution of the local axial component of the applied electrical field, particularly at the solid-liquid interface, which leads to local variations in the EOF slip velocity used to formulate the velocity boundary condition at the solid-liquid interface in the thin-EDL-limit [57]. Based on these results of numerical simulations it can be concluded that a "reference" plug-like velocity distribution in a single homogeneous channel does not imply the existence of a flat pore-level velocity profile in the interparticle pore space of a packed bed. Even the imposition of the slip-velocity boundary condition at the solid-liquid interface does not result in a locally flat profile. The deviation from the ideal plug-like EOF profile suggests that also hydrodynamic dispersion associated with EOF through a packed bed differs significantly from that in a single homogeneous "reference" capillary or channel.

To summarize, the results of numerical simulations (Figure 1.1) demonstrate that a locally flat velocity profile for electrokinetic flow through the interparticle pore space of packed beds which are employed for EC separations in capillary and chip format does not exist, even in the thin-EDL-limit and with uniform surface properties throughout the packing. These results contradict relatively early anticipation [59-61], in which the plug-like velocity distribution in a single-straight, open, homogeneous channel, has been translated to more complex porous media with a varying pore space morphology between the particles. Still this anticipation finds widespread acceptance [62-69].

1.3   Wall effects on packing microstructure and macroscopic flow heterogeneity

Due to the nonuniform radial distribution of voidage, permeability, and interstitial velocity in a critical region close to the confining wall, a small column diameter (d_c) to particle diameter (d_p) ratio influences the transport properties in fixed-bed reactors and chromatographic columns, which is an old and well investigated issue in engineering science [70, 71]. It has been shown in early studies and for packings of uniform spheres with a smooth surface that the interparticle porosity (ε_{inter}) starts with a maximum value of unity at the column wall, then displays damped oscillations with a period close to d_p over a distance of 4-5 d_p into the bulk of the bed, until the void fraction reaches values typical for random-close packings of particles (ε_{inter} = 0.38-0.4) [72]. This geometrical wall effect is explained by a decrease of packing order as the distance from the wall increases. It can have a strong impact on the macroscopic flow heterogeneity, axial dispersion, and particle-to-fluid heat and mass transfer, especially at column-to-particle diameter ratios below 25 when this critical wall region (wall annulus) begins to occupy a substantial volumetric fraction of the bed. This immediately addresses packed beds employed in capillary and chip EC systems where about 10-20 particle diameters over the channel cross-section are quite common.

Figure 1.2 shows radial porosity distributions in simulated confined packings of monosized spheres (lines), together with independently obtained experimental data (symbols) [57, 72, 73]. The porosity distributions share common features, in particular, a similar location and magnitude of the maxima and minima, as well as a similar decay of the oscillations at increasing distance from the wall. It means that these packings have similar macroscopic geometrical properties and radial variations in porosity related to the more ordered (layered) structure near the confining wall. It has been assumed that wall effects which are important for the dispersion with hydraulic flow become less pronounced in EC when the ζ-potential of the container wall is the same as that of the packing, implying that the macroscopic velocity profile is flat [30]. Indeed, a systematic appearance of radial porosity fluctuations close to the column wall has been neglected in describing EOF velocity profiles in packed beds at lower aspect ratios which are also relevant to capillary and chip EC systems [30, 44, 74]. Instead, only a mean bed porosity is usually considered.
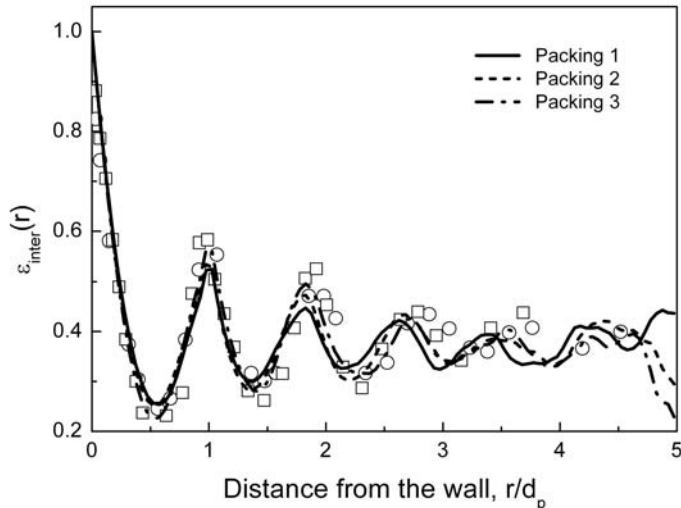

Figure 1.2 Radial distribution of interparticle porosity ε_{inter}(r) from the inner surface of a cylindrical column into its center for three simulated packings of monosized solid, dielectric spheres with a column-to-particle diameter ratio of 10 [57]. All simulated packings have the same average porosity of 0.37, but originate from different initial seeds. Symbols correspond to experimental data of Benenati and Brosilow [72] (circles) and Giese [73] (squares). Reprinted with permission from [57]. Copyright 2005 American Chemical Society.

Figure 1.3a shows the distribution of simulated interstitial velocities in packing 1 of Figure 1.2 [57]. Clearly, these data allow to conclude that radial variations of the axial EOF velocity in confined sphere

packings strongly correlate with the radial porosity distribution. Even for a uniform ζ-potential distribution ($\zeta_w = \zeta_p$) the EOF displays a significant heterogeneity caused by the geometrical wall effect. In other words, Figure 1.3a resolves a systematic pore-to-pore variation of EOF velocities close to the wall. This nonuniformity bears a close relation with the radial porosity distribution, similar to PDF [75].

The radial distribution of EOF velocities (Figure 1.3a) caused by fluctuations in packing porosity (Figure 1.2) can be analyzed through the local conductivity [57]. It should be recalled that the conductivity of a packed bed of nonconducting spheres saturated with electrolyte solution relative to that of the bulk solution results from [76] i) the reduction of void space and total cross-sectional area, ii) the decrease of local electrical field strength and an increase in migration distance for ions due to the tortuous nature of the interparticle channels, as well as (iii) dilatation and constriction of the channels. This may, in addition, become a function of the radial position inside the packed bed. In practice, the Tobias equation [77] is often used as an empirical relationship between conductivity ratio and porosity of a packed bed. Thus, the conductivity of the packing can be regarded as being a function of radial position in the wall annulus (higher conductivity than in the bulk packing). As a consequence, radial variations of the EOF velocity in confined packings (higher velocities in the wall annulus) strongly correlate with the actual radial porosity distribution [57].
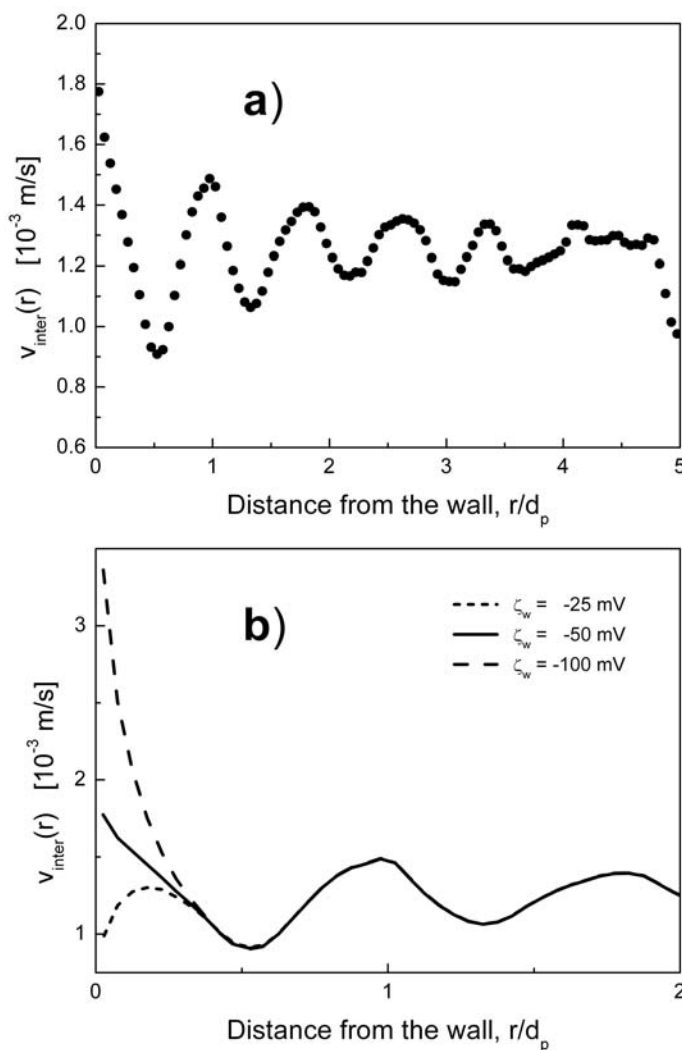

Figure 1.3 a) Radial distribution of the interparticle EOF velocity $v_{inter}(r)$ in packing 1 of Figure 2. Fluid phase properties as in Figure 1, $\zeta_w = \zeta_p = -50$ mV, and $E_{ext} = 50$ kV/m. b) Radial distribution of the interparticle EOF velocity in packing 1 of Figure 2 for different values of the ζ-potential at the inner surface of the confining cylindrical column (ζ_w as indicated; $\zeta_p = -50$ mV). Fluid phase properties as in Figure 1 and $E_{ext} = 50$ kV/m. Reprinted with permission from [57]. Copyright 2005 American Chemical Society.

In addition to this geometrical wall effect and its influence on velocity heterogeneity with PDF and EOF through confined packings, it is the general mismatch of ζ-potentials at the surfaces of the confining wall and the support particles which comprises an electrokinetic wall effect. It can influence the EOF heterogeneity, particularly at low column-to-particle diameter ratios [30, 44, 57]. For example, electrokinetic potentials at the inner surface of quartz capillaries up to -100 mV and above are not

unusual. For the buffers and ionic strengths used in EC this value may be regarded as an upper limit and ζ_w typically ranges between −50 mV and −100 mV [26, 78-80]. By contrast, ζ_p of most commercial, e.g., cation-exchange particles employed in capillary EC is significantly lower than ζ_w of the commonly used fused-silica capillaries [81]. Then, although these surfaces with sulfonic acid (cation exchange particles) and silanol groups (fused-silica capillary) both carry negative charge, differences between ζ_p and ζ_w can still become important. For chip EC, on the other hand, ζ_w of the employed microfluidic substrates (which confine the packed beds) may be significantly lower than ζ_w of the fused-silica capillaries [82], even lower than ζ_p of the stationary phase particles.

The differences in ζ_p and ζ_w influence both volumetric EOF and hydrodynamic dispersion which becomes important at low column-to-particle diameter ratios. For EOF through packed beds at low aspect ratio, it has been shown theoretically by Rathore and Horváth [30] and Liapis and Grimes [44] that the excess ζ-potential, resulting in a difference between the velocities associated with the capillary surface and the particles surface, can have a deleterious effect on the column cross-sectional flow profile and average velocity. These authors have extended the model of Overbeek and Wijga [27] for EOF through capillary columns in EC (which are usually packed with spherical particles) to account for the effect of differences in ζ-potential at the capillary inner wall and the particles external surface. They derived an expression for the EOF velocity in dependence of radial position. According to that model, if the ζ-potential of the capillary wall is identical to that of the support material, the EOF velocity becomes constant over the whole column cross-section, while differences in ζ-potential result in a decrease or increase of the local axial EOF velocities in a near-wall region of the bed (electrokinetic wall effect).

It should be pointed out that this theoretical model does not consider the documented fluctuations in the interstitial porosity and tortuosity of packed beds caused by the more ordered (layered) geometrical structure in the vicinity of the confining wall (cf. Figures 1.2 and 1.3a). Consequently, an underestimation of the interparticle porosity in the near-wall region or annulus by use of a mean porosity in the model of Rathore and Horváth [30] and also that adapted by Liapis and Grimes [44] results in artificially reduced values of the EOF velocity component close to the confining wall. This becomes more important for lower column-to-particle diameter ratios which characterize most packed beds realized in capillary EC, where aspect ratios below 25 are rather common.

Figure 1.3b allows to estimate more quantitatively the consequence of differences in ζ-potential at the particle and wall surfaces on the EOF nonuniformity. This figure shows the radial distribution of interparticle axial velocities in packing 1 of Figure 1.2 for different values of ζ_w (−25 mV, −50 mV, and −100 mV) at a constant ζ_p = −50 mV. Distributions coincide nearly perfectly as the distance from the wall becomes larger than only half a particle diameter, indicating that the value of ζ_w affects the axial EOF velocity just in direct vicinity to the wall. Thus, the electrokinetic wall effect operates over a smaller distance from the wall than the geometrical wall effect. Further, even with a match of ζ-potentials ($\zeta_w = \zeta_p$) an EOF velocity heterogeneity remains close to the wall due to the locally dominating porosity effect (leading to an increased conductivity) which may be reduced by carefully adjusting $\zeta_w < \zeta_p$ (Figure 1.3b).

In general, dispersion with EOF in confined sphere packings depends on differences in ζ-potential at the particle and wall surfaces. Still more important is the actual column-to-particle diameter ratio in view of the resulting radial porosity distribution function which reflects a volumetrically significant (geometrical) wall effect that is simply caused by packing hard spheres against a hard wall. A nonuniform size distribution can reduce the heterogeneity of interparticle axial EOF velocities in confined packings; smaller spheres better fill voids between the larger ones, especially between larger ones and the hard wall, thereby reducing the amplitude of local porosity fluctuations [57]. As a consequence, the EOF velocity field becomes more uniform.

Experimental investigations using pulsed field gradient nuclear magnetic resonance have demonstrated that significantly higher EOF velocities close to the wall than in the center of the column strongly affect hydrodynamic dispersion, leading to a long-time disequilibrium in the fluid molecules displacements [83, 84]. Figure 1.4 illustrates the electrical field-dependence of averaged propagator (displacement probability) distributions of the fluid (water) molecules in a packed capillary with low column-to-particle diameter ratio, thereby revealing the associated consequences for axial dispersion. Both the capillary wall and the particles surface carry negative charge, but in this case $\zeta_w \gg \zeta_p$. As the electrical field strength is increased (Figure 1.4a) the significantly faster wall component becomes visible through a decent shoulder towards higher molecular displacements at $E_{ext} = 21.1$ kV/m from an initially almost Gaussian distribution ($E_{ext} = 8.7$ kV/m). With a further increase of the applied field strength, the propagator distribution becomes very broad (Figure 1.4b) and the displacements of the fastest fluid molecules in the wall annulus (propagator front) are more than three times higher at $E_{ext} = 49.2$ kV/m than those moving in the central core of the packed bed. This macroscopic flow heterogeneity requires a trans-column equilibration of the fluid molecules, i.e., an exchange via lateral dispersion (mostly by diffusion) over the complete capillary radius to approach a Gaussian.
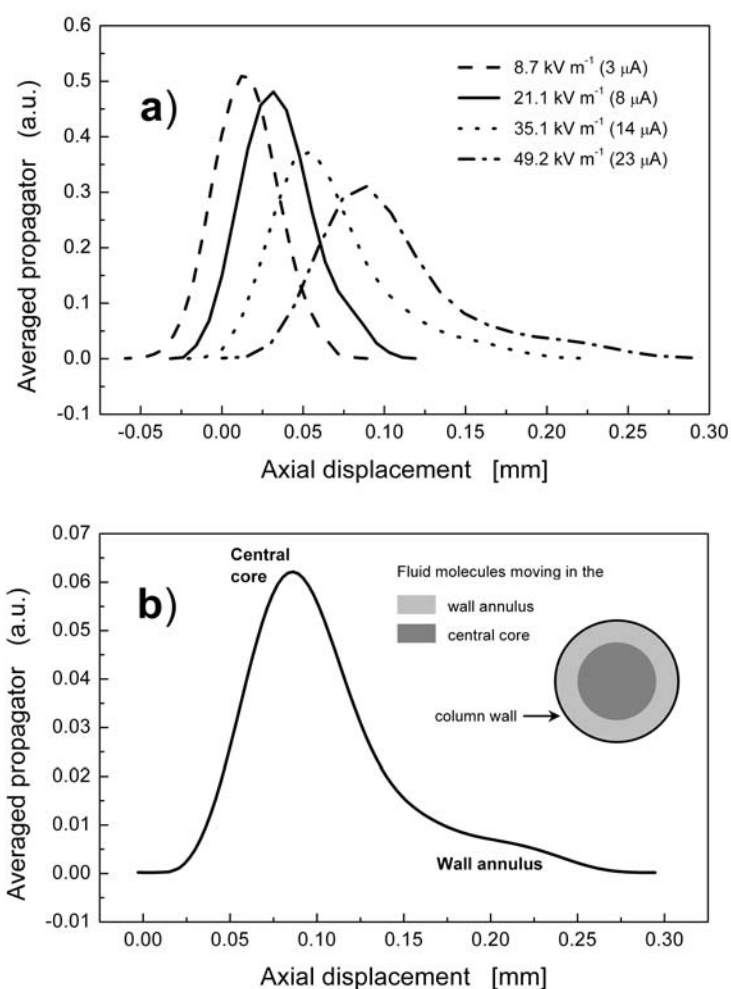

Figure 1.4 Electrokinetic wall effect. a) Axial displacement probability (averaged propagator) distributions of the fluid molecules as a function of applied field strength, electrical currents as indicated. b) Averaged propagator distribution for $E_{ext} = 49.2$ kV/m. Reproduced with permission from [87]. Copyright 2002 American Chemical Society.

To summarize, besides the electrokinetic wall effect, a geometrical wall effect reflected by fluctuations of the interparticle porosity in packed beds plays a more important role in capillary and chip EC than usually admitted, because aspect ratios typically remain below 25.

1.4   Electroosmotic perfusive flow in packed beds of porous particles

The term perfusion chromatography for packed beds of porous (permeable, conducting) particles refers to separation processes with non-zero intraparticle velocity. In classical solid-liquid chromatography it can be utilized for reducing the mobile phase mass transfer resistance originating in the intraparticle stagnant zone of packed beds [85-89]. Consequences of this phenomenon were recognized already very early, e.g., in size-exclusion chromatography [90] and catalyst design [91, 92], or for nutrient transport in biological pellets [93]. A driving force for intraparticle hydraulic flow [85, 94] resulting in a non-zero velocity component can assist or even dominate – depending on its magnitude relative to the time scales of analyte diffusion and adsorption-desorption – conventional, diffusion-limited intraparticle transport. It reduces holdup dispersion due to stagnant zones which dominates the longitudinal dispersion in packed beds of porous particles at reduced velocities (or Peclet numbers) above 25 [95].

However, mobile phase perfusion in packed beds of permeable particles is realized with hydraulic flow only when relatively high column pressure drops and particles with large pores are used. This, in turn, limits the intraparticle surface-to-volume ratio regarding the mechanical strength or adsorption capacity of a material. In general, perfusion with hydraulic flow becomes important only for the transport of slowly diffusing (large) molecules [87].

By contrast, electroosmotic perfusion through packed beds of porous particles proceeds with significantly higher intraparticle (electroosmotic) permeability [96-98] and contributes to a substantial reduction of velocity inequalities between inter- and intraparticle flow patterns. Concerning the electroosmotic permeability of packed capillaries the perfusive EOF has shown to offer a superior dispersion characteristics (compared to PDF) which accompanies a reduction of velocity extremes in the mobile phase flow pattern [42, 99-101]. In particular, plate heights and dispersion coefficients reduced by up to one order of magnitude with respect to those found with PDF have been reported [20, 42, 98, 99].
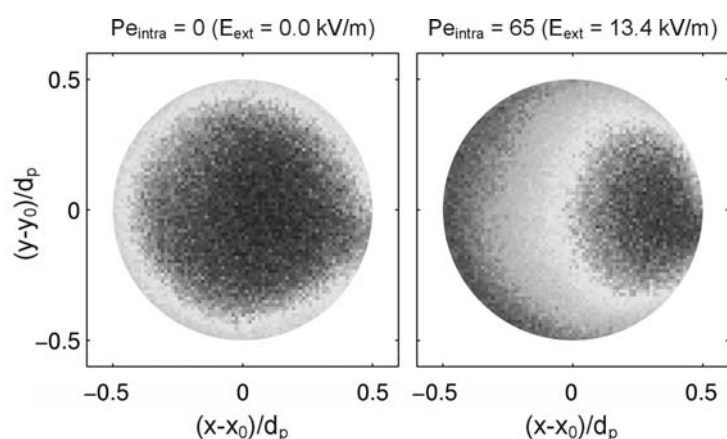

Figure 1.5 Two-dimensional distributions of electroneutral tracer representing the uptake by (and release from) a spherical mesoporous glass bead in a packed bed. The applied electrical field ($E_{ext} = 13.4$ kV/m) creates electroosmotic mobility from left to right which results in a substantial value of the intraparticle Peclet number ($Pe_{intra} = u_{intra}d_p/D_m$, where u_{intra} denotes the average intraparticle EOF velocity, d_p the particle diameter, and D_m the diffusion coefficient of the tracer in the mobile phase), indicating convection-dominated intraparticle transport by the EOF. Reproduced with permission from [107]. Copyright 2003 Wiley-VCH.

Figure 1.5 demonstrates that significant intraparticle EOF exists even under conditions of EDL overlap in the intraparticle pores. This has been shown by confocal laser scanning microscopy using a capillary packed with spherical mesoporous glass beads. By employing refractive index matching throughout the packing both transient and stationary intraparticle profiles of an electroneutral, nonadsorbing fluorescent tracer could be analyzed quantitatively, allowing the determination of intraparticle EOF velocities based on a simple mathematical model [102, 103]. As seen in Figure 1.5, diffusion-limited transport in the absence of an applied field produces distribution profiles with spherical symmetry during the tracer uptake by (and release from) a glass bead. This is well-known behaviour [104-108]. By contrast, an examination of the tracer distributions observed in the presence of an electrical field (E_{ext} = 13.4 kV/m) reveals deviations from this spherical symmetry. The intraparticle velocity field responds to the unidirectional electrokinetic driving force, as is evidenced by the tracer distributions which have become unsymmetrical in the macroscopic field direction. At the same time, they retain axial symmetry. Thus, the symmetry of the analyte profiles is reduced from spherical to axisymmetric. The applied field results in an intraparticle electroosmotic mobility from left to right in Figure 1.5. In other words, the intraparticle EOF during tracer uptake (release) moves the concentration minimum (maximum) downstream as compared to pure molecular diffusion, resulting in higher (lower) concentrations in the upstream half of the sphere than the downstream. This is caused by the fact that convection operates in the same (opposite) direction as diffusion in the upstream half of a bead, but opposite (parallel) to diffusion downstream.

An important parameter for analyzing intraparticle forced convection with EOF in packed beds of porous particles is the intraparticle EDL overlap represented by r_{intra}/λ_D [20, 42, 109-111], where r_{intra} denotes the mean pore radius. The results of detailed experimental studies of the electroosmotic mobility (μ_{eo}) in packed beds of particles with different intraparticle porosities and pore sizes are shown in Figure 1.6 [109]. Nonporous particles have been included in this study for comparison. These data confirm a different electrokinetic behaviour of porous (Figure 1.6b) vs. nonporous (Figure 1.6a) spherical particles consisting of the same base material. In particular, a continuous decrease of μ_{eo} with increasing ionic strength is found for nonporous particles (Figure 1.6a). It characterizes "normal" or "conventional" EDL behaviour insofar as, while the ionic strength increases, the EDL is compressed which results in a reduced shear-plane potential at the solid-liquid interface [28]. By contrast, μ_{eo} for the porous particles displays pronounced maxima at a location that depends on ionic strength in a particular case because of the different intraparticle pore sizes (Figure 1.6b) [109].

Thus, in contrast to the familiar behaviour of the hard (solid, dielectric) spheres the trend in μ_{eo} for the porous particles (Figure 1.6b) reveals differences which depend on intraparticle porosity and the actual EDL overlap, as reflected by the ratio r_{intra}/λ_D (the assumption of a thin EDL cannot be made inside the particles). With increasing concentration of Tris buffer from 10^{-4} M μ_{eo} first increases, then moves through a maximum at some particle-specific concentration between 10^{-3} and 10^{-2} M, followed by a decrease towards relatively similar curves above ca. 10^{-2} M Tris. Porous particles are permeable for EOF and conducting, depending on the intraparticle porosity and pore sizes. At lower buffer concentrations μ_{eo} for the solid spheres (Figure 1.6a) significantly exceeds that of any porous spheres used in that study (Figure 1.6b). It means that, as an originally solid, dielectric sphere is made permeable and conducting, the ratio

of specific conductivities within the now porous particle and bulk liquid will increase from zero, bending electrical field lines toward the particles interior which reduces the tangential field component at the particles external surface.

Consequently, this contribution from the porosity effect reduces EOF velocities associated with the shear stresses concentrated in the relatively thin EDL at the particles external solid-liquid interface, and it can explain the decreased values of μ_{eo} with respect to solid, dielectric spheres at lower ionic strengths (Figure 1.6b, between 10^{-4} and about 2×10^{-3} M Tris) where strong intraparticle EDL overlap prevails. However, this contribution to μ_{eo} of the porous particles is more than compensated at increasing buffer concentration by the perfusion effect due to the intraparticle-forced EOF, resulting also in a higher average velocity through the packing. The maximum in μ_{eo} then is a consequence of competitive contributions from this intraparticle EOF (increasing perfusion) and the normal EDL behaviour at the particles external surface. The latter effect which ultimately dominates (leading to the decrease of μ_{eo} above 2×10^{-3} M Tris, although intraparticle EDL overlap continues to be further reduced) has already been recognized as the origin of a continuous mobility decrease at increasing ionic strength for the nonporous spheres (Figure 1.6a).
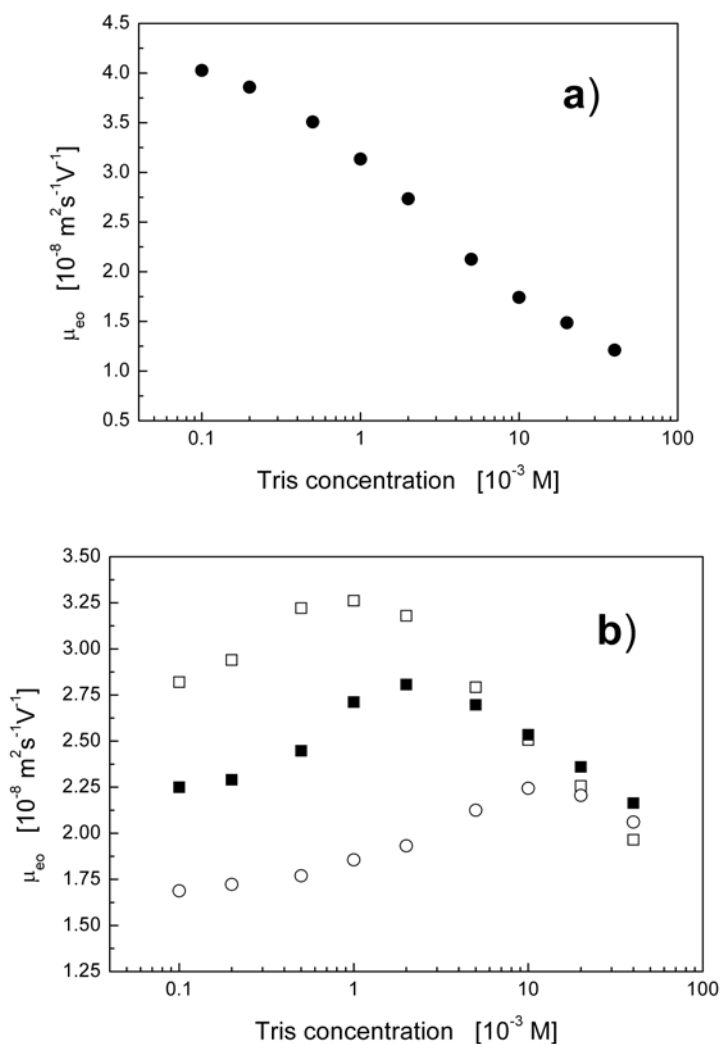

Figure 1.6 Electroosmotic mobility (μ_{eo}) in fixed beds (packed capillary columns) of spherical particles depending on the effective mobile phase Tris concentration in 80:20 acetonitrile/water (v/v). a) Nonporous particles (●). b) Porous particles with intraparticle mean pore radius (r_{intra}) of 20.5 nm (○), 52.5 nm (■), and 116 nm (□), respectively. Reprinted with permission from [109]. Copyright 2003 American Chemical Society.

To summarize, the dependence of μ_{eo} in packed beds is a consequence of basically three contributions [109, 110]: i) normal or conventional EDL behaviour at the particles external surface, leading to a decrease of mobility with increasing ionic strength, ii) generation of intraparticle volumetric EOF (increasing with increasing ionic strength), and iii) the porosity of a particle. The last contribution results from the fact that conducting electrolyte in the particle introduces a normal component to the electrical field at its outer surface. This reduces a fields tangential component, but because the latter determines velocity at the particles external surface, it is expected to decrease compared to a solid particle, the more as porosity increases. This is demonstrated by Figure 1.7 [109, 112].
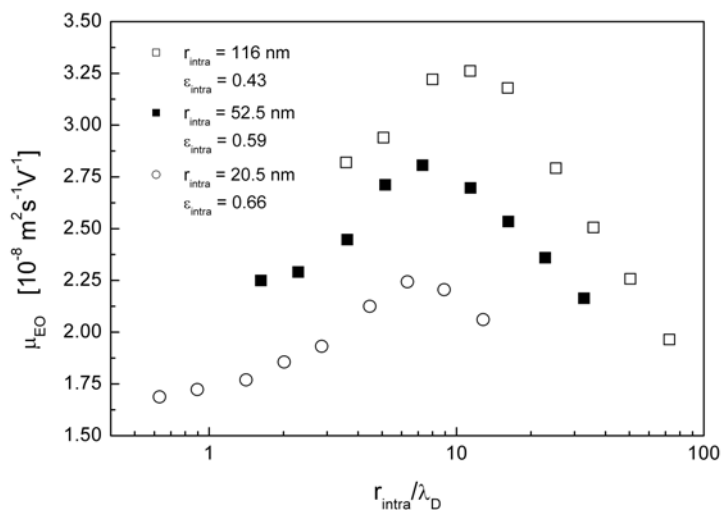
Figure 1.7 μ_{eo} vs. r_{intra}/λ_D for packed beds of spherical porous particles with different intraparticle mean pore radius (r_{intra}) and porosity (ε_{intra}). Same conditions as in Figure 6. Reproduced with permission from [114]. Copyright 2003 American Chemical Society.

Due to the relatively small particle diameters (d_p = 3-5 μm) and limitations in maximum electrical field strength and currents resulting from Joule heating, the plate height data in capillary and chip EC are usually acquired only over a limited range of EOF velocities, typically not exceeding 2-3 mm/s (translating to a limited range of Peclet numbers, Pe). Thus, it is difficult to adequately differentiate between dispersion processes originating in the flowing and the remaining stagnant zones of packed beds, especially in view of a plate height analysis [95, 98, 110, 113-116]. With PDF the stochastic velocity fluctuations in the interparticle pore space cause mechanical dispersion which grows linearly with Pe = $u_{av}d_p/D_m$ (where u_{av} is the average velocity through the bed and D_m the analyte or tracer diffusivity in the mobile phase). Further, regions of zero velocity inside the particles and close to their external surface give rise to nonmechanical contributions growing as Pe^2 (holdup dispersion) and Pe·ln(Pe) (boundary-layer dispersion), respectively [115].

Figure 1.8 compares axial dispersion coefficients (D_{ax}) normalized by D_m for EOF and PDF through packings of unusually large particles (d_p = 40 μm) in order to realize values of Pe with EOF up to 20 [98]. The EOF demonstrates an overwhelming performance. Compared to PDF the range over which molecular diffusion still controls the dispersion (D_{ax}/D_m < 1) extends to much higher values of Pe. Moreover, dispersion coefficients are reduced by up to one order of magnitude. The dependence of electroosmotic perfusion on r_{intra}/λ_D is

Figure 1.8 Axial dispersion (D_{ax}/D_m) in packed beds of porous particles vs. the Peclet number (Pe = $u_{av}d_p/D_m$, where u_{av} denotes the average velocity through a bed, d_p the mean particle diameter, and D_m the diffusion coefficient in the mobile phase) for pressure-driven flow (PDF) (○, □) and electroosmotic flow (EOF) (●, ■). Reprinted with permission from [98]. Copyright 2001 Wiley-VCH.

further illustrated by the two different intraparticle pore sizes in Figure 1.8. EDL overlap is effectively suppressed with the larger pores ($r_{intra}/\lambda_D \approx 25$), while it remains significant with the smaller pores ($r_{intra}/\lambda_D \approx 1$). Yet, the hydrodynamic dispersion for EOF through the bed of particles with smaller intraparticle
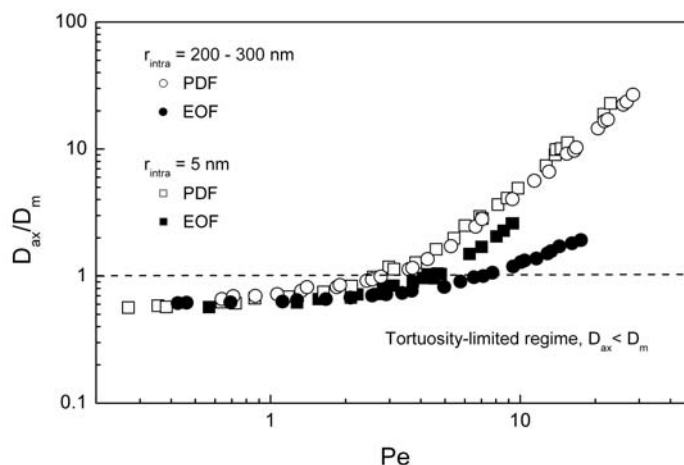
pores (r_{intra} = 5 nm) is still improved compared to PDF, although it is difficult to relate this improvement quantitatively to any physical mechanism like the electroosmotic perfusion and/or a reduced mechanical dispersion, because even these data with large particles are acquired over only a too limited range of Pe.

As shown in Figure 1.9 the highest Pe realized in EC with capillary columns and typical particle sizes (d_p ≈ 3 μm) [109] is necessarily much smaller than in Figure 1.8, by about one order of magnitude. With such a small particle size the electroosmotic perfusion mechanism has a little impact on axial dispersion. In other words, for all ionic strengths (Figure 1.9) the data remain within the diffusion-limited regime of axial dispersion ($D_{ax} < D_m$), although a slight improvement in D_{ax}/D_m (scaling with r_{intra}/λ_D) remains discernible.
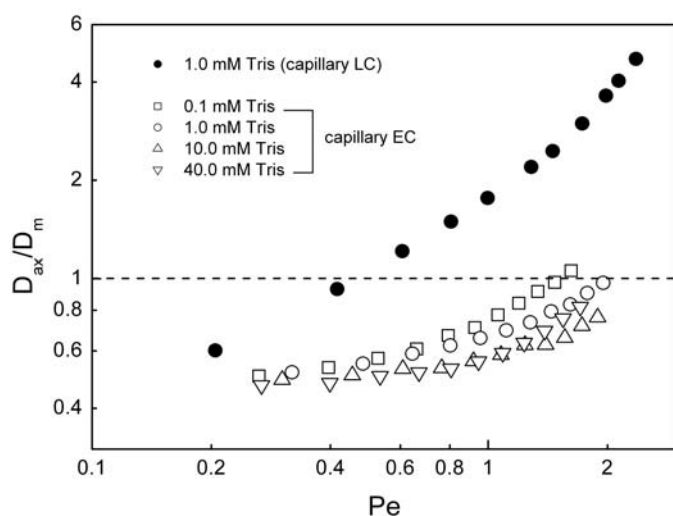

Figure 1.9 Influence of mobile phase Tris concentration in 80:20 acetonitrile/water (v/v) on D_{ax}/D_m of methylbenzoate vs. the Peclet number (Pe = $u_{av}d_p/D_m$, where u_{av} denotes the average EOF or PDF bed velocity, d_p the mean particle diameter, and D_m the diffusion coefficient in the mobile phase). The packing is made of porous C18-silica-particles with d_p = 2.45 μm and r_{intra} = 52.5 nm. Data for capillary LC with the same packing are included for comparison. Reproduced with permission from [115]. Copyright 2004, Wiley-VCH.

Two conclusions about intraparticle pore size and particle size can be made. Because of the different operational domain of the perfusion mechanism with EOF compared to PDF, very large pores are not needed in EC systems for realizing significant electroosmotic perfusion. The pore space morphology rather should be optimized in view of the surface-to-volume ratio, because packed beds of high-surface-area particles (with smaller pores) are required for difficult separations regarding resolution [117]. In general, any flow inside particles is advantageous for zone spreading because it reduces, in a global sense, the velocity inequality of the flow pattern [118]. However, it becomes less important compared to intraparticle diffusion as the particle diameter is reduced towards submicrometer dimensions. In other words, diffusive intraparticle mass transfer then is increasingly effective with respect to convective transport. For example, plate height data for columns packed with nanoparticles cannot be recorded for sufficiently high velocities that would allow to leave the regime where axial diffusion dominates the overall dispersion (Figure 1.9) which presents the ultimate limitation to performance [60, 119].

Finally, the diffusivities of relevant analytes span a range from 10^{-9} to 10^{-12} m^2/s and, thus, they also determine the relative importance of the electroosmotic perfusion mechanism via the achievable intraparticle Peclet number (Figure 1.5).

1.5   Conclusions

Employing advanced numerical simulations, it is now possible to obtain complete three-dimensional information on EOF velocity fields and resulting dispersion in packed beds. This insight is difficult to gain by experimental techniques. One major conclusion of these simulations is that the local (pore-level) velocity profile in the interparticle pore space of a bed of solid, dielectric spheres is nonuniform from a fundamental point of view (Figure 1.1). Deviation from the flat, plug-like EOF velocity profile observed in a single homogeneous capillary or channel (in the thin-EDL-limit) is caused by a nonuniform distribution of local electrical field strength in the packing which, in turn, can be directly related to local variations in cross-sectional area of the interparticle pore space. This dynamics of local EOF in a packed bed as compared to the much simpler, more readily anticipated "single-channel porous medium" (a single homogeneous capillary or channel) thus has a purely morphological origin.

The more ordered packing structure in confined sphere packings close to the column wall forms the basis for further EOF heterogeneity. The higher wall than bulk porosity over a distance on the order of 4-5 particle diameters from the wall (Figure 1.2) results in higher local axial velocities (Figure 1.3a). In addition, the local EOF velocity also depends on differences in ζ-potential at the column wall and particle surface. This effect prevails over a distance of less than one particle diameter from the wall (Figure 1.3b). While both effects (electrokinetic and geometrical wall effect) become relatively unimportant at increasing column-to-particle diameter ratio, they remain important for the performance of capillary and chip EC systems in the general line of miniaturization of the channel dimensions (Figure 1.4), which is usually not accompanied by a corresponding reduction of particle size. As a consequence, column-to-particle diameter (or channel-to-particle size) ratios on the order of 10-20 are quite common. Porosity fluctuations inherent to confined packings of spherical particles (geometrical wall effect) may be principally avoided using monoliths.

Experimental studies have been reviewed which illustrate the scaling of hydrodynamic dispersion with the average EOF velocity through packed beds, especially in comparison to hydraulic flow. In contrast to solid, dielectric spheres porous particles support the generation of intraparticle EOF (Figures 1.5-1.7). It can strongly reduce intraparticle mass transfer resistance (Figure 1.5), and the electroosmotic perfusion provides a mechanism by which significantly improved separation efficiencies with respect to hydraulic flow can be achieved using packed beds of porous, i.e., permeable and conducting particles (Figures 1.8 and 1.9).

References

[1]   Svec, F., Deyl, Z. (Eds.), *Capillary Electrochromatography*, Elsevier, Amsterdam 2001.

[2]   Eeltink, S., Kok, W. T., *Electrophoresis* 2006, *27*, 84-96.

[3]   Pumera, M., *Talanta* 2005, *66*, 1048-1062.

[4]   Stachowiak, T. B., Svec, F., Frechet, J. M. J., *J. Chromatogr. A* 2004, *1044*, 97-111.

[5]   Bandilla, D., Skinner, C. D., *J. Chromatogr. A* 2004, *1044*, 113-129.

[6]   Kasicka, V., *Electrophoresis* 2006, *27*, 142-175.

[7]   Gubitz, G., Schmid, M. G., *Electrophoresis* 2004, *25*, 3981-3996.

[8]   Liu, C. Y., Lin, C. C., *Electrophoresis* 2004, *25*, 3997-4007.

[9]   Scriba, G. K. E., *Electrophoresis* 2003, *24*, 2409-2421.

[10]   Dabek-Zlotorzynska, E., Celo, V., *Electrophoresis* 2006, *27*, 304-322.

[11]   Enlund, A. M., Hagman, G., Isaksson, R., Westerlund, D., *Trends Anal. Chem.* 2002, *21*, 412-427.

[12]   Mandrioli, R., Raggi, M. A., *Electrophoresis* 2006, *27*, 213-221.

[13]   Qin, F., Xie, C. H., Yu, Z. Y., Kong, L., Ye, M. L., Zou, H. F., *J. Sep. Sci.* 2006, *29*, 1332-1343.

[14]   Xie, C. H., Fu, H. J., Hu, J. W., Zou, H. F., *Electrophoresis* 2004, *25*, 4095-4109.

[15]   Li, W., Fries, D. P., Malik, A., *J. Chromatogr. A* 2004, *1044*, 23-52.

[16]   Svec, F., *J. Sep. Sci.* 2005, *28*, 729-745.

[17]   Klodzinska, E., Moravcova, D., Jandera, P., Buszewski, B., *J. Chromatogr. A* 2006, *1109*, 51-59.

[18]   Klampfl, C. W., *J. Chromatogr. A* 2004, *1044*, 131-144.

[19]   Hlushkou, D., Tallarek, U., *J. Chromatogr. A* 2006, *1126*, 70-85.

[20]   Nischang, I., Chen, G., Tallarek, U., *J. Chromatogr. A* 2006, *1109*, 32-50.

[21]   Sahimi, M., *Applications of Percolation Theory*, Taylor and Francis, London, 1994.

[22]   Rice, C. L., Whitehead, R., *J. Phys. Chem.* 1965, *69*, 4017-4027.

[23]   Gas, B., Stedry, M., Kenndler, E., *Electrophoresis* 1997, *18*, 2123-2133.

[24]   Colon, L. A., Reynolds, K. J., Alicea-Maldonado, R., Fermier, A. M., *Electrophoresis* 1997, *18*, 2162-2174.

[25]   Probstein, R. F., *Physicochemical Hydrodynamics*, John Wiley and Sons, New York, 1994.

[26]   Tsuda, T. (Ed.), *Electric Field Applications in Chromatography, Industrial and Chemical Processes*, VCH, Weinheim, 1995.

[27]   Overbeek, J. T. G., Wijga, P. W. O., *Rec. Trav. Chim. Pays-Bas* 1946, *65*, 556-563.

[28]   Lyklema, J., *Fundamentals of Interface and Colloid Science. Vol. II: Solid-Liquid Interfaces*, Academic Press, London, 1995.

[29]   Zeng, S. L., Chen, C. H., Mikkelsen, J. C., Santiago, J. G., *Sens. Actuators B* 2001, *79*, 107-114.

[30]   Rathore, A. S., Horváth, Cs., *J. Chromatogr. A* 1997, *781*, 185-195.

[31]   Griffiths, S. K., Nilson, R. H. *Anal. Chem.* 2000, *72*, 5473-5482.

[32]   Cummings, E. B., Griffiths, S. K., Nilson, R. H., Paul, P. H., *Anal. Chem.* 2000, *72*, 2526-2532.

[33]   Santiago, J. G., *Anal. Chem.* 2001, *73*, 2353-2365.

[34]   Dutta, P., Beskok, A., *Anal. Chem.* 2001, *73*, 1979-1986.

[35]   Li, D., *Colloids Surf. A* 2001, *195*, 35-57.

[36]   Ghosal, S., *Anal. Chem.* 2002, *74*, 771-775.

[37]   Gleeson, J. P., *J. Colloid Interface Sci.* 2002, *249*, 217-226.

[38]   Qiao, R., Aluru, N. R., *J. Chem. Phys.* 2003, *118*, 4692-4701.

[39]   Yang, J., Masliyah, J. H., Kwok, D. Y., *Langmuir* 2004, *20*, 3863-3871.

[40]   Xuan, X., Li, D., *J. Micromech. Microeng.* 2004, *14*, 290-298.

[41]   Pennathur, S., Santiago, J. G., *Anal. Chem.* 2005, *77*, 6772-6781.

[42]   Vallano, P. T., Remcho, V. T., *Anal. Chem.* 2000, *72*, 4255-4265.

[43]   Wu, R. C., Papadopoulos, K. D., *Colloids Surf. A* 2000, *161*, 469-476.

[44]   Liapis, A. I., Grimes, B. A., *J. Chromatogr. A* 2000, *877*, 181-215.

[45]   Paul, P. H., Garguilo, M. G., Rakestraw, D. J., *Anal. Chem.* 1998, *70*, 2459-2467.

[46]   Tallarek, U., Rapp, E., Scheenen, T., Bayer, E., Van As, H., *Anal. Chem.* 2000, *72*, 2292-2301.

[47]   Conlisk, A. T., McFerran, J., Zheng, Z., Hansford, D., *Anal. Chem.* 2002, *74*, 2139-2150.

[48]   Dutta, P., Beskok, A., Warburton, T. C., *J. Microelectromech. Syst.* 2002, *11*, 36-44.

[49]   Erickson, D., Li, D., *J. Phys. Chem. B* 2003, *107*, 12212-12220.

[50]   Fu, L.-M., Lin, J.-Y., Yang, R.-J., *J. Colloid Interface Sci.* 2003, *258*, 266-275.

[51]   Li, B. M., Kwok, D. Y., *J. Chem. Phys.* 2004, *120*, 947-953.

[52]   Hlushkou, D., Kandhai, D., Tallarek, U., *Int. J. Numer. Meth. Fluids* 2004, *46*, 507-532.

[53]   Van Theemsche, A., Gzil, P., Dan, C., Deconinck, J., De Smet, J., Vervoort, N., Desmet, G., *Anal. Chem.* 2004, *76*, 4030-4037.

[54]   Kirchner, J. J., Hasselbrink, E. F., Jr., *Anal. Chem.* 2005, *77*, 1140-1146.

[55]   Datta, S., Ghosal, S., Patankar, N. A., *Electrophoresis* 2006, *27*, 611-619.

[56]   Coelho, D., Shapiro, M., Thovert, J.-F., Adler, P. M., *J. Colloid Interface Sci.* 1996, *181*, 169-190.

[57]   Hlushkou, D., Seidel-Morgenstern, A., Tallarek, U., *Langmuir* 2005, *21*, 6097-6112.

[58]   Hlushkou, D., Apanasovich, V., Seidel-Morgenstern, A., Tallarek, U., *Chem. Eng. Commun.* 2006, *193*, 826-839.

[59]   Knox, J. H., Grant, I. H., *Chromatographia* 1987, *24*, 135-143.

[60]   Knox, J. H., *Chromatographia* 1988, *26*, 329-337.

[61]   Knox, J. H., Grant, I. H., *Chromatographia* 1991, *32*, 317-328.

[62]   Mistry, K., Krull, I., Grinberg, N., *J. Sep. Sci.* 2002, *25*, 935-958.

[63]   Mistry, K., Krull, I., Grinberg, N., *Electrophoresis* 2003, *24*, 1753-1763.

[64]   Simal-Gandara, J., *Crit. Rev. Anal. Chem.* 2004, *34*, 85-94.

[65]   Steiner, F., Scherer, B., *Electrophoresis* 2005, *26*, 1996-2004.

[66]   Szekely, L., Guttman, A., *Electrophoresis* 2005, *26*, 4590-4604.

[67]   de Bellaistre, M. C., Randon, J., Rocca, J. L., *Electrophoresis* 2006, *27*, 736-741.

[68]   Progent, F., Augustin, V., Tran, N. T., Descroix, S., Taverna, M., *Electrophoresis* 2006, *27*, 757-767.

[69]   André, C., Berthelot, A., Thomassin, M., Guillaume, Y. C., *Electrophoresis* 2006, *27*, 3254-3262.

[70]   Bey, O., Eigenberger, G., *Chem. Eng. Sci.* 1997, *52*, 1365-1376.

[71]   Giese, M., Rottschäfer, K., Vortmeyer, D., *AIChE J.* 1998, *44*, 484-490.

[72]   Benenati, R. F., Brosilow, C. B., *AIChE J.* 1962, *8*, 359-361.

[73]   Giese, M., *Untersuchung der Strömung in porösen Medien unter Berücksichtigung effektiver Viskositäten.* Ph.D. Thesis, TU München, Germany, 1997.

[74]   Kang, Y. J., Yang, C., Huang, X. Y., *Int. J. Eng. Sci.* 2004, *42*, 2011-2027.

[75]   Maier, R. S., Kroll, D. M., Bernard, R. S., Howington, S. E., Peters, J. F., Davis, H. T., *Phys. Fluids* 2003, *15*, 3795-3815.

[76]   Choudhary, G., Horváth, Cs., *J. Chromatogr. A* 1997, *781*, 161-183.

[77]   De la Rue, R. E., Tobias, C. W., *J. Electrochem. Soc.* 1959, *106*, 827-833.

[78]   Overbeek, J. Th. G., in: *Colloid Science*, Kruyt, H. R. (Ed.), Elsevier, Amsterdam, 1952, Chapter 5.

[79]   Hunter, R. J., Wright, H. J. L., *J. Colloid Interface Sci.* 1971, *37*, 564-580.

[80]   Vindevogel, J., Sandra, P., *J. Chromatogr.* 1991, *541*, 483-488.

[81]   Rathore, A. S., Wen, E., Horváth, Cs., *Anal. Chem.* 1999, *71*, 2633-2641.

[82]   Kirby, B. J., Hasselbrink, E. F., *Electrophoresis* 2004, *25*, 203-213.

[83]   Tallarek, U., Rapp, E., Seidel-Morgenstern, A., Van As, H., *J. Phys. Chem. B* 2002, *106*, 12709-12721.

[84]   Tallarek, U., Scheenen, T. W. J., Van As, H., *J. Phys. Chem. B* 2001, *105*, 8591-8599.

[85]   Davis, R. H., Stone, H. A., *Chem. Eng. Sci.* 1993, *48*, 3993-4005.

[86]   Gustavsson, P.-E., Larsson, P.-O., *J. Chromatogr. A* 1996, *734*, 231-240.

[87]   McCoy, M., Kalghatgi, K., Regnier, F. E., Afeyan, N., *J. Chromatogr. A* 1996, *743*, 221-229.

[88]   Nash, D. C., Chase, H. A., *J. Chromatogr. A* 1998, *807*, 185-207.

[89]   Meyers, J. J., Liapis, A. I., *J. Chromatogr. A* 1998, *827*, 197-213.

[90]   Van Kreveld, M. E., Van den Hoed, N., *J. Chromatogr.* 1978, *149*, 71-91.

[91]   Nir, A., Pismen, L. M., *Chem. Eng. Sci.* 1977, *32*, 35-41.

[92]   Rodrigues, A. E., Ahn, B. J., Zoulalian, A., *AIChE J.* 1982, *28*, 541-546.

[93]   Stephanopoulos, G., Tsiveriotis, K., *Chem. Eng. Sci.* 1989, *44*, 2031-2039.

[94]   Pfeiffer, J. F., Chen, J. C., Hsu, J. T., *AIChE J.* 1996, *42*, 932-939.

[95]   Kandhai, D., Hlushkou, D., Hoekstra, A. G., Sloot, P. M. A., Van As, H., Tallarek, U., *Phys. Rev. Lett.* 2002, *88*, art. no. 234501.

[96]   Venema, E., Kraak, J. C., Poppe, H., Tijssen, R., *J. Chromatogr. A* 1999, *837*, 3-15.

[97]   Vallano, P. T., Remcho, V. T., *J. Phys. Chem. B* 2001, *105*, 3223-3228.

[98]   Tallarek, U., Rapp, E., Van As, H., Bayer, E., *Angew. Chem. Int. Ed.* 2001, *40*, 1684-1687.

[99]   Stol, R., Kok, W. T., Poppe, H., *J. Chromatogr. A* 1999, *853*, 45-54.

[100]   Stol, R., Poppe, H., Kok, W. T., *Anal. Chem.* 2001, *73*, 3332-3339.

[101]   Dearie, H. S., Smith, N. W., Moffat, F., Wren, S. A. C., Evans, K. P., *J. Chromatogr. A* 2002, *945*, 231-238.

[102]   Tallarek, U., Paces, M., Rapp, E., *Electrophoresis* 2003, *24*, 4241-4253.

[103]   Tallarek, U., Rapp, E., Sann, H., Reichl, U., Seidel-Morgenstern, A., *Langmuir* 2003, *19*, 4527-4531.

[104]   Kim, H.-B., Hayashi, M., Nakatani, K., Kitamura, N., Sasaki, K., Hotta, J., Masuhara, H., *Anal. Chem.* 1996, *68*, 409-414.

[105]   Ljunglöf, A., Hjorth, R., *J. Chromatogr. A* 1996, *743*, 75-83.

[106]   Ljunglöf, A., Thömmes, J., *J. Chromatogr. A* 1998, *813*, 387-395.

[107]   Liljeborg, A., *Proc. SPIE* 1996, *2655*, 11-17.

[108]   Crank, J., *The Mathematics of Diffusion*, Clarendon Press, Oxford, 1956.

[109]   Chen, G., Tallarek, U., *Langmuir* 2003, *19*, 10901-10908.

[110]   Chen, G., Paces, M., Marek, M., Zhang, Y. K., Seidel-Morgenstern, A., Tallarek, U., *Chem. Eng. Technol.* 2004, *27*, 417-428.

[111]   Stol, R., Poppe, H., Kok, W. T., *J. Chromatogr. A* 2000, *887*, 199-208.

[112]   Miller, N. P., Berg, J. C., O'Brien, R. W., *J. Colloid Interface Sci.* 1992, *153*, 237-243.

[113]   Knox, J. H., *J. Chromatogr. A* 1999, *831*, 3-15.

[114]   Koch, D. L., Brady, J. F., *J. Fluid Mech.* 1985, *154*, 399-427.

[115]   Sahimi, M., *Flow and Transport in Porous Media and Fractured Rock*, VCH, Weinheim 1995, Chapter 9.

[116]   Tallarek, U., Bayer, E., Guiochon, G., *J. Am. Chem. Soc.* 1998, *120*, 1494-1505.

[117]   Enlund, A. M., Isaksson, R., Westerlund, D., *J. Chromatogr. A* 2001, *918*, 211-220.

[118]   Giddings, J. C., *Dynamics of Chromatography. Part I: Principles and Theory*, Marcel Dekker, New York, 1965.

[119]   Unger, K. K., Lüdtke, S., Grün, M., *LC•GC Int.* 1999, *12*, 870-874.

2   Concentration polarization effects in porous media

2.1   Perspective

In membranes, random-close sphere packings, or monoliths which contain charged solid-liquid interfaces several electrical fields may be superimposed. This includes the local fields near the wall of charged pores or around spacer groups and grafted polymer chains extending from the solid surface, Donnan potentials between different compartments, the quasi-equilibrium or primary EDL (λ_d) at phase boundaries, as well as externally applied electrical fields. Electrokinetic transport of bulk liquid and charged analytes through porous media induced by an external d.c. electrical field plays an important role in many analytical, technological, and environmental processes [1-9]. It relies on the electromigration of ions (background electrolyte), electrophoresis (charged analytes), as well as electroosmosis (bulk liquid) driven by the shear stresses which are concentrated in the EDL along a solid-liquid interface [10].

CEC combines the chromatographic separation based on a partitioning between stationary and mobile phases with the electrokinetic mobile phase transport and electrophoretic selectivity based on the different mobilities of charged analytes in the applied electrical field [5]. It has been demonstrated that EOF in CEC can achieve a significant increase in separation efficiency and allows to pack columns with smaller particles compared to LC [11-13]. The typical thickness of the classical (or primary) EDL (nanometer scale) is usually much smaller than any of the macropore dimensions ($r_{macro}/\lambda_d \gg 1$) in the sphere packings and monoliths (micrometer scale) employed in CEC. In the following the thickness of the primary EDL is, as typically done, approximated by the Debye screening length λ_D (Chapter 1, eq. 1.1) [10]. Thus, the macropore space in this so-called thin-EDL-limit contains quasi-electroneutral liquid, and volumetric EOF remains relatively independent of interparticle (or interskeleton) macropore dimensions (Chapter 1) [14].

While the electroosmotic perfusion mechanism has attracted attention in CEC in view of speed and especially separation efficiency as outlined in Chapter 1.4, it should be recognized that the intraparticle pore space in sphere packings simultaneously is an ion-permselective, i.e., charge-selective region due to the EDL overlap which persists over a wide range of experimental conditions in CEC ($r_{intra}/\lambda_d \ll 100$). With decreasing intraparticle EDL overlap the ion-permselectivity decreases and, concomitantly, volumetric EOF increases (Chapter 1.4). This charge-selectivity and its unique consequences for coupled charge and mass transport in CEC should not be underestimated. Ion-permselectivity is an often tailored characteristic of porous media which they may demonstrate as a whole (e.g., flat membranes which separate completely the adjacent solutions) or by means of discrete (e.g., meso- and/or microporous) ion-permselective domains in materials which are macroscopically charge-nonselective. Thus, the ion-permselectivity is also an inherent property of the intraparticle or intraskeleton mesopores of particulate and monolithic columns used in CEC [15-19]. In this respect, associated mesopore-scale EDL interaction leads to exclusion of co-ions and counter-ion

enrichment. At electrochemical equilibrium, without an applied field, the Donnan-potential balances the tendency of ions to level out the existing concentration differences [20]. It pulls cations back into the (negatively charged) intraskeleton pore space and anions back into the (positively charged) interskeleton compartment [20]. For ideal solutions we have:

$$\Phi_{Don} \equiv \Phi_{meso} - \Phi_{macro} = -\frac{RT}{z_i F} \ln \frac{c_{i,meso}}{c_{i,macro}} \, , \qquad (2.1)$$

with index i representing the co- and counter-ionic buffer components. The distribution coefficient $c_{i,meso}/c_{i,macro}$ which represents the ion-permselectivity of the system depends on ionic strength of the mobile phase, surface charge density in the mesopores, as well as on valencies of co- and counter-ionic species. Actually, these parameters similarly influence EDL overlap and resulting ion-exclusion in a double-layer model [10]. For porous media containing ideally ion-permselective regions the charge transport in these domains is exclusively achieved by the counter-ions [20].

2.2   Background and related work

The favoured permeation of counter-ions is the main transport characteristics of ion-exchange membranes, and ion-permselective transport is a basis for various electrochemical and electrokinetic processes including electrode reactions and electrodialysis [4, 21]. Thus, a better understanding of the coupled mass and charge transport in CEC may be achieved using models that have been developed for transport through ion-exchange membranes [21-29]. An important implication of coupled mass and charge transport is that under the influence of chemical or electrical potential gradients concentration polarization (CP) develops [30-39]. When strong electrical fields are superimposed in CEC on internal potential gradients they will induce CP, a complex of effects related to the formation of concentration gradients of ionic species in the electrolyte solution adjacent to a charge-selective interface upon the passage of electrical current normal to that interface [10].

This is illustrated in Figure 2.1a for parallel, locally flat interfaces separating quasi-electroneutral macropore space from a charge-selective domain, e.g., interskeleton or interparticle macropore space from the mesoporous segment in a monolith or mesoporous particle in a fixed bed.
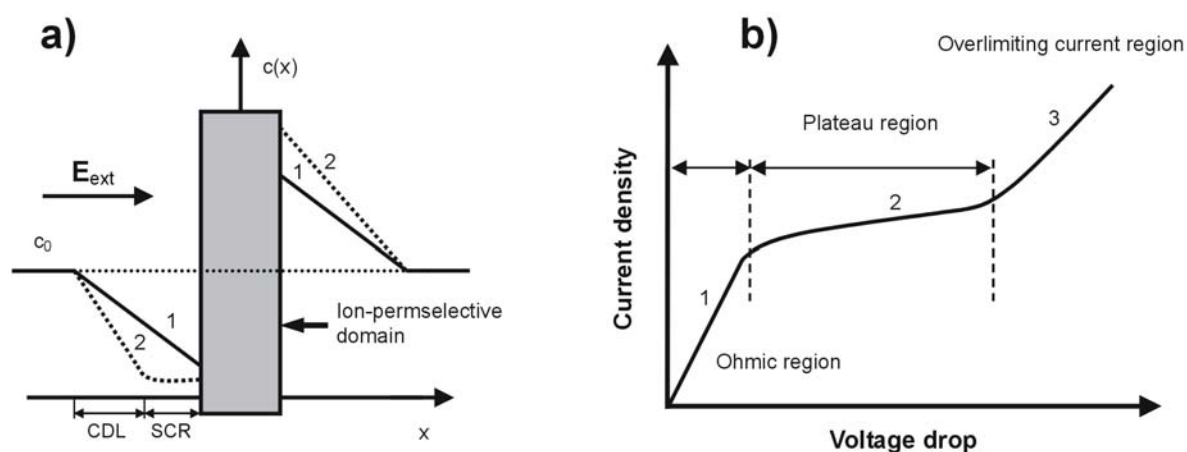

Figure 2.1 Different stages of locally induced CP at the interface between quasi-electroneutral and charge-selective domains, e.g., for a membrane, a porous particle in a fixed bed, or the skeleton of a monolith. a) Schematic distribution of ion concentrations in equilibrium CP with local electroneutrality in the depleted and enriched CP zones (stage 1), and under conditions of nonequilibrium CP with a secondary, electrical field-induced EDL (stage 2). The space charge region (SCR) in the depleted CP zone constitutes the mobile part of the secondary EDL. b) Characteristic regions of a voltage-current curve. Limiting current density and plateau length are key parameters of CP in membrane science.

On that side where counter-ions enter the charge-selective domain in the direction of the applied field the local interplay of convection by EOF, diffusion, and electromigration forms a convective diffusion boundary layer (CDL) with reduced ion concentrations relative to bulk solution. It comprises a depleted CP zone (Figure 2.1a; stage 1). At the opposite interface where counter-ions leave the charge-selective region the electrolyte concentration increases leading to an enriched CP zone. Thus, zones of increased and decreased ion concentration occur in the bulk fluid at the cathodic and anodic interfaces of a cation-selective domain, respectively, or at anodic and cathodic interfaces of an anion-selective domain. In the classical picture of CP local electroneutrality is preserved in the enriched and depleted CP zones (stage 1 in Figure 2.1a) [10]. While the classical theory of CP assumes ideal ion-

permselectivity, i.e., transport numbers of co-ions are zero, while this sum is unity for counter-ions because mobile co-ions are simply not present in the ion-permselective region, the experimental conditions in CEC are nonideal in this respect, but can be tuned by the actual EDL overlap (or Donnan-exclusion of co-ions) via the ionic strength.

The fraction of the current, which is carried by a certain ionic species, can be expressed by the ion transport or transference number which are given by [40]:

$$T_i = \frac{z_i J_i}{\sum_i z_i J_i}, \qquad (2.2)$$

and

$$t_i = \frac{T_i}{|z_i|} = \frac{|J_i|}{\sum_i z_i J_i}, \qquad (2.3)$$

where T_i and t_i are the transport and transference number of species i, J_i is its flux due to diffusive flux, electrical transference and convective transfer and z_i its valence. According to this definition, the transport number T_i is the product of the transference number t_i and the electrochemical valence z_i of the species. t_i is defined as the number of moles transferred by 1 faraday of electricity through a stationary cross section [20]. We consider the matrix (the pore space of the membrane or the intraparticle/intraskeleton pore space)

Figure 2.2 Development of CP at the anodic interface (depleted CP zone) between a bulk, macroporous and mesoporous, ion-permselective domain. The concentration (c^+) and transport number (z^+t^+) of a counter-ion in the latter exceed substantially those of the co-ion; t^+ denotes the transference number [20]. For simplicity we assume a symmetrical, strong background electrolyte; the external field (E_{ext}) is applied from left to right.

as stationary frame of reference. By definition, the transport numbers are positive for all ions and zero for (the electrically neutral) solvent. Thus the sum over all transport numbers or transference numbers is unity:

$$\sum_i z_i t_i = 1. \qquad (2.4)$$

It means that if we consider a homogeneous electrolyte, transference numbers in the quasi electroneutral macropore space are determined by the ratio of their mobilities [20]. In the ion-permselective pore space the concentration of counter-ions exceeds by far that of the co-ions. Then the electrical current is mainly accomplished by the former. This is illustrated in Figure 2.2. The sum of
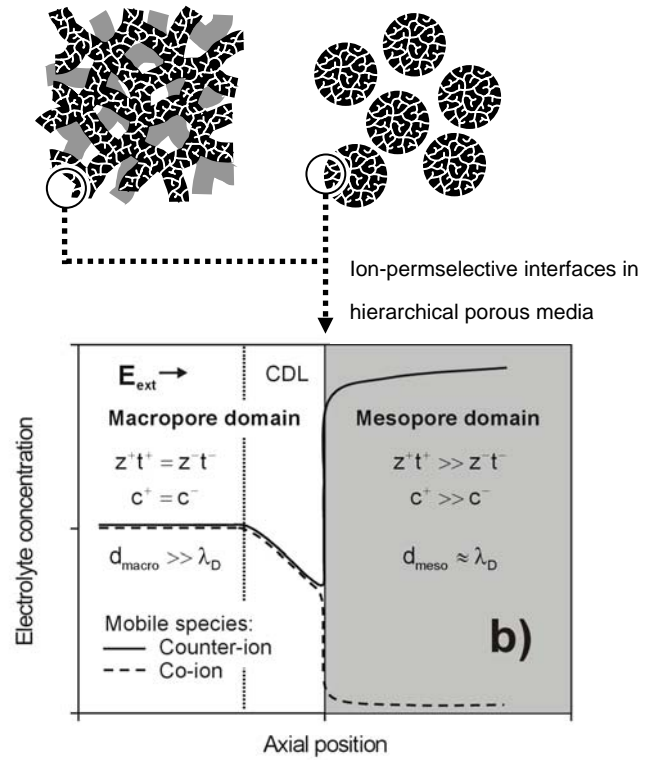
the transport numbers of the counter-ions in the ion-permselective pore space is always higher than that of the co-ions and their concentration in the ion-permselective pore space is always close to the fixed charges of the membrane. If more than one counter-ionic species is present in the system, which is assumed here for simplicity, the transport number of different counter-ions can be quite different, depending on charge numbers, diffusion coefficients and concentrations [41].

In contrast to the macroscopically charge-nonselective monoliths and particulate beds (Figure 2.2) which contain discrete ion-permselective domains (porous particles or skeleton) the adjacent CP zones have no direct contact for a membrane, although they depend on each other due to the transferred current (Figure 2.1a).

CP plays an important role in many electrokinetic processes because it affects both local ion concentrations and mass transport to preserve continuity of mass and charge fluxes. The depleted CP zone is a CDL which presents external fluid-side mass transfer resistance to counter-ion flux from bulk solution towards an ion-exchange materials external surface and, therefore, into the ion-permselective domain. At sufficiently low field strength, the voltage-current behaviour is expected to follow Ohms law (Figure 2.1b; region 1). At increasing field strength the concentration of ions in the depleted CP zone is reduced towards zero and diffusion-limited transport through the CDL approaches a maximum value which, in the classical description of CP, particularly in the context of electrodialysis, is also known as limiting current density (see region 2 in Figure 2.1b) [30, 31, 42-46]. The potential of overcoming limiting current densities has stimulated research on CP and its effects in electrodialysis. One possibility is to reduce the thickness of the depleted CP zone by vigorous stirring [35]. On the other hand, overlimiting current densities through ion-exchange membranes were also realized with macroscopically quiescent electrolyte solutions by increasing field strengths just further beyond values characterizing the plateau region. Detailed studies of this nonlinear regime have revealed periodically varying trans-membrane currents which begin oscillating at high frequencies for higher field strengths [47, 48]. A visualisation of the hydrodynamics has detected strong fluctuations in the adjoining liquid indicating convection close to the surface [49]. Nonequilibrium electroosmotic slip was proposed as mechanism for convection at a charge-selective interface [50]; for higher field strengths a secondary, nonequilibrium EDL (compared to the primary, quasi-equilibrium EDL) is electrokinetically induced at the interface of the depleted CP zone and the membrane pore fluid, where the concentration of counter-ions then exceeds that of co-ions by far (stage 2; Figure 2.1a) [50-54].

The nonequilibrium space charges are induced locally by the normal component of the applied field and disturb electroneutrality over a much larger length scale than the primary EDL [54]. Via volume force interaction of the mobile space charge region (see SCR; Figure 2.1a) with the tangential field component a nonequilibrium electroosmotic slip results between membrane surface and CDL. Then, the originally quiescent CP zone is convectively disturbed and a convective instability tends to destroy the CDL locally. Thus, the diffusion-limitation to mass transfer is removed in this region and overlimiting current densities through a membrane can be realized (Figure 2.1b; region 3) [55-58].

Compared with the idealized flat membrane geometry, systems of a single ion-permselective particle as well as fixed multiparticle systems show a similar local transport complexity (Figure 2.3). Thus, under typical conditions in CEC ion-permselectivity leads to a formation of depleted and enriched CP zones around the spherical-shaped particles. This is illustrated for a single particle in Figure 2.3 employing co-ionic (Figure 2.3a) and counter-ionic fluorescent tracer (Figure 2.3b) by quantitative confocal laser scanning microscopy (CLSM). The microscopic analysis of CP is realized employing refractive index matching of the liquid electrolyte with respect to the mesoporous silica-based particles [59]. It employs a microfluidic setup developed in our group, where single spheres can be fixed and it allows to realize application of controlled hydrodynamic flow [60]. For the co-ionic tracer, we can see an intraparticle exclusion at electrochemical equilibrium, i.e. its concentration is significantly lower than that in the external solution, which can be explained by a simple Donnan-exclusion mechanism. Vice versa, for the counter-ionic tracer, we can see an intraparticle enrichment at electrochemical equilibrium, i.e. its concentration exceeds significantly that of the external solution. With a macroscopic external electrical field CP is induced, which comprises a depleted CP zone at the anodic hemisphere (see Figure 2.2 for comparison) and an enriched CP zone at the cathodic hemisphere. These zones each occupy one half of a spheres surface and are seen to have rotational symmetry with respect to
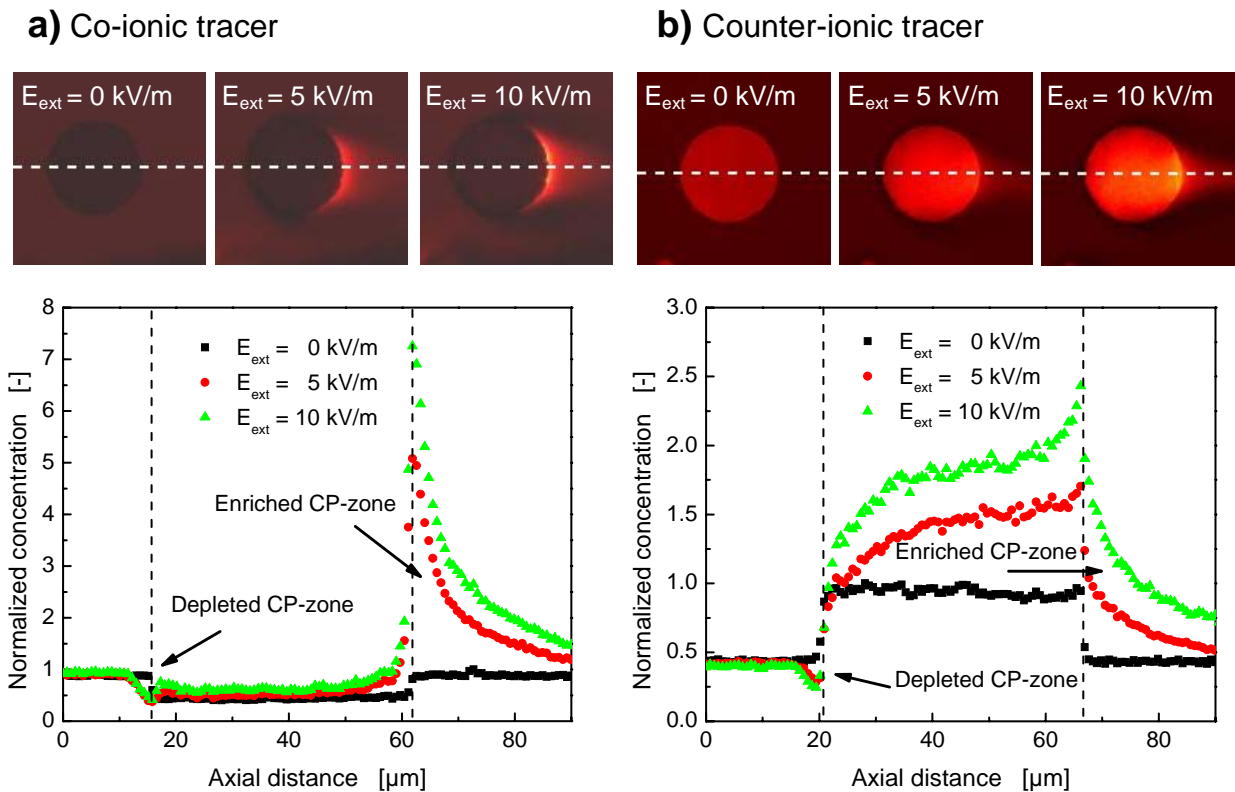

a) Co-ionic tracer   **b)** Counter-ionic tracer

Figure 2.3 CP visualized by quantitative confocal laser scanning microscopy (CLSM) with a single porous (cation-selective) particle, fixed in an open channel. Mobile phase: 90:10 DMSO/water (v/v) with 10 mM sodium-acetate containing a)10^{-5} M twice negatively charged Bodipy-disulfonate and b) 10^{-5} M positively charged Rhodmine 6G. The particles were 40 μm in size and had an intraparticle pore radius (r_{intra}) of 4.5 nm, resulting in an EDL overlap ($r_{intra}/\lambda_d \sim 2$). Applied PDF results in an average velocity though the channel of 1.1 mm/s. Axial centerline profiles were normalized with respect to their maximum values at electrochemical equilibrium (without superimposed external electrical field). The images were acquired using constant laser and detector settings optimized for each tracer.

the field direction [61]. In contrast to membranes anodic and cathodic compartments are connected via bulk solution in systems with discrete charge-selective spatial domains. Nevertheless, as transport of counterionic tracer increases with increasing electrical field strength because of increasing current density through the particle together with backward diffusive flux of counter-ionic tracer from the enriched CP zone, intraparticle concentration of (fluorescent) counter-ions is increasing significantly with the applied field strength.

The basic element of nonequilibrium electroosmotic slip, or in the literature referred to as electroosmosis of the second kind for curved interfaces is the secondary EDL which consists of a mobile (fluid-side) counter-ionic SCR and an immobile (particle-side) co-ionic SCR (Figure 2.4a). By the interplay of the limiting diffusive flux through the CDL and the strong electrokinetic flux of counter-ions within a spherical, ion-permselective particle nonequilibrium space charges can be induced locally at the solid-liquid interface (in the depleted CP zone of the anodic hemisphere) by the normal component of the applied field at an advanced stage of CP. However, the local normal component of the applied field varies systematically along this interface from the anodic pole of a bead, being maximum there, to the equator where it is zero. For the tangential field component it is just the opposite way; it is maximum at the equator, but zero at the pole. Consequently, both the intensity of the SCRs and velocity of electroosmosis of the second kind also vary systematically along the interface of the anodic hemisphere. Thus, from a hydrodynamic viewpoint, the thickness of the CDL changes considerably along the bead surface. In a
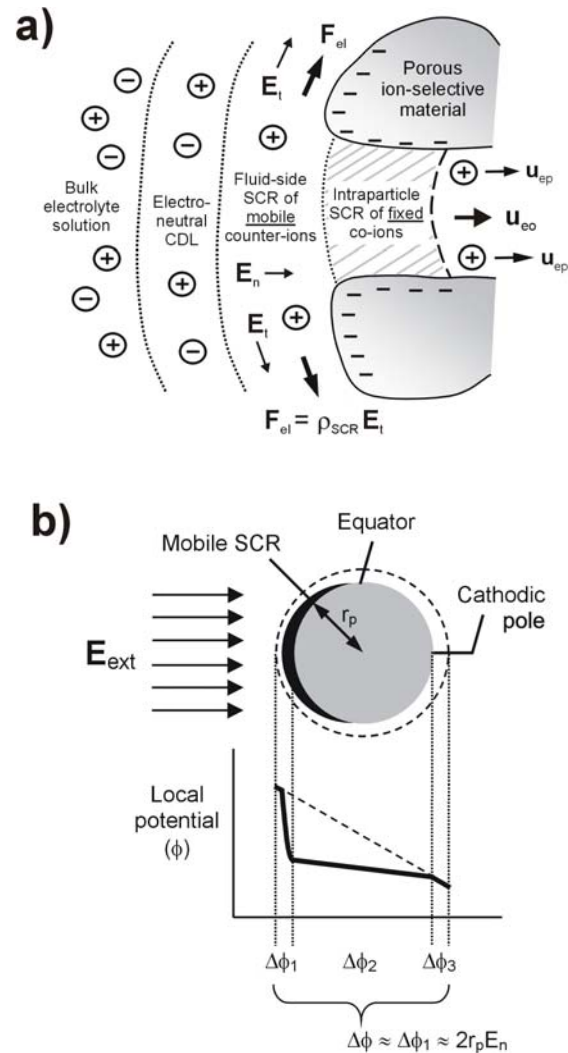

Figure 2.4 a) Induction of a nonequilibrium, secondary EDL in the depleted CP zone at the anodic interface between bulk, macroporous and ion-permselective domains by the normal field component (E_n). The electrokinetic transport of counter-ions in the charge-selective compartment represented by the electroosmosis and electrophoresis velocities (u_{eo} and u_{ep}) exceeds the diffusive transport of counter-ions through the CDL. The tangential field component (E_t) interacts locally with a charge density of the mobile counter-ions (ρ_{SCR}) leading to electroosmosis of the second kind within the macropore space. b) Potential drop (pole-to-pole) over a spherical particle including anodic CDL and mobile SCR, as well as the cathodic CP zone. The dashed line compares the potential drop in bulk electrolyte solution. Induced-charge electroosmosis at a particles external surface then is characterized by nonlinear local slip velocities $u_{eo} \propto \Delta\phi(E_n)E_t$; the overpotential $\Delta\phi$ here replaces the classical ζ-potential.

two-dimensional picture the depleted CP zone which represents intensity of the mobile SCR and thickness of the CDL close to a single, isolated spherical particle may be illustrated by the sickle-shaped region in Figure 2.4b.

Generally the resulting nonequilibrium electrokinetics have a number of implications which have been investigated for systems containing the particles either as fixed single spheres or as dilute suspensions. For freely-dispersed spheres (which are ionic or electrical conductors) a nonlinear dependence of electrophoretic velocities on applied field strength has been measured (electrophoresis of the second kind) [62]. Vice versa, in devices with fixed single spheres a nonlinear dependence of EOF slip velocities at the curved surface of a sphere on the field strength was revealed (electroosmosis of the second kind) [61]. To stress it again, the novelty of this electrokinetics is that the primary EDL is complemented by a secondary EDL which depends on the applied field strength concerning both its local dimension and charge density (Figure 2.4).

2.3 Implications for electrochromatography

In order to realize an increased surface-to-volume ratio almost exclusively porous particles are used in the engineering and life sciences, especially in view of separations and purification issues and desired capacity, throughput, and sample complexity, which require a large specific surface area [20, 63, 64]. Figure 2.5 illustrates that ion-permselectivity can be expected to develop in the intraparticle or intraskeleton mesopores of particulate and monolithic columns typically used in the aforementioned applications, including CEC [5, 65-68].

Because electrical fields (or currents), ion concentrations and velocity distributions are mutually dependent, much higher complexity arises in electrochromatographic systems when an external electrical field is superimposed on internal potential gradients, which has yet been nor realized or characterized in these systems. However, it is virtually obvious that the ideal single-particle picture (Figure 2.3), with respect to developing CP, must be strongly affected in multi-particle systems by the influence of approaching
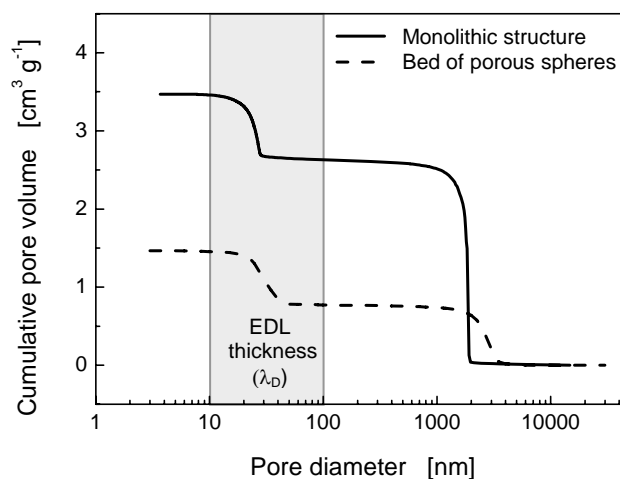

Figure 2.5 Illustration of bimodal pore size distribution in packed beds of porous particles and monolithic structures, consisting of interparticle (interskeleton) macropores and intraparticle (intraskeleton) mesopores; typical EDL dimensions (λ_D) indicate the ion-permselectivity on the mesopore scale.

neighbours via the local hydrodynamics and interaction of their CP zones. In this respect, an important difference between CEC practice and electrokinetic studies with disperse systems or single particles needs attention. While in CEC particulate systems composed of random-close sphere packings are used, dilute systems or single particles were encountered in these earlier investigations of the electrokinetic phenomena of the second kind [61, 69-71].

Further electrohydrodynamical implications of the aforementioned non-equilibrium electrokinetics are to be probed, since in scaling towards typical parameters in CEC it should be realized that electroosmosis of the second kind in first approximation depends linearly on a particle diameter, but squared on the applied field strength (Figure 2.4b) [71]. In view of CEC yet the question arises of how much of these phenomena can still be expected to develop and how much interaction of CP zones can be observed in the dense multiparticle systems and monolithic structures? A beneficial effect accompanying the nonlinear dynamics may be the development of pore pressure based on continuity arguments. Although the details of a microscopic operation in porous media and potential use of this effect for enhanced lateral fluid mixing (angular dependence of nonequilibrium electroosmotic slip) need resolving studies, the present thesis shows that it can be tuned to largely overcome a bottleneck in liquid-phase separations, namely analyte equilibration over the whole column cross-section.

Summarizing, this chapter demonstrates, that as a consequence of ion-permselectivity, CP forms a basic element of charge transfer between different regions in electrochromatographic media and, via local ionic strengths, also influences the density of electrical field lines and distribution of ζ-potential in the primary EDL along curved interfaces in particulate and monolithic beds. In this respect, an important consequence of CP is an adoption of the electrokinetic effects based on a nonequilibrium (or secondary) EDL that may be induced in the depleted CP zone by electrical field strengths realized in CEC, and which are explored in Chapters 3 and 4. Although mostly unexplored, CP also gains a fundamental, rather than special significance for CEC applications in active areas like proteomics and pharmaceutical analysis, which is to be shown in Chapter 5. Thus, the remainder of this work will focus on the illustration of nonequilibrium effects due to induced space charges as related to the potential for speed and efficiency in CEC, but more important the migration and retention dynamics of charged analytes relevant for (bio-) pharmaceutical applications.

References

[1] Ho, S. V., Sheridan, P. W., Athmer, C. J., Heitkamp, M. A., Brackin, J. M., Weber, D., Brodsky, P. H., *Environ. Sci. Technol.* 1995, *29*, 2528-2534.

[2] Tsuda, T. (Ed.), *Electric Field Applications in Chromatography, Industrial and Chemical Processes*, VCH, Weinheim, 1995.

[3] Coletta, T. F., Brunell, C. J., Ryan, D. K., Inyang, H. I., *J. Environ. Eng.* 1997, *123*, 1227-1233.

[4] Sørensen, T. S. (Ed.), *Surface Chemistry and Electrochemistry of Membranes*, Marcel Dekker, New York 1999.

[5] Svec, F., Deyl, Z. (Eds.), *Capillary Electrochromatography*, Elsevier, Amsterdam 2001.

[6] Delgado, A. V. (Ed.), *Interfacial Electrokinetics and Electrophoresis*, Marcel Dekker, New York 2002.

[7] Stone, H. A., Stroock, A. D., Ajdari, A., *Ann. Rev. of Fluid Mech.* 2004, *36*, 381-411.

[8] Li, D., *Electrokinetics in Microfluidics*, Academic Press, Oxford 2004.

[9] Stachowiak, T. B., Svec, F., Frechet, J. M. J., *J. Chromatogr. A* 2004, *1044*, 97-111.

[10] Probstein, R. F., *Physicochemical Hydrodynamics*, John Wiley and Sons, New York, 1994.

[11] Knox, J. H., Grant, I. H., *Chromatographia* 1991, *32*, 317-328.

[12] Choudhary, G., Horváth, Cs., *J. Chromatogr. A* 1997, *781*, 161-183.

[13] Luedtke, S., Adam, T., von Doehren, N., Unger, K. K., *J. Chromatogr. A* 2000, *887*, 339-346.

[14] Hlushkou, D., Seidel-Morgenstern, A., Tallarek, U., *Langmuir* 2005, *21*, 6097-6112.

[15] Colón, L. A., Burgos, G., Maloney, T. D., Cintrón, J. M., Rodríguez, R. L., *Electrophoresis* 2000, *21*, 3965-3993.

[16] Tanaka, N., Kobayashi, H., Nakanishi, K., Minakuchi, H., Ishizuka, N., *Anal. Chem.* 2001, *73*, 420A-429A.

[17] Legido-Quigley, C., Marlin, N. D., Melin, V., Manz, A., Smith, N. W., *Electrophoresis* 2003, *24*, 917-944.

[18] Eeltink, S., Decrop, W. M. C., Rozing, G. P., Schoenmakers, P. J., Kok, W. T., J. Sep. Sci. 2004, *27*, 1431-1440.

[19] Svec, F., *J. Sep. Sci.* 2005, *28*, 729-745.

[20] Helfferich, F., *Ion Exchange*, Dover, New York, 1995.

[21] Rubinstein, I., *Physical Electrochemistry*, Marcel Dekker, New York 1995.

[22] Morrison, F. A., Osterle, J. F., *J. Chem. Phys.* 1965, *43*, 2111-&.

[23] Gross, R. J., Osterle, J. F., *J. Chem. Phys.* 1968, *49*, 228-&.

[24] Fair, J. C., Osterle, J. F., *J. Chem. Phys.* 1971, *54*, 3307-&.

[25] Sen, P. N., *Phys. Rev. B* 1989, *39*, 9508-9517.

[26] Basu, S, Sharma, M. M., *J. Membr. Sci.* 1997, *124*, 77-91.

[27] Saracco, G., *Chem. Eng. Sci.* 1997, *52*, 3019-3031.

[28] Révil, A., Glover, P.W.J., Phys. Rev. B 1997, *55*, 1757-1773.

[29] Révil, A, *J. Colloid Interface Sci.* 1999, *212*, 503-522.

[30] Mandersloot, W., Hicks, R. E., *Ind. Eng. Chem. Proc. Des. Dev.* 1965, 4, 304-308.

[31] Khedr, G., Varoqui, R., *Ber. Bunsenges. Phys. Chem.* 1981, *85*, 116-122.

[32] Rubinstein, I., *J. Chem. Soc. Faraday Trans. II* 1990, *86*, 1857-1861.

[33]   Koter, S, Hamann, C.H., *J. Non-Equilib. Thermodyn.* 1990, *15*, 315-333.

[34]   Tanaka, Y., J. Membr. Sci., *57*, 217-235.

[35]   Manzanares, J. A., Kontturi, K., Mafe, S., Aguilella, V. M., Pellicer, J., *Acta Chem. Scand.* 1991, *45*, 115-121.

[36]   Krol, J.J., Wessling, M., Strathmann, H., *J. Membr. Sci.* 1999, *162*, 145-154.

[37]   Shaposhnik, V. A., Vasil'eva, V. I., Reshetnikova, E. V., *Russ. J. Electrochem.* 2000, *36*, 773-780.

[38]   Choi, J. H., Park, J. S., Moon, S. H., *J. Colloid Interface Sci.* 2002, *251*, 311-317.

[39]   Leinweber, F. C., Pfafferodt, M., Seidel-Morgenstern, A., Tallarek, U. *Anal. Chem.* 2005, *77*, 5839-5850.

[40]   Strathmann, H., *Ion exchange membrane separation processes*, Elsevier, Amsterdam 2004.

[41]   Zabolotsky, V. I., Manzanares, J. A., Nikonenko, V. V., Lebedev, K. A., Lovtsov, E. G., *Desalination* 2002, *147*, 387-392.

[42]   Seno, M., Yamagata, K., Shinoda, J., Yamabe, T., *J. Electrochem. Soc. Jpn.* 1966, *34*, 232-240.

[43]   Sata, T., Yamane, R., Mizutani, Y., *Bull. Chem. Soc. Jpn.* 1969, *42*, 279-&.

[44]   Yamane, R., Sata, T., Mizutani, Y., Onoue, Y., *Bull. Chem. Soc. Jpn.* 1969, *42*, 2741-&.

[45]   Forgacs, C., Ishibashi, N, Leibovitz, J., Sinkovic, J, Spiegler, K. S., *Desalination* 1972, *10*, 181-214.

[46]   Metayer, M., Bourdille, C., Selegny, E., *Desalination* 1973, 13, 129-146.

[47]   Rubinshtein, I., Zaltzman, B., Pretz, J., Linder, C., *Russ. J. Electrochem.* 2002, 38, 956-967.

[48]   Rubinstein, I, Shtilman, L., *J. Chem. Soc.* 1972, *75*, 231-246.

[49]   Li, Q., Fang, Y., Green, M. E., *J. Colloid Interface Sci.* 1983, 91, 412-417.

[50]   Rubinstein, I., Zaltzmann, B., *Phys. Rev. E* 2000, *62*, 2238-2251.

[51]   Manzanares, J. A., Murphy, W. D., Mafé, S., Reiss, H., *J. Phys. Chem.* 1993, *97*, 8524-8530.

[52]   Mishchuk, N. A., Takhistov, P. V., *Colloids Surf. A* 1995, *95*, 119-131.

[53]   Zabolotskii, V. I., Manzanares, J. A., Mafe, S., Nikonenko, V. V., Lebedev, K. A., *Russ. J. Electrochem.* 2002, *38*, 819-827.

[54]   Leinweber, F. C., Tallarek, U., *Langmuir* 2004, *20*, 11637-11648.

[55]   Rubinstein, I., Maletzki, F., *J. Chem. Soc. Faraday Trans. II* 1991, *87*, 2079-2087.

[56]   Rubinstein, I., *Phys. Fluids A* 1991, *3*, 2301-2309.

[57]   Zholkovskij, E. K., Vorotyntsev, M. A., Staude, E., *J. Colloid Interface Sci.* 1996, *181*, 28-33.

[58]   Vasil'eva, V. I., Shaposhnik, V. A., Grigorchuk, O. V., Malykhin, M. D., *Russ. J. Electrochem.* 2002, *38*, 846-852.

[59]   Tallarek, U., Paces, M., Rapp, E., *Electrophoresis* 2003, *24*, 4241-4253.

[60]   Ehlert, S., Hlushkou, D., Tallarek, U., *Microfluid. and Nanofluid.* 2007, accepted for publication.

[61]   Mishchuk, N. A., Dukhin, S. S., in: *Interfacial Electrokinetics and Electrophoresis*, Delgado, A. V. (Ed.), Marcel Dekker, New York 2002, pp. 241-275.

[62]   Barany, S, *Adv. Colloid Interface Sci.* 1998, *75*, 45-78.

[63]   Giddings, J. C., *Dynamics of Chromatography. Part I: Principles and Theory*; Marcel Dekker: New York, 1965.

[64]   Neue, U. D., *HPLC Columns: Theory, Technology, and Practice*; Wiley-VCH: New York, 1997.

[65]   Mistry, K., Krull, I., Grinberg, N., *J. Sep. Sci.* 2002, *25*, 935-958.

[66]   Rathore, A. S., *Electrophoresis* 2002, *23*, 3827-3846.

[67]   Legido-Quigley, C., Marlin, N. D., Melin, V., Manz, A., Smith, N. W., *Electrophoresis* 2003, *24*, 917-944.

[68]   Jiskra, J., Claessens, H. A., Cramers, C. A., *J. Sep. Sci.* 2003, *26*, 1305-1330.

[69]   Dukhin, S. S., *Adv. Colloid Interface Sci.* 1991, *35*, 173-196.

[70]   Mishchuk, N. A., Takhistov, P. V., *Colloids Surf. A* 1995, *95*, 119-131.

[71]   Barany, S., Mishchuk, N. A., Prieve, D. C., *J. Colloid Interface Sci.*1998, *207*, 240-250.

3 Electrohydrodynamics in hierarchically structured monolithic and particulate fixed beds

3.1 Introduction

This chapter investigates the basic dependence of EOF velocity and hydrodynamic dispersion in CEC on the variation of applied field and mobile phase ionic strengths employing silica-based particulate and monolithic fixed beds. The employed porous media have a hierarchical structure characterized by discrete intraparticle (intraskeleton) mesoporous and interparticle (interskeleton) macroporous spatial domains, as required for probing of the nonlinear or nonequilibrium dynamics described in Chapter 2. It is shown, that while the macroporous domains contain quasi-electroneutral electrolyte solution, the ion-permselectivity (charge-selectivity) of the mesoporous domains determines co-ion exclusion and counter-ion enrichment at electrochemical equilibrium (without superimposed electrical field) which depends on mesopore-scale EDL overlap and surface charge density. After investigating this profound adjustable, locally charge-selective transport realized under most general and typical conditions in LC, the general rather than exceptional importance of nonequilibrium CP and CP-based induced-charge electroosmosis in CEC is investigated. We first demonstrate CP and the nonlinear EOF dynamics in silica-based monoliths and sphere packings, then relate these phenomena to the morphology of the hierarchically structured materials, applied field strength, and local charge-selectivity, analyse this dynamics complementary by quantitative CLSM, and finally correlate induced-charge electroosmosis with improved separation efficiencies of electroneutral analytes under typical experimental conditions in CEC.

3.2   Experimental

Chemicals and materials. Tris(hydroxymethyl)aminomethane (Tris), acetonitrile, hydrochloric acid, and dimethylsulfoxide (DMSO) were purchased from Fluka (Sigma-Aldrich Chemie, Taufkirchen, Germany). Alkylbenzoates, naphthalene, anthracene, pyrene, and benzene sulfonic acid came from Merck (Darmstadt, Germany). Fluorescent dyes for CLSM studies, the electroneutral Bodipy 493/503 and twice negatively charged Bodipy-disulfonate, were obtained from Molecular Probes (Leiden, The Netherlands). The negatively charged fluorescent nanoparticles with a nominal size of 50 nm were purchased from Duke Scientific (Palo Alto, CA). Bare silica and C18-silica monoliths fixed in 100 or 50 µm i.d. and typically 50 cm long cylindrical fused-silica capillaries, as well as porous C18-silica particles with different intraparticle pore sizes, but comparable diameter (Table 3.1) were received as research samples from Merck (Darmstadt, Germany), together with mercury intrusion and nitrogen adsorption data needed for the determination of the intraparticle pore volumes and surface areas. As mean pore diameters increase the surface-to-volume ratio decreases significantly and is expectedly smallest for nonporous C18-silica particles (Micra 3 µm) obtained from Bischoff Chromatography (Leonberg, Germany). The structure of the monoliths is characterized by macropores with a mean diameter of about 2 µm and 13 nm mesopores [1], as is indicated in Figure 3.1.

Table 3.1

Physical data for the (non)porous C18-silica particles.

Particles	d_p [µm] [a]	V_{pore} [ml/g]	d_{pore} [nm] [b]	ε_{intra} [c]	A_s [m^2/g] [d]
Porous spheres	2.45	0.85	19	0.66	177.8
	2.45	0.97	25	0.68	109.3
	2.45	0.88	41	0.66	64.7
	2.46	0.65	105	0.59	21.1
	2.42	0.34	232	0.43	7.5
Nonporous	2.45		–		ca. 1 [e]

[a] Refers to the external surface-averaged particle diameter.

[b] Mean intraparticle pore diameter based on the mercury porosimetry data.

[c] Intraparticle porosity calculated according to $\varepsilon_{intra} = (1 + (1/\rho_{SiO}V_{pore}))^{-1}$, with ρ_{SiO} (density of the silica skeleton) taken as 2.24 g/ml.

[d] Specific surface area based on the nitrogen adsorption data.

[e] Finite, albeit small, because of the solid particles external surface area.

Thus, the morphology of the monoliths and fixed beds of porous particles reveals bimodal pore size distributions due to the intraskeleton (intraparticle) mesopores and interskeleton (interparticle) macropores (Figure 2.5). Particle size distributions were measured with a CILAS 1180 laser particle size analyzer (CILAS, Marcoussis, France) employing dilute suspensions in isopropanol.
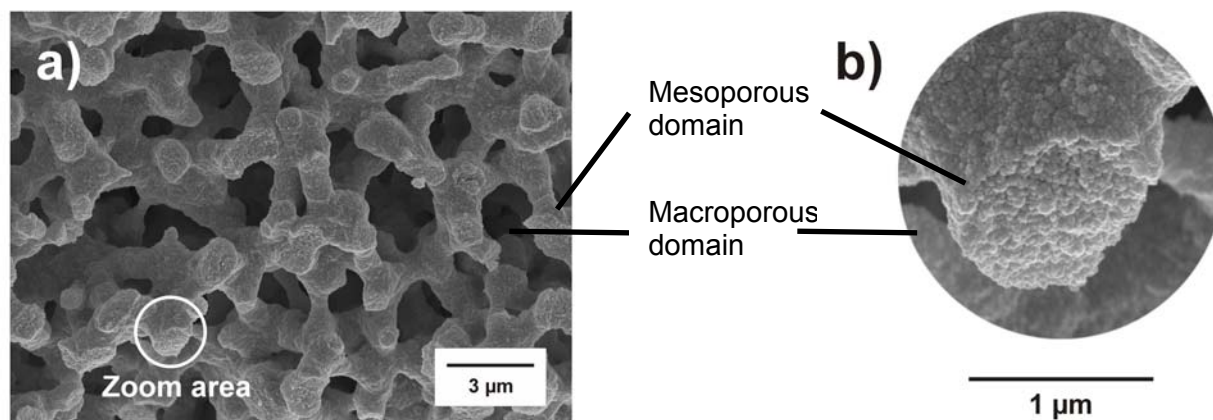
Figure 3.1 Scanning electron microscopy picture of a section of the silica-based monolithic capillary column (for a) and b) with different magnification) employed in this work indicating a bimodal pore size distribution with large flow-through pores (macropores) of about 2 µm, skeleton domains (mesoporous) of about 1 µm with high internal skeleton porosity (13 nm mesopores) [6].

Tris buffer solutions in 80:20 acetonitrile/water (v/v) were used as electrolyte. Mobile phases were filtered over 0.45 µm nylon membrane filters and degassed by ultrasonication. An aqueous stock solution of 0.1 M Tris (base form) was prepared using water purified with a Milli-Q-Gradient (Millipore GmbH, Eschborn, Germany). The pH was adjusted to 8.3 by titration with concentrated hydrochloric acid. Appropriate volumes of this stock solution, MilliQ water, and acetonitrile were then mixed to yield Tris buffer solutions of the desired ionic strengths in 80:20 acetonitrile/water (v/v), e.g., 1×10^{-3} M Tris in the final mobile phase corresponded to 5×10^{-3} M Tris in the aqueous part. The concentration of protonated Tris (acidic form) needed to estimate the thickness of the primary quasi-equilibrium EDL was determined using the Henderson-Hasselbalch equation (with pH $\approx$ pK$_a$). Fresh samples were prepared daily by dissolving test compounds directly in running mobile phase (usually 100 µg/ml).

Capillary electrochromatography. The particles were slurry-packed in 100 µm i.d., 360 µm o.d. fused-silica capillaries (Polymicro Technologies, Phonenix, AZ) with a modified procedure described previously [2], resulting in duplex columns. A WellChrom K-1900 pneumatic pump (KNAUER GmbH, Berlin, Germany) was used. As the slurry reservoir 500 µm i.d. glass-lined metal tubing has been utilized. MicroTight inline filters, which provided a temporary outlet frit during packing were obtained from Upchurch Scientific (Oak Harbor, WA, USA). An SSI two-way valve and SSI (dual-stem) three-way valve (ERC, Riemerling, Germany) between pneumatic pump and slurry reservoir were used for pressure release and slurry injection, respectively. Slurries were prepared by suspending an appropriate amount (usually 5 mg) of the dry particles in 100 µl acetone under ultrasonication for 1 min. The slurry reservoir was filled with a syringe. Subsequently, using water as a pushing fluid, particles were forced into the fused-silica capillary at set pressure. During the packing process the capillary (and optionally also the slurry reservoir) was placed in an ultrasonic bath to compact and stabilize the beds which reached a length of at least 300 mm within 30 min. The bed was inspected for uniformity with a microscope during packing. At a little higher pressure than used for the packing, permanent inlet and outlet frits of a bed were made by sintering the silica particles for 350 ms with an arc fusion splicer FSM-05S (Fujikura Tokyo, Japan) in its prefusion mode. Pressure was released to 200 bar, the MicroTight inline filter disconnected from the column, and the remainder of particles on

both sides were flushed out with water. Protocols for column packing and frit sintering were optimized with respect to the pore-sizes of a material and their mechanical stability. A packing pressure of only 250 bar was selected for the particles with 220 nm mean pore size, respectively. The detection window was prepared directly behind the outlet frit and on-column detection was performed at 230 nm. Packed columns were preconditioned with the mobile phase under pressure (usually 100 bar) and then conditioned electrokinetically, with subsequent buffer replenishment, until stable conditions have been obtained in view of baseline drift, current and reproducible, stable EOF. Effective field strengths over the packed segment were evaluated according to available theory and procedures [3, 4].

Monoliths were cut to desired length and assembled directly, i.e., without open tubular segments in a HP³ᴰCE instrument (Agilent Technologies, Waldbronn, Germany), and detection at 230 nm was made in-column. Measurements were run at controlled temperature of 298 K. Both vials were pressurized in order to minimize bubble formation. For obtaining reproducible results buffer replenishment and subsequent capillary equilibration was crucial [5]. This was ensured by subsequent injection of sample and running the same analysis method up to 20 times without buffer replenishment, where no drift in EOF velocity and efficiency has been observed. Such drifts may occur due to buffer electrolysis in the mobile phase vials and related pH changes, if the buffer capacity is exceeded [5].

Ethylbenzoate, butylbenzoate, naphthalene, phenanthrene, and pyrene were used as weakly retained, neutral analytes and thiourea as the flow field (average velocity) marker. Before each run capillaries were conditioned for 30 min at a voltage of 15 kV. Afterwards, new vials were used and the system was again equilibrated at 15 kV for another 7 min.
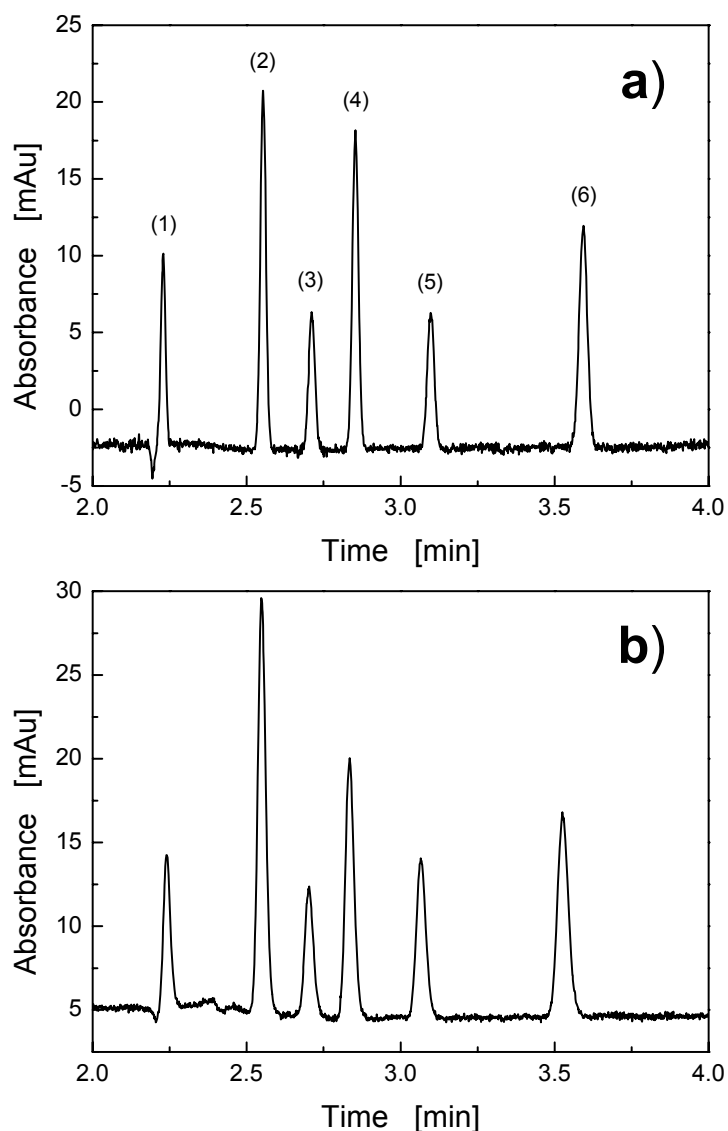

Figure 3.2   Representative electrochromatograms with a 316 mm (233 mm effective) × 100 μm i.d. C18-silica monolith. (1) Thiourea, (2) ethylbenzoate, (3) naphthalene, (4) butylbenzoate, (5) phenanthrene, and (6) pyrene. The eluent is 80:20 acetonitrile/water (v/v). a) 0.1 mM effective Tris concentration (thiourea: 3.85×10^5 N/m, ethylbenzoate: 3.69×10^5 N/m, pyrene: 3.29×10^5 N/m). b) 5 mM effective Tris concentration (thiourea: 1.95×10^5 N/m, ethylbenzoate: 2.02×10^5 N/m, pyrene: 1.90×10^5 N/m). Similar EOF velocities of about 1.7 mm/s have been selected for comparison.

Finally, the analysis was run at the desired voltage. In advance of each sequence the velocities for 15 kV and 30 kV were checked by individual injections and usually found to coincide with velocities measured during the complete sequence. Figure 3.2 shows typical electrochromatograms using 0.1 mM and 5 mM effective Tris concentration. The retention time (t_R) and number of theoretical plates (N) for a chromatographic peak were extracted by statistical moments analysis employing an algorithm written in Matlab (The MathWorks, Natick, MA). The efficiencies were generally comparable to Gaussian fitting, i.e., differences were marginal because the peaks always showed a high symmetry in both CEC and capillary LC modes.

Liquid chromatography. Capillary LC measurements with particulate beds were made on a configuration containing a degasser and SpectraFlow 501 UV/Vis detector (SunChrom, Friedrichsdorf, Germany) operated at 215 nm for on-column detection, and a MicroPro syringe pumping system (Eldex Laboratories, Napa, CA). For injection (3 bar for 3 s) a Model 7520 injector valve with a 0.5 µL sample loop (Rheodyne, Cotati, CA) was used. With the silica-based monoliths capillary HPLC was realized inside the HP^{3D}CE instrument using the available helium gas pressure in combination with short-end injection. Then, the same monolith as in CEC was cut to a length of 11 cm and connected to a 150 µm i.d. open capillary. The effective separation length was 8.4 cm. Inlet pressures from 2 to 11 bar were applied resulting in average velocities of approximately 0.5 to 2.5 mm/s,
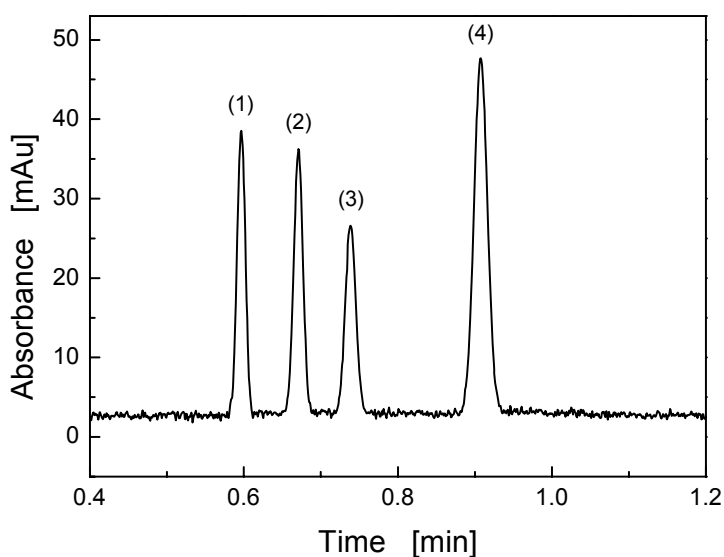

Figure 3.3 Representative chromatogram with a 110 mm (84 mm effective) × 100 µm i.d. C18-silica monolith obtained by short-end injection in the HP^{3D}CE. (1) Thiourea, (2) ethylbenzoate, (3) butylbenzoate, and (4) pyrene. The eluent is 80:20 acetonitrile/water (v/v) containing 5 mM effective Tris concentration (thiourea: 1.67×10^5 N/m, ethylbenzoate: 1.66×10^5 N/m, pyrene: 1.40×10^5 N/m). The velocity is 2.34 mm/s (inlet pressure: 10 bar).

respectively, according to the permeability of this type of monolith [6]. The use of the HP^{3D}CE for the capillary LC experiments has the advantage of realizing a similar system environment as in CEC with reproducible injection and without extra-column band broadening. This facilitates a comparison of separation efficiencies in capillary LC and CEC. Figure 3.3 shows a typical chromatogram obtained in the HP^{3D}CE system with hydraulic flow. As seen in Table 3.2 the reproducibility of average velocities was satisfactory.

Table 3.2

Reproducibility of hydraulic flow velocities in the HP[3D]CE instrument in the Short-end injection mode. Monolith length: 11 cm (8.4 cm effective). Mobile phase: acetonitrile/H_2O (pH 8.3) 80:20 (v/v) with 5 mM effective Tris concentration.

Inlet pressure [bar]	Average velocity [10^{-3} m/s]	RSD (%)
4	0.98	0.33
6	1.47	0.60
7	1.70	0.92
8	1.93	0.92
9	2.11	0.53
10	2.34	0.53
11	2.54	0.41

Confocal laser scanning microscopy. CLSM experiments were made on an Axiovert 100 confocal laser scanning microscope (Carl Zeiss, Jena, Germany) equipped with two continuous noble gas lasers (Argon ion laser: 488 nm, 25 mW maximum output power; Helium-Neon ion laser: 543 nm, 1 mW) and 40x oil immersion objective (1.3 NA). Images were acquired in section-scanning mode, i.e., in the xy-plane which is perpendicular to the optical axis, but parallel to the EOF direction. The geometry of the microfluidic device containing capillaries with particulate beds and monoliths allowed it to be inserted like a conventional microscopy slide into the respective frame. The principal experimental setup is illustrated in Figure 3.4.

Electrolyte reservoirs (1.5 ml volume) were made of PEEK and equipped with a standard 1/16" thread to insert and fix the capillaries. Fitting materials were purchased from Upchurch Scientific (Oak Harbor, WA). High voltage supply was realized using a 30 kV d.c. power generator (F.u.G. Elektronik, Rosenheim, Germany). Platinum wire electrodes were directly inserted into the electrolyte solutions of each vial. In advance of the measurements the confocal microscope was grounded.

The performance of the system was verified also for the measurement of EOF velocities complementary to the HP[3D]CE system by changing from the pure buffer solution in the inlet vial to dyed one containing nonadsorbing tracer (Bodipy 493/503) and following its elution with appropriate time-series. This CLSM setup allows much higher field strengths (up to 200 kV/m) than the HP[3D]CE instrument. The refractive index (RI) mismatch between the porous silica-based materials (RI $\approx$ 1.47) and saturating mobile phase containing acetonitrile (RI $\approx$ 1.33) causes significant loss of fluorescence light intensity at increasing optical penetration depth due to aberration and, therefore, hampers quantitative data evaluation [7]. RI mismatch was minimized by using a mobile phase consisting of

90:10 (v/v) DMSO and the aqueous Tris buffer. The mobile phase contained fluorescent dye at a concentration of 10^{-5} M.
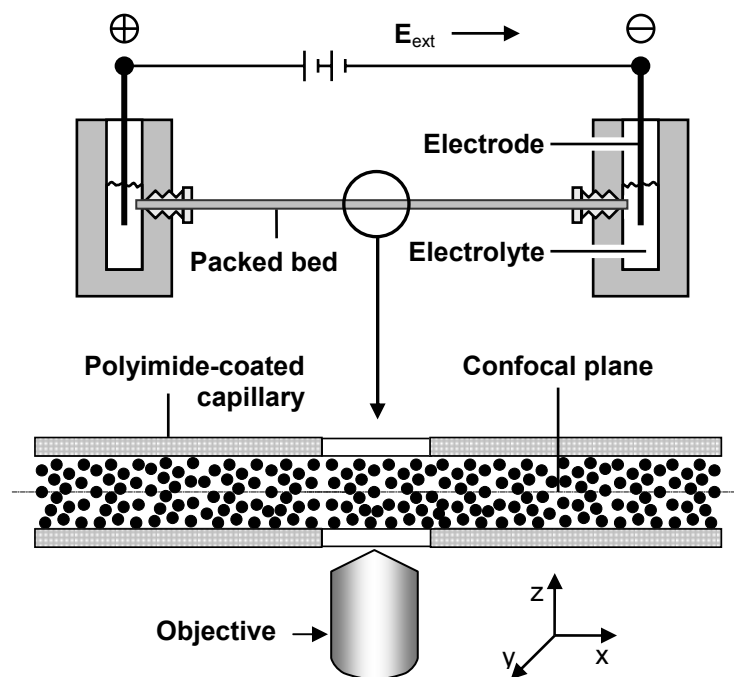

Figure 3.4 Schematic of the experimental setup used for the CLSM study of CP and EOF in fixed beds of the desired particles or optionally monolith. PEEK vials served as inlet and outlet reservoirs, into which stainless steel electrodes were inserted to apply the electrical fields. Polyimide-coating was removed at the center of the capillary. The setup allowed three-dimensional visualization of fluorescent tracers and their dynamics in the fixed beds optically matched to the fluid phase.

3.3   Results and discussion

We present the results of our investigations on coupled mass and charge transport in porous media in view of closely related phenomena, with an increase in complexity, to provide systematic and complementary insight. We start in Section 3.3.1 by recalling the existence of charge-selective transport and Donnan potentials (at electrochemical equilibrium, without externally applied electrical field) in the chromatographic media under very typical conditions. In Section 3.3.2 we document the more general rather than exceptional observed nonlinear EOF dynamics due to CP-based induced-charge electroosmosis in random-close sphere packings and monoliths used in CEC. We provide direct insight into operational domains of these phenomena in Section 3.3.3 employing quantitative CLSM, and in Section 3.3.4 analyze dependencies of CP and CP-based induced-charge electroosmosis on the hydrodynamic flow regime, mobile phase ionic strength, general charge-selectivity, applied field strength, and the morphology of the material. Finally, in Section 3.3.5 we demonstrate the consequences of these unique electrokinetic and electrohydrodynamic phenomena with respect to zone spreading in CEC.

3.3.1   Internal electrical fields in chromatographic media

In this work, we used the benzene sulfonic acid anion as a negatively charged tracer behaving co-ionic with respect to the surface charge of the encountered silica-based materials. The influence of the mobile phase ionic strength (corresponding to half of the Tris concentration) on the effective residence times of this co-ionic analyte employing hydraulic flow is shown in Figure 3.5 for the particulate materials characterized by different intraparticle mean pore sizes (see Table 3.1). While the benzene

sulfonic acid anion practically experiences only the interparticle porosity (ε_{inter}) at low ionic strength, it co-elutes with thiourea at high ionic strength when it experiences the total bed porosity given by $\varepsilon_{total} = \varepsilon_{inter} + (1 - \varepsilon_{inter})\varepsilon_{intra}$. Thus, the residence time of a co-ion depends sensitively on Donnan-exclusion from the intraparticle pore spaces [8] or, in other words (those of the EDL model), on the actual pore-scale EDL overlap [9]. The thickness of the primary EDL is approximated by the Debye screening length λ_D according to eq. 1.1 [9]. Depending on EDL overlap inside the particles represented by r_{intra}/λ_D (Figure 3.5) we observe a similar normalized behavior for the different pore diameters (d_{intra})
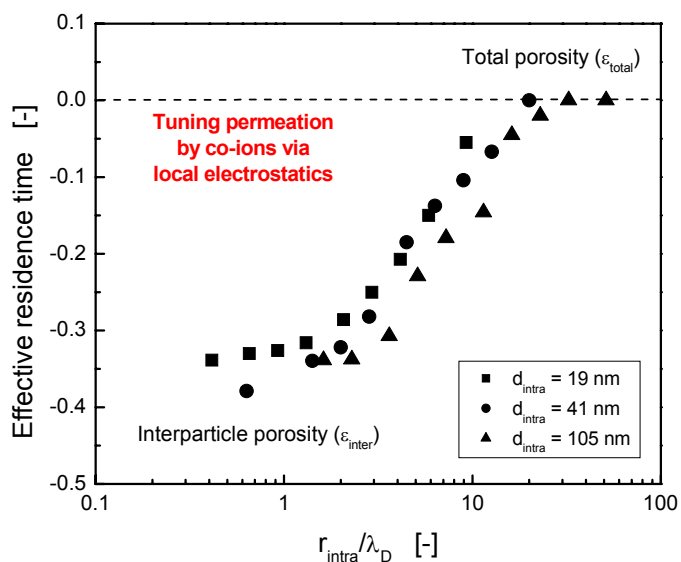

Figure 3.5   Effect of intraparticle EDL overlap on the effective residence time of a co-ionic analyte in HPLC. Capillary columns (150 mm × 100 μm i.d.) were packed with C18-silica particles (Table 1). Mobile phase is 80:20 acetonitrile/water (v/v) with varying Tris concentrations. Thiourea is employed as dead time (t_0) marker and the benzene sulfonic acid anion as a co-ionic analyte. Effective residence times t' = (t-t_0)/t_0 of the analyte were monitored with respect to r_{intra}/λ_D in order to facilitate a comparison between the different ionic strengths and intraparticle pore sizes.

and ionic strengths, with complete permeation (ε_{total}) and exclusion (ε_{inter} only) of the co-ionic tracer as extreme scenarios.

This fundamental and general, but relatively often unrecognized behavior is further analyzed by Figure 3.6a showing the radial distribution of normalized electrical potential over a pore cross-section at different aspect ratios r_{pore}/λ_D [9]. For $r_{pore}/\lambda_D \approx 1$ the EDL extends over the whole pore fluid. Thus, the pore becomes ion-permselective and effectively excludes the co-ions (cf. Figure 3.5). Their transport numbers decrease at increasing EDL overlap, while those of the counter-ionic species increase. For $r_{pore}/\lambda_D \gg 1$ the EDL is confined to just a thin layer at the pore walls, meaning that the whole pore fluid is quasi-electroneutral and charge-selectivity has disappeared (cf. Figure 3.5). Transport numbers of the co-ions and counter-ions become balanced. Basically, these extremes ($r_{pore}/\lambda_D < 1$ and $r_{pore}/\lambda_D \gg 1$) as well as the broad intermediate regime can be tuned in chromatographic practice by mobile phase ionic strength (λ_D) and the intraparticle or intraskeleton pore dimensions (d_{intra}). This adjustable electrostatic on-off behaviour [10-15]

Figure 3.6 a) Pore-scale distribution of electrical potential normalized by the surface potential ψ_s for different values of r_{pore}/λ_D (adapted from [9]). b) Dependence of r_{intra}/λ_D on the effective mobile phase Tris concentration for intraparticle and intraskeleton pores of the materials employed in this work.

for intraparticle permeation in conventional chromatographic media (Figure 3.5) is relevant also for the design of preparative separations and purification processes [16-18] as the actual electrolyte concentration determines the availability of chromatographic sites and effective porosity for co-ionic analytes, as well as pore-level concentrations of charged analytes (co-ion exclusion, counter-ion enrichment) in general.

Figure 3.6b demonstrates the dependence of r_{intra}/λ_D on mobile phase ionic strength for porous particles and monoliths employed in this work. It is important to realize a quite persistent EDL overlap ($r_{intra}/\lambda_D < 10$) in the intraparticle and intraskeleton meso- and macropores leading to co-ion exclusion

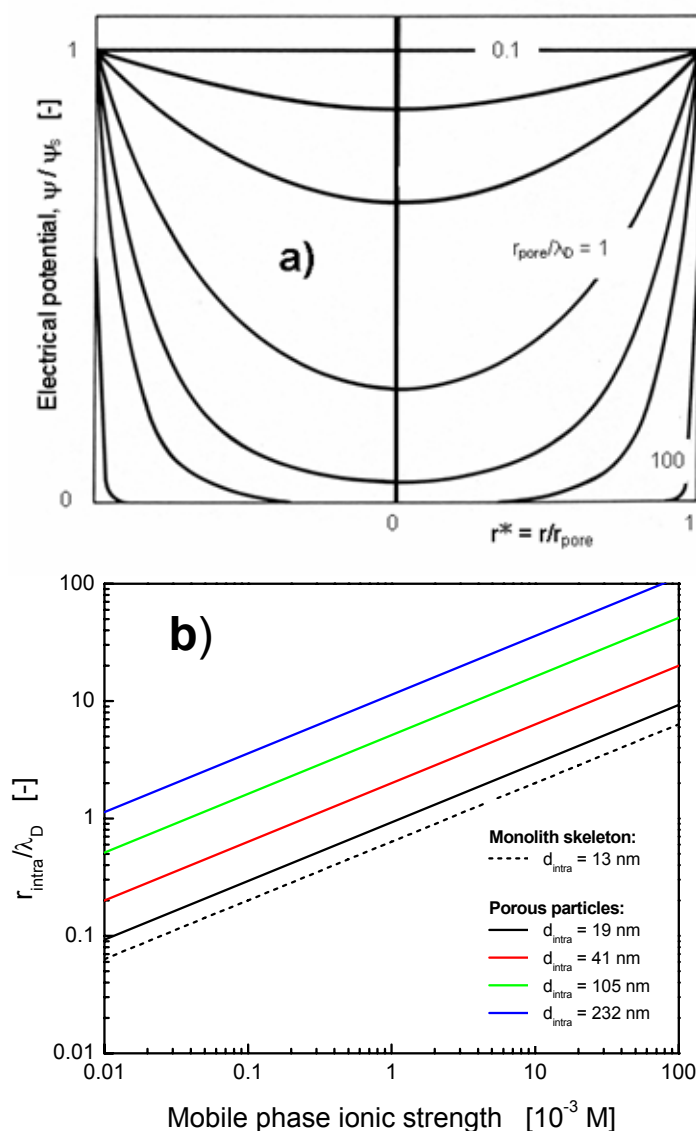and counter-ion enrichment in the pores under typical chromatographic conditions. In agreement with the trend in Figure 3.6a the dynamics seen in Figure 3.5 suggests the strongest changes in electrostatic exclusion between $1 < r_{intra}/\lambda_D < 10$, thereby demonstrating a unique dependence on pore size (r_{intra}) and ionic strength (λ_D). With respect to Figure 3.6b this range of r_{intra}/λ_D translates to ionic strengths between 1 and 100 mM which includes conditions very common to (electro)chromatography employing fixed beds of mesoporous particles or monoliths with a mesoporous skeleton.

To summarize, the electrical potential gradients which develop at the boundaries between the quasi-electroneutral interparticle (interskeleton) macropore space and the intraparticle (intraskeleton) charge-selective domain are important in LC where they influence distributions of charged analytes in the hierarchically structured porous media. In CEC they form the basis for CP induced locally by the electrical field superimposed externally on the internal potential gradients, which makes coupled mass and charge transport far more complex than in LC [19].

3.3.2 Concentration polarization, nonlinear electroosmosis, and perfusive flow

Regarding Chapter 2, the local presence of charge-selective interfaces together with the electrical field strengths in CEC of up to 100 kV/m can induce nonequilibrium CP which leads to a fundamental structural change of the EDL as the system moves away from quasi-equilibrium [20-26]. The mobile SCR (Figure 2.4) induced by the normal field component is the fluid-side part of the secondary, nonequilibrium EDL and interacts locally with the tangential component of the applied field to generate nonlinear (induced-charge) electroosmotic slip along curved interfaces in particulate or monolithic fixed beds employed in CEC [1]. Because the conductivity of this SCR (region of lowest electrolyte concentration and highest resistance) is much lower than that of the bulk solution, potential drop in the depleted CP zone occurs mainly in the secondary EDL. In other words, potential drop in the electrical field-induced, mobile SCR behaves like an electrokinetic potential, similar to the ζ-potential in classical, linear electroosmosis [27, 28]. However, in contrast to the latter, the potential due to nonequilibrium CP is independent of surface charge, but depends on both the size of the charge-selective domain and applied field strength (Figure 2.4) [28]. At decreasing field strength and/or charge-selectivity this potential is expected to turn smoothly into the classical ζ-potential [1, 19]. To demonstrate this behaviour we have recorded EOF velocities in silica-based monoliths in dependence of Tris buffer concentration (which modulates the charge-selectivity of the intraskeleton mesopores) and applied electrical field strength (which determines the local intensity of electromigration, thus, also the intensity of the induced CP zones).

Figure 3.7a shows part of these data. As the Tris concentration is decreased from 10 mM to 0.1 mM we witness the systematic development of a nonlinear contribution to the average EOF velocity as the electrical field strength
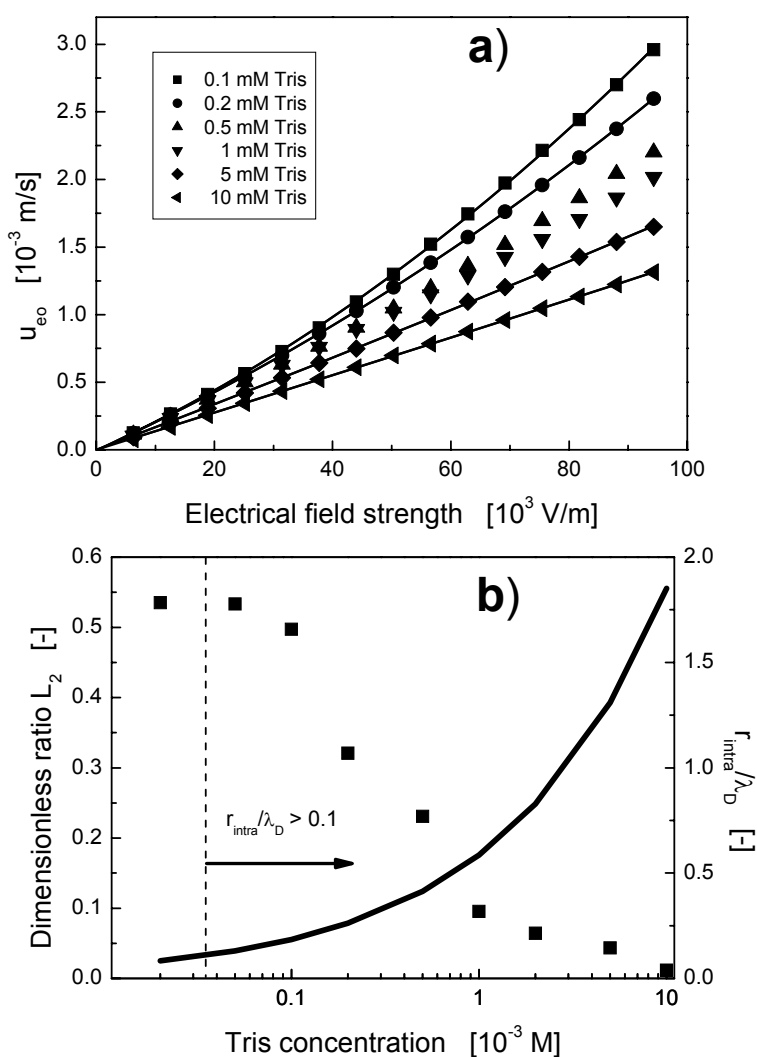

Figure 3.7 a) Average EOF velocities with thiourea as dead time marker in a 100 μm i.d. C18-silica monolith depending on the applied field and mobile phase ionic strengths. Mobile phase is 80:20 acetonitrile/water (v/v) containing varying Tris concentrations. b) Contribution of nonlinear with respect to linear behaviour in plots of EOF velocities against field strength over the range of employed Tris concentrations (squares). The developing nonlinearity clearly correlates with a decrease of r_{intra}/λ_D (solid line) towards 0.1. Data were obtained with the HP^{3D}CE instrument.

(acting over the monolith) is increased to almost 100 kV/m. This nonlinear contribution, particularly with 0.1 and 0.2 mM Tris, is evidenced by the second-order polynomial fits to the EOF data, while we observe linear behaviour with 5 and 10 mM Tris (Figure 3.7a). Due to nonlinear flow, velocities significantly higher than expected from linear dependence are realized. The dissipation of Joule heat cannot explain this nonlinearity because electrical current through the monolith depends linearly on applied field strength [1], as expected for a macroscopically charge-nonselective material. It also indicates that the contribution from EOF to the overall electrical current is negligible with respect to the bulk conductivity of the electrolyte solutions [29], i.e., the macropore space mostly carries quasi-electroneutral liquid. To estimate quantitatively relative contributions of linear (classical) and nonlinear (here, induced-charge) electroosmosis in the interskeleton macropores we analyzed both contributions in the EOF velocity curves via the L_2 (Euclidean) norm

$$L_2 = \left(\int (f_1 - f_2)^2 \, dx \bigg/ \int f_1^2 \, dx \right)^{1/2} , \qquad (3.1)$$

with $f_1 = ax$ and $f_2 = ax + bx^2$. The results of this analysis in Figure 3.7b clearly show that the contribution of the nonlinear electroosmosis correlates well with an increased charge-selectivity of the intraskeleton mesopores expressed by r_{intra}/λ_D. With a higher charge-selectivity of the intraskeleton mesopore space more intense space charges (comprising the secondary EDL) can be induced at a given field strength which, in turn, stimulates electroosmosis of the second kind in the interskeleton macropore space of a monolith [1, 19]. It is the basic relation between mobile phase Tris concentration (ionic strength) and the observed nonlinear EOF velocities (Figure 3.7).

Compared to the C18-silica monolith (Figure 3.7) we show in Figure 3.8a EOF velocities obtained with a bare silica monolith from the same original batch. However, these measurements were not run in the HP^{3D}CE instrument, but were made by CLSM in a home-built device (Figure 3.4) where the same
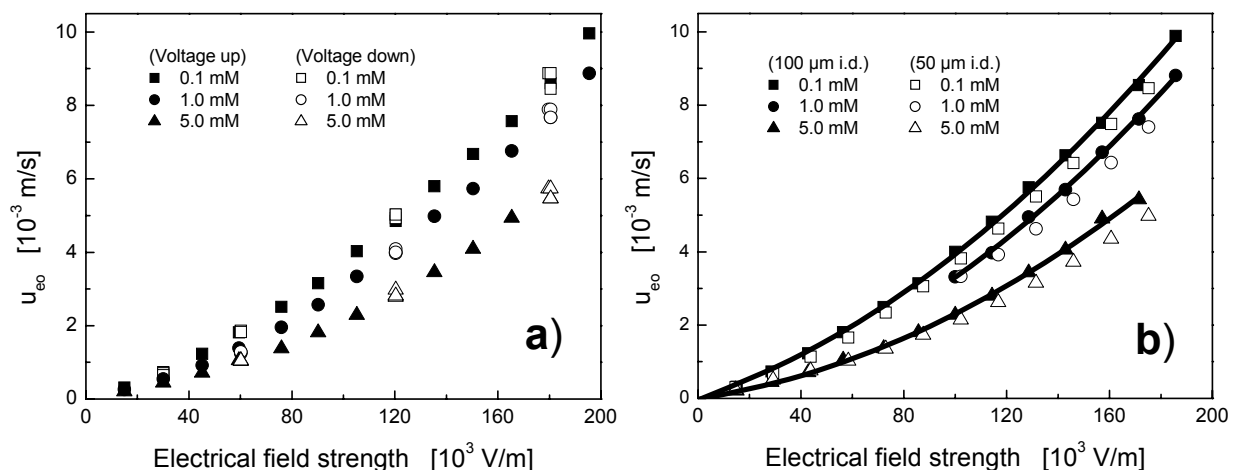

Figure 3.8 a) Average EOF velocities in a 100 μm i.d. bare silica monolith in dependence of applied field strength and mobile phase Tris concentration. b) Comparison of the EOF velocities in 100 μm and 50 μm i.d. bare silica monoliths. Second-order polynomial fits to the data with the 100 μm i.d. monolith are a guide to the eye. Data were obtained with the CLSM device. Mobile phase: 80:20 acetonitrile/water (v/v) with different Tris concentrations, as indicated. The electroneutral, nonadsorbing fluorescent dye (Bodipy 493/503) was used as the velocity marker.

monolith is fixed under the microscope, allowing applied field strengths of up to 200 kV/m. We used the electroneutral fluorescent dye (Bodipy 493/503) as EOF marker [19] and employed the same mobile phase as for the C18-silica monolith (Figure 3.7). The nonlinearity again is very pronounced, especially for the lower ionic strengths (Figure 3.8a). Velocities approaching 1 cm/s were measured very reproducibly. Data were first acquired at increasing voltage, then again at selected lower voltages. Figure 3.8a demonstrates that the system shows no hysteresis. To investigate the significance of wall effects due to porosity fluctuations (or even a wall gap) and effect of a related aspect ratio, i.e., column-to-macropore diameter ratio, on the average EOF velocities we compared 50 and 100 µm i.d. bare silica monoliths prepared following a similar protocol which should result in comparable morphologies. Figure 3.8b shows that absolute velocities agree within a few percent

meaning that differences in monolith morphology related to different capillary diameters are insignificant concerning the analyzed (nonlinear) flow behavior.

Figure 3.9a compares the velocities in 100 µm i.d. bare silica and C18-silica monoliths from the same batch. While we generally observe a nonlinear flow dynamics, we notice a decent attenuation of this dynamics in the C18-silica monolith. This is consistently caused by a lower surface charge density and related, i.e., weaker charge-selectivity of the mesopores, as well as a smaller classical ζ-potential compared with the bare-silica material. Nonlinear EOF behaviour with the bare silica monolith remains substantial even with 5 mM Tris. It is further illustrated in Figure 3.9b which compares the flow dynamics for C18-silica and bare silica monoliths with different capillary diameters (using 5 mM Tris throughout). While we observe a practically linear dynamics with the C18-silica materials (squares), only becoming slightly nonlinear with the unthermostated CLSM device due to
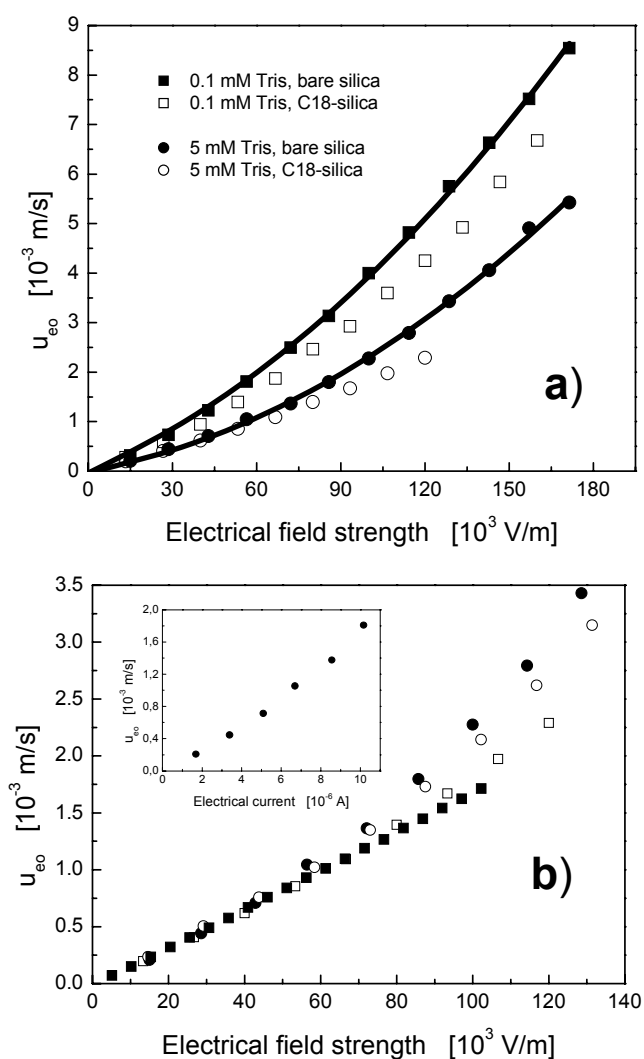

Figure 3.9 a) Comparison of EOF velocities in 100 µm i.d. bare silica and C18-silica monoliths. The data were obtained using the CLSM device. Mobile phase: 80:20 acetonitrile/water (v/v) with different Tris concentrations, as indicated. b) Comparison of EOF velocities with 5 mM Tris concentration in the mobile phase for different monoliths: (●) 100 µm i.d. bare silica, CLSM; (■) 50 µm i.d. bare silica, CLSM; (○) 100 µm i.d. C18-silica, CLSM; (◆) 100 µm i.d. C18-silica, HP[3D]CE. Inset: EOF velocity vs. electrical current for the 100 µm i.d. bare silica monolith.

Joule heating, the bare silica materials (circles) demonstrate a stronger nonlinearity. As revealed by the inset in Figure 3.9b this cannot only be explained by dissipation of Joule heat because of a significantly nonlinear velocity-current relation. To conclude, the key importance of the surface charge density (bare silica vs. C18-silica) results from its influence on the pore-level distribution of electrostatic potential (shown in Figure 3.6a in a dimensionless form) which directly influences the charge-selectivity and local intensity of CP, and thus the contribution of nonlinear electroosmosis at a given field strength.

The nonlinearity in the acquired EOF velocity data can be highlighted by a systematic variation of electroosmotic mobility (μ_{eo}) in dependence of the mobile phase Tris concentration. This is shown in Figure 3.10 (covering the range from 10^{-5} to 10^{-2} M Tris) for selected applied field strengths using the data in Figures 3.7a and 3.9a. First, we can retrieve a relatively common trend insofar as the mobility increases with the decreasing ionic strength of the solution to approach a maximum which has the character of a plateau. The most intriguing feature in
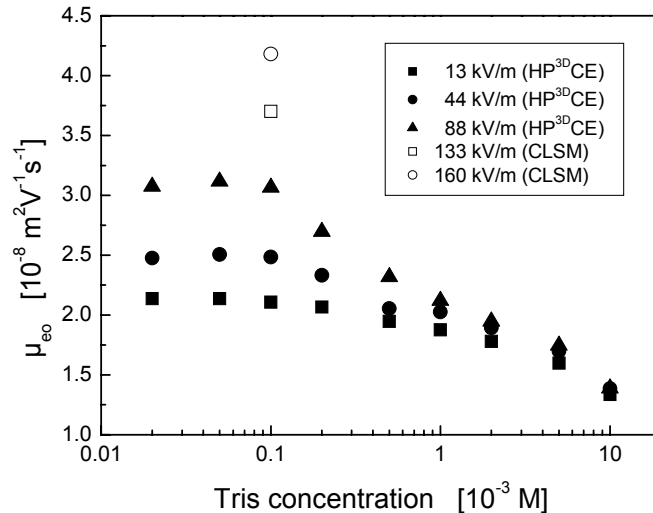

Figure 3.10   Electroosmotic mobility for the 100 µm i.d. C18-silica monolith against Tris concentration at selected field strengths, as indicated.

Figure 3.10 is that the electroosmotic mobility depends on applied field strength with constant mobile phase composition under isothermal (or nearly so) conditions. This dependence becomes aggravated as the ionic strength is reduced, particularly between 5 and 0.1 mM Tris (as seen in the different slopes of the curves in Figure 3.10). By contrast, for classical, linear EOF the mobility is independent of the applied field strength.

It appears rather simple to modulate the EOF behaviour (relative contributions of classical and induced-charge electroosmosis) in the silica-based monoliths, which are characterized by bimodal pore size distributions [30], via the applied field and mobile phase ionic strengths (Figures 3.7 to 3.10.). Thus, it seems important to analyze in more detail also related behaviour in fixed beds of porous particles, as the main prerequisite for CP effects is the presence of charge-selective pore space which, in this case, is presented by the permeable and conducting particles. The employed particles had a mean diameter of about 2.5 µm, but different intraparticle pore sizes (cf. Table 3.1). As seen in Figure 3.11a average EOF velocities (at constant ionic strength) increase substantially with the large-pore materials (105 and 232 nm) which effectively reduce the EDL overlap to produce stronger EOF inside these particles, thereby increasing also average EOF velocities (Chapter 1.4) [31-38]. For the measurements in Figure 3.11a the ionic strength (λ_D) remained constant and a variation of r_{intra}/λ_D was realized using the different mean pore sizes. The strongest ion-permselectivity and CP

effects are expected for particles with the smaller pores (19 and 25 nm). Indeed, we can resolve a clear nonlinearity in their velocity data as shown separately in Figure 3.11b. Even though it seems to be a small effect, it is systematic. Further, the nonlinearity has even not disappeared for the 40 nm-pore particles, only the dynamics for the large-pore particles is practically linear (Figure 3.11a). As with the monoliths this behaviour for porous particles depends sensitively on r_{intra}/λ_D which is not surprising when it is the fundamental, CP-related effect of induced-charge electroosmosis. It is usually overlooked in CEC practice because particles are small ($d_p < 10$ μm) and densely packed which causes significant multiparticle effects compared to the electrohydrodynamics evolving from a single (free) particle-picture [19]. Still, it does not mean that all CP-related effects become insignificant in CEC; only one possible consequence, nonlinear electroosmosis, seems to be relatively weak in common practice employing dense beds of small porous particles.

Compared to the sphere packings nonlinear electroosmosis is more intense in the monoliths which can be explained by the different ways of realizing the hierarchically structured

Figure 3.11 EOF velocity curves for the particulate beds in dependence of the intraparticle pore size (see Table 3.1 for further details). Mobile phase: 80:20 acetonitrile/water (v/v) with 0.1 mM Tris concentration. Data were obtained with the HP[3D]CE instrument.

pore space. For random-close sphere packings the interparticle pore dimensions are inherently associated with particle diameters, while for monoliths interparticle macropore dimensions can be adjusted independently from the size of the skeleton. Thus, the macropore domain in monoliths can offer more space relative to the size of the charge-selective domain when compared to the random-close packings of charge-selective particles. Figure 3.12 compares the intensities of nonlinear electroosmosis for the silica-based monoliths and porous particles. The EOF dynamics in a capillary packed with nonporous (i.e., impermeable and nonconducting) particles serves as the reference. In fact, we find linear behaviour with the nonporous particles over the complete range of Tris concentrations, while we notice an increasing nonlinearity for porous spheres as the intraparticle pore size is decreased (at 0.1 mM Tris). However, the nonlinearity developing in the monolith (with a comparable mesopore size) is still much stronger. Thus, Figure 3.12 also demonstrates that the
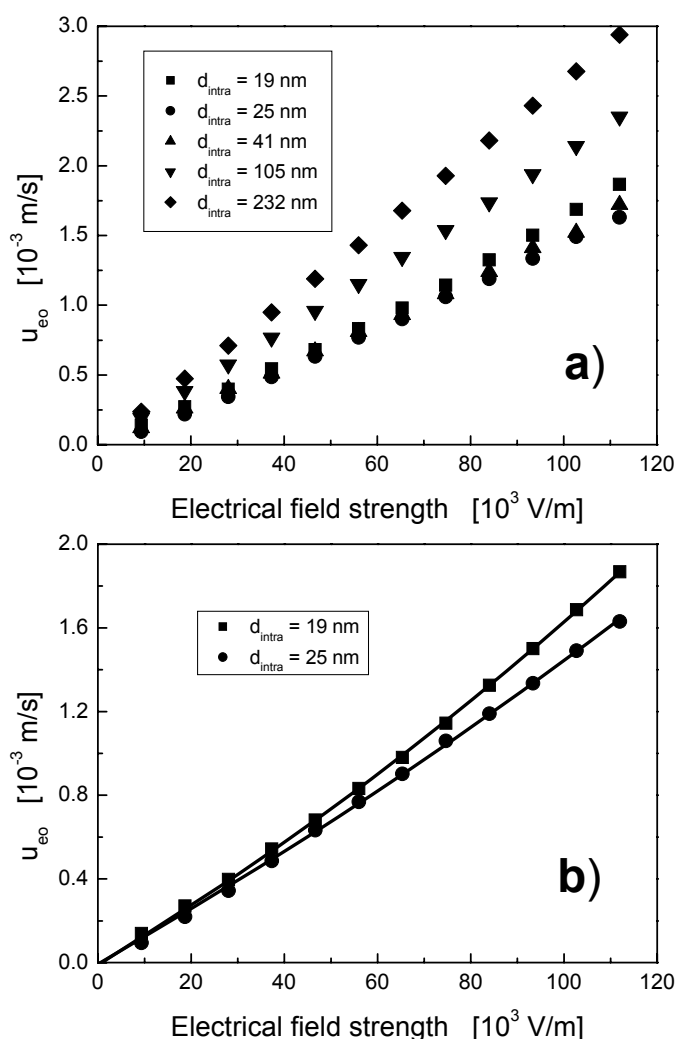
morphology of the charge-selective regions (e.g., size, interconnectivity, domain discreteness, spatial distribution, and shape factors) in hierarchically structured porous media critically determines the electrohydrodynamics in the macropore space. A clear evidence for induced-charge electroosmosis based on CP as operating phenomenon in the monoliths and sphere packings comes from the indifferent behaviour that is observed for the capillary packed with nonporous particles which simply does not contain charge-selective regions, but only the quasi-electroneutral interparticle macropore fluid.

Figure 3.12   Analysis of nonlinear contributions in the EOF data (via the L_2 norm; see eq. 3.1) acquired for particulate and monolithic fixed beds depending on mobile phase Tris concentration. Lines are drawn as a guide to the eye. Nonporous spheres are included for comparison demonstrating indirectly the existence of CP phenomena in beds of porous particles and the monolith.

Although selected data in the literature indicate nonlinear EOF behaviour in CEC with packed capillaries under conditions of substantial intraparticle EDL overlap (see, e.g., Figure 7 in [39], Figure 10 in [40], Figure 2 in [41], Figure 8 in [42], and Figure 4 in [43]) a more important consequence of CP is related to separation efficiency and especially the retention behaviour of charged analytes because the induced CP zones present an elegant route to a field-dependent, i.e., easily externally and sensitively tunable retention factor [44].
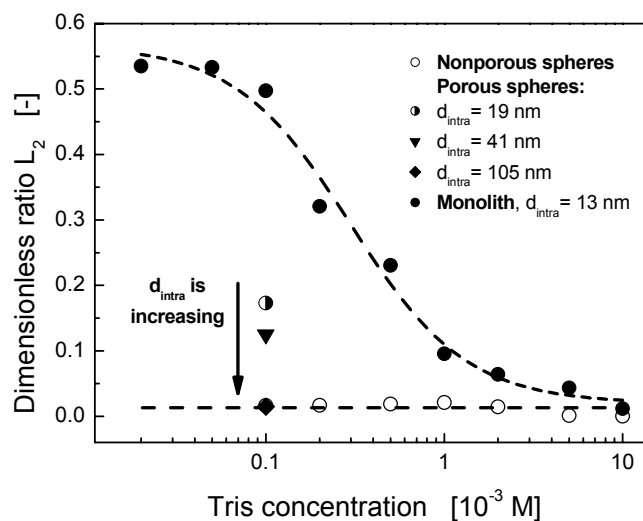
3.3.3 Confocal laser scanning microscopy for exploring the microscopic origin of nonlinear electroosmosis

To gain microscopic insight into the CP phenomenon operating in the monolithic structures we employed CLSM. The RI match between monolith skeleton and saturating liquid allowed a quantitative evaluation of the stationary distributions of fluorescent dyes used as indicator for the CP phenomenon in dependence of applied field and mobile phase ionic strengths. Although the data are not shown, we first used the RI matched mobile phase (90:10 DMSO/H_2O) and measured EOF velocities as a function of the applied field strength for selected Tris concentrations. In agreement with our previous data we found a nonlinear EOF dynamics, but velocities were expectedly smaller, roughly according to the ratio of ε_r/η accounting for a different relative permittivity (ε_r) and viscosity (η) of the liquid [45]. This prerequisite ensured that the same phenomena as in CEC will be operating during the CLSM studies.

Figure 3.13 demonstrates (for a bare silica monolith) the formation of CP zones under conditions favouring significant EDL overlap in the intraskeleton mesopores. As illustrated by the series of CLSM images and selected stationary profiles of fluorescent tracer distributions the applied field and mobile phase ionic strengths sensitively influence the intensity of CP in the complete material. While we cannot resolve differences in image contrast for the electroneutral tracer (Figure 3.13a) at any field strength, the image contrast in Figure 3.13b without applied field (left image) originates in the electrostatic Donnan-exclusion of the small co-ionic tracer (Bodipy-disulfonate) from the intraskeleton mesopores. Upon application of an electrical field the equilibrium distribution of this co-ionic tracer in the macropore space is drastically changed (right image in Figure 3.13b and related profile). Electrical-field-induced enriched and depleted CP zones can be readily detected with respect to the situation without applied field. This phenomenon becomes strongly attenuated at increased ionic strength which is shown in Figure 3.13c. Increased ionic strength reduces the EDL interaction within the mesopores and, thus, their charge-selectivity which, in turn, results in less intense CP zones (and induced-charge electroosmosis) at the same field strength as in Figure 3.13b. This finding agrees with EOF behaviour documented in Figures 3.7–3.9 where increasing ionic strength leads to a reduced contribution of nonlinear (CP-based induced-charge) electroosmosis to the overall EOF.

Further, we used charged (co-ionic) fluorescent, polystyrene-based nanoparticles with a nominal diameter of 50 nm that are size-excluded from the mesoporous monolith skeleton. Thus, contrast without electrical field (left image, Figure 3.13d) originates in the circumstance that the tracer only occupies the macropore space. Upon application of an electrical field we observe the development of enriched and depleted CP zones (right image in Figure 3.13d and related profile). They are sharper than for the small co-ionic tracer (right image, Figure 3.13b) because the nanoparticles are completely size-excluded from the mesoporous skeleton, while a nonideal ion-permselectivity allows the small tracer to penetrate the mesopore space. In contrast to size-exclusion of large tracer the electrostatic exclusion of small tracer is not complete. Therefore the right image in Figure 3.13b is more blurred. In addition, the co-ionic nanoparticles are not only electrostatically held (or trapped) in the enriched CP zones, but also due to their electrophoretic motion against cathodic interfaces in the whole material which are impenetrable for large analytes, but permeable for electrolyte. This effect has been revealed

during retention studies in preparative electrochromatography with large proteins [46]. The counterpart of enriched CP zones at cathodic interfaces in the bare silica monolith are depleted CP zones at the anodic interfaces [19]. Molecular diffusion limits coupled mass and charge transport in these boundary layers.
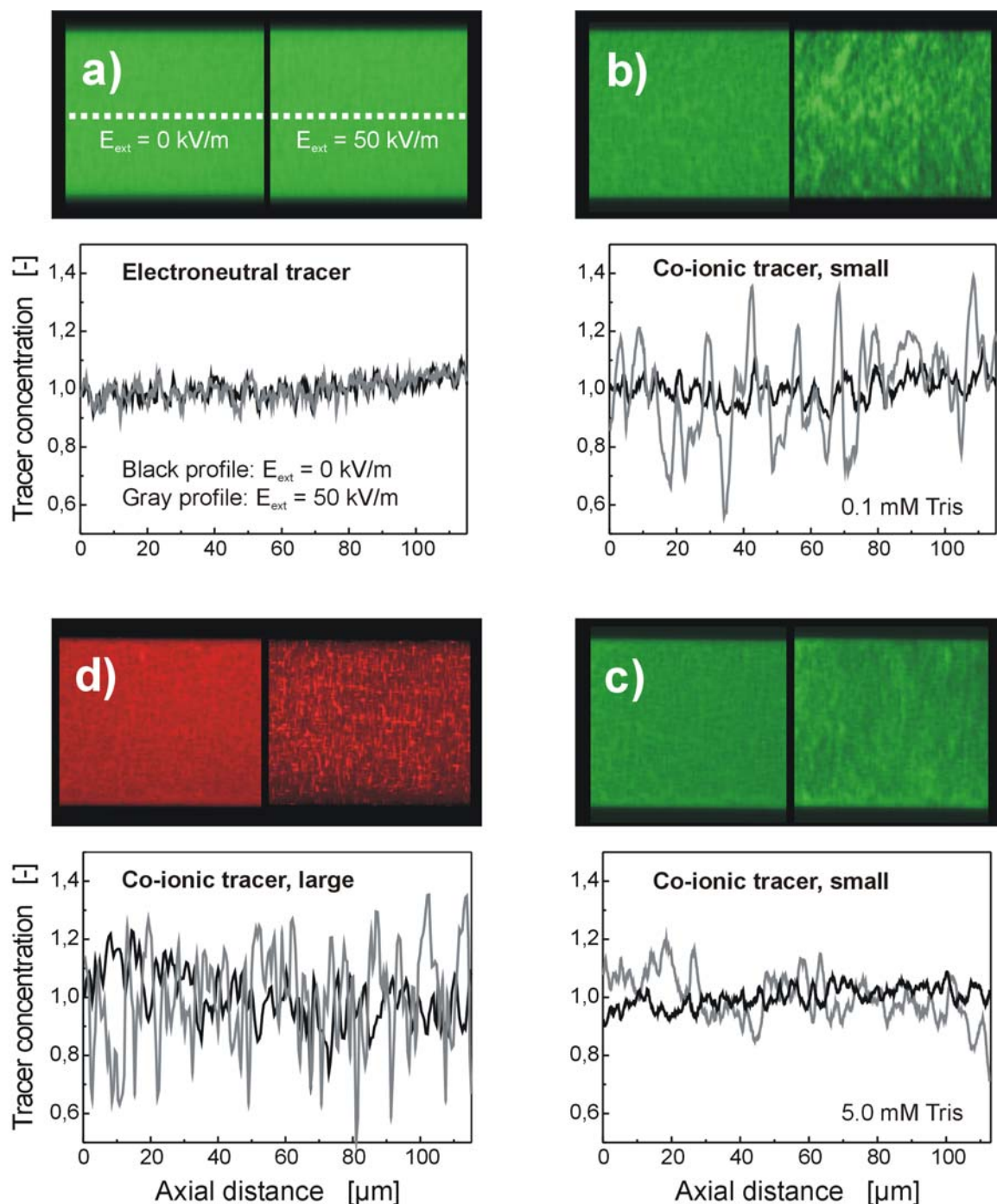

Figure 3.13 Visualisation of CP in a 100 μm i.d. bare silica monolith using quantitative CLSM. Mobile phase: 90:10 DMSO/water (v/v) with different Tris concentrations and 10^{-5} M fluorescent tracer. a) Electroneutral Bodipy and 0.1 mM Tris. b) Bodipy-disulfonate (twice negatively charged, here co-ionic tracer) and 0.1 mM Tris. c) Bodipy-disulfonate and 5 mM Tris. d) Negatively charged nanoparticles, size-excluded from the mesoporous skeleton. Images to the left and the black profiles correspond to stationary distributions without externally applied electrical field, images to the right and the gray profiles correspond to stationary distributions with an applied field strength of 50 kV/m. The profiles were normalized with respect to their mean values. All images were acquired with constant laser and detector settings optimized for each fluorescent tracer.

We next investigated by CLSM random-close sphere packings in view of CP. Figure 3.14 shows images and related centerline profiles of stationary distributions of co-ionic tracer (Bodipy-disulfonate; twice negatively charged) using capillaries packed with small-pore particles (d_{intra} = 19 nm), large-pore particles (d_{intra} = 232 nm), and nonporous particles. In comparison to Figure 3.13, we now changed the
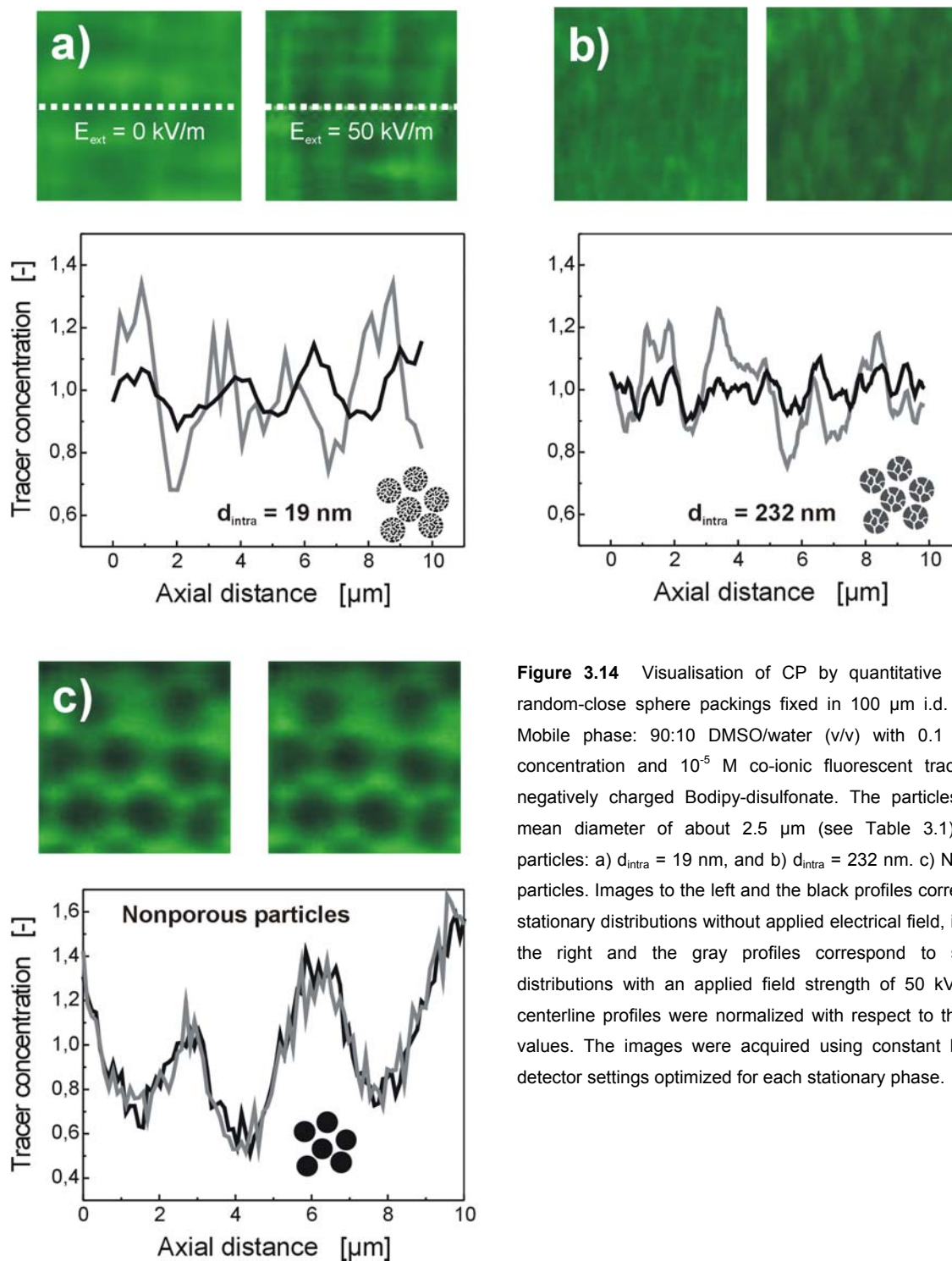

Figure 3.14 Visualisation of CP by quantitative CLSM in random-close sphere packings fixed in 100 µm i.d. columns. Mobile phase: 90:10 DMSO/water (v/v) with 0.1 mM Tris concentration and 10^{-5} M co-ionic fluorescent tracer, twice negatively charged Bodipy-disulfonate. The particles have a mean diameter of about 2.5 µm (see Table 3.1). Porous particles: a) d_{intra} = 19 nm, and b) d_{intra} = 232 nm. c) Nonporous particles. Images to the left and the black profiles correspond to stationary distributions without applied electrical field, images to the right and the gray profiles correspond to stationary distributions with an applied field strength of 50 kV/m. Axial centerline profiles were normalized with respect to their mean values. The images were acquired using constant laser and detector settings optimized for each stationary phase.

intraparticle pore size at constant mobile phase composition in order to modulate r_{intra}/λ_D and, thus, the local intensity of CP. While CP becomes clearly visible for particles with small pores (Figure 3.14a), it is attenuated, but still discernible for large-pore particles (Figure 3.14b), and practically absent in the

fixed bed of nonporous particles (Figure 3.14c). This direct CLSM observation complements nicely our earlier results on the EOF behaviour reported in Figures 3.11 and 3.12. To summarize, an increasing aspect ratio (r_{intra}/λ_D), realized by increased ionic strength (Figure 3.13b and 3.13c) or increased pore size (Figure 3.14a and 3.14b), reduces the charge-selectivity of the intraparticle (or intraskeleton) pore space, the intensity of electrical-field-induced CP, and consequently also the maximum amount of possible induced-charge electroosmosis in the overall EOF dynamics.

To conclude, as revealed by the chromatographic data in Figures 3.7 and 3.11, with an increasing r_{intra}/λ_D the nonlinear EOF dynamics turns smoothly into classical, linear behaviour. This fundamental dependence is corroborated by the CLSM data (Figures 3.13 and 3.14) which illustrate the accompanying (decreasing) local intensity of CP in these monoliths and sphere packings. In addition to a critical ratio r_{intra}/λ_D also the macropore space morphology is important, i.e., how much space do CP zones have to develop (or to breathe freely), how do they interact with each other in complex porous media, and how much induced-charge electroosmosis can still be stimulated based on the result of these interactions? At least, it is obvious that the ideal single-particle picture for which the theory of electroosmosis of the second kind has been developed [28] must be strongly affected in dense multiparticle systems by the influence of approaching neighbours via the local hydrodynamics and interaction of the neighboured or directly adjacent CP zones, especially in view of a spherical symmetry and the particle arrangement in dense systems [19]. However, we still resolve substantial CP in fixed beds of particles with a diameter as small as 2.5 μm representing CEC practice, simply caused by the presence of the charge-selective regions. In this respect, we have already noted that the monoliths show a different morphology. First, due to their continuous skeleton, relatively extended CP zones (less confined than in a bed of discrete particles) penetrate the material like a spider web. Second, compared to the size of charge-selective domains, macropores in a monolith offer larger dimensions than in a random-close packing of
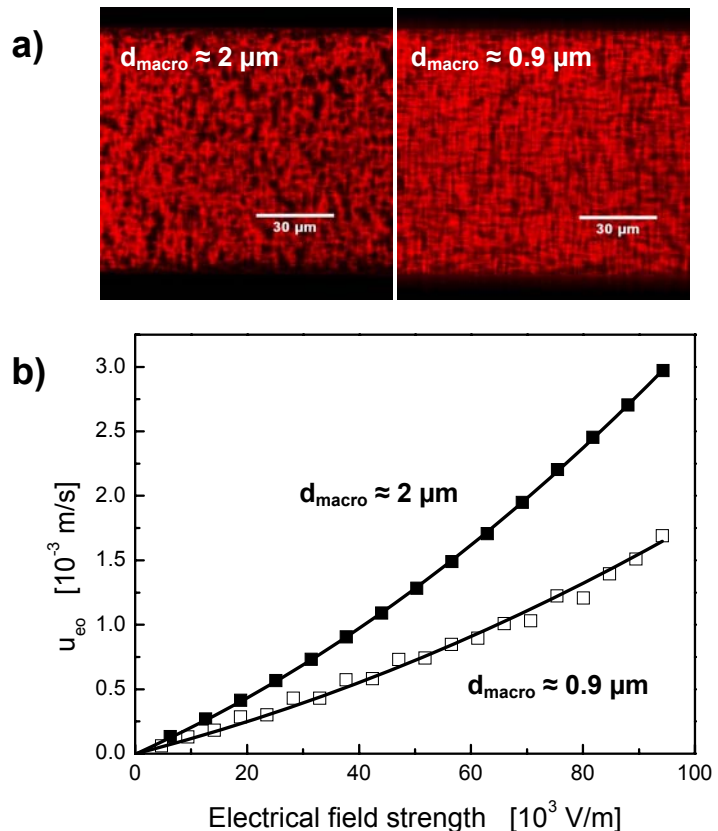
Figure 3.15 Comparison of EOF velocities for C18-silica monoliths having different mean macropore dimensions (d_{macro}), as indicated. a) Visualisation of monolith morphology by quantitative CLSM employing 90:10 DMSO/H_2O (pH ≈ 7) as RI-matching mobile phase and 10^{-5} M positively charged Rhodamine 6G as counter-ionic, fluorescent tracer. No electrical field is applied. Rhodamine 6G strongly adsorbs at the monoliths surfaces and is enriched by the mesoporous skeleton at electrochemical equilibrium. b) EOF velocities obtained with 80:20 acetonitrile/water (v/v) as mobile phase containing 0.1 mM Tris.

porous particles, corresponding to an arrangement in which particles are artificially diluted, i.e., removed from each other by a distance of the order of the particle radius.

However, Figure 3.15 demonstrates that also for monoliths a further reduction of macropore dimensions can result in a significant reduction of the nonlinear, CP-based induced-charge EOF which is caused by a stronger interaction of depleted and enriched CP zones leading to attenuation of CP. In addition, overlap of the primary EDL may become noticeable in the macropore space of the monolith reducing also the amount of classical, linear EOF (Figure 3.15b). Concerning classical EOF a beginning EDL overlap can be counteracted by an increased ionic strength, but concerning nonlinear EOF, this change will reduce charge-selectivity of the mesopore space and, thus, attenuate further the whole CP phenomenon (Figure 3.13). This is a good example for demonstrating the principally different origins of quasi-equilibrium (classical) and induced-charge electroosmosis in a hierarchically structured material and it shows that both phenomena coexist in CEC under common conditions.

3.3.4   Theoretical background

In order to analyze most critical coupled mass and charge transport phenomena relevant to an understanding of CP-based induced-charge electroosmosis in CEC we consider a locally flat interface between a bulk, macroporous compartment and an ion-permselective region (with a negative internal and external surface charge density) to represent local interfaces in monoliths with bimodal pore size distributions and fixed beds of permeable particles (Figures 2.1, 2.2 and 2.4). Next, we have to analyze the governing transport phenomena and limitations arising to the left and right of the charge-selective interface as we increase the applied field strength (cf. Figures 3.7–3.11).

Flux density of a positively charged counter-ion in the charge-selective domain (J_{intra}^+) consists of diffusive flux (J_{diff}^+), electrical transference (J_{el}^+), and convective transfer (J_{con}^+) by EOF associated with the primary, i.e., quasi-equilibrium EDL at the internal surface [8]

$$
\begin{aligned}
J_{intra}^+ &= J_{diff}^+ + J_{el}^+ + J_{con}^+ \\
&= -D_{intra}^+ \left(\nabla c_{intra}^+ + z^+ c_{intra}^+ \frac{F}{RT} \nabla \phi \right) + c_{intra}^+ \mathbf{u}_{eo,intra} \, , \\
&= -D_{intra}^+ \nabla c_{intra}^+ + c_{intra}^+ (\mathbf{u}_{ep,intra}^+ + \mathbf{u}_{eo,intra})
\end{aligned}
\tag{3.2}
$$

where D_{intra}^+ is the intraskeleton (or intraparticle) effective diffusion coefficient of a counter-ion, e.g., the protonated Tris molecule in the context of the present work, c_{intra}^+ is the intraskeleton (or intraparticle) concentration, and ϕ denotes the local electrical potential. Most important to our analysis, this equation illustrates a strong dependence on the applied field strength of the molar flux density of a counter-ionic species in the charge-selective domain via the electrophoretic and EOF velocities ($\mathbf{u}_{ep,intra}^+$ and $\mathbf{u}_{eo,intra}$) which, in addition, are co-directional for counter-ionic species [8, 21].

In the macroporous compartment where counter-ions enter the charge-selective domain from the bulk solution (in the direction of the applied field) the electrolyte concentration decreases. Co-ions migrate in the opposite direction, away from the interface, and because this local withdrawal cannot be compensated by supply from the intraskeleton or intraparticle pore space (which excludes co-ions) the co-ion concentration decreases. Therefore, the unique interplay of charge-selectivity, electromigration, convection, and diffusion results in the formation of a CDL. To guarantee local electroneutrality in this depleted CP zone the counter-ion concentration decreases accordingly. As the field strength is further increased the molar flux density of the counter-ion through this boundary layer (J_{CDL}^+) for an ideal, ion-permselective interface approaches an upper limiting regime with

$$
J_{CDL,max}^+ = -D_{inter}^+ \frac{c_{inter}^+}{\delta_{CDL}} \, ,
\tag{3.3}
$$

where D_{inter}^+ and c_{inter}^+ denote the molecular diffusivity and concentration of the counter-ion in the bulk interskeleton (or interparticle) liquid, and δ_{CDL} is the thickness of the diffusion boundary layer.

While the exact dependencies of J_{intra}^+ and $J_{CDL,max}^+$ (to the right and left of the charge-selective interface) on local hydrodynamics and electrokinetics are not relevant in the present context, it is most important to anticipate on the basis of eqs. 3.2 and 3.3 a different dependence of both contributions on the applied field strength. $J_{CDL,max}^+$ depends weaker on the field strength by the thickness of the CDL being an inverse function of velocity [21, 28]. Thus, as the field strength is increased in CEC we approach a critical value ($\nabla\phi_{crit}$) at which these contributions become equal. Through the eyes of a counter-ionic species it is expressed as

$$J_{intra}^+ = -D_{intra}^+ \nabla c_{intra}^+ + c_{intra}^+ (u_{ep,intra}^+ + u_{eo,intra}^+) = -D_{inter}^+ \frac{c_{inter}^+}{\delta_{CDL}} = J_{CDL,max}^+ . \tag{3.4}$$

Caused by the significant charge-selectivity we have $u_{eo,intra}^+ \ll u_{ep,intra}^+$ and if we further neglect the diffusive contribution in J_{intra}^+ which is small relative to strong electrical transference (J_{el}^+) we arrive at

$$z^+ c_{intra}^+ D_{intra}^+ \frac{F}{RT} \nabla\phi_{crit} = D_{inter}^+ \frac{c_{inter}^+}{\delta_{CDL}} , \tag{3.5}$$

which, upon rearrangement, results in a simple expression illustrating qualitatively relevant parameters that influence the value of the critical field strength

$$\frac{1}{\delta_{CDL}} \frac{D_{inter}^+}{D_{intra}^+} \frac{c_{inter}^+}{c_{intra}^+} = \frac{z^+ F}{RT} \nabla\phi_{crit} . \tag{3.6}$$

The first factor in eq. 3.6 ($1/\delta_{CDL}$) is a complex function of velocity or, more precisely, of the local distribution of velocities caused by the complex morphology of the porous medium. In sphere packings it is influenced by particle size and shape, their distribution functions, and packing density. In general, with higher velocities δ_{CDL} is becoming smaller in average and the critical field strength is expected to increase. However, the thickness of the hydrodynamic boundary layer varies significantly in complex porous media like sphere packings with cusp regions between particles or in monoliths. In this respect, it should be recognized that the pore-level profile of EOF in fixed beds of spherical particles, even in the thin-EDL-limit, is not uniform and also shows a strong correlation with porosity fluctuations caused by varying packing densities (Figures 1.1 and 1.3a) [47]. The second factor in eq. 3.6 ($D_{inter}^+ / D_{intra}^+$) represents changes in effective diffusion behaviour of the counter-ionic species in the charge-selective domain with respect to the bulk solution. This includes the tortuosity factor which lumps together geometrical and topological aspects as well as adsorption to the oppositely charged surface. As, due

to these parameters, D_{intra}^{+} is reduced below D_{inter}^{+} the critical field strength shows a corresponding increase. Finally, the last factor in eq. 3.6 ($c_{inter}^{+}/c_{intra}^{+}$) accounts for the counter-ion selectivity within the charge-selective domain. The higher the charge-selectivity the smaller $c_{inter}^{+}/c_{intra}^{+}$ and the critical field strength. We have already shown that the charge-selectivity depends on surface electrical potential and EDL overlap represented by the aspect ratio r_{intra}/λ_D (cf. Figures 3.7-3.12). If there is more than one counter-ionic species present in the system (which we assumed here for simplicity) relative contributions in competitive charge transport are governed by charge numbers, diffusion coefficients, and concentrations as reflected in the transport numbers [48, 49].

To conclude from this qualitative analysis using eq. 3.6, there exist different routes for tuning CP in a hierarchically structured material, which address externally controllable variables like the electrical field strength, electroosmotic and hydraulic flow rates, mobile phase ionic strength and pH, as well as material characteristics like particle or skeleton size, macro- and mesopore porosities, mean pore size, pore interconnectivity, and surface charge. The relevance of the critical field strength for CEC is that it separates the classical (near-equilibrium) and induced-charge (nonequilibrium) regimes of CP. At field strengths above the critical one the discrimination of the charge transport in the CDL with respect to the charge-selective domain becomes climactic meaning that electrokinetic flux of counter-ions in the latter begins to exceed the supply of counter-ions through the CDL. This transition to a nonequilibrium CP is accompanied by an induction of regions in both compartments which carry nonequilibrium space charge of opposite sign, i.e., a counter-ionic (mobile) SCR in the macroporous compartment and a co-ionic (immobile) SCR of unscreened, fixed surface charge in the mesoporous domain [19]. The mobile SCR (Figure 2.4) induced by the normal field component can be regarded as the fluid-side part of this secondary, nonequilibrium EDL interacting locally with the tangential component of the applied field to generate nonequilibrium electroosmotic slip along curved interfaces in particulate and monolithic beds employed in CEC. It leads to a strong enhancement of the lateral velocity components which, in turn, influences hydrodynamic dispersion. In this context, a convectively accelerated lateral equilibration of analyte molecules is expected to reduce the axial zone spreading because, under typical conditions in (electro)chromatography, radial dispersion remains diffusion-limited [47, 50]. Thus, as a next step we analyze separation efficiencies depending on the intensity of nonequilibrium CP, complementary to the already documented EOF dynamics in particulate and monolithic fixed beds (Figures 3.7–3.12).

3.3.5   Separation efficiencies for electroneutral analytes

Particulate fixed beds in CEC. As alternative to an adjustment of mean pore size the mobile phase ionic strength (at constant pore size) can be varied to systematically tune intraparticle EDL overlap represented by r_{intra}/λ_D. Due to dominating suppression of intraparticle EDL overlap at increasing Tris concentration the intraparticle EOF is increased (Figure 3.11a). Concomitantly, in the interparticle pore space classical EDL behaviour dominates, i.e., the increasing ionic strength compresses the EDL resulting in a reduced shear plane potential [51]. As a consequence, the intraparticle-to-interparticle flow ratio increases which improves flow homogeneity over the column cross-section and decreases mass transfer resistance in the mobile phase enabling higher flow velocities and separation efficiencies [2, 31-38]. This electroosmotic perfusion effect dominates the trend in separation efficiencies at increasing ionic strength, even with small porous particles ($d_p \approx 2.5$ μm) as shown in Figure 3.16. As expected, the improvement in separation efficiencies becomes most relevant for the small-pore material (d_{intra} = 19 nm; Figure 3.16a), while for the large-pore material the increase in r_{intra}/λ_D (due to the increase in Tris concentration from 0.1 to 5 mM) results in a smaller improvement (d_{intra} = 232 nm; Figure 3.16b).
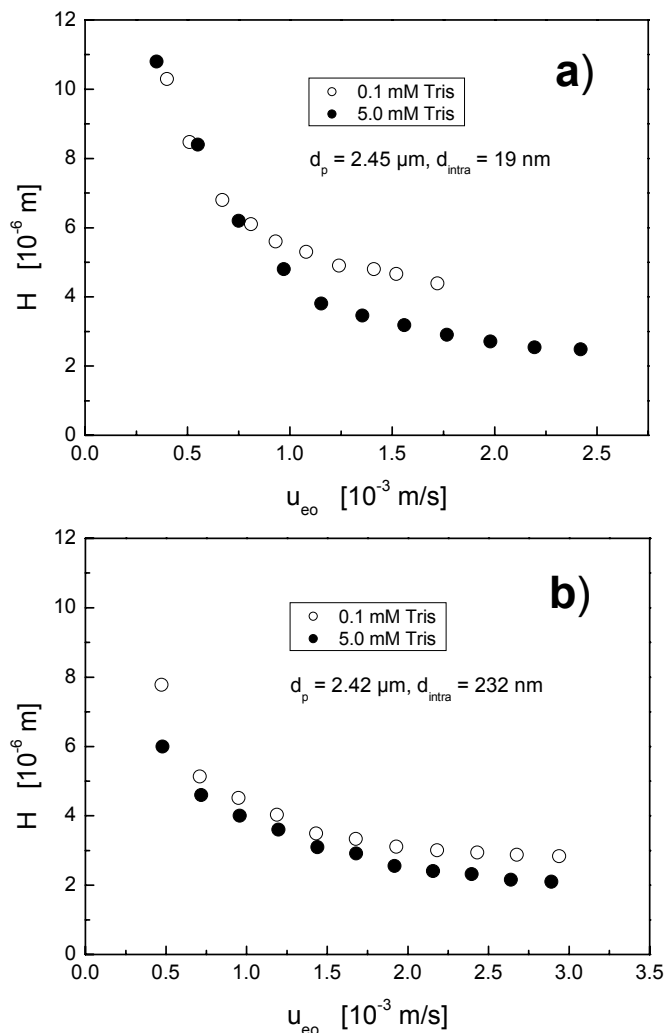
Figure 3.16   Plate height curves for ethylbenzoate obtained with particulate beds fixed in 100 μm i.d. capillaries. Mobile phase: 80:20 acetonitrile/water (v/v) with different Tris concentrations. a) Small-pore particles (d_{intra} = 19 nm), and b) large-pore particles (d_{intra} = 232 nm). Data were acquired on the HP^{3D}CE instrument.

Monolithic fixed beds. While the electroosmotic perfusion mechanism and documented behaviour with the particulate beds are quite familiar [2, 31-38], the dependence of separation efficiency on mobile phase ionic strength in CEC is different for the monoliths. In the silica-based monoliths we encounter a thin porous skeleton of about 1 μm thickness (providing the high surface-to-volume ratio) and relatively large macropores of the order of 2 μm [52]. These sizes can be adjusted independently from each other [52]. With such a thin mesoporous skeleton the electroosmotic perfusion has only limited relevance and mass transfer resistance in the mobile phase is more pronounced in view of the

interskeleton macropore-level Taylor dispersion [47]. Then, increasing mesopore-level EOF hardly compensates for velocity extremes in the macropore space and higher ionic strengths promote thermal effects rather than noticeably improving separation efficiency which is consistent with our experimental results.

In the monolithic structures the CP-based induced-charge electroosmosis not only significantly influences the overall EOF dynamics in dependence of ionic strength, but also separation efficiencies.

An advantage of the monolith morphology in this respect is that by means of its thin, axially extending skeleton it provides charge-selectivity and CP without creating a large region of (at low ionic strength) quasi-stagnant fluid. This is more unfavourable for a bed of porous particles with the spheres inherent surface-to-volume ratio. As a consequence, the perfusion mechanism is more important for particulate beds. For monoliths, by contrast, we witness a significant decrease in the plateau plate heights (Figure 3.17) as ionic strength is decreased. This improvement parallels the increasing contribution of nonlinear electroosmosis in the EOF dynamics (Figure 3.7). Now, both phenomena, the nonlinear EOF dynamics and increasing separation efficiency at decreasing ionic strength (between 10 and 0.1 mM Tris) can be consistently explained by intensified operation of the (CP-based) induced-charge electroosmosis. This nonlinear EOF

Figure 3.17 Plate height data in CEC obtained with a 316 mm (233 mm effective) × 100 µm i.d. C18-silica monolith in the HP^{3D}CE. Mobile phase: 80:20 acetonitrile/water (v/v) with different Tris concentrations. a) Plate height curves for ethylbenzoate. b) Extracted plateau plate heights over the whole Tris concentration range.

depends on both the normal and tangential components of the applied field via creation of a space charge (induction step) and volume force exerted on the mobile part of this secondary EDL (interaction step), respectively. The improvement in separation efficiency can be connected directly to induced-charge electroosmosis because the enhanced nonlinear EOF (which can be tuned via r_{intra}/λ_D) translates to higher local lateral velocities in the whole monolith. These components increase a lateral pore-scale dispersion which, in turn, reduces axial dispersion. In particular, we find an improvement in plateau plate heights by a factor of two while moving from 5 mM to 0.1 mM Tris (Figure 3.17), which is
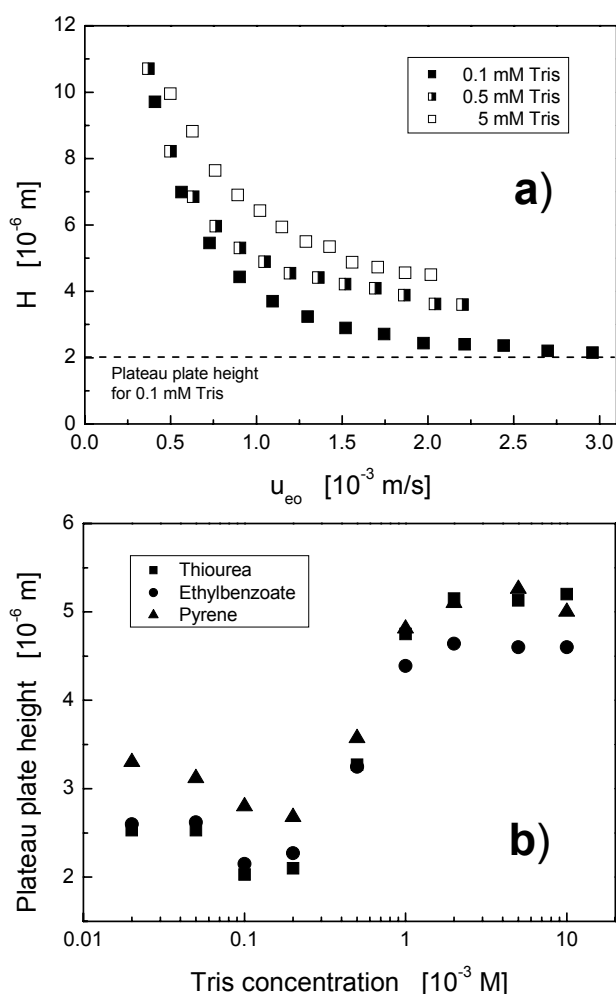
in good agreement with our earlier experimental results [1].

We finally compared the remarkable separation efficiencies obtained with the monolith in CEC ($H \approx 2$ μm for 0.1 mM Tris, see Figure 3.17) to those in capillary LC. We used the short-end injection technique in the HP[3D]CE instrument to remove the bias usually introduced in such a comparison due to different injection histories. As demonstrated in Figure 3.18 minimum plate heights of about 6 μm are reached, comparable to the performance in CEC with 5 mM Tris ($H \approx 4.5$ μm). Thus, full performance advantage of CEC over capillary LC is reached only with ionic strengths stimulating strong CP and induced-charge electroosmosis (Figures 3.17 and 3.18). By contrast, the minimum plate heights in capillary LC remain independent of the ionic strength (Figure 3.18). This confirms that the dependence on Tris concentration of the plateau plate heights in CEC for the silica-based monoliths is caused by a unique combination of nonlinear electrokinetics and electrohydrodynamics, as explained, and not by an effect specific for the Tris system used in this work, e.g., due to a concentration-dependent adsorption of Tris on the silica-based surface and related consequences [53]. This is in agreement with our earlier work demonstrating a general dependence of nonlinear electroosmosis in monoliths on mobile phase ionic strength employing different buffer and electrolyte systems [19].
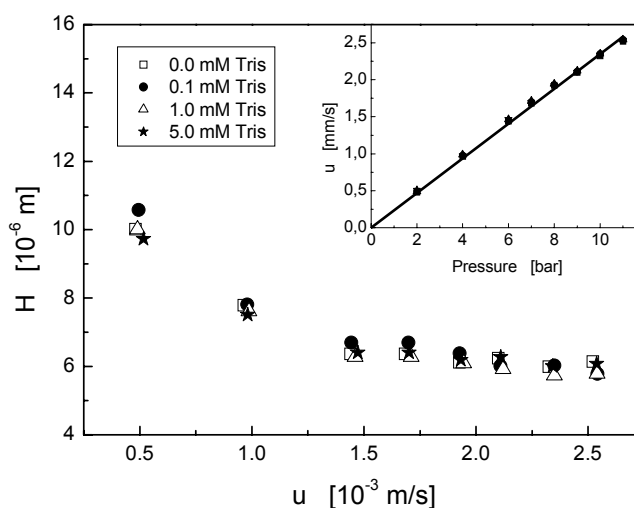

Figure 3.18 Plate height curves for ethylbenzoate in capillary HPLC employing short-end injection in the HP[3D]CE using a 110 mm (84 mm effective) × 100 μm i.d. C18-silica monolith. Mobile phase: 80:20 acetonitrile/water (v/v) with different Tris concentrations.

3.4   Conclusions and perspectives

Investigations on coupled mass and charge transport (background electrolyte) in hierarchically structured porous materials employed in CEC (beds of permeable, conducting particles and monoliths) have revealed that CP and (CP-based) induced-charge electroosmosis (Figure 2.4) are phenomena with a general rather than special significance under very common experimental conditions. These unique electrokinetic phenomena as well as the hydrodynamic consequences sensitively depend on material characteristics (pore space morphology in general, including the realization of hierarchical design and interconnectivity between different sets of pores; surface charge density), fluid phase properties (ionic strength as most important property influencing local charge selectivity), and the applied field strength. Systematically acquired data have revealed the influence of these parameters, thereby addressing the relevance of internal electrical potential gradients and a dependence on local EDL interaction (Figures 3.5 and 3.6), the differences in morphology of silica-based capillary monoliths and random-close packings of porous particles, as well as chemical surface modification, in view of the actual intensity of nonlinear (induced-charge) electroosmosis (Figures 3.7–3.12), and consequences of increased lateral velocities due to the nonlinear slip for reducing axial hydrodynamic dispersion, again pointing towards the differences in pore space morphology of monoliths and sphere packings (Figures 3.16 and 3.17).

All these data suggest that the existence of CP and the relative intensity of CP (and CP-based phenomena) with respect to perfusive flow are the key to understanding salient features in CEC which includes the electrohydrodynamics, associated hydrodynamic dispersion, as well as the migration and retention of charged analytes. Our data demonstrate that CP is practically always present unless ionic strengths of about 100 mM are employed for removing the charge-selectivity of the mesopore space or, in other words, to make the mesopore space charge-nonselective like the macropore space. Our data further demonstrate that extremely high nonlinear EOF velocities (with one to two orders of magnitude above the classical, linear velocities) observed for single, large particles (d_p > 100 μm) are not realized in dense systems of small particles, even for high field strengths (E_{ext} > 100 kV/m), due to the adverse effects caused by a small particle diameter, the local hydrodynamics, and interaction of CP zones from neighboured particles. These aspects are investigated in the next chapter in comparison to the single (undisturbed) particle dynamics (Figures 2.3 and 2.4). The realization of nonlinear electroosmosis in view of high-speed separations is still more favourable for tailored monolithic structures compared to the relative unflexibility of adjusting pore dimensions in random-close sphere packings. Thus, the monoliths are promising for chip devices where higher field strengths than typical in CEC can be easily realized, thereby increasing the intensity of induced-charge electroosmosis (cf. Figure 3.8).

Complementary to the macroscopic data (Figures 3.7-3.12) our quantitative CLSM measurements (Figures 3.13 and 3.14) reveal directly the CP phenomenon in the sphere packings and monoliths, as well as its sensitive dependence on the local charge-selectivity (Figure 3.6), including surface charge density and pore-scale EDL overlap expressed by r_{pore}/λ_D. Thus, CEC presents a good example illustrating the importance of both classical (linear) and induced-charge (nonlinear) electroosmosis in

the overall EOF dynamics. Then, adequate theory of EOF in CEC must include linear behaviour in quasi-electroneutral macropore space (Helmholtz-Smoluchowski model; thin quasi-equilibrium EDL), as well as a nonlinear framework by nonequilibrium electroosmosis (Mishchuk-Dukhin model; extended nonequilibrium EDL) which originates in the charge-selectivity of meso- and/or microporous domains in hierarchically structured materials employed in CEC and was discussed in Chapter 2 (Figure 2.4). The reported behaviour covers all kinds of monoliths and packed particulate beds (except those obtained with nonporous particles, Figure 3.12). Limiting linear behaviour will be observed as the thickness of the primary EDL becomes much smaller than any pore dimensions (thin-EDL-limit) and, on the other hand, as the potential drop in the electrical field-induced mobile SCR becomes much larger than the classical ζ-potential (nonlinear behaviour). However, neither case is realized in current CEC practice which operates in an intermediate, slightly nonlinear regime.

Thus, typical velocities in current CEC display an only moderately, nevertheless systematically nonlinear dynamics in dependence of the applied field and mobile phase ionic strengths. However, the increased slip velocities tangential to the curved interfaces provide a unique mechanism by which the pore-scale lateral, traditionally diffusion-limited equilibration of analytes is enhanced convectively. This can reduce axial zone spreading for both electroneutral and charged analytes in materials promoting a significant development of the induced-charge electroosmosis, as demonstrated for the monoliths (see Figures 3.12 and 3.17). In addition, for charged analytes an important consequence of CP is related to the effective migration and retention behaviour because the local intensity of CP, thus, also residence time of charged with respect to electroneutral analytes in the CP zones, sensitively depends on applied field and mobile phase ionic strengths, which is analyzed in more detail in the next chapter by using quantitative CLSM and packed beds of strong cation-exchange-particles. In turn, the retention factor of charged analytes in CEC becomes a complicated function of the parameters that determine the local intensity of CP which is shown in Chapter 5. Further CP-related studies are shown to resolve basic issues of the retention dynamics of charged analytes in CEC which are still puzzling chromatographers.

References

[1]   Nischang, I., Tallarek, U., *Electrophoresis* 2004, *25*, 2935-2945.

[2]   Chen, G., Paces, M., Marek, M., Zhang, Y. K., Seidel-Morgenstern, A., Tallarek, U., *Chem. Eng. Technol.* 2004, *27*, 417-428.

[3]   Choudhary, G., Horváth, Cs., *J. Chromatogr. A* 1997, *781*, 161-183.

[4]   Rathore, A. S., Horvath, C., *Anal. Chem.* 1998, *70*, 3069-3077.

[5]   Kelly, M. A., Altria, K. D., Clark, B. J., *J. Chromatogr. A* 1997, *768*, 73-80.

[6]   Leinweber, F. C., Tallarek, U., *J. Chromatogr. A* 2003, *1006*, 207-228.

[7]   Tallarek, U., Rapp, E., Sann, H., Reichl, U., Seidel-Morgenstern, A., *Langmuir* 2003, *19*, 4527-4531.

[8]   Helfferich, F., *Ion Exchange*, Dover, New York, 1995.

[9]   Probstein, R. F., *Physicochemical Hydrodynamics*, John Wiley and Sons, New York, 1994.

[10]   Kemery, P. J., Steehler, J. K., Bohn, P. W., *Langmuir* 1998, *14*, 2884-2889.

[11]   Kuo, T. C., Sloan, L. A., Sveedler, J. V., Bohn, P. W., *Langmuir* 2001, *17*, 6298-6303.

[12]   Ku, J. R., Stroeve, P., *Langmuir* 2004, *20*, 2030-2032.

[13]   D. Stein, M. Kruithof, C. Dekker, Phys. Rev. Lett. 93 (2004) 035901.

[14]   Schmuhl, R., Keizer, K., van den Berg, A., ten Elshof, J. E., Blank, D. H. A., *J. Colloid Interface Sci.* 2004, *273*, 331-338.

[15]   Plecis, A., Schoch, R. B., Renaud, P., *Nano Letters* 2005, *5*, 1147-1155.

[16]   Guiochon, G., Golshan-Shirazi, S., Katti, A.M. *Fundamentals of preparative and nonlinear chromatography.* Academic Press, Boston, 1994.

[17]   Pujar, N. S., Zydney, A. L., *J. Chromatogr. A, 796*, 229-238.

[18]   Burns, D. B., Zydney, A. L., *Aiche Journal* 2001, *47*, 1101-1114.

[19]   Tallarek, U., Leinweber, F. C., Nischang, I., *Electrophoresis* 2005, *26*, 391-404.

[20]   Manzanares, J. A., Murphy, W. D., Mafé, S., Reiss, H., *J. Phys. Chem.* 1993, *97*, 8524-8530.

[21]   Leinweber, F. C., Tallarek, U., *Langmuir* 2004, *20*, 11637-11648.

[22]   Nikonenko, V. V., Zabolotskii, V. I., Gnusin, N. P., *Sov. Electrochem.* 1989, *25*, 262-266.

[23]   Dukhin, S. S., Mishchuk, N. A., *Colloid J. USSR* 1990, *52*, 390-393.

[24]   Mishchuk, N. A., Dukhin, S. S., *Colloid J. USSR* 1990, *52*, 427-431.

[25]   Rubinstein, I., *Electro-Diffusion of Ions*, SIAM Studies in Applied Mathematics, Philadelphia 1990.

[26]   Rubinstein, I., Zaltzmann, B., *Math. Models Methods Appl. Sci.* 2001, *11*, 263-300.

[27]   Mishchuk, N. A., Takhistov, P. V., *Colloids Surf. A* 1995, *95*, 119-131.

[28]   Mishchuk, N. A., Dukhin, S. S., in: *Interfacial Electrokinetics and Electrophoresis.* Delgado, A. V. (Ed.), Marcel Dekker, New York, 2002, Chapter 10.

[29]   Wan, Q.-H., *J. Chromatogr. A* 1997, *782*, 181-189.

[30]   Minakuchi, H., Nakanishi, K., Soga, N., Tanaka, N., *Anal. Chem.* 1996, *68*, 3498-3501.

[31]   Li, D., Remcho, V. T., *J. Microcolumn Sep.* 1997, *9*, 389-397.

[32]   Venema, E., Kraak, J. C., Poppe, H., Tijssen, R., *J. Chromatogr. A* 1999, *837*, 3-15.

[33]   Wen, E., Asiaie, R., Horváth, Cs., *J. Chromatogr. A* 1999, *855*, 349-366.

[34]   Vallano, P. T., Remcho, V. T., *Anal. Chem.* 2000, *72*, 4255-4265.

[35]   Stol, R., Poppe, H., Kok, W. T., *Anal. Chem.* 2001, *73*, 3332-3339.

[36]   Vallano, P. T., Remcho, V. T., *J. Phys. Chem. B* 2001, *105*, 3223-3228.

[37]   Tallarek, U., Rapp, E., Seidel-Morgenstern, A., Van As, H., *J. Phys. Chem. B* 2002, *106*, 12709-12721.

[38]   Tallarek, U., Pačes, M., Rapp, E., *Electrophoresis* 2003, *24*, 4241-4253.

[39]   van den Bosch, S. E., Heemstra, S., Kraak, J. C., Poppe, H., *J. Chromatogr. A* 1996, *755*, 165-177.

[40]   Choudhary, G., Horváth, Cs., *J. Chromatogr. A* 1997, *781*, 161-183.

[41]   Wan, Q.-H., *J. Chromatogr. A* 1997, *782*, 181-189.

[42]   Cikalo, M. G., Bartle, K. D., Myers, P., *J. Chromatogr. A* 1999, *836*, 35-51.

[43]   Stol, R., Kok, W. Th., Poppe, H., *J. Chromatogr. A* 2001, *914*, 201-209.

[44]   Nischang, I., Reichl, U., Seidel-Morgenstern, A., Tallarek, U., *Langmuir,* submitted*.*

[45]   Geiser, L., Mirgaldi, M., Veuthey, J.-L., *J. Chromatogr. A* 2005, *1068*, 75-81.

[46]   Rudge, S. R.; Basak, S. K.; Ladisch, M. R., *AIChE J.* 1993, *39,* 797-808.

[47]   Hlushkou, D., Seidel-Morgenstern, A., Tallarek, U., *Langmuir* 2005, *21*, 6097-6112.

[48]   Zabolotsky, V. I., Manzanares, J. A., Nikonenko, V. V., Lebedev, K. A., Lovtsov, E. G., *Desalination* 2002, *147*, 387-392.

[49]   Nikonenko, V., Lebedev, K., Manzanares, J. A., Pourcelly, G., *Electrochim. Acta* 2003, *48*, 3639-3650.

[50]   Tallarek, U., Albert, K., Bayer, E., Guiochon, G., *AIChE J.* 1996, *42*, 3041-3054.

[51]   Chen, G., Tallarek, U., *Langmuir* 2003, *19*, 10901-10908.

[52]   Ishizuka, N., Minakuchi, H., Nakanishi, K., Soga, N., Nagayama, H., Hosoya, K., Tanaka, N., *Anal. Chem.* 2000, *72*, 1275-1280.

[53]   Rapuano, R., CarmonaRibeiro, A. M., *J. Colloid Interface Sci.* 1997, *193*, 104-111.

4 Confocal laser scanning microscopy study of the electrical field induced concentration polarization at curved ion-permselective interfaces

4.1 Introduction

Related to the previous chapter (with a focus on separation science), this work is motivated by correlating more quantitatively the locally observed CP dynamics with the macroscopically resulting (net) EOF in fixed beds of strong cation-exchange (SCX) particles. The microscopic analysis of CP is realized using CLSM employing refractive index matching of the liquid electrolyte with respect to the mesoporous SCX silica-based particles. For this quantitative investigation particulate beds of 10 μm and 5 μm diameter particles, yet typical for chromatographic applications, have been employed. With respect to this particle diameter and the spatial resolution capability of CLSM this approach facilitates a microscale flow diagnostics in optically opaque media, as has been shown in Chapter 3. It provides access over well defined temporal and spatial domains to transient and stationary distributions of a variety of fluorescent tracers used as indicator for CP under a given set of conditions, being defined by the material characteristics (e.g., packing density, bead shape and diameter, intraparticle pore size and porosity, surface charge density), mobile phase composition (ionic strength, pH, type of electrolyte or buffer), and the applied field strength. Results obtained with the dense multiparticle systems (fixed beds of cation-selective particles) are compared with the CP-based nonlinear electrokinetics reported earlier in the literature within the single-free particle picture and are set in context with the results obtained in Chapter 3. After getting profound fundamental insight into the dynamics of packed beds, electrical-field-induced CP in hierarchically structured silica-based monoliths, again with a close interrelation to the evolving electrohydrodynamics, is investigated. Here specifically the influence of mobile phase properties are addressed, especially also in view of modulating surface electrical potential due to buffer pH effects. Therefore, related CP phenomena are studied with different mobile phases and an influence on the macroscopic electrohydrodynamics is investigated.

4.2   Experimental

Reagents and materials. Sodium acetate trihydrate (p.a., ≥ 99.5%), acetic acid (≥ 99.5%), and DMSO (spectrophotometric grade) were purchased from Sigma-Aldrich Chemie GmbH (Taufkirchen, Germany). Fluorescent tracer molecules were the same as in Chapter 3, besides Rhodamine 6G (Fluka BioChemika) as counter-ionic tracer, which was purchased from Sigma-Aldrich Chemie GmbH (Taufkirchen, Germany). The spherical propylsulphonic acid-modified silica particles (Spherisorb SCX) with a mean diameter (d_p) of 5 or 10 μm, an intraparticle mean mesopore size (d_{intra}) of 10 nm, and a surface area of about 220 m^2/g were a gift from Waters Co. (Milford, MA, USA). Bare silica monoliths in 100 μm i.d. and typically 50 cm long cylindrical fused-silica capillaries were received as research samples from Merck (Darmstadt, Germany). They are characterized by macropores with a mean diameter of about 2 μm and 13 nm mesopores (Figure 3.1). A fluid phase consisting of a 90:10 (v/v) mixture of DMSO and aqueous sodium acetate buffer (pH 5.0) was used in all experiments for refractive index matching to the silica-based materials (porous particles and capillary column). An aqueous stock solution of 0.5 M sodium acetate was prepared using doubly-distilled water from a Milli-Q-Gradient water purification system (Millipore GmbH, Eschborn, Germany). The pH was adjusted to pH 5.0 by titration with concentrated acetic acid. Appropriate volumes of this stock solution, MilliQ water, and DMSO were then mixed to yield acetate buffer solutions of the desired ionic strengths in 90:10 DMSO/water (v/v). The fluid phase contained 10 μM of either of the aforementioned fluorescent tracer molecules. Further studies, using a mobile phase of 80:20 AcN/H$_2$O and aqueous buffer, were prepared as described in Chapter 3.2.

Microfluidic device and sphere packing. Fused-silica capillaries (75 μm i.d. × 360 μm o.d., Polymicro Technologies, Phoenix, AZ, USA) were packed by a modified slurry technique using a WellChrom pneumatic pump K-1900 (Wissenschaftliche Gerätebau KNAUER GmbH, Berlin, Germany) as described earlier (Chapter 3.2). This time the slurry was prepared in 1 M sodium acetate, which also has been subsequently used as a pushing solvent for column packing to bring the strong SCX-particles in its sodium form and avoid electrostatic repulsion between the particles of same charge. Before permanent inlet and outlet frits of a bed were made by sintering the silica particles the columns were conditioned by flushing them with 10 mM NaCl for at least one hour. Column conditioning for the CLSM studies was realized over night with the respective fluid phase (containing the fluorescent tracer) at a flow rate of ca. 100 nL/min using a syringe pump (Harvard Apparatus, Holliston, MA, USA). The principal experimental setup is illustrated in Figure 3.4. If not stated otherwise, images were acquired as xy-sections of 28.79 μm × 28.79 μm with a resolution of 256 × 256 data points in a slice of thickness 1 μm. Generally, two consecutive scans were averaged for a better signal-to-noise ratio.

4.3.   Results and discussion

4.3.1   Dense particulate systems

Dynamics on the single-particle scale. Figures 4.1 and 4.2 show CLSM images of a segment of a fused-silica capillary packed with the spherical SCX particles (d_p = 10 μm, d_{intra} = 10 nm) acquired using co-ionic tracer (BODIPY^{TM} 492/515 disulfonate, Figure 4.1) or the counter-ionic tracer (Rhodamine 6G, Figure 4.2). Under fluid phase conditions favouring a significant EDL overlap inside these mesoporous particles, i.e., when the EDL thickness is comparable with d_{intra} (Figure 2.5) [1], the formation around a particle of anodic depleted and cathodic enriched CP zones in the presence of an applied electrical field (E_{ext}) is readily anticipated. Image contrast without field (E_{ext} = 0 kV/m) observed for the co-ionic tracer (Figure 4.1) results from its electrostatic exclusion from the intraparticle pore space and is a well known phenomenon [2]. The application of an electrical field influences the co-ion concentration systematically throughout the whole fixed bed; it displays peculiar features of increase and depletion around the strongly cation-selective particles. From a macroscopic point of view it leads to the induction of "mountains" and "valleys" in electrolyte concentration, reflecting alternating CP zones with increased and reduced ionic strength around the discrete particles in the fixed bed. The axial and lateral profiles (axial profiles are coaxial, lateral profiles are perpendicular to the direction of the applied field and EOF) extracted from the CLSM images in Figure 4.1 reveal that, while a single particle ideally has rotational symmetry with respect to E_{ext}, the CP zones of the selected particle become significantly distorted by the proximity

Figure 4.1 Local CP dynamics in and around a single particle in a fixed bed of the strongly cation-selective particles (d_p = 10 μm, d_{intra} = 10 nm) in dependence of the applied electrical field strength (E_{ext} as indicated), as seen by the co-ionic tracer (BODIPY^{TM} 492/515 disulfonate). Fluid phase ionic strength: 10 mM. The CLSM images demonstrate the induction of enriched and depleted CP zones through the whole packing. Profiles were normalized with respect to their maximum intensity at E_{ext} = 0 kV/m. Axial and lateral profiles (with respect to the direction of E_{ext} and the resulting macroscopic EOF) refer to the dashed lines in the images.

with neighbouring particles in a dense multiparticle system like the fixed bed (see Figure 2.3 for comparison).

In Figure 4.2 we observe for the counter-ionic tracer an image contrast that stems from its intraparticle enrichment (at $E_{ext} = 0$ kV/m) and which intensifies with E_{ext}. However, neither distinctive CP zones around the particles nor the slope within a particle characterizing the backward diffusion from the enriched CP zone can be detected in the profiles in Figure 4.2. The small dimension of the particles ($d_p = 10$ µm) does not allow the clear visualization of the CP zones against the backdrop of a strong intraparticle enrichment increasing with the current density through a particle (at increasing E_{ext}), and backward diffusive flux acts on such a time and length scale that the profiles in

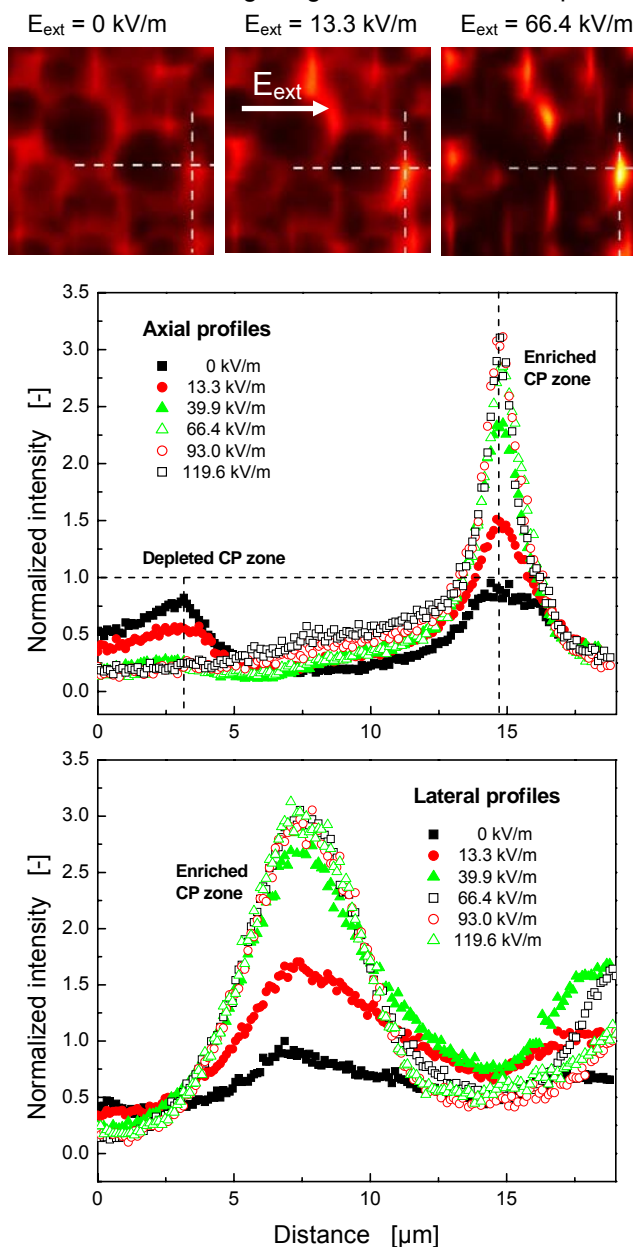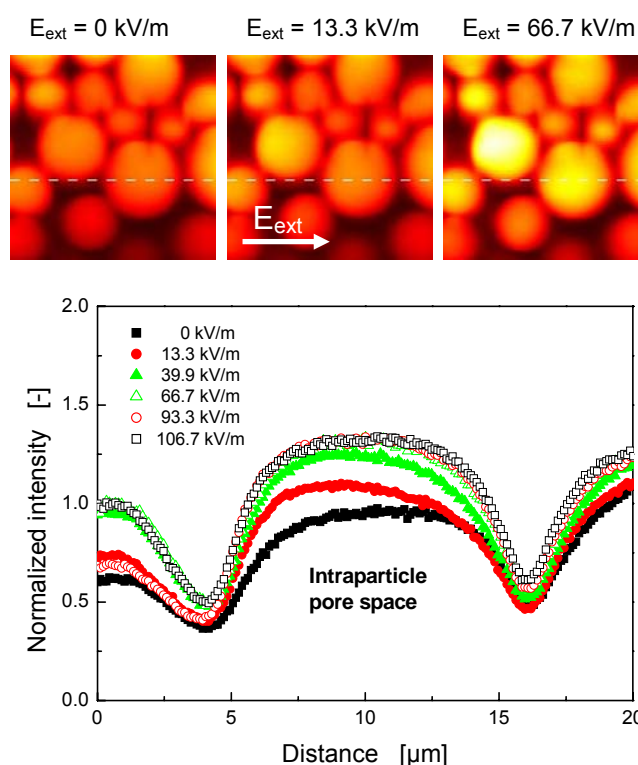**Figure 4.2** Local CP dynamics in and around a single particle in a fixed bed of the strongly cation-selective particles ($d_p = 10$ µm, $d_{intra} = 10$ nm) in dependence of the applied electrical field strength (E_{ext} as indicated), as seen by the counterionic tracer (Rhodamine 6G). Fluid phase ionic strength: 10 mM. Axial profiles were taken along the dashed lines in the images and normalized with respect to their maximum intensity at $E_{ext} = 0$ kV/m.

average display only a pronounced enrichment. The profiles for both, co-ionic and counter-ionic tracer, show a similar dependence on E_{ext}. An upper limit for the maximum co-ion concentration in the enriched CP zone corresponding to a minimum co-ion concentration in the depleted CP zone is approached at $E_{ext} = 60$-70 kV/m (Figure 4.1). The maximum intraparticle concentration of the counter-ionic tracer is realized in a comparable range for E_{ext} (Figure 4.2).

The relative intensity of the evolving CP is analyzed in more detail in Figure 4.3 based on the profiles shown in Figure 4.1 (co-ionic tracer). In view of a classical analysis of CP [3-5] Figure 4.3 clearly reflects mutual ion concentration differences at the anodic and cathodic phase boundaries of a particle with respect to the bulk solution. They increase with E_{ext} and can be translated to an increasing current density through the cation-selective intraparticle pore space of a particle. The transport of ionic species towards a particle (in the direction of E_{ext}) is diffusion-controlled by the depleted CP zone (anodic CDL). At increasing E_{ext} the steepness of the respective concentration gradients increases until a limiting behaviour is approached. This should be interpreted as reaching the limiting current density locally through the anodic interface of a particle. The local co-ion concentration in the anodic CDL is reduced towards zero at $E_{ext} = 60$-70 kV/m, and this field strength also reflects the maximum ion concentration in the enriched CP zone (Figure 4.3). In the plateau regime electrokinetic transport

through a particle exceeds diffusion-limited transport through the depleted CP zone; thus, in this plateau regime (E_{ext} > 60-70 kV/m) charge transport through a particle is determined by the transport

characteristics in the adjoining anodic CDL (depleted CP zone). In other words, with the increasing field strength, i.e., while the electrical current through a particle increases and ionic concentration in the depleted CP zone is decreased towards zero (Figure 2.1), a transition occurs from intraparticle to (extraparticle) boundary layer-dominated transport behavior on the single-particle scale in the fixed bed.
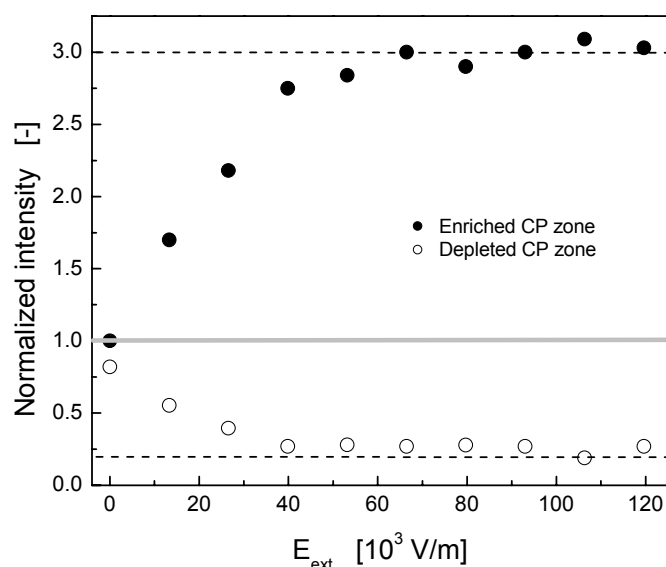
Figure 4.3 Dependence of tracer intensity in the stationary, enriched and depleted CP zones around a single particle in the fixed bed (d_p = 10 μm, d_{intra} = 10 nm) on the applied electrical field strength. Data were extracted from the axial profiles in Figure 4.1.

Multiparticle effects in fixed beds. In a random-close packing of particles the symmetrical shape with respect to E_{ext} of the anodic depleted and cathodic enriched CP zones observed around a single-free particle (Chapter 2, Figures 2.3 and 2.4) [6] becomes significantly influenced by neighbouring particles as was already indicated in Figure 4.1. The enriched CP zone of a particle in a fixed bed feeds electrolyte concentration to the depleted CP zones of neighboured downstream particles. This is most pronounced when the particles are located directly behind each other as is shown in more detail in Figure 4.4 for a cusp region between two particles in the packing (this region is indicated by the white arrow in the image for E_{ext} = 40 kV/m). The feeding of electrolyte concentration from the enriched CP zone of the upstream particle into the depleted CP zone of the downstream particle can render impossible the local observation of the depleted CP zone at the downstream particle (see profiles in Figure 4.4b and the schematic). By contrast, in the upper profiles (Figure 4.4a) and the lower profiles (Figure 4.4c) the formation of a depleted CP zone of the downstream particle becomes detectable upon the application of E_{ext}. At these positions (and illustrated by the schematic) the enriched CP zone of the upstream particle does not extend far enough to interact sufficiently strong with the depleted CP zone the downstream particle; along the middle profile (Figure 4.4b) the two beads actually come closest. The analysis in Figure 4.4 resolves the mutual interplay between enriched and depleted CP zones in the interparticle pore space of fixed beds and thereby demonstrates the importance of such multiparticle effects for the locally surviving CP.
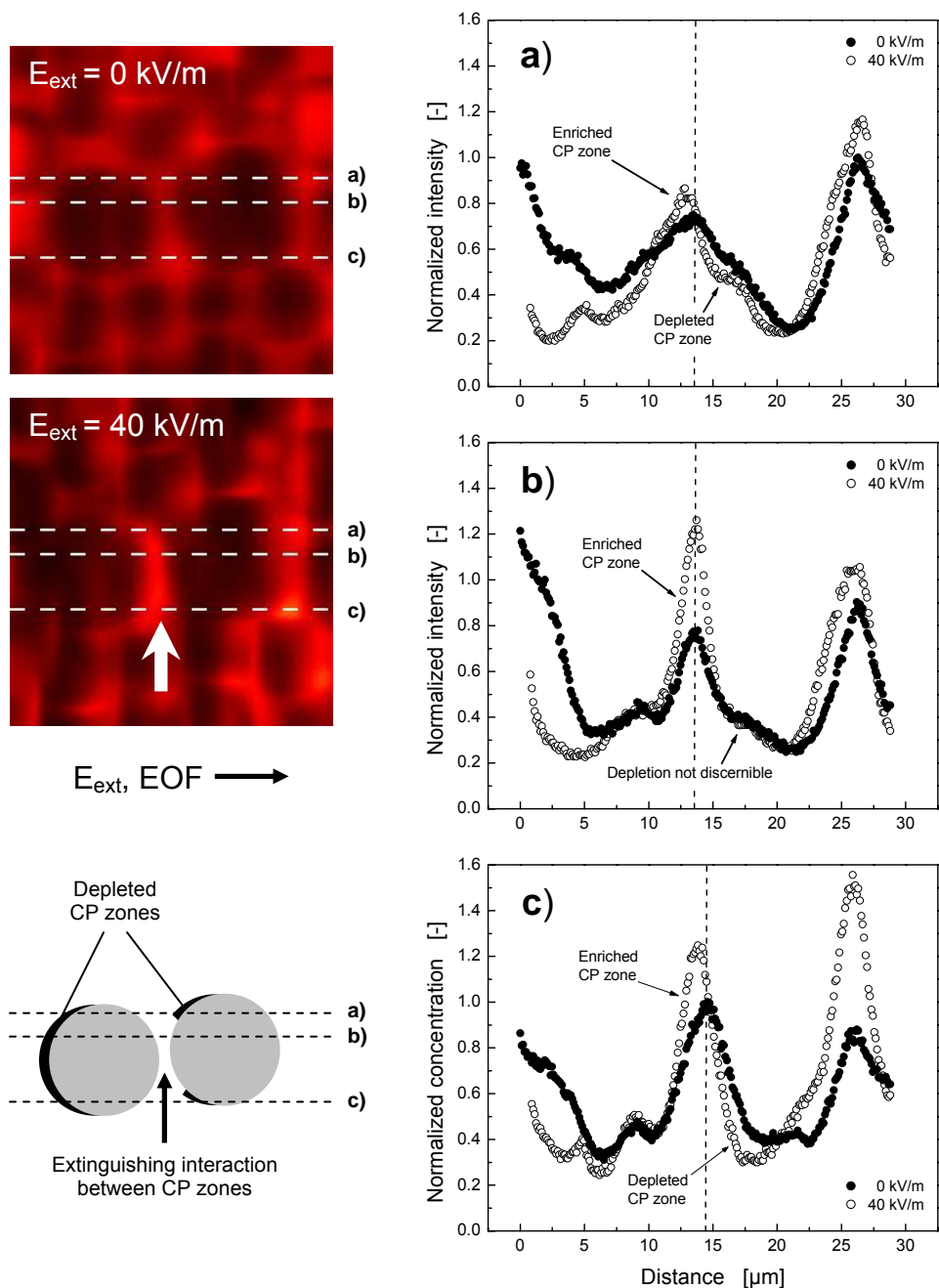
Figure 4.4 Visualization and analysis of multiparticle effects on CP in fixed beds at a fluid phase ionic strength of 10 mM. The enriched CP zone of the upstream particle is directly feeding electrolyte concentration to the nearest particle downstream. The three graphs compare the intensity profiles obtained with and without applied field along the three dashed lines (labelled accordingly) in the images. The intensity of local multiparticle effects depends on the distance between the ion-permselective interfaces of the individual particles and their relative orientation. The schematic helps to illustrate the local situation in the fixed bed.

Influence of fluid phase ionic strength. The dependence of CP on ionic strength of the bulk electrolyte was investigated using the co-ionic tracer. The ionic strength dependence of CP is illustrated in Figure 4.5 for a selected particle in the fixed bed. At the beginning of this experiment the laser and detector settings of the microscope were optimized to include the brightest region of the images, i.e., the enriched CP zone at the lowest investigated ionic strength (10 mM acetate buffer)

with E_{ext} = 52.6 kV/m. This field strength and ionic strengths in this experiment were chosen to avoid Joule heating. For subsequent experiments the microscope settings were kept constant and the system was dynamically equilibrated with a higher ionic strength fluid phase until a steady state was achieved. Care was taken to work in the linear range of the detector. Both, with and without electrical field, we observe a decrease in image contrast with increasing ionic strength. For E_{ext} = 0 kV/m it results from an increase of the intraparticle co-ion concentration due to the increased screening of surface charge and a corresponding decrease of the particles cation-selectivity. With E_{ext} = 52.6 kV/m the decrease in image contrast at increasing ionic strength corresponds to the attenuation of CP which is also a consequence of the decreasing cation-selectivity of a particle, though even at an effective ionic strength of 40 mM the CP phenomenon is still clearly discernible (Figure 4.5).
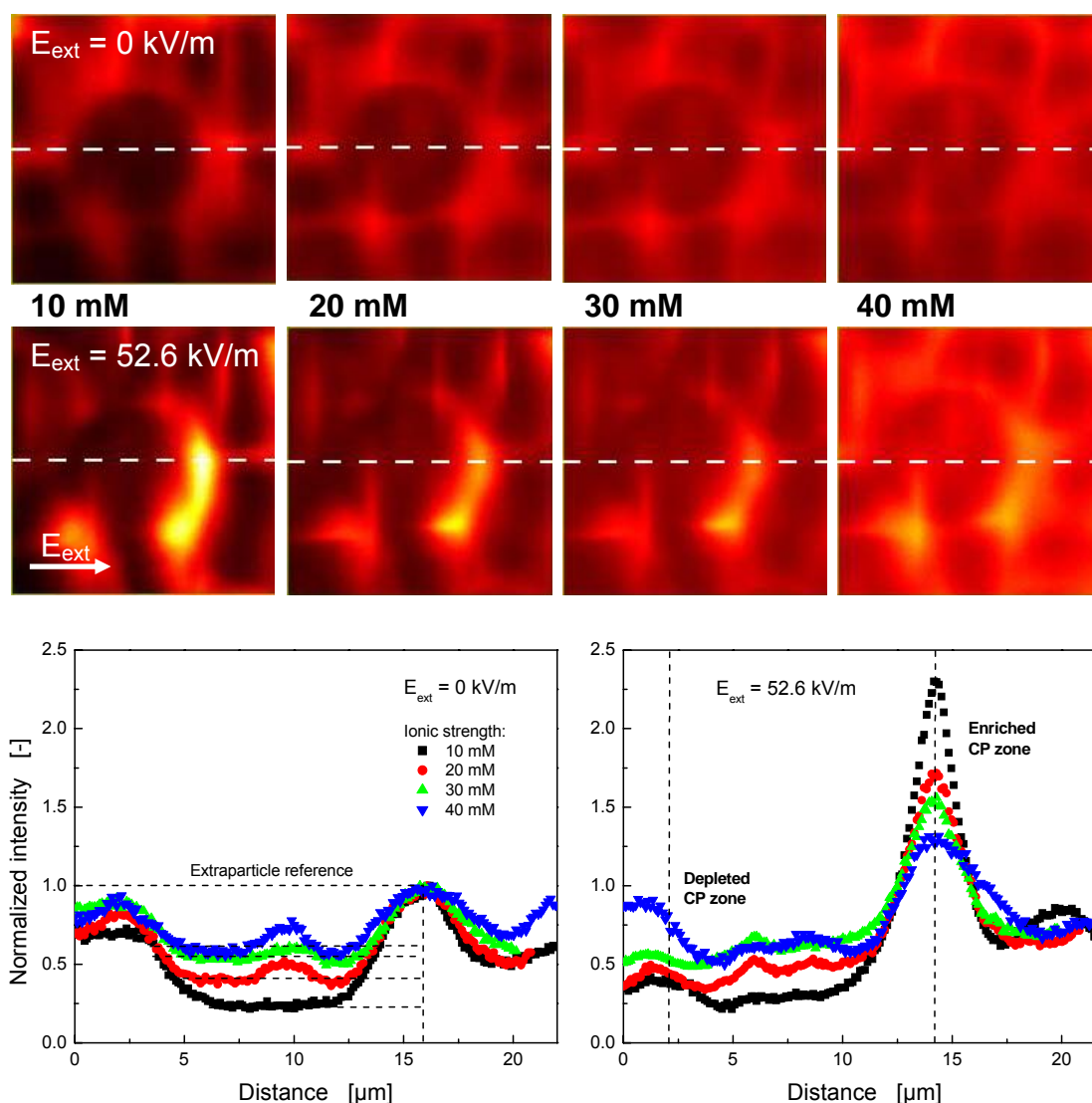
Figure 4.5 Ionic strength dependence of the co-ion distribution on a single particle scale, as reflected by the co-ionic tracer. The fluid phase was 90:10 (v/v) DMSO/aqueous sodium acetate buffer (pH 5.0) at varying effective ionic strengths (from left to right: 10 mM, 20 mM, 30 mM, 40 mM). Laser and detector settings were optimized for an effective ionic strength of 10 mM and E_{ext} = 52.6 kV/m. Subsequently the column was equilibrated with fluid phase of higher ionic strength until a steady state was achieved. All images were aquired under identical laser and detector settings. Tracer concentrations were normalized with respect to extraparticle intensity at E_{ext} = 0 kV/m (as indicated).

The ionic strength dependence of the local co-ion concentration (with and without E_{ext}) is summarized in Figure 4.6. Data points were extracted from the profiles shown in Figure 4.5 along the dashed vertical lines. With increasing ionic strength (and $E_{ext} = 0$ kV/m), i.e., decreasing EDL overlap inside a particle, the co-ion exclusion is reduced as is indicated by an increasing concentration inside the particle at constant extraparticle concentration; the intraparticle concentration (Figure 4.6, open circles) approaches a limiting value which is reduced compared to the extraparticle concentration according to the porosity of a particle [7]. This is

Figure 4.6 Ionic strength dependence of the SCX particles ion-permselectivity and of the electrical field-induced CP, as reflected by the co-ionic tracer. Data were extracted from the axial profiles in Figure 4.5. The ion-permselectivity of the system decreases with increasing ionic strength of the fluid phase resulting in an increased intraparticle co-ion concentration and attenuated CP.

in accordance with the behaviour found in LC practice employing charged co-ionic tracer, where a beds total (effective) porosity could be modulated with EDL overlap inside the particles (Figure 3.5) and approaches the total bed porosity at very high ionic strength. Coming back to Figure 4.6, with increasing ionic strength (and $E_{ext} = 52.6$ kV/m) the reduced cation-selectivity of a particle clearly results in a decrease of the relative enrichment and depletion of the electrolyte concentration in the CP zones, i.e., in an attenuation of the CP phenomenon in the fixed bed at constant E_{ext} (Figure 4.6, closed symbols), which can be alternatively also achieved by increasing intraparticle pore dimensions at constant mobile phase ionic strength (Figures 3.14a and 3.14b).
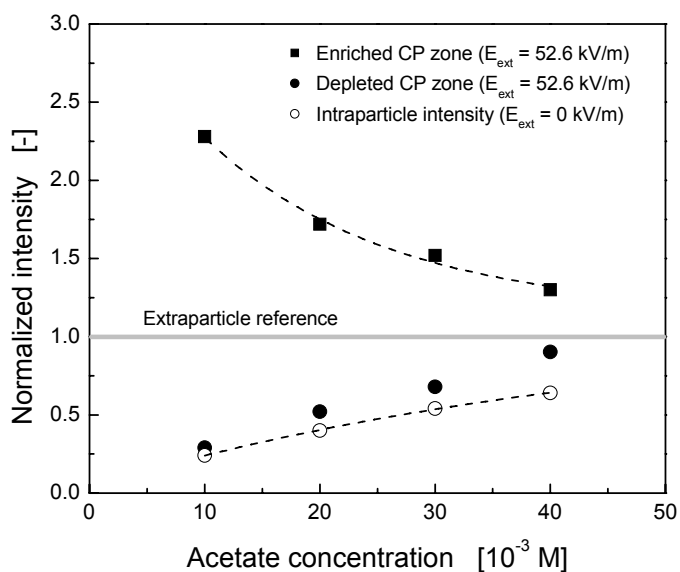
Macroscopic electrohydrodynamics. Results from the CLSM data presented so far in view of a local CP dynamics in fixed beds of strongly cation-selective particles in dependence of the applied field strength (Figures 4.1-4.3) and fluid phase ionic strength (Figures 4.5 and 4.6) are further supported and complemented by the observation of the macroscopic fluid dynamics. In these experiments the uncharged, nonadsorbing fluorescent molecule BODIPY[TM] 493/593 was employed as tracer of the EOF velocity field inside the random-close packing. In general, the electroosmotic mobility μ_{eo} which is the ratio of the average EOF velocity u_{eo} and E_{ext} is determined by measuring u_{eo} as a function of E_{ext}. In Chapter 1.4 μ_{eo} in fixed beds of porous particles was discussed to be basically composed of different contributions, including i) normal or conventional EDL behaviour at the particles external surface, ii) intraparticle volumetric EOF, and iii) porosity of a particle [8]. An additional factor in view of the earlier discussed contributions is that the intraparticle EDL overlap influences the ion-permselectivity of a particle (cf. Figure 4.6) which, in turn, determines the intensity of CP and a CP-based nonequilibrium EOF at higher field strengths [1], which has been clearly shown in Chapter 3 under typical electrochromatographic conditions.

In Figure 4.7a the average flow velocity (expressed via μ_{eo}) of the investigated material (d_p = 10 µm, d_{intra} = 10 nm) is shown for various effective ionic strengths and applied field strengths up to 120 kV/m. For the case realized in our work, the unique trend of μ_{eo} corroborates the operation of a fundamental effect. For example, μ_{eo} measured at an effective ionic strength of 10 mM (Figure 4.7a, solid circles) shows an interesting dependence on E_{ext} with a pronounced slope beginning at approximately 40 kV/m. This indicates the onset of a significantly nonlinear dynamics which can be readily explained by an increasing contribution of the nonequilibrium electroosmotic slip to the overall EOF in the fixed bed.

As E_{ext} is increased ionic concentrations in the depleted CP zone (anodic CDL) of a particle in the bed are decreased towards zero and electrical current through a particle is expected to approach a limiting value. For electrokinetic flow along the conductive, cation-selective surface of a particle this regime (below the limiting current density) corresponds to quasi-equilibrium, linear EOF for which the diffusive part of the primary EDL essentially preserves its common structure [3]. At higher field strength charge transport in the anodic CDL becomes climactic with respect to intraparticle electrokinetic transport, meaning that electrokinetic flux of counter-ions in the particle begins to exceed their supply through the CDL. The onset of a significantly nonlinear

Figure 4.7 Electroosmotic mobilities $\mu_{eo} = u_{eo}/E_{ext}$ in a capillary (75 µm i.d.) packed with the SCX particles (d_p = 10 µm, d_{intra} = 10 nm). The fluid phase was a 90:10 (v/v) DMSO/aqueous sodium acetate buffer (pH 5.0). a) Dependence of μ_{eo} on applied electrical field strength at different effective ionic strengths. b) Dependence of μ_{eo} on ionic strength at selected values of E_{ext}.

dynamics in Figure 4.7a with an effective ionic strength of 10 mM at $E_{ext} \approx$ 40 kV/m reflects the range where we observed the steepest concentration gradients in the solution adjacent to a cation-selective particle in the fixed bed (Figure 4.3) which showed a hardly discernible further dependence on E_{ext} (Figure 4.3). The maximum local intensity of CP is then approached, translating to the limiting current density through a particle. This limiting current density and applied E_{ext} thus mark the transition to the nonlinear EOF behaviour dominated by a contribution of the nonequilibrium electroosmotic slip based
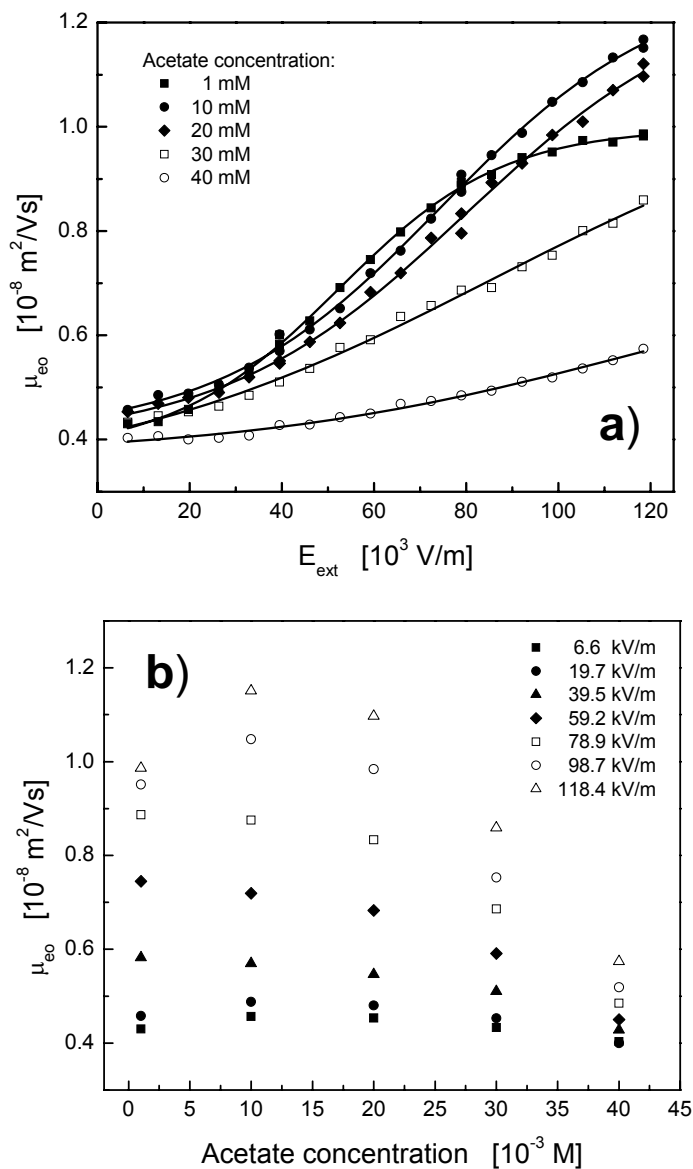
on the secondary EDL (Figure 2.4b). In agreement with our CLSM studies the observed intensity and onset of nonlinearity depend on the fluid phase ionic strength and are significantly attenuated and shifted to higher E_{ext} at higher ionic strength (Figure 4.7a). An increased ionic strength reduces the cation-selectivity of a particle and, in turn, attenuates the intensity of the CP phenomenon, as analyzed in Figures 4.5 and 4.6. It explains the relatively small nonlinear μ_{eo} dynamics for the highest ionic strength in Figure 4.7a, although CP and its microscopic consequences are still discernible (Figures 4.5 and 4.6). In contrast, μ_{eo} increased by a factor of approximately 2-3 with respect to the expected classical, linear EOF behavior is observed for 10 mM effective ionic strength at the highest E_{ext} of 120 kV/m.

Figure 4.7b shows the variation of μ_{eo} with the fluid phase ionic strength. We see a relatively common trend insofar as μ_{eo} increases with decreasing ionic strength to approach a plateau or spurious maximum at about 10 mM acetate buffer. While a decrease in μ_{eo} with increasing ionic strength above the 10 mM represents normal behaviour when EDL overlap is negligible (i.e., the EDL continues to be compressed resulting in a reduced shear plane potential) [3], the increase in μ_{eo} from below that concentration towards a spurious maximum can have several reasons [8, 9]. The most intriguing conclusion emanating from the data in Figure 4.7b is that μ_{eo} depends significantly on E_{ext} at constant mobile phase composition, under conditions that can be assumed as isothermal. Further, the increase in μ_{eo} with E_{ext} becomes much stronger as the acetate buffer concentration is reduced towards 10 mM as is clearly seen in the different slopes of these curves. This ionic strength dependence (see also Figure 4.6) demonstrates an increasing contribution of the nonequilibrium electroosmotic slip to u_{eo} being more pronounced at higher field strength, which clearly resolves an additional factor in form of a field strength dependence of μ_{eo}, which was not observed in Figure 1.6b, acquired for particle diameters of only 2.5 µm and much lower ion-permselectivity. Any slight nonlinear contribution thus not obscures the principal trend for (equilibrium) linear electroosmosis for relatively small porous particles as shown in Figure 1.6b.

Finally, it is instructive to compare μ_{eo} and its electrical field-dependence in the fixed beds of the strongly cation-selective particles with data on this nonequilibrium electrokinetics (or electrokinetics of the second kind) available from the literature. In the focus of such a comparison should be the actual nonlinearity in the dense multiparticle systems (fixed beds) with respect to the expectations based on the single-free particle picture which prevails, e.g., in an electrophoresis experiment. Electrophoresis of the second kind has been studied intensively [6, 10-13]. Figure 4.8 shows electrokinetic mobilities of strongly cation-selective particles as a function of the applied field strength. Electrophoretic mobilities (μ_{ep}) measured for single spherical particles with diameters from 500 to 1 µm are taken from Barany [12] and compared to μ_{eo} determined in our work for capillaries packed with 10 and 5 µm-sized particles. Our data have been re-scaled to the physical properties of a purely aqueous fluid phase used in that study of electrophoresis of the second kind [12]. Monitoring μ_{eo} at an ionic strength of 10 mM clearly shows that generally higher E_{ext} are necessary for the smaller particles (d_p = 5 µm) to induce a significantly nonlinear EOF behavior (Figure 4.8, solid circles). This is expected because nonequilibrium electroosmotic slip in first approximation depends linearly on particle size and squared

on applied field strength [6, 14]. In other words, the ratio of nonlinear (second kind) to linear (classical or first kind) EOF velocities depends linearly on d_p and E_{ext} (Figure 2.4b).

The data for μ_{ep} in Figure 4.8 demonstrate that the small particles (d_p = 1-10 µm) move with almost the same mobility when E_{ext} is below 2 kV/m. In this regime of E_{ext} and d_p electrophoresis follows the classical pattern (linear behaviour). As E_{ext} increases, the larger particles begin to move faster. For smaller particles, a higher E_{ext} is required to induce electrophoresis of the second kind [12]. For d_p = 10-500 µm and E_{ext} = 2.5-20 kV/m the electrical field-dependence of μ_{ep} is close to linear (with almost the same slope), demonstrating the second-order dependence of electrophoretic

Figure 4.8 Electrokinetic mobility for SCX particles as a function of the applied electrical field strength. Values for μ_{eo} from this work are compared with μ_{ep} reported by Barany [12]. μ_{eo} data have been re-scaled to the physical properties of a purely aqueous fluid phase used in the study of μ_{ep}. Numbers in the graph indicate the mean particle size.

velocities on E_{ext}. For larger fields (20-100 kV/m) the curves taper off to approach saturation. This can be related to the increasing importance of a tangential drift of the mobile SCR, because of high local convection due to this nonlinear slip, which can be locally orders of magnitude higher than linear EOF (remember also the angular dependence of EOF velocities in this nonlinear framework illustrated in Figure 2.4b) and also simply the fact that the particles move at higher Reynolds numbers, which thins the CDL significantly and prevents the SCR with its inherently increasing potential to grow further. Both factors cause a decrease in electrophoretic velocity [12, 13].
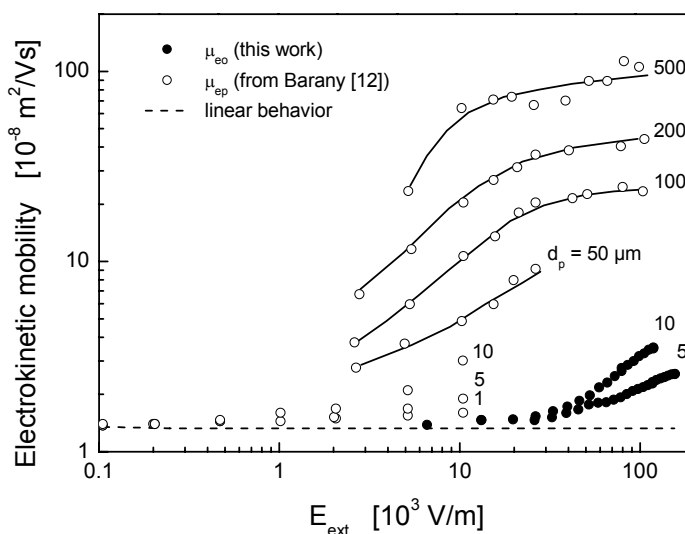
Compared to μ_{ep} measured in dilute particle suspensions, the μ_{eo} data obtained with fixed beds (dense multiparticle systems) demonstrate the onset of a noticeably nonlinear behavior only at much higher field strengths (Figure 4.8). In principle, electrophoresis is an integral characteristic of electroosmosis. However, even when accounting for the tortuosity of fixed beds with respect to the single-free particle picture [8], a purely geometrical effect which reduces the macroscopically measured μ_{eo} in dense multiparticle systems relative to μ_{ep} for a dilute suspension of an electrophoresis experiment, μ_{eo} is still significantly smaller than μ_{ep} for a given field strength and particle size. This can be, in part, due to differences in the cation-selectivity of the different SCX particles (those used in this work and by Barany [12]), but also originates in the multiparticle effects demonstrated here by CLSM. The proximity of particles in a dense multiparticle system (fixed bed) simply means that due to the actual pore space morphology complex extinguishing interactions occur between close or overlapping CP zones (Figure 4.4). This results in a reduced, locally effective CP and consequently in higher field strengths needed to induce nonequilibrium EOF in a fixed bed of particles with respect to the single-free particle picture.

In general this chapter demonstrates in a close relation to Chapter 2 and Chapter 3, that with increasing field strength a limiting current density (locally) through a particle in a packed bed is approached, meaning that charge transport locally through a particle becomes controlled by the dynamics in the adjoining extraparticle convective-diffusion boundary layer (depleted CP zone). It also indicates that transport on a single particle scale with enriched and depleted CDL is controlled by intraparticle transport behavior at lower field strength and moves to extraparticle convective-diffusion boundary layer dominated transport behavior, directly characterizing the transition from linear to nonlinear electrokinetics (Figure 2.4b).

4.3.2 Monolithic structures

The enforced recent development of rigid monolithic support structures has contributed to many technological processes, especially in the chromatographic sciences [15-18]. These support structures can be polymer-based or silica-based in nature. Because of their ease of preparation especially organic polymer-based monoliths gain increasing popularity [18-20]. Monolithic stationary phases as chromatographic beds can be prepared in capillary columns and microfluidic devices, which makes them very promising as an alternative to packed beds, because particles are increasingly difficult to handle and retain in such small dimensions [21]. Further convenience includes that monoliths are chemically anchored to the confining container or the column wall, which makes the need of retaining frits unnecessary. The structure of silica based monoliths displays micrometer-sized sponge-like interconnected mesoporous silica skeletons and macropores transecting the whole skeleton (also called through pores). A cross sectional segment of such silica monolith has already been shown in Figure 3.1 and the preparation of such type of monolith has been reviewed in [22, 23]. Compared to conventional particulate fixed beds employed in LC, monolithic materials combine relatively high capacity (selectivity), mobile phase velocity (high permeability) and mass transfer efficiency (short diffusion path length in the relatively thin skeleton) in a unique manner [17, 18]. In contrast to the discontinuous solid phase encountered in sphere packings due to discrete particles, monolithic structures have a continuous skeleton. These are particularly useful in CEC because of their possible implementation as flexible meterware. However, qualitatively similar to the sphere packings the pore space in a monolith often consists of a macroporous interskeleton region (containing bulk fluid phase) and meso- and/or microporous intraskeleton compartments. The latter exhibit properties comparable to the intraparticle pore space in sphere packings, e.g., an intraskeleton ion-permselectivity and perfusive EOF. Consequently, another similarity or common feature between the hierarchically-structured pore space in sphere packings and monoliths in view of the present analysis is the formation of CP zones (cf. Figure 4.1) under conditions favouring a significant EDL overlap in the intraskeleton compartments of a monolith (Figures 2.5 and 3.6).

This is demonstrated by Figure 4.9 for a bare silica capillary monolith which contains interskeleton macropores and intraskeleton mesopores. The neutral tracer serves as a reference (Figure 4.9a). As illustrated by the series of CLSM images and selected intensity profiles for the co-ionic fluorescent tracer, E_{ext} sensitively influences a development of CP in this material. While the image contrast in Figure 4.9b (left image) originates from a Donnan-exclusion of the tracer from the intraskeleton mesopore space due to EDL overlap caused by the relatively low ionic strength, CP develops if E_{ext} is superimposed (Figure 4.9b, right image). This process is clearly evidenced by the "mountains" and "valleys" in fluorescence intensity reflecting enriched and depleted CP zones with increased and decreased background electrolyte concentration, respectively, which demonstrate the systematic change in the equilibrium distribution of ionic species in the interconnected pore space. Using charged (co-ionic) fluorescent, polystyrene-based nanoparticles with a nominal diameter of 50 nm the contrast without E_{ext} (left image, Figure 4.9c) originates in the circumstance that the tracer is size-excluded from the mesopore space. Upon application of E_{ext} we observe the development of enriched and depleted CP zones (right image in Figure 4.9c and related profile). They are sharper than for the
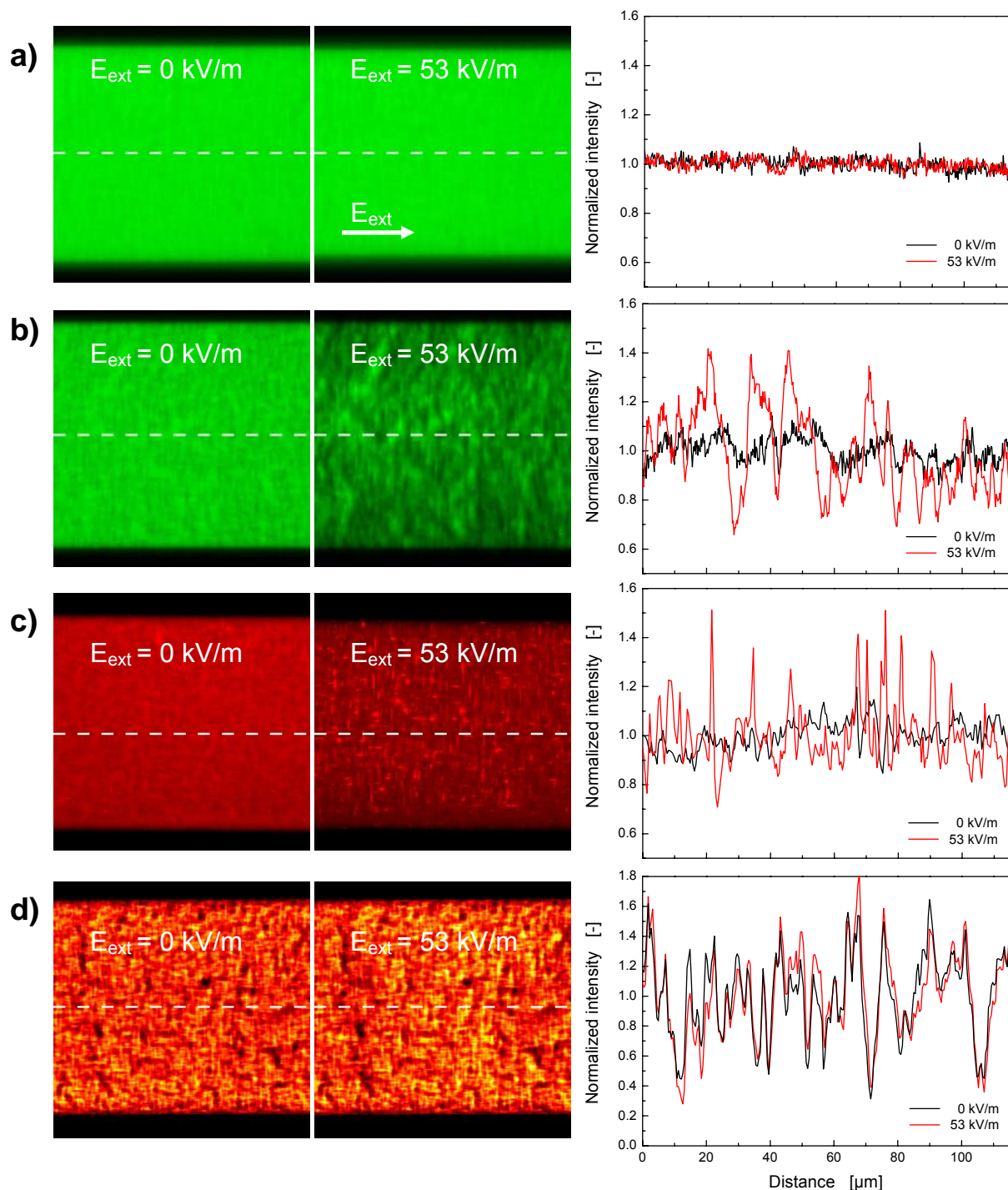
Figure 4.9 CP dynamics in a silica capillary monolith (100 µm i.d.) with cation-selective skeleton in dependence of the applied electrical field strength (E_{ext} as indicated), as seen by a) Bodipy 493/593 as a neutral tracer, b) co-ionic tracer (BODIPY[TM] 492/515 disulfonate), c) Polystyrene nanoparticles (50 nM) as co-ionic size excluded tracer, and d) Rhodamine 6G as counterionic tracer in a fluid phase of 90:10 (v/v) DMSO/aqueous sodium acetate buffer (pH 5.0) with an effective ionic strength of 0.1 mM. Profiles were normalized with respect to their mean intensity at E_{ext} = 0 kV/m. Images were acquired as xy-sections of 115.16 µm × 115.16 µm with a resolution of 512 × 512 data points in a slice of thickness 1 µm.

small co-ionic tracer (right image, Figure 4.9b) because the nanoparticles are completely size-excluded from the mesoporous skeleton, while a nonideal ion-permselectivity allows the small (co-ionic) tracer to penetrate the mesopore space. Further and most important for counter-ionic analytes is

the fact that they show strong adsorption to the oppositely charged surface and in average are increasingly enriched (in addition to their enrichment at electrochemical equilibrium) by the mesoporous skeleton with increasing E_{ext} (Figure 4.9d.).

Figure 4.10 shows that for the co-ionic tracer a development of electrical-field-induced CP systematically develops in the whole material. It leads to the development of "mountains" and "valleys" in electrolyte concentration with the spatial position fixed but with varying intensity (development) at each position. Scanning the confocal plane up and down revealed increasing and decreasing intensity of the spots at one E_{ext}. In this respect, it should be recognized that the pore-level profile of EOF in fixed beds of spherical particles and also monoliths, even in the thin-EDL-limit, is not uniform and is a complex function of velocity or, more precisely, of the local distribution of velocities caused by the complex morphology of the porous medium (Chapter 1) which also influences the (local) thickness of the hydrodynamic boundary layer and thus also transport properties in the locally depleted CP zone (Chapter 3.3.4), which is basically inaccessible by our experimental approach and such small spatial dimensions. In the monolithic material the shape with respect to E_{ext} of the anodic depleted and cathodic enriched CP zones observed in comparison to spherical symmetry thus is also expected to become influenced by the branching of the sponge-like structure as may be schematically illustrated in Figure 4.10. The enriched CP zone of a vertical (with respect to flow direction) branch feeds electrolyte concentration to the depleted CP zones of another branch directly diverting the skeleton further downstream. This is most pronounced when the branching is directly located behind an enriched CP zone. The feeding of electrolyte concentration from the enriched CP zone of the upstream branch into the depleted CP zone of the downstream branch can render impossible the local observation of the depleted CP zone at the downstream branch when the branches actually come closer.

In Figure 4.11 we see that for the counterionic tracer image contrast stems from its intraskeleton enrichment (at E_{ext} = 0 kV/m) which also intensifies with E_{ext}. However, neither distinctive CP zones around the mesoporous skeleton nor any slope characterizing the backward diffusion from the enriched CP zone can be detected in the profiles in Figure 4.11, which clearly stems from the small spatial length dimensions and was also not resolvable for the relatively small particles in Figure 4.2. This enrichment can be explained by an increasing current density through the mesoporous pore space (in analogy to the particle dynamics in Figure 4.2), which together with the diffusive backflux induces the effective intraskeleton (pore level) concentration to increase with increasing E_{ext}. Still the profiles in average display a systematic pronounced enrichment (Figure 4.11) clearly increasing with E_{ext}, meaning that the intraskeleton pore level concentrations of this single charged counter-ionic tracer are increased. As for the particulate beds, evolving CP becomes significantly tuned by E_{ext} (at constant mobile phase ionic strength). For example, as seen for the co-ionic tracer, its concentration is monotonically increasing and decreasing locally with increasing E_{ext} (Figure 4.12), reflecting enriched and depleted CP zones throughout the whole material. The electrolyte concentrations in the CP zones tend to approach an asymptotic value which is influenced by the actual ion-permselectivity of the mesopore space and actual (electro-)hydrodynamic convection through the material, determining the
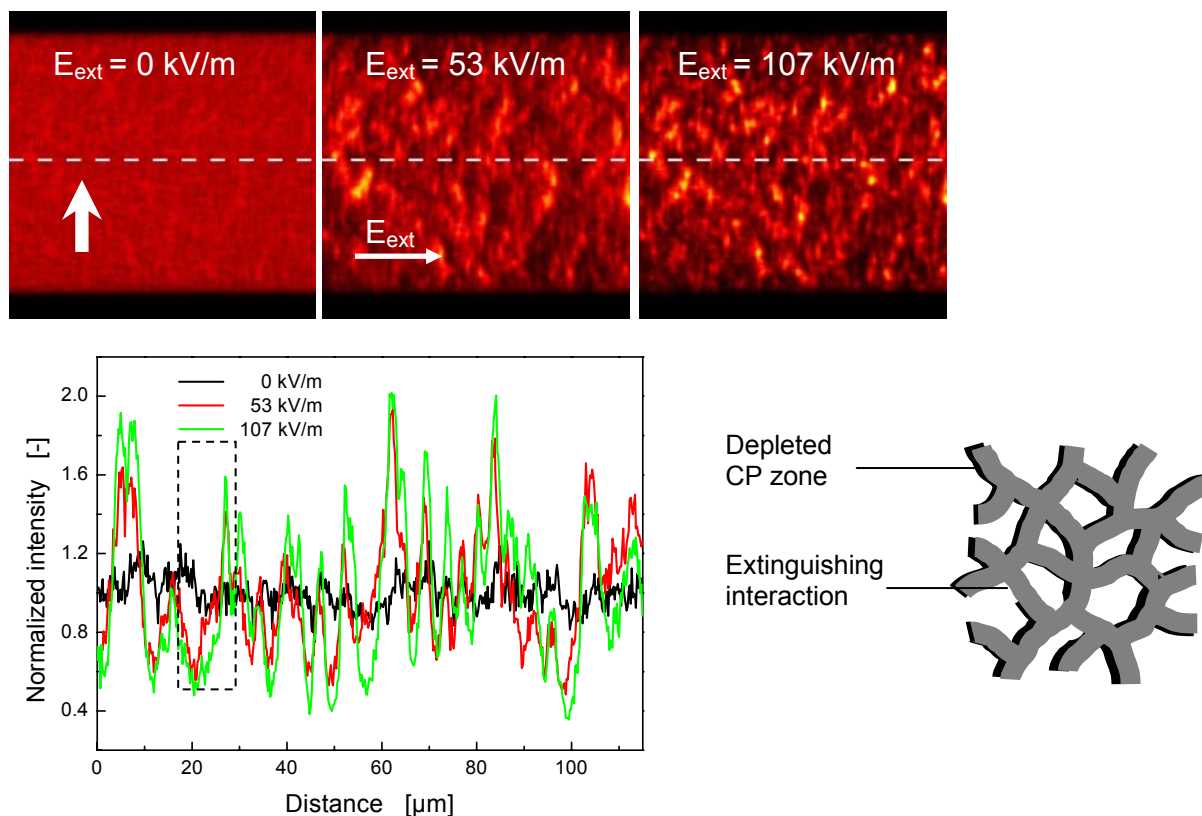
Figure 4.10 Macroscopic CP dynamics in and around a cation-selective monolithic skeleton in dependence of the applied electrical field strength (E_{ext} as indicated), as seen by the co-ionic tracer (BODIPY™ 492/515 disulfonate) in a fluid phase of 90:10 (v/v) DMSO/ aqueous sodium acetate buffer (pH 5.0) with an effective ionic strength of 0.1 mM. Profiles were normalized with respect to their mean intensity at E_{ext} = 0 kV/m. Axial profiles (with respect to the direction of E_{ext} and the resulting macroscopic EOF) refer to the enriched and depleted CP zones along the profile. Images were acquired as xy-sections of 115.16 µm × 115.16 µm with a resolution of 512 × 512 data points in a slice of thickness 1 µm.
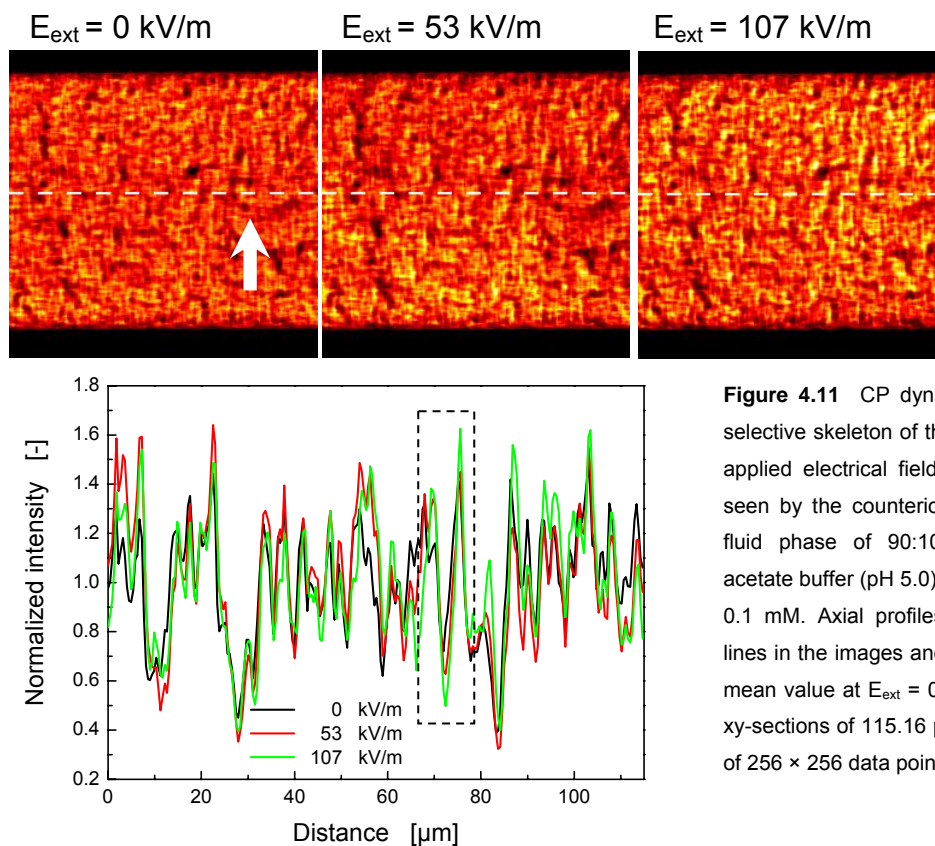
Figure 4.11 CP dynamics in and around the cation-selective skeleton of the monolith in dependence of the applied electrical field strength (E_{ext} as indicated), as seen by the counterionic tracer (Rhodamine 6G) in a fluid phase of 90:10 (v/v) DMSO/aqueous sodium acetate buffer (pH 5.0) with an effective ionic strength of 0.1 mM. Axial profiles were taken along the dashed lines in the images and normalized with respect to their mean value at E_{ext} = 0 kV/m. Images were acquired as xy-sections of 115.16 µm × 115.16 µm with a resolution of 256 × 256 data points in a slice of thickness 1 µm.

local thickness of the CDL, as has been discussed in Chapter 3.3.4 and shown in Chapter 4.3.1. In the plateau regime (for the selected position) electrokinetic transport locally through the monolith skeleton exceeds diffusion-limited transport through the depleted CP zone; thus, in this plateau regime (E_{ext} > 80-90 kV/m) charge transport locally through the skeleton is determined by the transport characteristics in the adjoining anodic CDL (depleted CP zone). In other words, with the increasing field strength, i.e., while the electrical current through the mesopore space
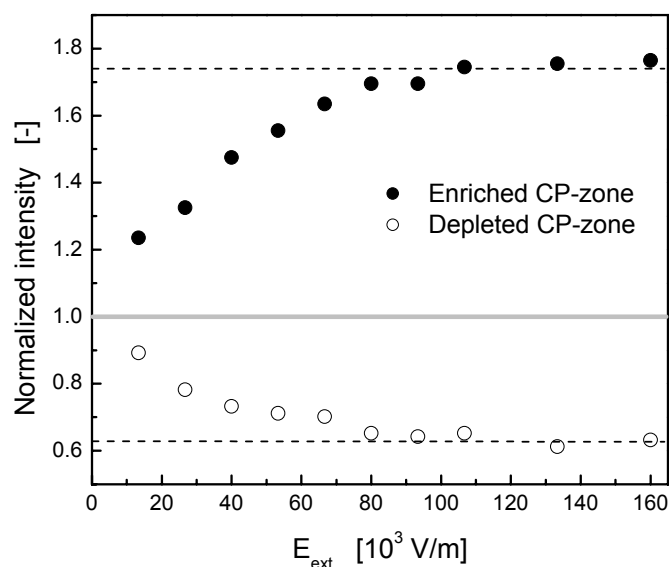

Figure 4.12 Dependence of co-ionic tracer intensity in the stationary, enriched and depleted CP zones at the region of interest (see dashed box and arrow in figure 4.10. as indication) on the applied electrical field strength.

increases and ionic concentration in the depleted CP zone is decreased towards zero (Figure 4.12), a transition occurs from intraskeleton to interskeleton boundary layer-dominated transport behavior on the local skeleton scale in the monolith. However, at the same time as the ionic strength is increased and EDL overlap in the mesopore space reduced (Figure 4.13), the CP phenomenon is expectedly attenuated because the transport numbers for co-ionic species inside the monolith skeleton increase, while those for counter-ions correspondingly decrease. Thus, the mesopore space becomes less ion-permselective and the CP zones are less intense. In comparison to the packed particulate beds, for the monoliths CP was also systematically developing throughout the whole hierarchically structured pore space (Figure 4.13). Important to note is that the ionic strength range (0.1mM to 10 mM) in Figure 4.13 represents the manifestation of CP phenomena, which develop in the whole material. This ionic strength region may be partly reflected in the (internal) surface charge density of the material (see Figure 3.6a). It should be remembered that the intraskeleton pore size ($r_{intra} \approx 13$ nm) of the monolith is in the same order of magnitude as the intraparticle pore size of the cation-exchange particles (Figure 4.5). A decreasing surface charge density, in comparison e.g. to the ion-exchange surfaces, results in a decreasing ion-permselectivity of the mesopores in the monolith and thus stimulates electrical field induced CP over a lower ionic strength region (see Figure 4.6 in comparison with Figure 4.13). We have seen in Figure 3.6a that decreasing surface electrical potential requires lower ionic strength to tune required ion-permselectivty and thus electrical field-induced CP. In other words lower ionic strengths are needed to induce significant ion-permselectivity and related CP phenomena for the monolith (Figure 4.13).

Finally electrohydrodynamic features in this ionic strength region (0.1 to 10 mM) necessarily lead, at elevated electrical field strengths, to nonequilibrium electroosmositic slip with varying intensity locally along curved interfaces where the transport discrimination of counter-ionic species between the macroporous and mesoporous pore space becomes climactic. It results in macroscopically nonlinear

u_{eo} behaviour. Thus, depending on the intensity of nonequilibrium CP, i.e., the actual potential drop in the SCR (Figure 2.4), nonlinear contributions to the overall EOF can significantly modify the conventional picture of linear electroosmotic slip velocities. It is illustrated in Figure 4.14a using a bare silica monolith with bimodal pore size distribution and mobile phase conditions leading to strong EDL overlap on the intraskeleton mesopore scale (see Figure 4.13). Figure 4.14a confirms a clearly nonlinear u_{eo} behaviour (expressed by $\mu_{eo} = u_{eo}/E_{ext}$) for various mobile phase ionic strengths. This unique trend corroborates the operation of a rather fundamental effect. It means that the initially linear behaviour (at relatively low E_{ext}) becomes increasingly dominated by nonequilibrium electroosmosis, even before we approach an asymptotic value of developing CP (see Figure 4.12). This macroscopic nonlinearity must have its origin in electrical-field-induced CP and a locally variable limiting current density, reflecting the transition to nonequilibrium electroosmotic slip in agreement with the dynamics in the packed beds.

After having interrelated the dependence of electrical-field-induced CP in these optically opaque media

Figure 4.13 Ionic strength dependence of the co-ion distribution in a hierarchical monolithic structure. The fluid phase was 90:10 (v/v) DMSO/aqueous sodium acetate buffer (pH 5.0) at varying effective ionic strengths. Laser and detector settings were optimized for an effective ionic strength of 0.1 mM and $E_{ext} = 53$ kV/m. Subsequently the column was equilibrated with fluid phase of higher ionic strength until a steady state was achieved. All images were aquired under identical laser and detector settings. Tracer concentrations were normalized with respect to the average intensity at $E_{ext} = 0$ kV/m. Images were acquired as xy-sections of 115.16 μm × 115.16 μm with a resolution of 512 × 512 data points in a slice of thickness 1 μm.

(Figures 4.10, 4.11 and 4.13) with the macroscopically observable electrohydrodynamics (4.14a), it is the influence of mobile phase composition which then has been investigated in these structures. It is the 90:10 DMSO/H$_2$O system, which has been used for our CLSM studies in this chapter throughout, but the 80:20 AcN/H$_2$O system has been employed for our electrochromatographic separations (Chapter 3). Thus the remainder of this chapter is focusing on the physicochemical parameters of the
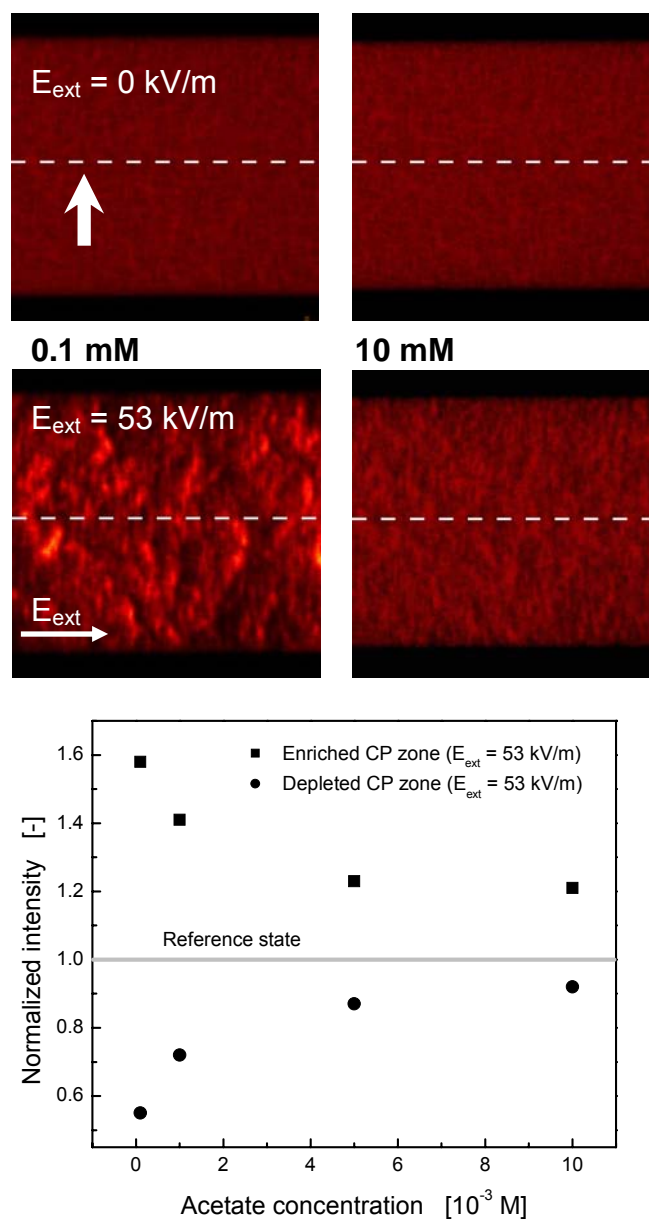
mobile phase on developing electrical field induced CP with an eye on the related nonequilibrium electroosmotic slip.

There is a wealth of solvents, which can be used as hydro-organic background electrolytes, which in view of the desired application have to fulfill different criteria, e.g. by achieving significant EOF for transporting bulk fluid in open channel systems or packed beds. Therefore they usually have to show sufficient relative permittivity (ε_r) and relatively low viscosity (η_f). The effect of $\varepsilon = \varepsilon_0 \varepsilon_r$ (where ε_0 denotes the absolute permittivity) and η_f on μ_{eo} for linear (equilibrium) EOF and nonlinear (nonequilibrium) EOF for a given system is described by $\mu_{eo} \propto \varepsilon/\eta_f$. Thus neglecting other physicochemical effects, two solvent systems may be compared [24].

Figure 4.14 Double logarithmic plot of $\mu_{eo} = u_{eo}/E_{ext}$ in the bare silica monolith as a function of E_{ext} in a mobile phase which consisted of a) 90:10 DMSO/H$_2$O (v/v) (pH = 5.0) containing acetate buffer (ionic strength as indicated), and b) in a mobile phase which consisted of 80:20 (v/v) Acetonitrile/H$_2$O (pH 8.3) containing Tris-HCl buffer (concentration as indicated).

Using a mobile phase of 80:20 AcN/H$_2$O, with a viscosity of η_f = 1.01 mPas and relative permittivity of ε_r = 42.8 (ε_r/η_f = 42.4), shows that mobility generally is reflecting higher values (Figure 4.14b) than for a mobile phase of 90:10 DMSO/H$_2$O with a viscosity of η_f = 2.6 mPas and ε_r = 49.6 (ε/η_f = 19) [24]. However other factors are still discernable, which may contribute to the relatively higher μ_{eo} for the 80:20 AcN/H$_2$O system. Using the AcN/H$_2$O system at a mobile phase pH-value of pH = 8.3, a slightly higher μ_{eo} (based on equilibrium linear electroosmosis at low field strength) is observed by comparing Figure 4.14b with Figure 4.14a. These higher velocities ground in the increasing surface electrical potential [3], because of a higher degree of dissociation of silanol groups and subsequently resulting net EOF velocities, as frequently reported in the literature [25, 26]. Their increasing dissociation also in the intraskeleton pore space, subsequently increases the ion-permselectivity (Figure 3.6a) and thus decreases the field strength at which nonequilibrium electroosmosis starts to influence the overall electrohydrodynamics, as is also in agreement with Chapter 3. This is shown in Figure 4.14b. It can be seen that for the 0.1 mM Tris in Figure 4.14b already a nonlinear velocity relation is revealed (increasing μ_{eo} with E_{ext}) at a voltage of

20 kV, in contrast to Figure 4.14a, where μ_{eo} still displays the classical (field independent) behaviour. Further it may be implied that due to the higher fluid velocities, by a factor 4 to 5, δ_{CDL} is becoming smaller in average and thus nonlinear velocities earlier start tapering off (see Figure 4.14b in comparison to Figure 4.14a). This is also observed for the packed beds (Figure 4.7a).

4.4   Conclusions

This chapter has analyzed the local CP dynamics in fixed beds of strongly cation-selective spherical particles with respect to the macroscopic EOF dynamics, particularly in view of a contribution of CP-based nonequilibrium electroosmotic slip. CP was visualized by CLSM employing refractive index matching of the fluid phase with respect to the solid skeleton of the mesoporous particles (Figures 4.1-4.5). The electrical field-dependence of the CP pattern (Figure 4.1) demonstrates that a limiting current density is approached locally through a particle at increasing E_{ext} (Figure 4.3). Electrical current through a particle in the fixed bed is controlled by the intraparticle transport characteristics at low field strengths, while it becomes controlled by the behavior in the depleted CP zone (anodic CDL) towards the limiting current regime at higher field strengths.

The CP pattern in a fixed bed of particles is modulated by the arising multiparticle effects, i.e., the interaction of neighboring CP zones (Figure 4.4). We were able to directly correlate the induction and development of CP to the evolving nonlinear dynamics accessible through the macroscopically measurable EOF velocities (Figure 4.7). While the local intensities in the depleted and enriched CP zones approach asymptotic behavior (Figure 4.3), e.g., ionic concentration in the depleted CP zone is reduced towards zero at increasing field strength, we observe the onset of a significantly nonlinear contribution to the overall EOF dynamics (Figure 4.7). In the framework of nonequilibrium CP this suggests that a secondary EDL is electrokinetically induced by the applied field, consisting of a mobile SCR in the depleted CP zone and an immobile SCR in the adjacent pore space of a particle.

It has been shown that nonequilibrium electroosmosis based on this secondary EDL survives in dense multiparticle systems and is a result of the mutual interplay of a variety of parameters, including pore space morphology and applied field strength, but also factors modulating the counterion-selectivity of a particle, e.g., the intraparticle pore size and surface charge density, or the fluid phase ionic strength (Figure 4.6). In contrast to dimensions of the primary EDL the CP zones around a particle have a considerable larger size (Figure 4.1) which results in extinguishing interactions in dense multiparticle systems such as the fixed beds (random-close packings). Consequently, electrokinetic mobilities based on μ_{eo} in a fixed bed and μ_{ep} for a dilute suspension of the same (or similar) particles from an electrophoresis experiment cannot be quantitatively compared with each other (Figure 4.8).

The hierarchically-structured pore space of fixed beds of particles encountered in this work (charge-nonselective interparticle macropore space; counterion-selective intraparticle mesopore space) is a good example illustrating the importance of both classical (linear) and nonequilibrium (nonlinear) electroosmosis in the macroscopic EOF dynamics in more complex porous media. Borderline cases are observed as the thickness of the primary EDL becomes much smaller than any pore size (linear EOF behavior) and, on the other hand, as potential drop in the mobile SCR of the secondary EDL becomes much larger than the classical zeta-potential (nonlinear EOF behaviour) (Figure 4.8).

In contrast to the random-close sphere packings where the interparticle (void space) dimensions are directly related to the particle diameters the silica-based monoliths used in this work are a promising

alternative. They are manufactured by a two-step process, resulting in bimodal pore size distributions and morphologies different from the packed beds. The resulting bimodal pore size distributions translate to particulate systems in which ion-permselective spheres would be relatively loosely placed in space [1], as we have already noted that decreasing the macropore space results in an attenuated nonlinearity also in the monolithic structure (Figure 3.15). Thus, nonequilibrium electroosmotic slip, which grounds in the ion-permselectivity of the thin, but axially extending monolith skeleton (depending on macropore dimensions) and the induced CP is expected to develop better in the interskeleton macropores than in close packings of ion-permselective particles. In this respect, we have already noted that the monoliths show a different morphology. Further, due to their continuous skeleton, relatively extended CP zones (less confined than in a bed of discrete particles) penetrate the material like a spider web (Figure 4.9).

Employing packed beds and monolihts for separations in CEC, it is important to note that the induction of CP and its dependence on applied field (Figures 4.1-4.3 as well as Figures 4.10-4.12) and mobile phase ionic strength (Figures 4.5, 4.6 and 4.13) may have a strong impact on the retention of charged analytes as electroneutral analytes are generally insensitive for tracing CP (Figure 4.9a). These investigations have to include the migration and retention behaviour of electroneutral analytes with respect to charged analytes because the CP zones are the basic element of charge transfer between the quasi electroneutral macropore space and the ion-permselective intraparticle/intraskeleton pore space.

References

[1]   Nischang, I., Chen, G., Tallarek, U., *J. Chromatogr. A* 2006, *1109*, 32-50.

[2]   Helfferich, F., *Ion Exchange*, Dover Publications: New York, 1995.

[3]   Probstein, R. F., *Physicochemical Hydrodynamics*, Wiley: New York, 1994.

[4]   Sørensen, T. S., Ed. *Surface Chemistry and Electrochemistry of Membranes*, Marcel Dekker: New York, 1999.

[5]   Delgado, A. V., Ed. *Interfacial Electrokinetics and Electrophoresis*, Marcel Dekker: New York, 2002.

[6]   Mishchuk, N. A., Dukhin, S. S., In *Interfacial Electrokinetics and Electrophoresis*, Delgado, A. V., Ed., Marcel Dekker: New York, 2002, pp. 241-275.

[7]   Tallarek, U., Rapp, E., Sann, H., Reichl, U., Seidel-Morgenstern, A., *Langmuir* 2003, *19*, 4527-4531.

[8]   Chen, G., Tallarek, U., *Langmuir* 2003, *19*, 10901-10908.

[9]   Hidalgo-Álvarez, R., Martín, A., Fernández, A., Bastos, D., Martínez, F., de las Nieves, F. J., *Adv. Colloid Interface Sci.* 1996, *67*, 1-118.

[10]   Dukhin, S. S., *Adv. Colloid Interface Sci.* 1991, *35*, 173-196.

[11]   Barany, S., *Adv. Colloid Interface Sci.* 1998, *75*, 45-78.

[12]   Barany, S., Mishchuk, N. A., Prieve, D. C., *J. Colloid Interface Sci.* 1998, *207*, 240-250.

[13]   Ben, Y., Demekhin, E. A., Chang, H. C., *J. Colloid Interface Sci.* 2004, *276*, 483-497.

[14]   Mishchuk, N. A., Takhistov, P. V., *Colloids Surf. A* 1995, *95*, 119-131.

[15]   Svec, F., Frechet, J. M. J., *Ind. Eng. Chem. Res.* 1999, *38*, 34-48.

[16]   Tanaka, N., Kobayashi, H., Nakanishi, K., Minakuchi, H., Ishizuka, N., *Anal. Chem.* 2001, *73*, 420A-429A.

[17]   Leinweber, F. C., Lubda, D., Cabrera, K., Tallarek, U., *Anal. Chem.* 2002, *74*, 2470-2477.

[18]   Svec, F., Huber, C.G., *Anal. Chem.* 2006, *78*, 2100-2107.

[19]   Hilder, E.F., Svec, F., Frechet, J.M.J., *Electrophoresis* 2002, *23*, 3934-3953.

[20]   Svec, F., Peters, E.C., Sykora, D., Yu, C., Frechet, J.M.J., *J. High Resol. Chromatogr.* 2000, *23*, 3-18.

[21]   Rozing, G., *LC GC Europe*, 2003, *16*, 14-19.

[22]   Siouffi, A.-M., *J. Chromatogr. A* 2003, *1000*, 801-818.

[23]   Shi, Z., Feng, Y., Da, S. *J. Liq. Chromatogr. Rel. Technol.* 2003, *26*, 2881-2896.

[24]   Geiser, L., Mirgaldi, M., Veuthey, J.-L., *J. Chromatogr. A* 2005, *1068*, 75-81.

[25]   Cikalo, M. G., Bartle, K. D., Myers, P., *Anal. Chem.* 1999, *71*, 1820-1825.

[26]   Deyl, Z., Svec, F. (Eds.), *Capillary Electrochromatography*, Journal of Chromatography Library, Vol. 62, Elsevier, Amsterdam 2001.

5 Retention dynamics of charged analytes in electrochromatography

5.1 Key to analyte migration and retention in electrochromatography

5.1.1 Introduction

Besides having fundamental relevance for coupled mass and charge transport in CEC the CP phenomenon presents a unique mechanism by which the retention behaviour of charged analytes may be modulated directly by the applied field strength (in contrast to widely accepted theory), as well as the mobile phase ionic strength which influences EDL overlap and, thus, the charge-selectivity of the particles (Chapter 3 and Chapter 4) [1, 2]. Although the existence of CP has been shown with the electrochromatography of proteins in relatively early papers [3-5], this phenomenon is usually overlooked in CEC. At the same time, the retention of charged analytes has strongly puzzled chromatographers and still remains largely unresolved. Many groups have investigated this topic in the past [6-26]. It is often assumed that retention in CEC is composed of independent contributions from the chromatographic behavior in LC and electromigration in CZE which implies that the retention factor in electrochromatography does not depend on the field strength. While in a few cases an influence of applied voltage (other than due to the development of Joule heat) on the retention of charged analytes and discrepancies with the aforementioned picture of the retention factor have been reported, the physical mechanism responsible for this behaviour has been unknown. Instead, most investigations in CEC have focused on the influence of mobile phase composition (pH, ionic strength, percentage of organic modifier), but did not consider systematically analyte retention as a function of the applied field strength. This is surprising because electrical field strength is a major external control variable in any electrochromatographic or field-assisted operation.

In this chapter we demonstrate that CP is the key to understanding a fundamental and general, rather than exceptional electrical field-induced retention of counterionic analytes in CEC. For this purpose we employ fixed beds of porous cation-exchange particles and study the retention of small, single positively charged analytes depending on applied field and mobile phase ionic strengths. These investigations are complemented and their implications confirmed with CLSM studies, which can resolve CP and its operational domain on a particle scale in a packed bed. This is realized with a setup similar to our earlier investigations of "multiparticle effects" in Chapter 4 (Figure 3.4) [1]. Further, we use fixed beds of nonporous (impermeable, nonconducting) particles, which have already been demonstrated to show no sign of CP in Chapter 3 (Figures 3.12 and 3.14c) [2], and additionally fixed beds of bare-silica particles with different intraparticle pore sizes, but the same base chemistry. As analytes we used small neutral, as well as small single positively charged analytes of pharmaceutical relevance. They are behaving counterionic to the stationary phase and experience electromigration in the EOF direction. This choice of analytes appears useful to address a difference in the retention mechanism between charged and neutral analytes in CEC, because charged analytes are expected to participate in electrical field-induced CP.

5.1.2 Experimental Section

Chemicals and Materials. Sodium acetate, acetic acid, and HPLC grade acetonitrile came from Sigma-Aldrich Chemie (Taufkirchen, Germany). Ambroxol hydrochloride, lidocaine hydrochloride, papaverine hydrochloride, imipramine hydrochloride, nortriptyline hydrochloride, and caffeine were also purchased from Sigma-Aldrich Chemie, while toluene used as the EOF velocity marker and paracetamol came from Merck (Darmstadt, Germany).

Spherisorb SCX particles were the same as in Chapter 4 (nominal size: 5 μm, pore size: 10 nm) and were a gift from Waters (Milford, MA). Micra NPS particles (nominal size: 3 μm) were a gift from Bischoff (Leonberg, Germany). Nucleosil 100-5 and Nucleosil 4000-5 particles (nominal size: 5 μm, pore size: 10 nm and 400 nm, respectively) were purchased from Macherey-Nagel (Düren, Germany). Particles were packed in 50 μm i.d., 360 μm o.d. fused-silica capillaries from Polymicro Technologies (Phoenix, AZ) by an optimized slurry packing method described in Chapter 4.2, except for the bare silica particles, were packed bed fabrication was realized as in Chapter 3.2 and in analogy to [27]. In both cases duplex columns were created. A detection window was prepared directly behind the outlet frit. Columns had a similar length of the packed bed segment (240 mm) and total length (323 mm). They were assembled in a HP^{3D}CE capillary electrophoresis instrument (Agilent Technologies, Waldbronn, Germany). Detection was made at 210 nm and measurements were run at controlled temperature of 298 K. Both vials were pressurized at 10 bar for minimizing bubble formation.

Acetate buffer solutions in 80:20 acetonitrile/water (v/v) were used as electrolyte. The mobile phase was filtered over 0.45 μm nylon membrane filters and degassed by ultrasonication. An aqueous stock solution of 200 mM acetate was prepared with water purified on a Milli-Q-Gradient (Millipore, Eschborn, Germany). The pH was adjusted to 5.0 by titration with concentrated acetic acid. Next, appropriate volumes of this stock solution, Milli-Q water, and acetonitrile were mixed to yield acetate buffer solution of the desired ionic strength. Fresh samples were prepared on a daily basis by dissolving analytes directly in running mobile phase (60 μg/ml). For the CLSM studies background electrolyte contained 10^{-5} M of either of the following fluorescent dyes: BODIPY^{TM} 493/503 (electroneutral tracer) and BODIPY^{TM} disulfonate (twice negatively charged) from Molecular Probes (Leiden, The Netherlands), or positively charged Rhodamine 6G (Fluka, Taufkirchen, Germany). The setup for the CLSM studies is similar to the one described in Chapter 3 (Figure 3.4).

5.1.3 Results and Discussion

The primary goal of this work is to demonstrate and explain electrical field-dependent retention of counterionic analytes in CEC by means of the electrical field-induced CP (Chapter 4) [1]. For this purpose, Figure 5.1.1 shows representative electrochromatograms of the test mixture (three electroneutral and five positively charged analytes) obtained on the strong cation-exchange stationary phase. It is seen that the retention window for the positively charged, i.e., counterionic analytes is shifted (indicated by the red arrow) to longer times relative to that for the electroneutral analytes, while the applied voltage is increased from 2 kV (Figure 5.1.1a) to 26 kV (Figure 5.1.1b). At first glance this is a surprising result and difficult to explain because the counterionic analytes experience electromigration in the EOF direction. This observation forms the origin for our deeper investigations on the influence of applied field strength on the counterionic analytes migration and retention in CEC.
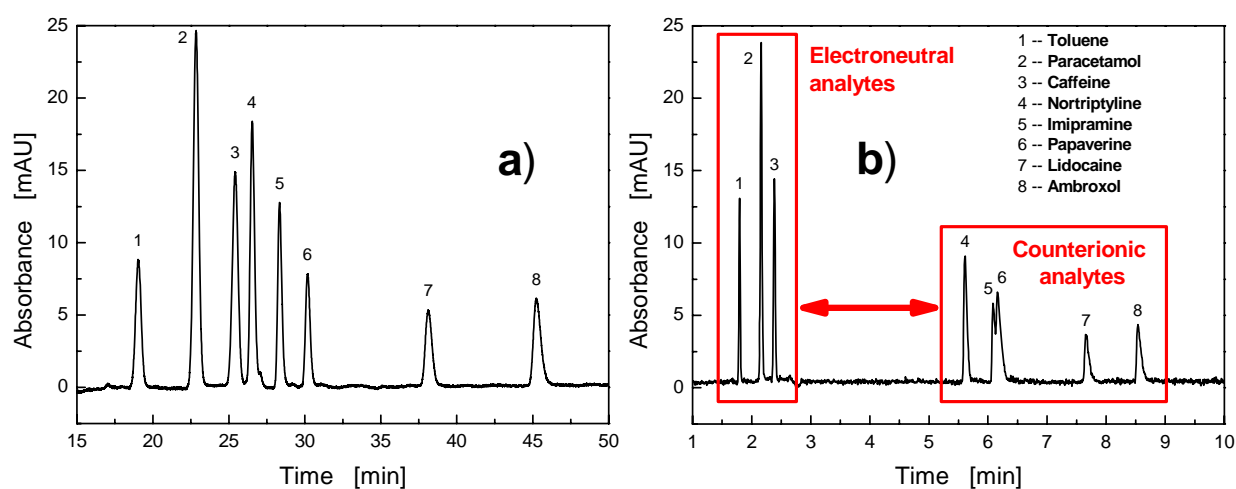
Figure 5.1.1 Representative electrochromatograms of the test mixture (containing three electroneutral and five counterionic analytes) for different applied voltages, a) 4 kV and b) 26 kV. Stationary phase: Spherisorb SCX particles (d_p = 5 µm, d_{intra} = 10 nm). Mobile phase ionic strength: 40 mM.

The dependence of residence times in the packed capillary on applied voltage (from 2 kV up to 30 kV) is reported in more detail by Figure 5.1.2. Considering different slopes in this plot for the two groups of counterionic and electroneutral analytes it is evident that the behaviour implied by Figure 5.1.1 develops systematically, i.e., at increasing field strength the residence time of the group of counterionic analytes is delayed with respect to the electroneutral analytes. In other words, the residence times of electroneutral analytes decrease faster than those of the counterionic analytes. It means that the retention factor in its classical definition k' = (t_r − t_0)/t_0 for counterionic analytes becomes a function of the

Figure 5.1.2 Dependence of residence times (t_r) in the packed capillary on applied voltage. Stationary phase: Spherisorb SCX particles. Mobile phase ionic strength: 4 mM.

applied field strength (where t_r is the residence time of a counterionic analyte and t_0 that of the flow field marker). This is demonstrated in Figure 5.1.3a. As the applied voltage is increased from 2 kV to

30 kV k' of the counterionic analytes increases by a factor of 3.5 to 4, while k' of the electroneutral analytes is constant within 1 %. This electrical field-independent behaviour of 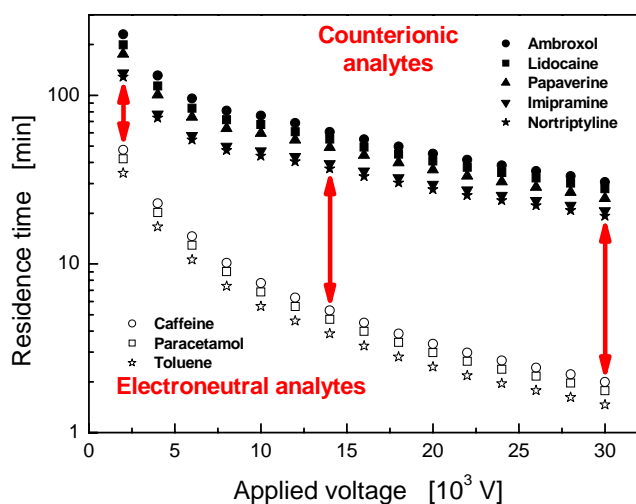neutral analytes is in agreement with expectations under isothermal conditions [28]. By contrast, the electrical field-dependence of k' is substantial and similar for all counterionic analytes, which are single positively charged. They display a range of molecular weights from 299.84 for nortryptiline to 416.56 for ambroxol. Yet it appears difficult to extract differences in their electrical-field dependent retention behaviour. Figure 5.1.3b shows that k' of the counterionic analytes (represented by lidocaine) decreases at increasing ionic strength, but retains its basic dependence on applied voltage.

Thus, Figure 5.1.3 reveals a clear electrical field-dependence of the retention factor for counterionic analytes. To explain the strong increase of k' at increasing field strength by electrical field-induced CP [1], we have to analyze closer the origin of this phenomenon in a capillary packed with strong cation-exchange particles. Their internal surface charge, together with the pore size of 10 nm and a typical Debye screening length (characterizing the EDL thickness) of the same order causes substantial EDL interaction on the intraparticle mesopore level (Chapters 2, 3 and 4) [2]. It leads to co-ion exclusion and counterion enrichment by a particle at electrochemical equilibrium (Figure 2.3) [29]. Further, this charge-selectivity depends on the mobile phase ionic strength as shown in Figure 4.5. For example, with an ionic strength sufficiently high that the EDL thickness is much smaller than the intraparticle pore size the pore fluid becomes quasi-electroneutral. Then, the intraparticle pore space is charge-nonselective and intraparticle ion concentration distributions resemble those in bulk solution [2].

Under most typical conditions, however, the intraparticle (meso)pore space is charge-selective [2] and significant CP is induced when an electrical field is superimposed (cf. Figure 4.1). In the present
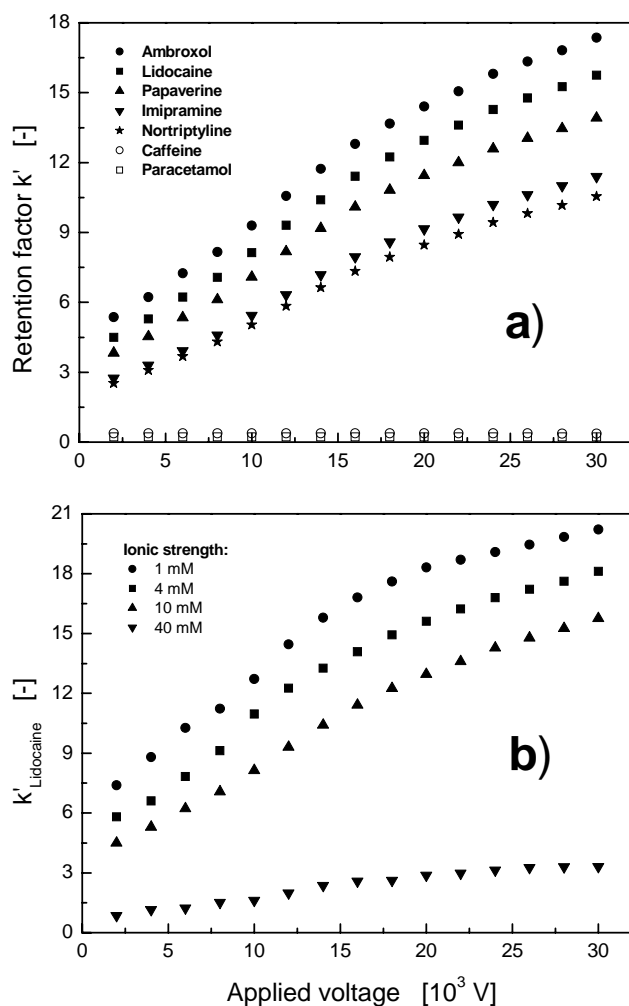

Figure 5.1.3 Dependence of the retention factor k' = $(t_r - t_0)/t_0$ on applied voltage. Stationary phase: Spherisorb SCX particles. a) Mobile phase ionic strength: 10 mM. b) Electrical field-dependence of k' for lidocaine at different ionic strengths. Toluene is used as t_0 marker.
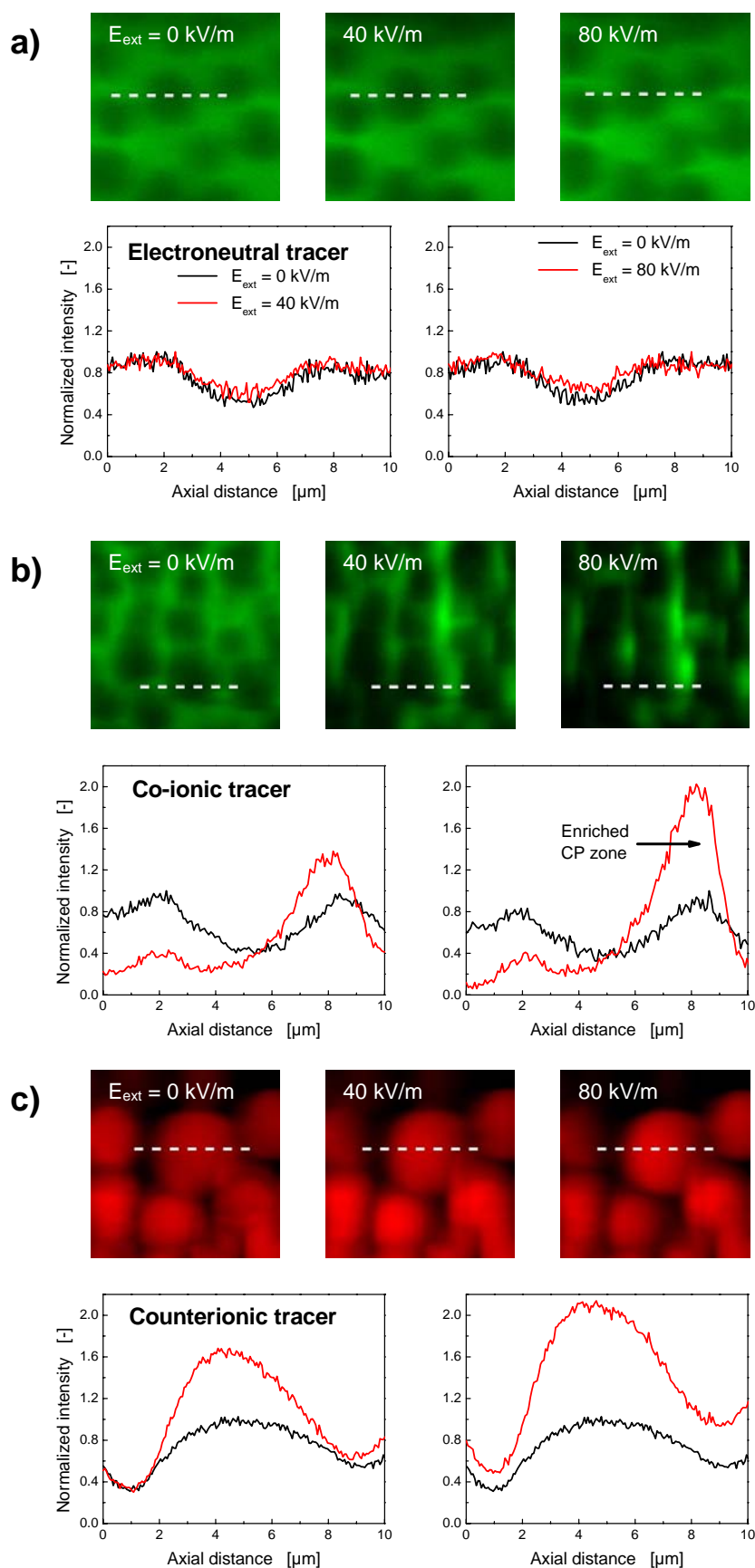
Figure 5.1.4 Visualisation of electrical field-induced CP in a packed 75 µm i.d. fused-silica capillary by CLSM (0.06 µm x 0.06 µm pixels in a slice of thickness 1 µm). Stationary phase: Spherisorb SCX particles (d_p = 5 µm, d_{intra} = 10 nm). Same mobile phase as employed in the CEC measurements; ionic strength: 4 mM. a) BODIPY[TM] (electroneutral tracer), b) BODIPY[TM] disulfonate (twice negatively charged), c) positively charged Rhodamine 6G. The stationary profiles were normalized with respect to electrochemical equilibrium.

example, sodium ions of the acetate buffer migrate from the interparticle macropore space into a cation-exchange (cation-selective) particle via its anodic hemisphere. Co-ions (acetate ions) migrate in opposite direction, away from a particles external anodic surface. This withdrawal cannot be compensated by the relatively few co-ions in the intraparticle mesopore space (which excludes co-ions due to the EDL overlap). Thus, the co-ion concentration decreases as a consequence of coupled mass and charge transfer normal to the charge-selective surface of a particle. To preserve local electroneutrality in the macropore space also the counterion concentration decreases (Figures 2.1, 2.2, and 2.3). The interplay of a particles charge-selectivity, the local electromigration, diffusion, as well as convection forms a depleted CP zone (convective-diffusion boundary layer) at the cation-exchange particles external anodic surface (anodic hemisphere). At its cathodic surface (cathodic hemisphere) the counterions leave a particle in the direction of the applied field. They are neutralized by co-ions which results in an enriched CP zone. These gradients in bulk electrolyte concentration around a charge-selective particle depend on the applied voltage, i.e., their steepness increases with the field strength (Figure 4.3). As a consequence, counterionic analytes which inherently participate in coupled mass and charge transport spend more time in the packed column relative to electroneutral analytes via these field-induced CP zones as their intensity is increased. Thus, k' increases with the applied field strength as shown in Figure 5.1.3. This explains how the external electrical field from a general point of view is able to tune the retention of counterionic analytes.

To provide a direct proof for the operation of electrical field-induced CP and its concrete influence on retention of counterionic analytes we have employed CLSM with the same packed capillary and mobile phase as in CEC (Figures 5.1.1–5.1.3). Electroneutral, co-ionic, and counterionic fluorescent tracers were used to address the fundamental differences in the transport behaviour of charged and electroneutral species. Stationary profiles of a respective tracer inside an ion-exchange particle of the packing and the adjoining interparticle fluid are shown in Figure 5.1.4 at different applied field strength (and at electrochemical equilibrium, E_{ext} = 0 kV/m). Figure 5.1.4a does not reveal changes in the distribution of electroneutral tracer upon the application of an electrical field. Its concentration is reduced inside the particle (with respect to the interparticle fluid) because of a particles porosity and abberation caused by refractive index mismatch between the particles solid and fluid saturating its pores. While a refractive index matching mobile phase can be used to minimize this optical artefact [1, 30] (Chapter 4), in the present context it appeared more illustrative to realize the same conditions in these microscopic CLSM as in the macroscopic CEC measurements.

The field-independent distribution of the electroneutral tracer seen in Figure 5.1.4a is not difficult to understand, this tracer is simply not involved in charge transport. By contrast, for the co-ionic tracer (Figure 5.1.4b) we reveal the induction by an applied field of regions with reduced and increased concentrations relative to electrochemical equilibrium. They represent the presence of the depleted and enriched CP zones, as well as a dependence of their intensity on applied field strength. For counterionic tracer (Figure 5.1.4c) we witness a significant increase of its intraparticle concentration at increasing field strength which reflects the increasing k' for counterionic analytes, demonstrated in Figure 5.1.3 from a macroscopic point of view. The main difference between co-ionic and counterionic

tracer is that the former is electrostatically excluded from a particle and the latter enriched at electrochemical equilibrium. The applied field then induces depleted and enriched CP zones around a particle (Figure 2.3). It stimulates an increased diffusive flux into a particle by the enriched zone. This results in locally increased intraparticle concentrations of both types of charged tracers with respect to electrochemical equilibrium [31], as evidenced by Figure 5.1.4. Thus, as a consequence of CP, the residence time of a charged analyte can be directly tuned with the applied electrical field and k' be manipulated accordingly (Figure 5.1.3). Electroneutral analytes cannot experience the field-dependent ion concentration gradients as they do not participate in any charge balance.
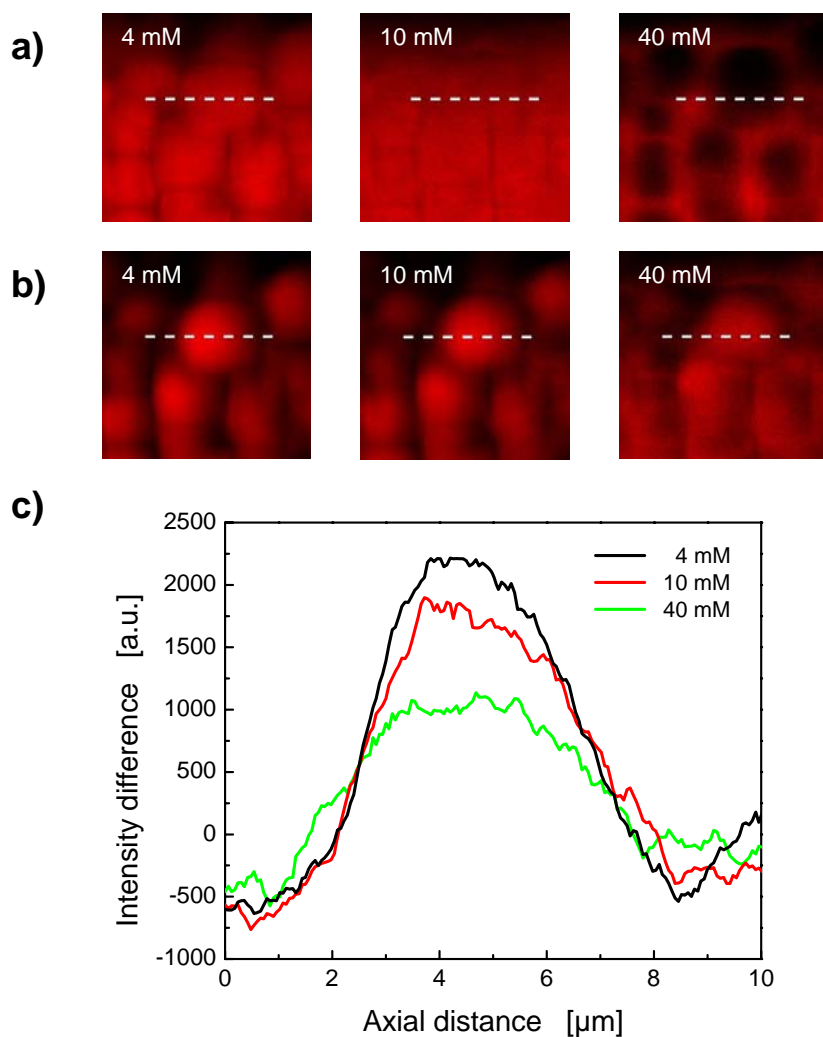
Figure 5.1.5 Visualisation of electrical field-induced CP in a packed 75 µm i.d. fused-silica capillary by CLSM (0.06 µm x 0.06 µm pixels in a slice of thickness 1 µm). Stationary phase: Spherisorb SCX particles (d_p = 5 µm, d_{intra} = 10 nm). Same mobile phase as employed in the CEC measurements, but with counterionic fluorescent tracer (Rhodamine 6G); ionic strength as indicated. a) Tracer distribution at electrochemical equilibrium (E_{ext} = 0 kV/m). b) Stationary distribution at E_{ext} = 40 kV/m. c) Profiles through a particle and the adjoining interparticle fluid (positions in the packing are indicated by the dashed lines), demonstrating for each ionic strength the intensity difference observed at E_{ext} = 40 kV/m with respect to electrochemical equilibrium.

While Figure 5.1.4 reveals the electrical field-dependence of CP in a packed bed of charge-selective adsorbent particles by CLSM, Figure 5.1.5 demonstrates the dependence on mobile phase ionic strength (at constant applied field strength). Increasing ionic strength reduces the charge-selectivity of

the particles by a better screening of their internal surface charge. In other words, the decreasing intraparticle EDL overlap (the EDL thickness decreases as the ionic strength increases) results in a reduction of counterion enrichment at electrochemical equilibrium which is illustrated in Figure 5.1.5a. As the electrical field is superimposed the decreased cation-selectivity of the particles results in a reduced intensity of the field-induced CP phenomenon, i.e., in weaker concentration gradients in the depleted and enriched CP zones (cf. Figure 4.5). This, in turn, stimulates a smaller diffusive backflux into a particle from the enriched CP zone with respect to electrochemical equilibrium which is seen in the fluorescence profiles (Figure 5.1.5c). Thus, as the mobile phase ionic strength is increased, the reduced charge-selectivity of the particles at constant field strength leads to an attenuation of the CP zones which, therefore, become less intense hold-up ("trapping") regions for the counterionic with respect to electroneutral analytes. Consequently, in addition to classical ion-exchange behaviour, also this ionic strength dependence of CP contributes to the trend in Figure 5.1.3b. In general, the functional dependence of retention on ionic strength observed in ion-exchange liquid chromatography will become modulated for its electrochromatographic variant by the field-induced CP.

To summarize, the macroscopic CEC data in Figure 5.1.3 have been illuminated microscopically by CLSM and shown to reflect CP and its dependence on the applied field strength (Figure 5.1.4) and ionic strength of the bulk fluid (Figure 5.1.5). These comprehensive data and their conclusions can be complemented by the following two simple series of CEC measurements. The first one employs porous particles with i) small and ii) large intraparticle pores with respect to the actual EDL thickness. Thus, while intraparticle EDL overlap, charge-selectivity, and the electrical field-induced CP effects on analyte retention should be significant with the small pores, they are assumed to become unimportant with large enough pores (see Figures 3.14a and 3.14b). The second measurement series employs nonporous (impermeable, nonconducting) particles which should not demonstrate electrical field-induced analyte retention in CEC, because hard spheres simply have no charge-selective intraparticle pore space and, thus, no capability of imparting charge-selective transport behaviour, the prerequisite for observing CP in an applied electrical field (Figure 3.14c).

Figure 5.1.6 demonstrates a favourable agreement between the electrical field-(in)dependent retention data (here collected for lidocaine and nortriptyline) and expectations based on a scaling of CP in the employed fixed beds. In particular, we observe a linear dependence of k' on the applied field strength (Figure 5.1.6a) with the bare-silica particles having small intraparticle pores ($d_{intra} = 10$ nm), while this clear electrical field-dependence of k' indeed disappears with the large-pore particles ($d_{intra} = 400$ nm). Also with the nonporous bare-silica particles (Figure 5.1.6b) we cannot reveal a significant electrical field-dependence of analyte retention, for example, k' of nortriptyline increases marginally from –0.35 at 2 kV applied voltage to –0.32 at 30 kV. Thus, the data in Figure 5.1.6 for the porous ($d_{intra} = 10$ nm and 400 nm) and nonporous bare-silica particles complement retention behaviour observed with the strong cation-exchange particles ($d_{intra} = 10$ nm) in Figure 5.1.3, as well as implications of the CLSM studies (Figures 5.1.4 and 5.1.5). As porous particles are charge-selective due to intraparticle EDL overlap ($d_{intra} = 10$ nm) significant CP is electrokinetically induced in the interparticle macropore space. The intensity of the (depleted and enriched) CP zones depends on the applied field and mobile phase

ionic strengths. This introduces a fundamental electrical field-dependence of k' for the charged analytes. On the other hand, as the porous particles become charge non-selective due to the vanishing intraparticle EDL overlap (d_{intra} = 400 nm), or because they are simply nonporous (impermeable for fluid and electrically nonconducting), this kind of CP cannot be induced by the applied field. Than, k' for the charged analytes (under isothermal conditions) is independent of the electrical field strength.
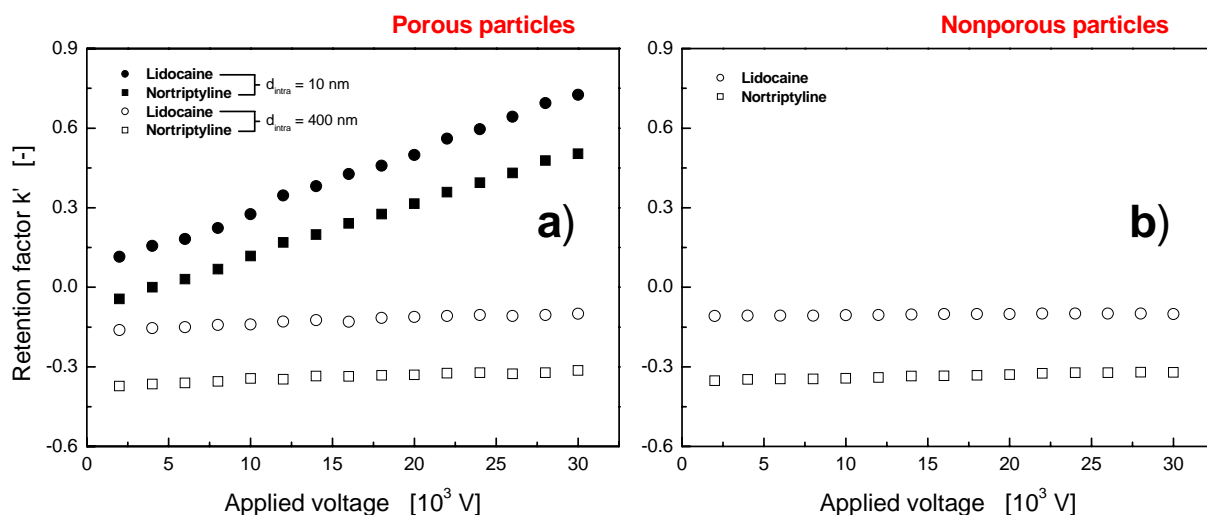

Figure 5.1.6 Dependence of the retention factor on applied voltage. Mobile phase ionic strength: 1 mM. Stationary phases: a) Nucleosil bare-silica particles (d_p = 5 µm, d_{intra} = 10 nm or 400 nm), and b) Micra NPS particles (d_p = 3 µm).

With the comprehensive chromatographic (Figures 5.1.3 and 5.1.6) and microscopic (Figures 5.1.4 and 5.1.5) data on the existence and operational domain of CP at hand it is illustrative to review some related work in the literature. The purpose of this analysis is to show that many results can be better understood in a context of the electrical field-induced CP. It is neither a complete, nor a quantitative analysis of data. With the selected examples we intend to bring more attention to this phenomenon which features a general importance in electrochromatography. For example, the significant increase of k' with applied field strength similar to this work (see Figure 5.1.3a), but for acidic compounds in strong anion-exchange CEC [12] can be easily explained by CP, it can also contribute to the field-induced variation of the capacity factor observed by Kitagawa et al. [10] and provides a general physical basis for redistribution of charged analyte on the scale of a single ion-exchange particle of the packing (including adjacent CP zones) in dependence of the applied field strength. Thus, when experiencing CP it is not surprising that retention in CEC cannot be adequately reconstructed by simply using chromatographic retention from LC and electromigration from CZE experiments [25] or that, at least, some (field-dependent) inconsistencies remain. Finally, in their pioneering work with a size-exclusion electrochromatography system Rudge et al. [3] have shown that the migration rates of large co-ionic proteins decreased (i.e., they were retained stronger) at increasing electrical field strength. For example, even though the convective (mostly due to hydraulic flow) and electrophoretic velocities acted in the same direction, bovine hemoglobin demonstrated an electrochromatographic velocity that was lower than the convective velocity, and decreased with increasing field strength [4]. In the context of the present work such co-ionic analytes which are size-excluded from the charge-

selective particles present a special case. Like any co-ionic analyte involved in coupled mass and charge transport in porous media, irrespective of its size, these analytes get electrostatically trapped in the enriched CP zones which depend on the applied field strength [1, 31]. In addition, because large proteins are size-excluded from the particles they will be held there (against backdiffusion) by the electrical field which itself penetrates the intraparticle pore space. Size-exclusion of charged analytes is no prerequisite for experiencing CP and the electrical field-modulated retention, but as a co-ionic analyte becomes size-excluded from the charge-selective particles the influence of electrical fields on its retention is aggravated due to this steric effect [3-5, 32].

5.1.4 Conclusions

This work has revealed an inherent electrical field-dependence of the retention factor for small counterionic analytes under rather typical electrochromatographic conditions (Figure 5.1.3). All analytes throughout are single charged in nature and they display a mass to charge ratio from 299.84 for nortryptiline to 414.56 for ambroxol. It has been demonstrated by microscopic CLSM measurements (Figures 5.1.4 and 5.1.5) and macroscopic CEC studies (Figure 5.1.6) that such a dependence is caused by the electrical field-induced CP. This phenomenon develops due to coupled mass and charge transport normal to charge-selective interfaces which are unique to electrochromatographic applications employing fixed beds of porous particles. Strong EDL overlap prevailing over a wide range of experimental conditions in relatively small, but typical intraparticle pores ($d_{intra} \approx 10$ nm) makes the particles charge-selective. It causes co-ion exclusion and counterion enrichment at electrochemical equilibrium. For example, it was shown in Chapter 3 that with mesoporous particles mobile phase ionic strengths on the order of 100 mM (see Chapter 3, Figure 3.6b) or higher are necessary for removing their charge-selectivity [2]. Due to a significant charge-selectivity under common conditions a superimposed electrical field induces depleted and enriched CP zones in the background electrolyte around the particles (Chapter 4.3.1). The intensity of these CP zones depends on the field strength and charge-selectivity of the particles, i.e., on surface charge density, pore sizes, and the mobile phase ionic strength. For example, as the field strength is increased the electrolyte concentration gradients in the CP zones become more intense (Figure 4.1). This explains the electrical field-dependence of the retention factor for charged analytes which participate in coupled mass and charge transport through the material (and the CP zones). Thus, at increasing field strength charged relative to electroneutral analytes reside longer on a particle scale via the CP zones and k' increases. By contrast, k' becomes field-independent (under isothermal conditions) in a packed bed of porous particles as their charge-selectivity disappears and CP cannot be induced by the applied field. It has been clearly demonstrated in this work (Figure 5.1.6) that this is the case with sufficiently large intraparticle pores and/or high mobile phase ionic strength, as well as for a bed of nonporous particles.

Under most general conditions in electrochromatography the retention factor of charged analytes must be considered as a field-dependent parameter. This can explain why retention data measured in similar systems, but at different field strength can differ significantly (Figure 5.1.3) and may have contributed artificially to an apparent unreproducibility in CEC practice. It also implies that the approach adopted in the literature by which retention in CEC is synthesized from chromatographic retention in LC and electromigration in CZE must be questioned as it assumes that the retention factor in CEC does not depend on the applied field strength. In other words, relevant transport through the field-dependent CP zones in a packed column is incorrectly removed by an open-tubular CZE experiment which itself provides a field-independent mobility. Finally, because the CP zones stand for conductivity gradients which develop on a particle-scale (cf. Figure 4.1), throughout the whole packed bed, the dynamics in these zones is expected to contribute also to an intrinsic zone sharpening in CEC.

It is concluded that CP, which represents field-induced dynamic changes in the local distribution of ionic species in hierarchically-structured materials, has severe consequences for coupled mass and charge transport behaviour observed on a macroscopic scale. This includes not only analyte retention, but also zone spreading. With relevance to these phenomena CP becomes the key to understanding CEC.

With respect to these findings, in Chapter 5.2 we investigate the retention dynamics of peptides with beds of strong SCX-particles, both in LC and CEC. These peptides display more pronounced differences in molecular mass and also charge than the analytes employed in this study. Further, we vary the pH of the mobile phase influencing the charged state of the peptides. In contrast to LC, electrolyte ionic strength in CEC not only reduces electrostatic interactions with the charged stationary phase, but also changes the intensity of electrical field induced CP developing in the whole material (Figures 4.6 and 5.1.5) by modulating the particles charge selectivity. This behaviour is systematically investigated in the following chapter and resolves the retention dynamics in LC with respect to the retention dynamics in CEC under consideration of the physicochemical parameters of the different peptides and with respect to developing CP.

5.2 Tuning retention and selectivity of peptides in electrochromatography

5.2.1 Introduction

In recent decades CEC has been proposed to gain increasing importance as a micro high performance liquid separation technique for the separation of peptides and proteins, mostly by investigating practical aspects [33]. It is often considered as being a hybrid of CZE and LC [34, 35]. It offers separation efficiencies that are sometimes better than in LC. Generally it may enable modulation of selectivity and sample capacity like in LC [35]. The use of silica-based stationary phases with reversed phase properties is a well established technique at medium and basic mobile phase pH [36], but suffers from suppressed EOF at lower pH values. Thus for low mobile phase pH applications ion-exchangers on silica-based materials have been successfully developed and employed for the separation of basic solutes at sufficient EOF velocity [36]. Substantial EOF velocity is crucial for any standalone electrochromatographic system.

CEC retention is often assumed to be composed of independent contributions from the chromatographic behaviour in LC and electromigration in CZE and relatively simple models using chromatographic and electrophoretic formalisms have been developed [11, 14, 22]. These models throughout imply that the retention factor in electrochromatography is independent of the applied voltage. Such dependencies may of course have been overlooked if the retention of peptides is studied at a specific (constant) field strength by, i) variation of the organic modifier content modulating hydrophobic/hydrophilic interactions with the stationary phase, and ii) by background electrolyte ionic strength to investigate the (pure) ion exchange mechanism. Nevertheless studies on peptide retention are still very rare in the literature and it appears that CEC is hard to handle for the analysis of more complex molecules. The most systematic studies on peptide retention in CEC have been reviewed recently in a minireview by Walhagen et al. [37] and have been highlighted by a set of quite complicated equations describing the retention factor in CEC including, impact of the sorbent surface chemistry and selectivity options for the separation of peptides (pH, ion-pairing, sorbent surface). It was specifically concluded in this review that separations of peptides in CEC depend on an interplay between i) electrostatic interactions (modulated by the ionic strength of background buffer electrolyte), ii) hydrophobic interactions (content of organic modifier, e.g. acetonitrile), and iii) electrophoretic mobility [37]. The reviewed pioneering works have been often adapted also for the discussion of peptide separation in ion-exchange CEC. Separation of small peptides has been recently realized by Ye et al. [12], especially also in comparison to CZE to stress the selectivity and retention order aspect, including also the ionic strength dependence of peptide retention at one selected voltage. Fu et al. [20] recently studied hydrophilic interaction CEC employing very high ionic strength sacrificing reasonable elution time for the employed strong cation-exchange type of stationary phase and also investigated the ionic strength dependence of peptide retention. In another example, Zhang et al. [14] have studied peptide retention in weak cation-exchange CEC and extracted the LC retention factor under the assumption that electrophoretic mobility is (only) affected by the porous nature of the sorbents, i.e. it is influenced by the tortuous flow path and the restricted diffusivity in the stationary phase. Consequently the peptide mobility estimated by a CZE experiment (which by itself shows field independent mobilities) has been translated to a mobility in the

column by a correction factor, which lumps together effect of column structure and mobile phase modulator such as commonly used salt and organic solvent [14]. We have seen in Chapter 5.1 that such assumptions may lead to severe misinterpretations, since this approach does not explain any field strength dependence of analyte retention. Further the authors did not confirm the validity of extracted LC retention from CEC retention through experiment. To stress again throughout these studies no electrical-field dependence of the retention dynamics have been addressed nor systematically investigated.

Just in a few cases an influence of applied voltage (other than due to the development of Joule heat) on the retention of charged analytes (including peptides) and discrepancies with the aforementioned simple picture of the retention factor have been reported [23, 25, 38], especially when employing ion-exchange types of stationary phases. In particular, in a very recent publication on the separation of oostatic peptides with a strong SCX stationary phase an increase in retention of peptides with increasing electrical field strength has been observed [39]. The peptides throughout were all weakly charged. In Chapter 5.1 retention of small single positively charged analytes has been systematically studied and revealed an increase in their retention factor with increasing applied voltage.

Concluding from the previous chapters, it is important to note that in comparison to LC-based ion-exchange chromatography the coupled mass and charge transport in CEC becomes even more complex due to electrical-field induced CP [1, 2, 40, 41]. It was shown that in a dense packing (in comparison to a single particle dynamics, e.g. Figure 2.3) the CP zones from neighbouring particles interfere with each other, leading to a more complex pattern concerning the morphology of the material with respect to developing CP ("interconnected mountains and valleys") by a complex interplay of the (local) electrokinetics and hydrodynamics [1] (Figures 4.1 and 4.4). Nevertheless electrical-field-induced concentration polarisation has been clearly proved to share common features in these hierarchically structured porous media (packed beds, monoliths) by showing, i) a clear dependence on applied voltage (Figures 4.1-4.3), and ii) electrolyte ionic strength (Figures 4.5 and 4.6), which were reflected in the increasing retention behaviour of the single charged counterionic species traversing these field dependent concentration gradients, which are not recognized by neutral analytes (Figures 5.1.3 and 5.1.4).

Usually a peptide molecule contains both acidic and basic residues and thus its net charge is pH dependent. At some intermediate pH the net charge may be zero, then the peptide is at its isoelectric point (pI). Generally, the pI is dependent on the type of amino acids and molecular structure of the peptide molecule. As a peptide can carry net positive, zero or negative charge (characterized by a pH titration curve), the so called "net charge concept" has been used for predicting retention behaviour in ion-exchange media. Nevertheless this concept may fail short. Even though net charge of a peptide may be zero it does not mean that the respective peptide is devoid of charge [42]. Data in the literature show that distribution of the charge may be important regarding the interaction with the charged stationary phase and thus retention on ion-exchange columns even at the pI. It also implies that the number of charges interacting with the charged stationary phase at any pH can either be greater or less than the estimated net charge [42]. In contrast, for CZE the net charge concept may be more useful for prediction of migration behaviour. Electrophoretic mobility at the respective pI usually tends to be zero [43].

With respect to our previous studies (Chapter 5.1) this chapter investigates the migration and retention behaviour of peptides in strong cation-exchange CEC at two selected pH values i) by investigation of LC retention in dependence of ionic strength of the background electrolyte, ii) by determination of electrophoretic mobilities of the peptides as indicator for their electromigration behaviour (CZE), and iii) by investigating CEC retention in dependence of both electrolyte ionic strength and applied field strength. These investigations appear necessary because electrical-field-induced CP may be obscuring the before mentioned contributions (ion-exchange mechanism and electrophoretic mobility) to the retention behaviour of peptides as any CP may also be responsible for adjustment of pore-level concentrations (e.g. Figure 4.2) of charged counterionic analytes and thus their retention behaviour in CEC.

It is then important to understand the physicochemical origins of peptide and protein retention in CEC but also related electrical-field-assisted processes, as any influence on CP potentially modifies charged analyte retention (Chapter 5.1), which yet is to be investigated for different peptides having different charge numbers and molecular mass (diffusion coefficient). It is shown that these parameters are important for relative contributions in competitive charge transport between the background electrolyte counter-ion and the peptides of variable charge both in the intraparticle pore space and adjoining depleted CP zone. It may describe the dependence of peptide retention in CEC on the applied electrical field strength in a regime where a transition occurs from intraparticle to (extraparticle) boundary layer-dominated transport behavior on the single-particle scale in the fixed bed (Figures 2.1 and 4.3), with each regime being different in nature regarding the transport dynamics of charged species. The reported behavior in this chapter demonstrates that peptide charge determines its complex migration behaviour from a principal point of view, and within this behaviour it becomes modulated by the molecular mass (diffusion coefficient).

5.2.2 Experimental Section

Chemicals and Materials. Sodium phosphate dibasic (Na_2HPO_4), sodium phosphate monobasic (NaH_2PO_4) and HPLC grade acetonitrile came from Sigma-Aldrich Chemie (Taufkirchen, Germany). [Met5]Enkephaline, Oxytocine, Luteinizing hormone releasing hormone (LHRH) and [Arg8]Vasopressine (all as acetate salts) were also purchased from Sigma-Aldrich Chemie, while toluene used as the EOF velocity marker came from Merck (Darmstadt, Germany).

Spherisorb SCX particles (nominal size, d_p = 3 µm, intraparticle pore size, d_{intra} = 10 nm) were a research gift from Waters (Milford, MA) and had similar physical properties as the SCX particles used in Chapter 4. Because of their strong ion-exchange capacity peptides are strongly retarded and thus higher ionic strength of the background electrolyte is necessary to adjust for a reasonable elution time. In order to keep thermal effects as small as possible, particles were packed in only 30 µm i.d., 360 µm o.d. fused-silica capillaries from Polymicro Technologies (Phoenix, AZ) by the optimized slurry packing method described in Chapter 4, which creates duplex columns. A detection window was prepared directly behind the outlet frit. Columns had a packed bed segment length of 83 mm and total length of 323 mm. Electrophoretic mobilities of the peptides were determined with PVA-coated capillaries purchased from Agilent Technologies (Waldbronn, Germany) employing the same buffer solutions as in the electrochromatographic studies.

Phosphate buffer solutions in 60:40 acetonitrile/water (v/v) were used as electrolyte. The mobile phase was filtered over 0.45 µm nylon membrane filters and degassed by ultrasonication. Aqueous stock solutions of 500 mM phosphate, with pH = 2.7 and 7.0 (to modulate respective peptide charge) were prepared with water purified on a Milli-Q-Gradient (Millipore, Eschborn, Germany). The pH was adjusted to the desired value by mixing appropriate quantities of Na_2HPO_4 and NaH_2PO_4. Next, appropriate volumes of this stock solution, Milli-Q water, and acetonitrile were mixed to yield phosphate buffer solutions of the desired ionic strength. Fresh samples were prepared on a daily basis by mixing appropriate buffer solutions with the analytes such that the composition was identical to that of the running mobile phase (with an effective analyte concentration of 0.75 mM).

Capillary columns were assembled in a HP[3D]CE capillary electrophoresis instrument (Agilent Technologies, Waldbronn, Germany). Detection was made at 210 nm and measurements were run at controlled temperature of 298 K. Both vials were pressurized at 10 bar for minimizing bubble formation. LC was also performed with the HP[3D]CE instrument using the available helium gas pressure. For that case the same column as in CEC was used with an inlet pressure of 10 bar. The use of the HP[3D]CE for the LC experiments has the advantage of realizing an identical system environment as in CEC with reproducible injection and without extra-column band broadening. This also facilitates a comparison of separation performance in LC and CEC, but also the determination of the respective capacity factors under the influence of the different driving forces [2].

5.2.3 Results and Discussion

EOF velocity. To demonstrate the EOF behaviour we have recorded EOF velocities inside the packed capillaries in dependence of phosphate buffer concentration ranging from 10 mM up to 60 mM and an applied voltage ranging from 0 to 30 kV over the duplex column. As shown in Figure 5.2.1a, we can retrieve a relatively common trend insofar as the EOF velocity (u_{eo}) increases with decreasing ionic strength of the solution to approach a maximum value at 10 mM ionic strength. A continuous decrease of u_{eo} with increasing ionic strength is explainable by the "normal" or "conventional" EDL behaviour [44] (Chapter 1, Figure 1.6). As ionic strength increases the EDL is compressed resulting in a reduced shear-plane potential at the solid-liquid interface. Important to note is that thermal effects seem to be almost entirely negligible (see Figure 5.2.1b) for the studied system and may explain the slight nonlinearity with the higher ionic strength (Figure 5.2.1a), i.e. a plot of EOF velocity against current revealed a linear behaviour (data not shown). For lower ionic strength a distinct even stronger nonlinearity than for the higher ionic strength is discernable that cannot be explained by a nonlinear electrical current, i.e. a significantly nonlinear velocity-current relation was obtained (similar to Figure 3.9b) [2]. This has to be attributed to electrical field-induced CP and related nonequilibrium electroosmosis, which has been extensively studied and described in the present thesis (Chapters 3 and 4) [1, 2, 44, 45].
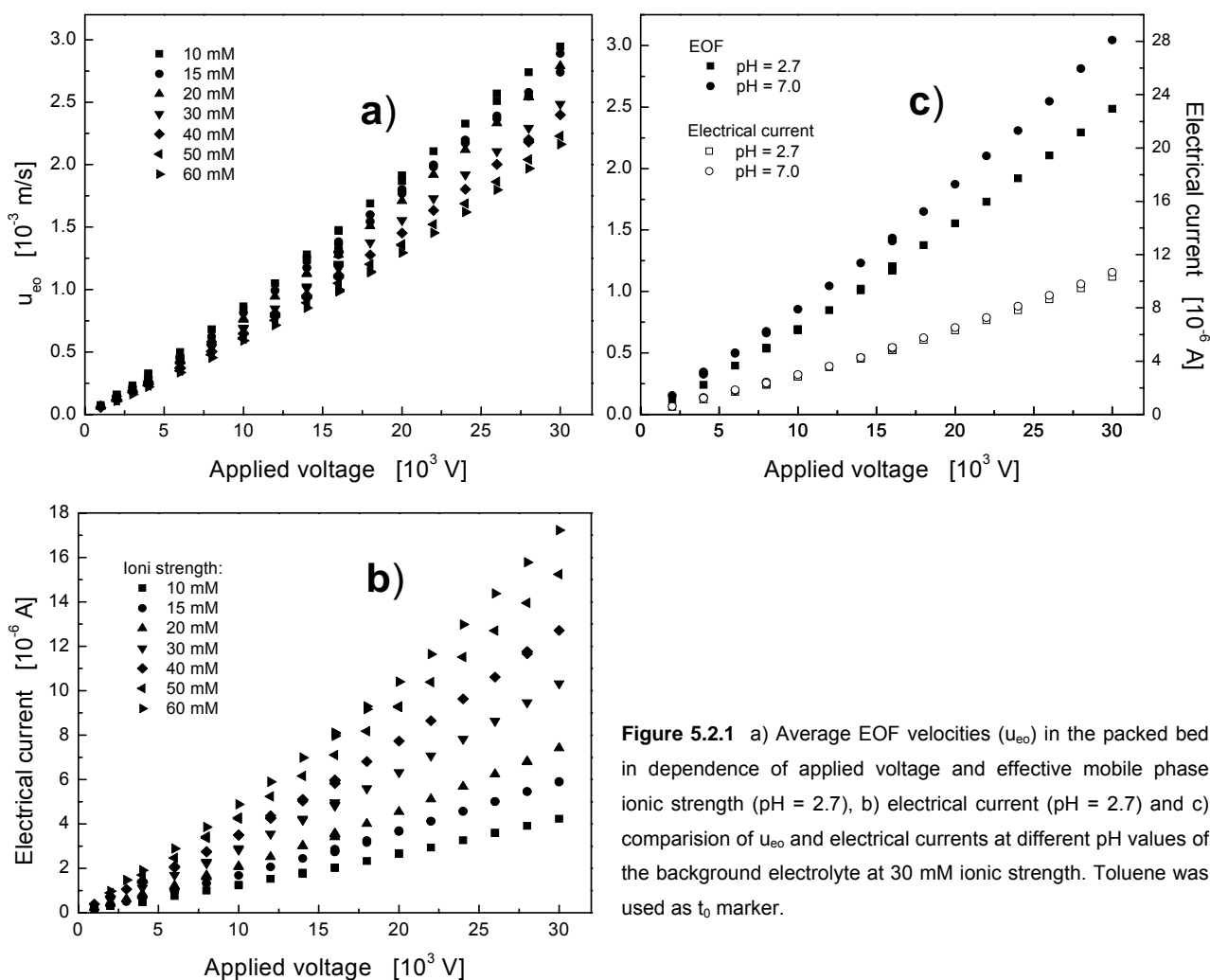

Figure 5.2.1 a) Average EOF velocities (u_{eo}) in the packed bed in dependence of applied voltage and effective mobile phase ionic strength (pH = 2.7), b) electrical current (pH = 2.7) and c) comparision of u_{eo} and electrical currents at different pH values of the background electrolyte at 30 mM ionic strength. Toluene was used as t_0 marker.

Increasing the pH of the background electrolyte results in increasing dissociation of residual silanol groups of the stationary phase, resulting in slightly higher u_{eo}, even though the electrical current at the same ionic strength is almost identical (Figure 5.2.1c) [36].

Peptide properties. With respect to the previous chapter the main goal of this work is to demonstrate the electrical field strength dependence of the retention dynamics of peptides due to electrical field-induced CP. Table 5.2.1 shows the properties of the four model peptides studied at the different pH values of the mobile phase. Important to note is that all peptides have a positive net charge at pH = 2.7. The net charge of all peptides is significantly reduced at pH = 7.0. The dependence of mobility on pH showed the expected change with respect to data in the literature using pure aqueous mobile phase [46].

Table 5.2.1

Properties of the used model peptides

Peptide	Mass	No. of residues	Net charge/No. of charge interactions[1] [-]		μ_{ep} [10^{-9} m^2/Vs] (Var %)	
			pH = 2.7	pH = 7	pH = 2.7	pH = 7
[Met5]Enkephaline	573.66	5	+0.56/+0.72	≈0/n.d.	0.84 (0.50)	n.d.
Oxytocine	1007.19	9	+1 /+0.84	+0.24/n.d.	0.85 (0.43)	0.02 (0.15)
LHRH	1183.27	10	+2/+1.82	+1.48/n.d.	1.22 (0.44)	0.71 (0.44)
[Arg8]Vasopressine	1084.23	9	+2/+1.80	+1.24/n.d.	1.33 (0.82)	0.75 (0.09)

[1]Number of charge interactions of the peptides with the surface of the strong cation-exchange column where determined in LC according to the approach of Kopaciewicz et al. [42]. Note that the number of charges interacting with the surface may be greater or less than the net charge, but appears to be a useful estimate to evaluate or approach the net charge at pH = 2.7.

Most important for our study is that Oxytocine and [Arg8]Vasopressine differ only in one amino acid residue that increases the net charge of [Arg8]Vasopressine. Further they are structurally related by sharing the same disulfide bridge, constraining the conformation of the molecule. Thus they have a similar hydrophobicity and similar size at pH = 2.7 [47]. The elution order of the peptides in CZE extracted from the mobility data shown in Table 5.2.1 is that observed in CZE using aqueous phosphate buffer with a pH of approximately pH = 2.5 (cf. technical bulletin for P2693 from Sigma, http://www.sigmaaldrich.com/sigma/ datasheet/p2693dat.pdf). At pH = 7.0 the relevant amino group is deprotonated resulting in a decrease of the net charge for all peptides. Interestingly, [Arg8]Vasopressine shows a similar electrophoretic mobility at pH = 7.0 as Oxytocine at pH = 2.7. (Table 5.2.1). Its electrophoretic mobility is slightly reduced, because of its sligthly higher mass and slightly different charge.

Retention dynamics.   The primary focus of this work is to demonstrate and elucidate electrical-field-dependent retention of peptides in CEC by means of the electrical-field-induced CP [1, 2, 38]. For this purpose, four model peptides have been employed all bearing positive net charges at pH = 2.7. Figure 5.2.2 shows a typical separation with 60 mM phosphate and an applied voltage of either 4 kV or 30 kV. While at a relatively low applied voltage [Met5]Enkephaline (by accident) nearly coelutes with the EOF, it experiences significant retention at an applied voltage of 30 kV. Generally both, [Met5]Enkephaline and Oxytocine appear to experience an increased retention at higher voltages, while LHRH and [Arg8]Vasopressine appear to experience a lower retention at the higher voltage. A systematic study of the retention factor in its classical

definition with $k' = (t_r - t_0)/t_0$ (where t_r is the residence time of the peptide and t_0 that of the flow field marker) revealed that the increase in retention for [Met5]Enkephaline and Oxytocine, but also the decrease in retention of LHRH and [Arg8]Vasopressine systematically depends on applied voltage. All four peptides (bearing a net positive charge) showed a systematic dependence on the applied voltage (Figure 5.2.3). The retention window for [Met5]Enkephaline and Oxytocine is shifted to longer times relative to that for the EOF velocity marker (reflecting an increasing k' value), while the retention window of the twice positively charged peptides is shifted to shorter times relative to that of the EOF velocity marker (reflected by decreasing k') with
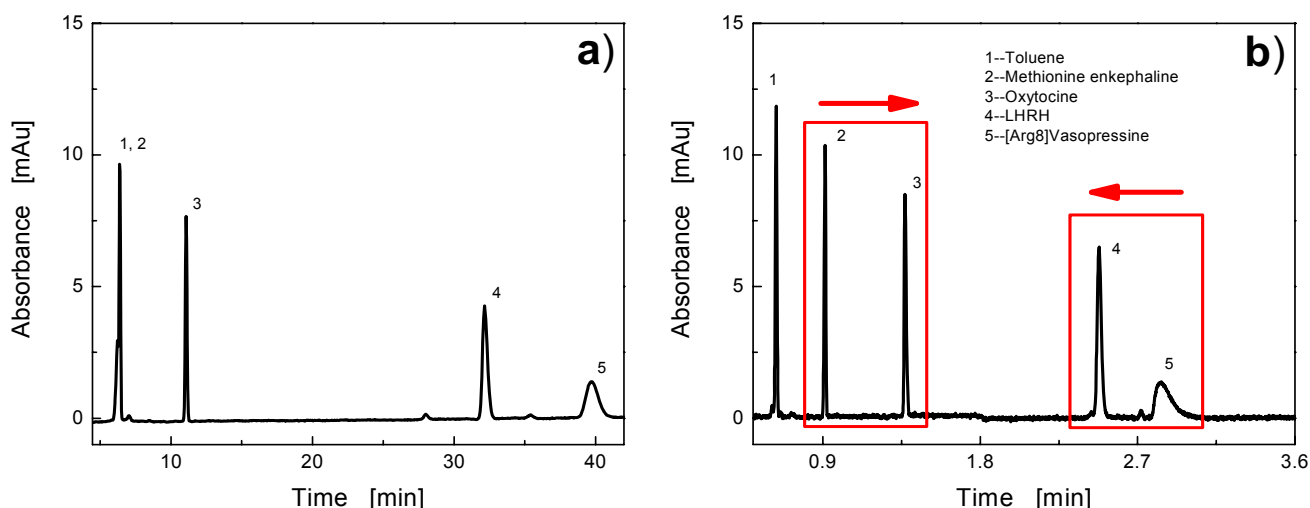
Figure 5.2.2 Representative electrochromatograms of the test mixture, containing four model peptides (see Table 5.2.1 for details) at different applied voltages, a) 4 kV and b) 30 kV. Mobile phase ionic strength: 60 mM (pH = 2.7).
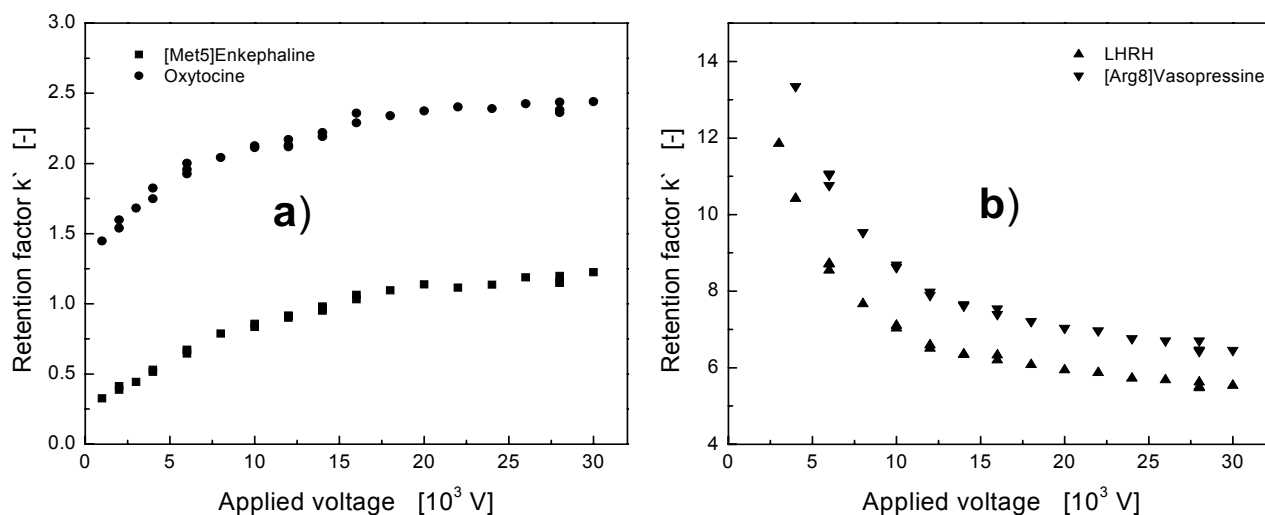
Figure 5.2.3 Dependence of the retention factor $k' = (t_r - t_0)/t_0$ on applied voltage at a mobile phase ionic strength of 30 mM (pH = 2.7).

increasing applied voltage. At first glance this is a surprising result. The only difference appears to be the charge number of the respective peptides, because Oxytocine has a similar molecular weight and size as [Arg8]Vasopressine, but in contrast to the latter is increasingly retarded with increasing voltage (see Table 5.2.1 and Figure 5.2.3). The shift of [Met5]Enkephaline and Oxytocine to higher retention times has been similarly observed in a study of counterionic, single positively charged pharmaceutical compounds and thus reflects the studies presented in Chapter 5.1 [38]. The electrical-field-dependence of k' is substantial for [Met5]Enkephaline and Oxytocine, which also at the same time differ significantly in mass and charge (Table

5.2.1 and Figure 5.2.3a for a mobile phase of pH = 2.7). These differences may be reflected in the different slopes of k' at very low voltages, for example, Oxytocine with a higher molecular mass shows a stronger dependence on applied voltage. For LHRH and [Arg8]Vasopressine the decrease in retention appears to be similar, the curves in Figure 5.2.3b seem to be only shifted by a factor over the whole range of applied voltages. Their similar behaviour may be due to their similar mass and charge under these conditions (Table 5.2.1 for pH = 2.7, Figure 5.2.3b). In all four cases retention approaches an asymptotic value at the utmost applied voltages. If retention were studied only in this high voltage region, at applied voltages above 15 kV, it would not appear to be strongly affected by the applied voltage. Nevertheless it is significantly different from the retention factor at very low voltages.

Figure 5.2.4 shows that k' of [Met5]Enkephaline decreases at increasing ionic strength, but retains its basic dependence on applied voltage with slightly decreasing initial slopes at the higher ionic strength. The most striking result of this study is that even though all peptides should experience significant electromigration in EOF direction (Table 5.2.1), [Met5]Enkephaline and Oxytocine show higher than LC-retention in CEC at lower ionic strength (below 40 mM), which in addition is modulated by the applied voltage (Figure 5.2.5). Generally, an increased ionic strength decreases electrostatic interaction of the analyte with the charged stationary phase and thus reduces LC retention (see open circles in Figure 5.2.5), which is a well

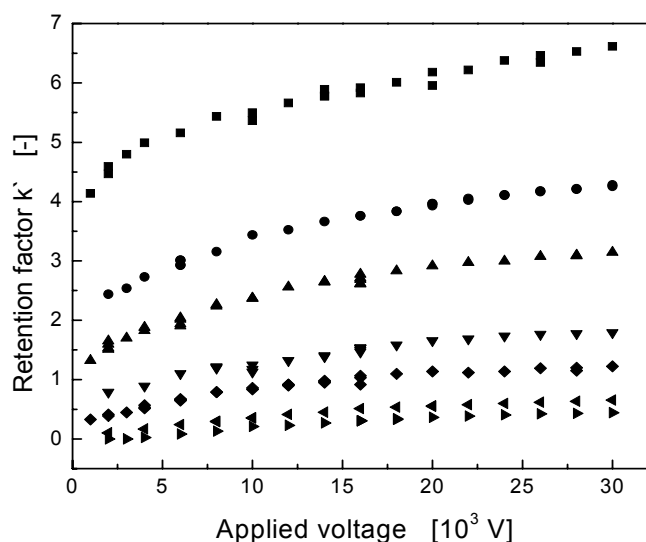**Figure 5.2.4** Dependence of the retention factor k' = $(t_r - t_0)/t_0$ of [Met5]Enkephaline on applied voltage at different mobile phase ionic strength (pH = 2.7): (■) 10 mM (●) 15mM, (▲) 20 mM, (▼) 30 mM, (◆) 40 mM, (◄) 50 mM, (▶) 60 mM.
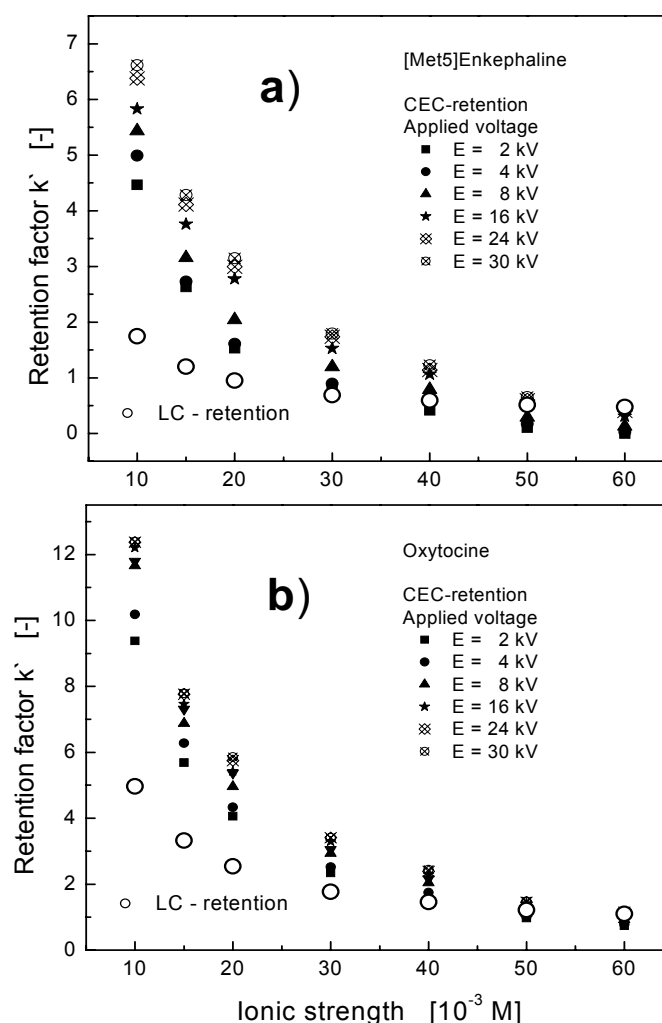

Figure 5.2.5 Dependence of the retention factor k' = $(t_r - t_0)/t_0$ on ionic strength in LC and CEC (at different applied voltages). Mobile phase pH = 2.7.

investigated phenomenon [29, 42, 48]. At the same time increasing ionic strength decreases the charge selectivity of the mesopore space and thus decreases related electrical-field-induced CP (Chapter 4, Chapter 5.1) [1, 2, 38]. This also amounts to a decrease of CP-contributed retention for the charged peptides in CEC in comparison to LC-contributed retention at increasing ionic strength (see Figure 5.2.5). It is further reflected by the different slopes in the k'-voltage-curve at the different ionic strength in Figure 5.2.4 and thus the respective intensity of developing electrical-field-induced CP. It means that at similar applied voltages CP with increasing ionic strength is attenuated (Figure 4.6). It implies that with increased ionic strength higher field strength are necessary to induce a comparable intensity of electrical-field induced CP. Further, the field strength at which a transition occurs from intraparticle to (extraparticle) boundary layer-dominated transport behaviour observed for fixed beds of the SCX-particles (Figures 4.3) clearly scales with the ionic strength of the background electrolyte (Figure 4.6) and thus necessarily also reflects the approaching plateau value in the retention dynamics. It cannot be modulated further, when boundary layer-dominated transport, that is, the (over)limiting current regime, prevails. If lower electrical field strength could be realized (in our case hampered by the endurably long analysis time) this retention in CEC could be realized for the whole range from LC retention (or even lower) to the utmost tunable retention in Figure 5.2.5 even at the very low ionic strength. It is yet difficult to achieve, because of the relatively strong CP even at very low voltages, which induces retention to increase drastically. In contrast, at sufficiently high ionic strength, retention in CEC can be smaller than the observed LC retention due to the reduced electrostatic interactions. Then electrophoretic forces may become strong enough to result in a lower retention than observed for LC at ionic strength higher than 30 mM for [Met5]Enkephaline and 40 mM for Oxytocine in Figure 5.2.5. Anyway CEC retention still retains its electrical-field dependence, because CP is still discernable (Chapter 4, Figure 4.5) but the slope of the k'-voltage curve is significantly lower and stretched to higher electrical field strength (Figure 5.2.4). It accounts for the higher field strength needed to induce significant CP (Figures 4.5 and 4.6) at the higher ionic strength. In other words the increasingly CP-composed retention in CEC generally makes a quantitative description of retention behaviour via simple parameters, considering pure electrostatic aspects (accessible via retention in LC) and electrophoretic forces (mobility in CZE), almost impossible [11, 14, 22, 23, 25]. From a principal point of view retention in CEC should at least reflect the same value as LC retention. It should be remembered that all peptides are experiencing electromigration in the EOF direction which points towards the inconsistency of existing theoretical concepts. Further, it is shown that similar retention for LC in comparison to CEC is approached at different ionic strength for each peptide simply reflecting the different ionic strength dependencies of k' of the peptides with different applied voltages (Figure 5.2.5), which was already indicated in Figure 5.2.3a, where the k'-voltage-curve has higher slopes at the low voltages and reaches earlier the respective plateau regime if its slope is stronger and thus retention is stronger CP-composed.

A systematic screening of the CEC retention factor for LHRH and [Arg8]Vasopressine also revealed a general dependence on applied voltage, but with a different trend (Figure 5.2.6). Generally at increasing ionic strength retention in CEC significantly decreases for these higher charged peptides, as shown for LHRH (Figure 5.2.6), but at the same time also retains its electrical-field dependence even at 60 mM ionic strength. Most peculiar, the LC retention is always higher than the CEC retention. Also for these analytes, CEC retention then can be systematically tuned by an applied voltage (Figure 5.2.7). At lower ionic strength

retention is increased both in LC and CEC. The CEC retention appears to approach LC retention at the higher ionic strengths (Figure 5.2.7).

To conclude, the present studies on peptide retention in CEC reflect a modulation of retention (decreasing or increasing) on the applied voltage and analyte charge, which is the essentially varying property under otherwise comparable conditions. As the data for the single-charged peptides almost perfectly fit to the data of the single charged counterionic analytes investigated in Chapter 5.1, we tried to complement the so far
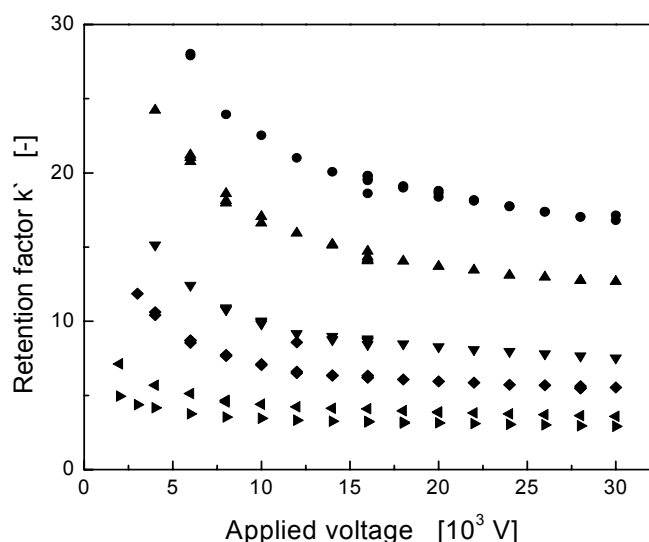
Figure 5.2.6 Dependence of the retention factor k' = $(t_r - t_0)/t_0$ of LHRH on applied voltage at different ionic strengths (pH = 2.7): (●) 15 mM, (▲) 20 mM, (▼) 30 mM, (◆) 40 mM, (◀) 50 mM, (▶) 60 mM.
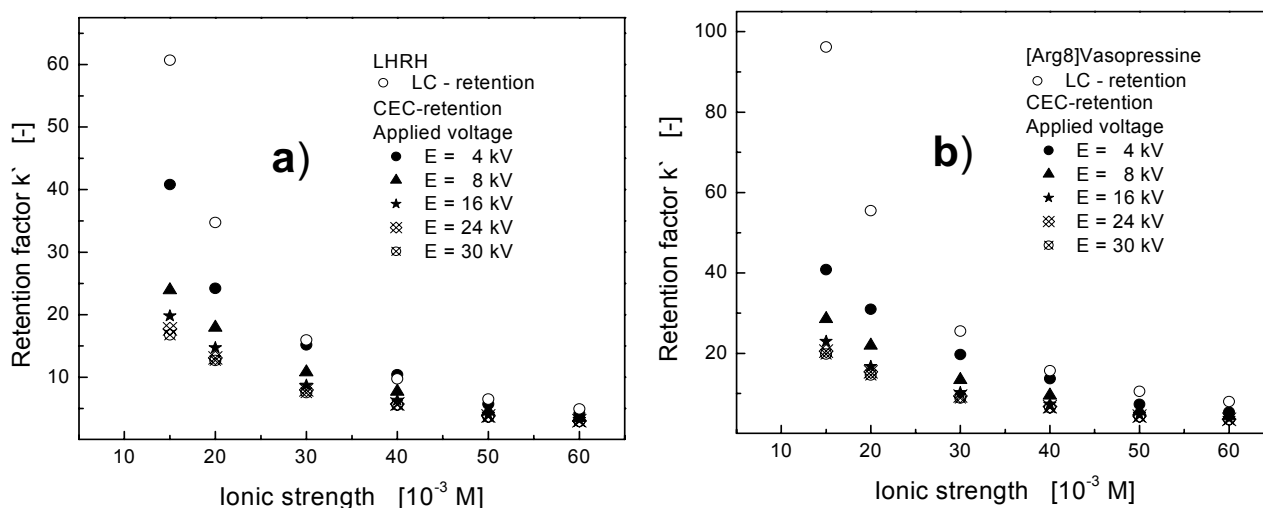
Figure 5.2.7 Dependence of the retention factor k' = $(t_r - t_0)/t_0$ in LC and CEC on ionic strength of the background electrolyte (pH = 2.7) at different applied voltages in CEC.

presented data by the following simple CEC experiment. It employs the same column but a different buffer solution pH. We have shown earlier (Figure 5.2.1c) that at pH = 7.0, u_{eo} under otherwise identical conditions is increased, due to the dissociation of residual silanol groups of the stationary phase. At the same time CP is still operative in the packed bed. Thus, with a significant intraparticle EDL overlap, charge-selectivity and the electrical field-induced CP, effects on retention are expected to be modulated via the respective peptide net charges. LC retention and peptide electrophoretic mobility also have been monitored and are shown in Table 5.2.2.

As expected LC retention of Oxytocine decreases significantly at pH = 7.0. Further it shows a vanishing electrophoretic mobility indicating that its net charge is close to zero (Table 5.2.2). LC retention for LHRH and [Arg8]Vasopressine also significantly decreases due to the increasing deprotonation of the relevant amino group. Their electrophoretic mobility at the same time decreases to the expected value (regarding

their decreased net charge at pH = 7.0) and is in the same order of magnitude as that of Oxytocine at pH = 2.7.

Table 5.2.2

LC retention and electrophoretic mobility of peptides at different pH values of the background electrolyte

30 mM Phosphate		pH = 2.7 (VAR %)	pH = 7(VAR %)
Oxytocine	k'_{Lc}	1.77 (0.99)	0.21 (0.24)
	μ_{ep}	0.85 (0.43)	0.0183 (0.15)
LHRH	k'_{Lc}	15.97(1.10)	1.76 (0.44)
	μ_{ep}	1.22 (0.44)	0.705 (0.44)
[Arg8]Vasopressine	k'_{Lc}	25.53 (1.33)	2.71 (0.43)
	μ_{ep}	1.33 (0.82)	0.75 (0.09)

Figure 5.2.8a demonstrates an almost field-independent retention of Oxytocine at pH = 7.0 in comparison to the field dependent retention at pH = 2.7. Further, retention for the almost neutral (in view of net charge) molecule reflects a value similar to LC retention (see Table 5.2.2 and Figure 5.2.8a), as is in agreement with the earlier demonstrated results (Figures 3.2 and 3.3 as well as Figure 5.1.3a), which have shown that neutral analytes retention dynamics are not influenced by applied voltages (see also Figure 5.1.4a) [38], because they are simply not participating in coupled mass and charge transport.

Figure 5.2.8 Dependence of the retention factor k' = $(t_r - t_0)/t_0$ on applied voltage at a mobile phase ionic strength of 30 mM with different pH values (pH = 2.7 and 7.0, respectively) of the background electrolyte.

The electrical-field-dependent retention data collected for LHRH and [Arg8]Vasopressine reveal an increasing retention with increasing applied voltage at pH = 7.0, being in contrast to the behaviour at pH = 2.7, which has demonstrated that retention decreases with increasing voltage (Figure 5.2.8b). It validates experimentally that the effective net charge of the peptide is a fundamental property determining the respective scaling of k' with the applied voltage. Their increase in retention falls in the same order of magnitude as that of Oxytocine at pH = 2.7, which is further illustrated in Figure 5.2.9. Interestingly the retention of both LHRH and [Arg8]Vasopressine is also higher than for LC at pH = 7.0 (Figure 5.2.9, Table 5.2.2), in contrast to their behaviour at pH = 2.7 (see Figure 5.2.7), where their retention is lower than for LC. They also show similar slopes and saturation of the k'-voltage-curves, according to their similar mass and charge also at pH = 7.0.
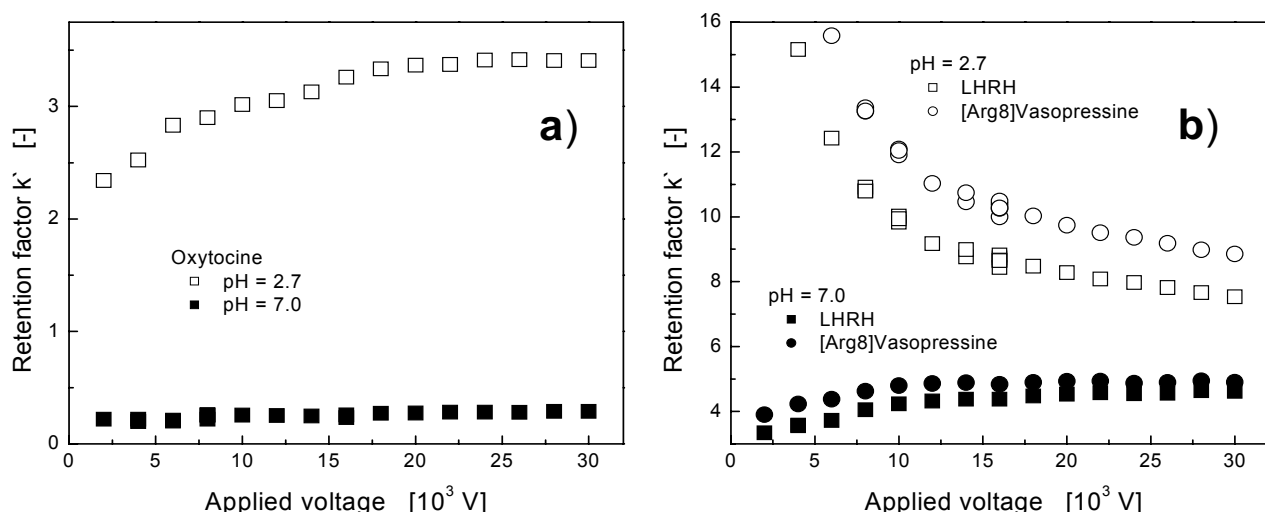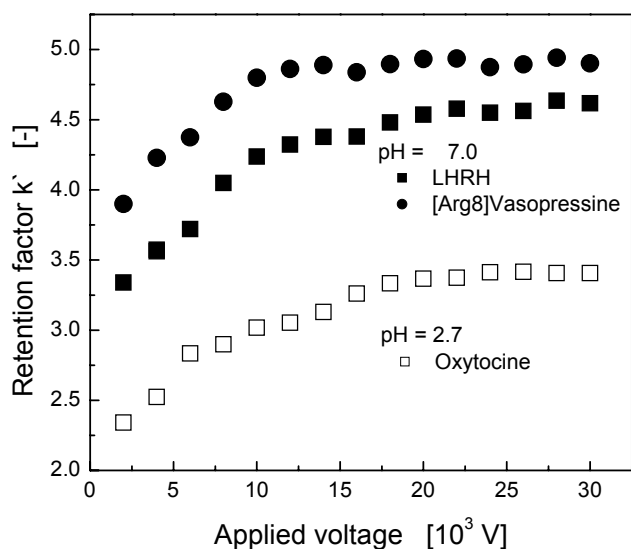
Figure 5.2.9 Dependence of the retention factor k' = $(t_r − t_0)/t_0$ on applied voltage at a mobile phase ionic strength of 30 mM with different pH values (pH = 2.7 and 7.0, respectively) of the background electrolyte.

In order to explain this behaviour we have to analyze relevant transport parameters in these systems of ion-permselective particles and related consequences for charged analytes in a similar fashion as in the previous chapter. This explanation has a strong hypothetical character. Generally, the increasing voltage increases the steepness of the concentration gradients of the background electrolyte around the ion-permselective interfaces (see Figure 2.1a) which, in analogy, is also revealed around the spherical particles in a packed bed (Chapter 4) [1, 38]. Assuming a locally flat three-layered system for simplicity (e.g. Figure 2.1), which consists of the two CDLs (enriched and depleted) facing the ion-permselective domain this situation becomes even more complex when considering the transport of the analyte species in the CP zones and ion-permselective pore space. If more than one counterionic species is present in the ion-permselective system (in addition to the Na$^+$-ions of the background electrolyte) relative contributions to the overall mass and charge flux in competitive charge transport are governed by charge numbers, diffusion coefficients, and concentrations of the counterionic species as reflected in their respective transport numbers [49, 50]. It was shown recently for the membrane geometry, that transport of two ions of the same sign, which may differ in their charge number, depends on current density through the system, mainly also because the transport properties inside the membrane and the depleted CP zone (through which the charged analytes have to enter the ion-permselective pore space are quite different. This may be explained by the fact that different species are naturally competing in current transport. Considering transport in the ion-permselective pore space it is generally assumed that counterions are mainly transported by electromigration. The flux density $\bar{j}_i$ of a species i through the ion-permselective pore space then may be approximated by [50]:

$$\bar{j}_i = \frac{\bar{t}_i i}{z_i F},\qquad (5.1)$$

where $\bar{t}_i = z_i^2 \bar{D}_i \bar{c}_i / \sum_{j=1}^{3} z_j^2 \bar{D}_j \bar{c}_j$. $\bar{t}_i$ denotes the transport number, i the electrical current, z_i the electrochemical valence (charge number), F is the Faraday constant, $\bar{D}_i$ the diffusion coefficient of the

counterions, and $\bar{c}_i$ is the intraparticle concentration of species i. Overbars denote the membrane (or particle) phase. $\bar{c}_i$ is obtained by the Donnan-model. j denotes all ionic species present in the ion-permselective pore space (background electrolyte counterion, i.e. Na^+-ion, peptide of variable charge, and buffer co-ion). It is considered that transport number of co-ions can be neglected [49], when the intraparticle pore space is strongly ion-permselective [49]. Counterions are enriched by the ion-permselective pore space. The distribution coefficient of counterions in comparison to external solution depends on the charge number, the ion-permselective pore space prefers counterions of higher charge (eq. 2.1) [29]). The selectivity of the ion-exchangers, i.e. the selection of one counter-ion in preference to the other may also have other causes, e.g. equivalent solvated volume [29].

Starting with a relatively simple example of the Na^+-ion ($z_1 = +1$) of the background electrolyte and a small counterionic tracer ($z_2 = +1$) with much lower concentration and smaller diffusion coefficient, we have to consider the fact that the transport numbers through the membrane summed over both species have to satisfy the condition $\bar{t}_1 + \bar{t}_2 \approx 1$ (eq. 2.4 [51]). Thus the two charge carriers are sharing the transport of the current density. Na^+-ions of the background electrolyte are (relatively) more intensively transferred than the tracer, via their higher intraparticle concentrations and smaller diffusion coefficient, thus that t_{Na+} is much higher than t_{Pept+}, but still need to be supplied through the gradients in the diluted solution bulk (depleted CP zone), which becomes increasingly a bottleneck for their transport at increasing field strength. As we have seen by the strong intraparticle enrichment of the fluorescent counterionic tracer in Figure 4.2 (which resembles a small single charged counterionic analyte) increasing with E_{ext}, this indicates that its transport number is increasing with the current density through a particle, which is yet not limited by diffusive transport through the depleted CP zone. The increasing transport number of the tracer thus reflects or better implies that the transport number of the Na^+-ion of the background electrolyte necessarily has decreased in the system at increasing current densities. This generally may explain from a principal point of view the increasing k' of the single charged peptides, i.e. while electrical current density is increased they are more intensively transported through the depleted CP zone (and, thus, the intraparticle pore space) until boundary layer dominated transport prevails. In other words the transport number of the single charged analyte with higher mass is higher than at low current densities and the transport number of the Na^+-ion is lower than that at low current densities.

If a twice positively charged peptide ($z = +2$) is competing in current transport with the Na^+-ion of the background electrolyte now two charge carriers of different charge are sharing the transport of the current density. Peptide-ions are relatively stronger enriched than the single charged peptides (see Donnan-potential [29]) and are via their higher $\bar{c}_i$ (eq. 2.1) in comparison with the single charged peptides and z_i^2 (eq. 5.1) much stronger transported. They also have to be supplied through the gradients in the diluted solution bulk which inherently becomes increasingly a bottleneck for their transport. Thus its transport number is decreasing with current density through a particle, which is yet realized by an increasing transport number of the Na^+-ions of the background electrolyte. This generally may explain from a principal point of view the

decreasing k' of the twice charged peptides, i.e. while electrical current density is increased they are increasingly less transported through the depleted CP zone and intraparticle pore space until boundary layer dominated transport prevails. In other words the transport number of the twice charged analyte is higher at low current densities and the transport number of the Na^+ -ion is lower at low current densities. With increasing current density the transport number of the twice charged peptide decreases and transport of Na^+-ions increases. Competition of charge transport prevails whenever there are different species present in the system. Assuming a similar charge as the background electrolyte counterion for e.g. a peptide the ratio of their transport numbers in the membrane is solely described by the ratio of their concentration and diffusion coefficients. Important here is that the transport number of the Na^+ -ion in the low voltage region is higher than that at high voltages, which results in an increasing transport number of the single charged peptides at the higher voltages in comparison to low voltages. Further the increase in transport number of peptides is inherently also related to their diffusion coefficient, modulating the electrical field dependence of k' (Figure 5.2.3a).

It is suggested that from a more chromatographic point of view, that the transport of single-charged peptides [Met5]Enkephaline and Oxytocine, increases through the three-layered system and thus via adjusting their increasing pore-level concentrations retention increases with increasing electrical field strength (similar to Figure 4.2). Then the peptides are more intensively transported, which becomes modulated by their diffusion coefficient. It was shown that retention is stronger increased the higher the analytes mass (see different slopes observed for [Met5]Enkephaline and Oxytocine in Figure 5.2.3a). LHRH and [Arg8]Vasopressine (both twice charged) show similar decreasing retention behaviour at pH = 2.7 (Figure 5.2.3b), which is in accordance with their similar charge and mass (diffusion coefficient). Lowering the net charge of LHRH and [Arg8]Vasopressine suddenly induces their effective transport numbers through the system to increase with increasing voltage, resulting in an increase of their pore level concentrations and subsequently their retention factor increases with increasing voltage (Figure 5.2.8b), accompanied by a decrease of the transport number of the Na^+-ion. This scaling mainly has to be attributed to the net charge number of the peptides (Figure 5.2.8) and thus their transport number. Generally, the transition from intraparticle to extraparticle (boundary-layer) dominated transport behaviour is also reflected in the k'-voltage curve with its slope from very low voltages achieving plateau values at high voltages. Further important is that this behaviour generally may be observed with strong ion-permselectivity on a mesoporous particle scale, but its relative importance will be modulated with decreasing this charge selectivity where the transport of the background electrolyte co-ion also gains increasing importance. Thus, also the functional dependence of retention on ionic strength observed in ion-exchange liquid chromatography will become modulated for its electrochromatographic variant by the electrical-field-induced CP, including the relative importance of competitive charge transport, modulated by the permselectivity of the mesopore space (Figures 5.2.5 and 5.2.7 and also Figure 4.5). At increasing ionic strength it moves away from ideal ion-permselectivity and, when there is no permselectivity and pore level concentrations of charged species (including the analytes) resemble those in bulk solution (which is principally impossible to achieve, see Chapter 3), transport number differences are governed by their difference in mobility only, which makes the contribution to the separation process purely describable by their respective mobility and at the same time independent of applied voltage (Figures 5.1.6 and 5.2.8a).

Selectivity tuning. The strongest change of retention occurs at relatively low applied voltages, which is reflected in the initial slopes at the k'-voltage-curve (see Figure 5.2.3a). The selectivity for the two groups of peptides, which show increasing and decreasing retention behaviour, respectively, was investigated as a function of the applied voltage. Selectivity in LC separations is defined as the ratio of the capacity factors of the compounds of interest to be separated [52]. Figure 5.2.10 shows the selectivity for the two groups of peptides depending on buffer ionic strength at different applied voltages. Most important is that for LC the selectivity is similar for all ionic strengths at pH = 2.7 (see grey points in Figure 5.2.10). Slight changes in selectivity (Figure 5.2.10a) are explainable via different dependencies of peptide retention with respect to ionic strength, depending on the amount of charges in the peptide interacting with the charged stationary phase and their molecular mass (Table 5.2.1) [42]. CEC selectivity at high applied voltages is not improved in comparison to LC, which at first does not show any advantage of using CEC in comparison to LC, even though one may obey decreased dispersion and thus higher peak capacities. However, at relatively low
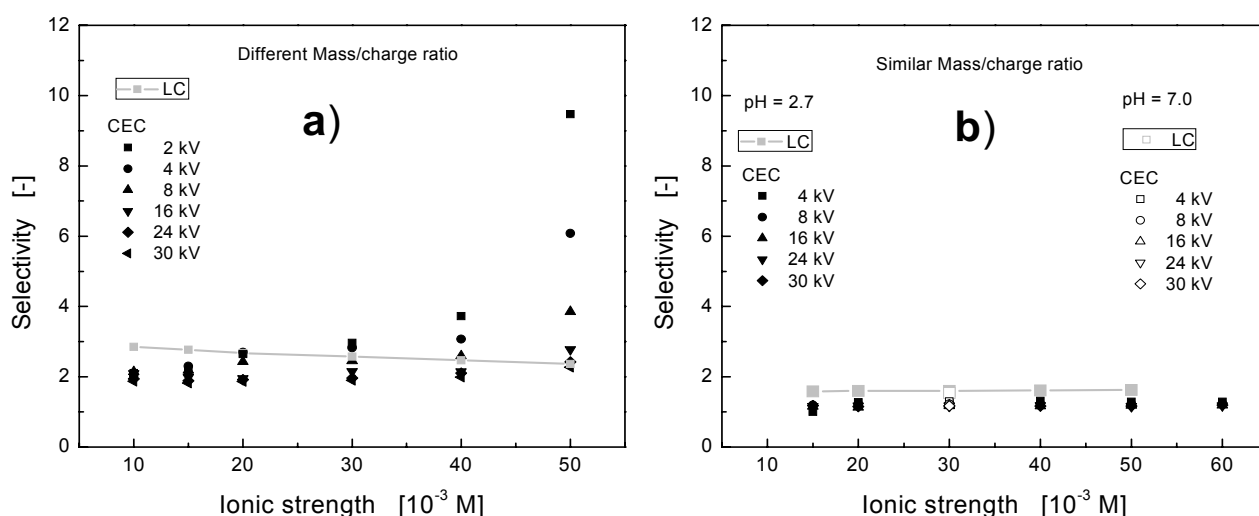
Figure 5.2.10 Selectivity for the separation of peptides in LC and CEC (at different applied voltages) in dependence of the mobile phase ionic strength. a) [Met5]Enkephaline and Oxytocine at pH = 2.7, and b) LHRH and [Arg8]Vasopressine at pH = 2.7 and 7.0.

applied electrical field and reduced electrostatic interactions, selectivity is significantly modulated by the applied voltage (e.g. for the 30 mM and higher ionic strength in Figure 5.2.10a). This implies that in view of selectivity, which is of utmost importance for bio-analytical applications, the applied voltage has a significant influence (without shortcomings in dispersion) via the different dependencies of LC retention and CP-composed retention. While this is very pronounced for peptides with different mass and similar charge (Figure 5.2.10a), the peptides LHRH and [Arg8]Vasopressine do not show this selectivity behaviour, most probably because they have similar mass and charge (5.2.10.b) and similar dependencies of the k'-voltage-curve. Increasing the pH to pH = 7.0 does not significantly alter the selectivity (here monitored for the 30 mM ionic strength) because both peptides have a similar pH-dependence of their net charge and thus their k'-voltage curves are shifted by a factor over the whole range of applied voltages. Generally it can be implied that operating CEC at the highest available voltages does not always result in optimum selectivity, but suffers of course at lower voltages from the respective total analysis time. One of the most promising routes to tune selectivity would be to use LC systems with electrical-field assistance (low applied voltages are sufficient) and then tune selectivity by simply changing the applied voltage or applying voltage gradients.

Then the electrical field-induced CP zones and residence times of the charged analytes are modulated. This greatly can affect selectivity and may increase also resolution in difficult bio-analytical separations.

From a general perspective LHRH and [Arg8]Vasopressine have a similar mass and charge and similar pH titration curves and separation may always be difficult to accomplish in CZE (Table 5.2.1), despite the fact of massively reduced dispersion by utilizing stacking phenomena in CZE. Regarding this issue it will be also difficult to tune their selectivity by modulation of electrical field-induced CP (Figure 5.2.10b). Oxytocine and [Met5]Enkephaline with their different mass and charge may also be difficult to separate under our conditions in CZE because of their similar charge-to-mass (size) ratio determining electrophoretic migration velocity (see Table 5.2.1). As due to their different mass and charge their differential migration and selectivity is achieved by an ion-exchange mechanism, which can optionally be modulated and the desired selectivity be adjusted beyond the pure ion-exchange mechanism with utilisation of an applied voltage in CEC or electrical-field assisted processes.

5.2.4   Conclusions

This work has revealed an electrical field-dependence of the retention factor for peptides under typical electrochromatographic conditions (Figure 5.2.2). It has been demonstrated that peptides retention fundamentally depends on electrical-field-induced CP, influenced by the respective electrical field strength (Figure 5.2.3). As peptides have to traverse the field-dependent CP zones it is their charge which is mainly responsible for their retention behaviour (Figure 5.2.8). Such dependence is caused by the electrical field-induced CP and competitive charge transport of peptides with the counterionic buffer electrolyte component. Due to a significant charge-selectivity under almost all conditions in CEC employing porous particles, a superimposed electrical field induces depleted and enriched CP zones in the background electrolyte around the particles (Figure 4.1). The intensity of these CP zones (background electrolyte) depends on the field strength and charge-selectivity of the particles. Most importantly the phenomenon of electrical-field-induced CP and related ion-permselective transport also induces a change in residence times of peptides depending on their net charge and diffusion coefficient (molecular mass). It may be explained by an increase of the effective transport number for the single charged peptides with increasing field strength (similar to Figures 4.2 and 5.1.4c, observed for a small single charged counterionic analyte) accomplished by a decrease in the transport number of the background buffer electrolyte component. A decrease of effective transport number for the twice charged counterionic peptides with increasing field strength, which clearly resembles analyte charge aspects, is accomplished by a corresponding increase for the background electrolyte buffer component. It has been indicated that effective transport numbers are dependent on coupled transport in the intraparticle and adjoining depleted CDL, with each regime reflecting different transport behaviour.

It is concluded that CP, which represents field-induced dynamic changes in the local distribution of ionic species (intraparticle pore level concentrations) in hierarchically-structured materials is a key for understanding retention of charged analytes including peptides and proteins. This can explain systematic behaviour [23, 39], where the retention dynamics of peptides has been shown to depend on applied voltage in CEC systems with ion-exchange materials and comprising ion-permselectivity on the intraparticle mesopore scale. Studies on retention in CEC may always be difficult to compare between different investigators, as specific setups and field strength aspects (e.g. duplex columns, home-built devices) together with sensitive electrical-field induced CP may obscure principal trends, which might lead to severe misinterpretations regarding the physicochemical meaning of a retention factor in CEC. It can also be concluded from the experimental data (Figure 5.2.3a) that retention in CEC in dependence of applied voltage not only depends on the peptides charge, but also on their molecular mass, as reflected in their diffusion coefficient. The higher their mass at a specific charge, the slower transference in the depleted CP zone and intraparticle pore space, and this is inducing their retention to increase (even) stronger with electrical field strength in comparison to a peptide with similar charge, but lower molecular mass. Thus generally retention in CEC hardly contains thermodynamic information as in LC, simply because of the importance of the electrical-field-induced CP, changing the pore-level concentrations of charged analytes which are shown to be significantly different than expected from the pure electrostatic enrichment depletion effects (Donnan-potential or EDL-model). It thus describes more importantly the migration and retention behaviour of any charged analytes in columns typically employed for CEC.

Further, the physicochemical basis for the respective decrease and increase in retention can just be made accessible by appropriate transport models, which have to be developed to support the hypothesis for the experimentally observed behaviour. These models have to include a well identified set of parameters and clarify the respective transport in- or decrease of ionic species of different valence (e.g. reflecting peptides of different charge number) with respect to the relative transport behaviour of the background electrolyte buffer components (e.g. the Na^+ in the present system) in competitive charge transport. It critically has to access the intraparticle ion-permselective transport behaviour at very low voltages, where the Donnan-model applies and the transport behaviour in the diluted solution bulk, where at limiting current densities most of the potential drop and transport in the whole system is accomplished and where transport properties differ from those at low voltages (intraparticle-dominated transport behaviour).

References

[1]   Nischang, I., Reichl, U., Seidel-Morgenstern, A., Tallarek, U., *Langmuir,* submitted.

[2]   Nischang, I., Chen, G., Tallarek, U., *J. Chromatogr. A* 2006, *1109*, 32-50.

[3]   Rudge, S. R., Basak, S. K., Ladisch, M. R., *AIChE J.* 1993, *39*, 797-808.

[4]   Basak, S. K., Ladisch, M. R., *AIChE J.* 1995, *41*, 2499-2507.

[5]   Basak, S. K., Velayudhan, A., Kohlmann, K., Ladisch, M. R., *J. Chromatogr. A* 1995, *707*, 69-76.

[6]   Euerby, M. R., Gilligan, D., Johnson, C. M., Roulin, S. C. P., Myers, P., Bartle, K. D., *J. Microcolumn Sep.* 1997, *9*, 373-387.

[7]   Wu, J.-T., Huang, P., Li, M. X., Lubman, D. M., *Anal. Chem.* 1997, *69*, 2908-2913.

[8]   Spikmans, V., Lane, S. J., Tjaden, U. R., van der Greef, J., *Rapid Commun. Mass Spectrom.* 1999, *13*, 141-149.

[9]   Kitagawa, S., Tsuda, T., *Anal. Sci.* 1998, *14*, 571-575.

[10]   Kitagawa, S., Watanabe, H., Tsuda, T., *Electrophoresis* 1999, *20*, 9-17.

[11]   Dittmann, M. M., Masuch, K., Rozing, G. P., *J. Chromatogr. A* 2000, *887*, 209-221.

[12]   Ye, M., Zou, H., Liu, Z., Ni, J., *J. Chromatogr. A* 2000, *887*, 223-231.

[13]   Enlund, A. M., Isaksson, R., Westerlund, D., *J. Chromatogr. A* 2001, *918*, 211-220.

[14]   Zhang, J., Zhang, S., Horváth, Cs., *J. Chromatogr. A* 2002, *953*, 239-249.

[15]   Bedair, M., El Rassi, Z., *Electrophoresis* 2002, *23*, 2938-2948.

[16]   Xiang, R., Horváth, Cs., *Anal. Chem.* 2002, *74*, 762-770.

[17]   Liu, Z., Otsuka, K., Terabe, S., *J. Chromatogr. A* 2002, *959*, 241-253.

[18]   McKeown, A. P., Euerby, M. R., Lomax, H., *J. Sep. Sci.* 2002, *25*, 1257-1268.

[19]   Steiner, F., Lobert, T., *Chromatographia* 2003, *58*, 207-211.

[20]   Fu, H., Jin, W., Xiao, H., Huang, H., Zou, H., *Electrophoresis* 2003, *24*, 2084-2091.

[21]   Bedair, M., El Rassi, Z., *J. Chromatogr. A* 2003, *1013*, 47-56.

[22]   Rathore, A. S., McKeown, A. P., Euerby, M. R., *J. Chromatogr. A* 2003, *1010*, 105-111.

[23]   Progent, F., Taverna, M., *J. Chromatogr. A* 2004, *1052*, 181-189.

[24]   Enlund, A. M., Andersson, M. E., Hagman, G., *J. Chromatogr. A* 2004, *1044*, 153-158.

[25]   Valette, J. C., Demesmay, C., Rocca, J. L., Verdon, E., *Chromatographia* 2005, *62*, 393-399.

[26]   Channer, B., Skellern, G. G., Euerby, M. R., McKeown, A. P., Rathore, A. S., *J. Chromatogr. A* 2005, *1095*, 172-179.

[27]   Chen, G., Pačes, M., Marek, M., Zhang, Y., Seidel-Morgenstern, A., Tallarek, U., *Chem. Eng. Technol.* 2004, *27*, 417-428.

[28]   Chen, G., Tallarek, U., Seidel-Morgenstern, A., Zhang, Y., *J. Chromatogr. A* 2004, *1044*, 287-294.

[29]   Helfferich, F., *Ion Exchange*, McGraw-Hill: New York, 1962.

[30]   Tallarek, U., Pačes, M., Rapp, E., *Electrophoresis* 2003, *24*, 4241-4253.

[31]   Tallarek, U., Leinweber, F. C., Nischang, I., *Electrophoresis* 2005, *26*, 391-404.

[32]   Tan, G., Shi, Q., Sun, Y., *Electrophoresis* 2005, *26*, 3084-3093.

[33]   Bandilla, D., Skinner, C. D., *J. Chromatogr. A* 2004, *1044*, 113-129.

[34]   Mistry, K., Grinberg, N., *J. Liq. Chromatogr. Rel. Technol.* 2004, *27*, 1179-1202.

[35]   Adu, J. K., Lau, S. S., Watson, D. G., Euerby, M. R., Skellern, G. G., Tettey, J. N. A., *Electrophoresis* 2005, *26*, 3445-3451.

[36]   Cikalo, M. G., Bartle, K. D., Myers, P., *Anal. Chem.* 1999, *71*, 1820-1825.

[37]   Walhagen, K., Boysen, R. I., Hearn, M. T. W., Unger, K. K., *J. Pept. Res.* 2003, *61*, 109-121.

[38]   Nischang, I., Spannmann, K., Tallarek, U., *Anal. Chem.* 2006, *78*, 3601-3608.

[39]   Rocco, A., Aturki, Z., D'Orazio, G., Fanali, S., Šolínová, V., Hlaváček, J., Kašička, V., *Electrophoresis* 2007, *in press*.

[40]   Sørensen, T. S. (Ed.), *Surface Chemistry and Electrochemistry of Membranes*, Marcel Dekker: New York, 1999.

[41]   Leinweber, F. C., Pfafferodt, M., Seidel-Morgenstern, A., Tallarek, U., *Anal. Chem.* 2005, *77*, 5839-5850.

[42]   Kopaciewicz, W., Rounds, M. A., Fausnaugh, J., Regnier, F. E., *J. Chromatogr. A* 1983, *266*, 3-21.

[43]   Cifuentes, A., Poppe, H., *Electrophoresis* 1997, *18*, 2362-2376.

[44]   Nischang, I., Tallarek, U., *Electrophoresis* 2007, *28*, 611-626.

[45]   Nischang, I., Tallarek, U., *Electrophoresis* 2004, *25*, 2935-2945.

[46]   Sutcliffe, N., Corran, P. H., *J. Chromatogr. A* 1993, *636*, 95-103.

[47]   Gu, B., Chen, Z., Thulin, C.D., Lee, M. L., *Anal. Chem.* 2006, *78*, 3509-3518.

[48]   Stahlberg, J., *Anal. Chem.* 1994, *66*, 440-449.

[49]   Zabolotsky, V. I., Manzanares, J. A., Nikonenko, V. V., Lebedev, K. A., Lovtsov, E. G., *Desalination* 2002, *147*, 387-392.

[50]   Nikonenko, V., Lebedev, K., Manzanares, J. A., Pourcelly, G., *Electrochim. Acta* 2003, *48*, 3639-3650.

[51]   Strathmann, H., *Ion exchange membrane separation processes*, Elsevier, Amsterdam 2004.

[52]   Neue, U. D., *HPLC Columns: Theory, Technology, and Practice*; Wiley-VCH: New York, 1997.

6   Global Summary

In this thesis the most fundamental aspects of CEC are addressed. It is shown that CEC is far more complex than may be anticipated from the two components involved in this method. The first one is CZE, which (as an electrokinetic separation method) appears to be almost under control, because of its increasing number of applications in the pharmaceutical industry. The second one is LC, which is the strongest working horse for almost all analytical separation problems at hand and has no competitor in view of reliability and robustness. In this line it will keep its strong role among analytical separation techniques. The most important implementations for CEC are an increase of the complexity of phenomena involved in the mobile phase transport through a hierarchical porous medium ("Flow aspects") and also "Transport aspects" of charged analytes. These phenomena have been systematically addressed in the present thesis. The unique combination of quantitative optical imaging techniques (Chapter 4) and chromatographic field studies (Chapter 3) revealed a quantitative orthogonal view on the investigated flow aspects in electrochromatographic separation systems. The investigated phenomena are highlighted in Chapter 5 and are successfully employed for separations in the pharmaceutical and bio-analytical field, being more important for resolving the relevant transport aspects of analytical target molecules in hierarchically structured porous media. In the following the most important results from the different chapters are briefly outlined.

Internal electrical fields in chromatographic media − Transport in LC
Electrical potential gradients which develop at the boundaries between the quasi-electroneutral interparticle (interskeleton) macropore space and the intraparticle (intraskeleton) charge-selective domain in chromatographic beds are important in LC, where they influence distributions of charged analytes in the hierarchically structured porous media. They are determined by equilibrium electrostatics in LC-practice. Thus, the porous particle or porous monolith skeleton becomes ion-permselective; it enriches counter-ions and excludes co-ions. At electrochemical equilibrium, an electrical phase-boundary potential, the so-called Donnan potential (eq. 2.1), balances the tendency of the ionic species to level out the chemical potential gradients. Most important, a broad intermediate regime between the extremes of global thin-EDL-limit (any of the pore dimensions are significantly larger than the EDL) and discrete local ion-permselectivity (intraparticle/intraskeleton pore dimensions are of the same order of magnitude as the EDL) must be regarded as common practice in LC (Figure 3.5 and 3.6) and, thus, ion-permselective transport has a general rather than special significance for coupled mass and charge transport through packed beds and monoliths (Figure 6.1, **"Fundamental aspects"**).

The adjustable electrostatic on-off behaviour for intraparticle permeation in conventional chromatographic media is relevant for the design of preparative separations and purification processes as the actual electrolyte concentration determines the availability of chromatographic sites and effective porosity for co-ionic analytes (Figures 3.5 and 4.5), as well as pore-level concentrations

of charged analytes (co-ion exclusion, counter-ion enrichment) in general (Figure 6.1, **"Practical Aspects"**).

External electrical fields − Electrohydrodynamical flow aspects in porous media

Experimental studies have been reviewed (Figures 1.8 and 1.9) and performed (Figure 3.16 and 3.17) which illustrate the scaling of hydrodynamic dispersion with the average EOF velocity through packed beds and monoliths, especially in comparison to hydraulic flow (Figure 3.18). In contrast to solid, dielectric spheres porous particles support the generation of intraparticle EOF (Figure 1.5), but – due to EDL overlap in sufficiently small intraparticle pores at typical ionic strengths – demonstrate ion-permselective behaviour as well (Figure 2.3). Intraparticle EOF can strongly reduce intraparticle mass transfer resistance, and the electroosmotic perfusion provides a mechanism by which significantly improved separation efficiencies (Figures 1.5, 1.8 and 1.9) with respect to hydraulic flow can be achieved using packed beds of porous, i.e., permeable and conducting particles.
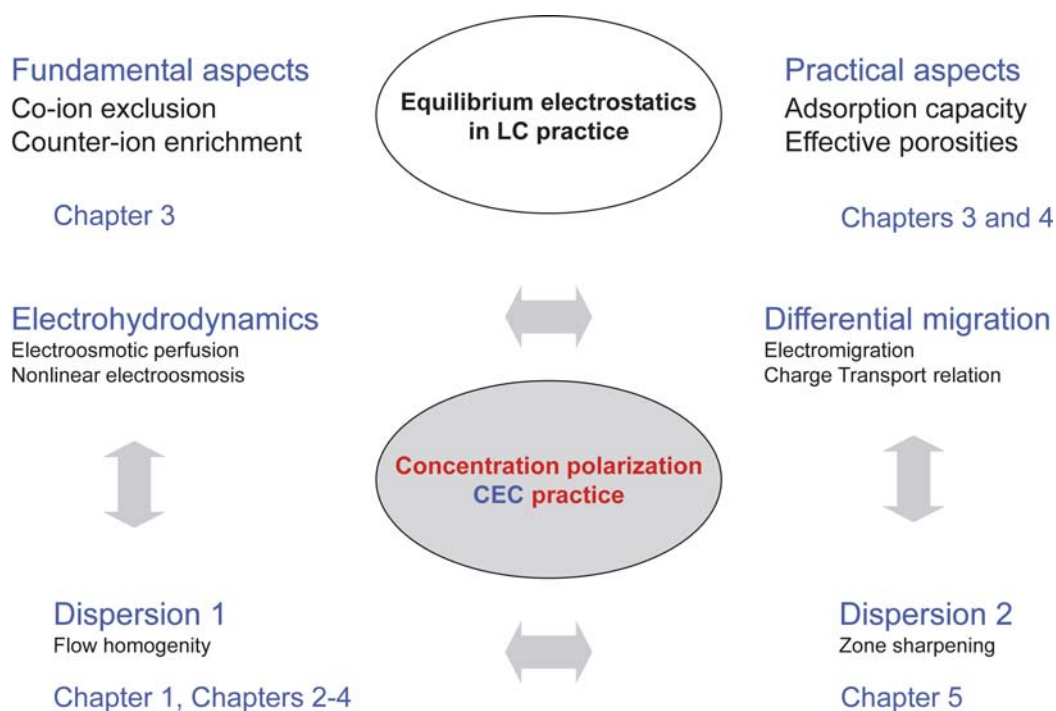
Figure 6.1 Relation of the phenomena in CEC as discussed and investigated in this thesis.

Most important coupled mass and charge transport in hierarchically structured porous materials used in CEC implies the development of electrical-field-induced concentration polarisation (CP) and a CP-based nonlinear electrokinetics with a general rather than limited significance under very common experimental conditions (Figures 3.12 and 4.7). These unique, inherently observed electrokinetic phenomena (CP and nonlinear EOF) as well as the hydrodynamic consequences sensitively depend on material characteristics (pore space morphology, including the realization of a hierarchical design and the interconnectivity between different sets of pores; surface charge density), fluid phase properties (ionic strength as most important property influencing local charge selectivity), and the

applied field strength. All these parameters have been investigated in the present thesis (Figure 6.1, **"Electrohydrodynamics"**).

Systematically acquired data have demonstrated the key role of internal electrical potential gradients and the dependence on local EDL interaction, as well as differences in the morphology of silica-based monoliths and packed beds in view of the achievable intensity of CP-based nonlinear electroosmosis (Figures 3.12). It includes consequences of increased lateral velocities due to this nonlinear slip in reducing axial hydrodynamic dispersion, again pointing towards the differences in pore space morphology of monoliths and packed beds (Figures 3.16, 3.17, reflected in Figure 6.1 as **"Dispersion 1"**).

The collected data show that the existence of CP and the relative intensity of CP (and CP-based phenomena) with respect to perfusive flow are the key to understanding salient features in CEC which includes the electrohydrodynamics, associated hydrodynamic dispersion, as well as the migration and retention of charged analytes, investigated in the second main part of this thesis.

Migration, retention and selectivity aspects for charged analytes − Transport aspects

For charged analytes an important consequence of CP is related to the effective migration and retention behaviour because the local intensity of CP, thus, also the residence time of charged with respect to electroneutral analytes in the CP zones and intraparticle pore space, sensitively depends on applied field and mobile phase ionic strengths (Figures 2.1, 4.1, 4.3, 4.5, 4.6, 5.1.4, 5.1.5). The CP phenomenon, with its intensity depending on applied field strength and electrolyte ionic strength, reflects electrical field induced electrolyte concentration gradients. These CP zones are recognized by any charged species migrating through the porous medium but not the neutral analytes. In turn, the retention factor of charged analytes in CEC becomes a complicated function of parameters that determine the local intensity of CP which have been analyzed in this work (Figure 6.1, **"Differential migration"**). As demonstrated in Figure 5.1.3a k' of single positively charged counterionic analytes is increased by more than a factor of 3. Thus their residence time shows a slower decrease than that of the electroneutral analytes at increasing field strength (Figure 5.1.2) and consequently it leads to an increase in k'.

Further CP-related studies resolved basic issues of the retention dynamics of charged analytes in CEC which had been puzzling chromatographers before (Figures 5.1.1, 5.1.3, 5.1.6 as well as Figure 5.2.8). From a more practical point of view it shows that the usual mass to charge correlation as in CZE (used to describe a specific mobility) is not sufficient to explain the electrokinetic contribution to the separation process in CEC. In contrast, retention in LC does not contain any valuable information regarding the retention factor in CEC, where it is usually influenced by electrical-field-induced CP (Figures 5.2.5 and 5.2.7.). Generally this behaviour is identified to be caused by mass transport phenomena in the CP zones and ion-permselective intraparticle/intraskeletton pore space and a generally competitive charge transport of the analyte molecules with each other and with the background buffer components. It can be used to increase performance of complex separations by

superimposing electrical fields in LC. It is shown that in contrast to only single-charged analytes with similar molecular weight (Figure 5.1.3a), the retention factor of counterionic analytes, related to their physicochemical properties, e.g. by varying charge and molecular weight, becomes even more complex but always displays a transition from a regime where charge transport is governed by intraparticle behaviour to a regime at increasing field strength where it only depends on the transport characteristics in the depleted CDL. Thus, the retention of any counterionic analyte reflects this transition from intraparticle to boundary-layer dominated transport (Figure 5.2.3) and depending on charge numbers this transition is displayed by a decrease or an increase in analyte retention. Within this increase or decrease it becomes modulated by their molecular mass (Figure 5.2.3a), causing selectivity differences in dependence of the applied electrical field strength (Figure 5.2.10a).

Thus also under very typical conditions the significantly induced CP not only potentially modifies analyte retention (via effective transport intensity in competitive charge transport), but also reflects the development of significant conductivity gradients which develop on a particle-scale in packed beds or locally in monolithic structures (cf. Figures 4.1 and 4.9), systematically throughout the whole chromatographic bed. These dynamics are indicated to contribute also to an intrinsic zone sharpening in CEC (Figures 5.1.1 and 5.2.2, reflected in Figure 6.1 as **"Dispersion 2"**) and influence the peak shape of the analytes through possible stacking or (destacking) phenomena. This is indicated by the massively increased efficiencies of any charged conterionic analytes. They are a factor of two up to three higher than for the electroneutral analytes, even though in Figure 5.1.1 their retention factor increases by a factor of three to four, which contradicts rules of classical linear chromatography. Further it is seen that their peak shape resemble tailing behaviour, which indicates an intrinsic stacking process. A similar behaviour is indicated for the peptides shown in Figure 5.2.2, which yet becomes even more complicated regarding their increase or decrease in retention factor.

Summarizing it can be concluded that the collected original research results and reviewed literature reflect the basic ingredients of CEC. In particular it opens routes for increasing robustness and applicability of CEC for the separation of both neutral and charged analytes. For neutral and ion-suppressed analytes possible benefits surely arise from increased efficiencies with an optimized perfusive flow field (Figures 1.8 and 3.16) or morphology-related optimization of a nonlinear EOF (Figure 3.17). In addition method transfer from LC to CEC is straightforward for neutral analytes and no discrepancies between retention in both modes have been observed in this work (Figures 5.1.3a and 5.2.8a). In contrast for charged analytes we generally have to consider a development of electrical-field induced CP in the hierarchically structured porous medium and related transport phenomena of charged analytes and the background electrolyte buffer components, having different concentrations, diffusion coefficients, and charge numbers. Yet all participate in charge transport, which makes the retention factor far more complex in CEC than is described by superimposed, simple chromatographic and electrophoretic formalisms alone (Figures 5.2.5 and 5.2.7). Tuning electrical field-induced CP provides an interesting route for selectivity tuning in CEC and related electrical-field-assisted processes (Figure 5.2.10).

Appendix 1:   List of symbols and abbreviations

Vector symbols:

i	[A]	electrical current
J	[mol·m^{-2}·s^{-1}]	molar flux density

Latin symbols:

$c_{i,\infty}$	[mol l^{-1}]	equilibrium concentration of type i ions beyond the EDL
c_i	[mol l^{-1}]	concentration of type i ions
c^+	[mol l^{-1}]	concentration of counter-ionic species
c^-	[mol l^{-1}]	concentration of co-ionic species
d_c	[m]	column inner diameter
d_{intra}	[m]	mean intraparticle pore diameter
d_p	[m]	mean particle diameter
D	[m^{2}s^{-1}]	diffusion coefficient
D_{ax}	[m^{2}s^{-1}]	axial dispersion coefficient
D_m	[m^{2}s^{-1}]	free molecular diffusion coefficient of analyte in mobile phase
E_{ext}	[V m^{-1}]	electrical field strength
H	[m]	height equivalent to a theoretical plate
I	[mol l^{-1}]	mobile phase ionic strength
k'	[-]	retention factor, $k' = (t_r - t_0)/t_0$
L_2	[-]	L_2 (Euclidean) norm
N	[m^{-1}]	plate number
Pe_{av}	[-]	average Peclet number
Pe_{intra}	[-]	intraparticle Peclet number
r_{pore}	[m]	pore radius
r_{intra}	[m]	intraparticle pore radius
T	[-]	transport number
t	[-]	transference number
t_0	[s]	elution time of tracer
t_r	[s]	elution time of tracer
u_{av}	[m s^{-1}]	average velocity through the porous medium
u_{eo}	[m s^{-1}]	average EOF velocity through the porous medium
u_{ep}	[m s^{-1}]	electrophoretic velocity
u_{inter}	[m s^{-1}]	interparticle velocity
u_{intra}	[m s^{-1}]	intraparticle velocity
z	[-]	charge number/electrochemical valence

Greek symbols:

δ_{CDL}	[m]	thickness of the convective diffusion layer
ε_{inter}	[-]	interparticle porosity
ε_{intra}	[-]	intraparticle porosity
ε_r	[-]	relative permittivity of the electrolyte solution
ε_{total}	[-]	total porosity of packed column
η_f	[Pas]	dynamic viscosity of the mobile phase
ϕ	[V]	local electrical potential
λ_D	[m]	Debye screening length
ζ	[V]	zeta-potential
ζ_p	[V]	zeta-potential at the particle surface
ζ_w	[V]	zeta-potential at the column or capillary wall
μ_{eo}	$[m^2 V^{-1} s^{-1}]$	electroosmotic mobility
μ_{ep}	$[m^2 V^{-1} s^{-1}]$	electrophoretic mobility

Subscripts:

CDL	convective diffusion layer
crit	critical
eo	electroosmotic
i	ionic species
intra	intraparticle or intraskeleton pore space
meso	mesopore space
macro	macropore space
w	wall
p	particle

Superscripts:

+	counterionic species
-	coionic species

Physical constants:

F	Faraday constant	$9.648 \cdot 10^4$	$C\ mol^{-1}$
R	universal gas constant	8.31451	$J\ mol^{-1} K^{-1}$
ε_0	absolute permittivity	$8.854 \cdot 10^{-12}$	$As\ V^{-1} m^{-1}$

Abbreviations

CLSM	Confocal laser scanning microscopy
CDL	Convective diffusion layer
CEC	Capillary electrochromatography
CP	Concentration polarization
CZE	Capillary zone electrophoresis
EC	Electrochromatography
EDL	Electrical double layer
EOF	Electroosmotic flow
HPLC	High performance liquid chromatography
LC	Liquid chromatography
SCR	Space charge region
SCX	Strong cation-exchange

Curriculum Vitae

Ivo Nischang
Waldstr. 25 c
39340 Haldensleben   +49 3904 65065
Germany   Ivo.nischang@gmx.de

Personal Data:

born on 17th March 1980 in Haldensleben (Germany), unmarried

Professional Experience:

09/2003-today	Otto-von-Guericke-Universität Magdeburg (Germany) Research assistant at the Institute of Process Engineering
08/2001-03/2002	Åmic AB (Developer and producer of Bio-MEMS components), Uppsala (Sweden) Research affiliate in collaboration with department of Analytical Chemistry, University of Uppsala (Sweden).

Education:

05/2004-today	Otto-von-Guericke-Universität Magdeburg (Germany) Ph.D. student (DFG-project TA 268/1-1, TA 268/1-2: "Influence of internal and external electrical fields on the transport of charged analytes in porous media")
04/2003-08/2003	Diploma thesis at the Otto-von-Guericke- Universität Magdeburg (Germany): "Characterization of silica-based monoliths for electrochromatography"
09/1999-03/2003	Studies of Chemistry at the University of Applied Sciences Magdeburg (Germany), Diploma in Analytical Chemistry ("With distinction")
06/1998	Abitur, Friedrich-Ludwig-Jahn-Gymnasium, Haldensleben (Germany)

Scholarships and Prizes:

2007	**Chromatography-Award** of the working group "Separation science" of the German Chemical Society for outstanding contributions to analytical separation techniques
2006	**Young scientist award** at the MSB`2006 sponsored by Waters Corporation. Selected best contribution from nineteen oral contributions by Ph.D. students, interspersed in the presentation program and in a dedicated session (international jury chaired by Jean-Luc Veuthey of the University of Geneva, Switzerland)
2006	**Selected best presentation** at the annual PhD-students' symposium of the working group "Separation Science", Section "Analytical Chemistry" of the German Chemical Society (GDCh) (voted by the audience)
08/2001-03/2002	**Leonardo da Vinci Scholarship** offered by the European Union

List of scientific publications in peer-reviewed journals:

[1]   Oliver Klett, Ivo Nischang and Leif Nyholm

        Deviceless decoupled electrochemical detection of catecholamines in capillary
        electrophoresis using gold microband array electrodes.

        Electrophoresis **2002**, *21*, 3678-3682.

[2]   Ivo Nischang and Ulrich Tallarek

        Nonlinear electroosmosis in hierarchical monolithic structures.

        Electrophoresis **2004**, *25*, 2935-2945.

[3]   Ulrich Tallarek, Felix C. Leinweber and Ivo Nischang

        Perspective on concentration polarization effects in electrochromatographic
        separations.

        Electrophoresis **2005**, *26*, 391-404.

[4]   Ivo Nischang, Guofang Chen and Ulrich Tallarek

        Electrohydrodynamics in hierarchically-structured monolithic and particulate fixed
        beds.

        Journal of Chromatography A **2006**, *1109*, 32-50.

[5]   Ivo Nischang, Katja Spannmann and Ulrich Tallarek

        Key to analyte migration and retention in electrochromatography.

        Analytical Chemistry **2006**, *78*, 3601-3608.

[6]   Ivo Nischang and Ulrich Tallarek

        Fluid dynamics in capillary and chip electrochromatography.

        Electrophoresis **2007**, *28*, 611-626.

[7]   Ivo Nischang, Udo Reichl, Andreas Seidel-Morgenstern and Ulrich Tallarek

        Concentration polarization and nonequilibrium electroosmotic slip in dense
        multiparticle systems.

        Langmuir, submitted for publication.

[8]   Ivo Nischang and Ulrich Tallarek

        Confocal laser scanning microscopy study of the electrical field-induced concentration
        polarization in monolithic structures.

        In preparation.

[9]   Ivo Nischang and Ulrich Tallarek

        Tuning retention and selectivity of peptides in electrochromatography.

        In preparation.

Poster presentations at international meetings:

[1] <u>Oliver Klett</u>, Ivo Nischang, Olle Larsson and Leif Nyholm

Decouplerfree elimination of high voltage-field effects in electrochemical detection of neurotransmitters in on-chip capillary electrophoresis

9th International Conference on Electroanalysis 2002, European Society for ElectroAnalytical Chemistry

[2] <u>Ivo Nischang</u> and Ulrich Tallarek

Experimental evidence for electroosmosis of the second kind in capillary electrochromatography with silica-based monoliths

17th International Symposium on Microscale Separations & Capillary Electrophoresis (HPCE 2004), Salzburg, Austria

[3] <u>Ivo Nischang</u> and Ulrich Tallarek

Nonlinear electroosmosis in hierarchical monolithic structures

27th International Symposium on Capillary Chromatography (2004), Riva del Garda, Italy

[4] <u>Ivo Nischang</u>, Guofang Chen, Dieter Lubda, Gerard Rozing and Ulrich Tallarek

Electrohydrodynamics in hierarchically-structured porous media: From electroosmotic perfusion to strong concentration polarisation and nonlinear electroosmosis

18th International Symposium on MicroScale Bioseparations (MSB 2005), New Orleans, USA

[5] <u>Ivo Nischang</u>, Felix C. Leinweber and Ulrich Tallarek

Electrical field-induced concentration polarisation in random-close sphere packings and monolithic structures studied by confocal laser scanning microscopy

18th International Symposium on Micro-Scale Bioseparations (MSB 2005), New Orleans, USA

[6] <u>Ivo Nischang</u>, Guofang Chen and Ulrich Tallarek

Electrohydrodynamics in hierarchically-structured monolithic and particulate fixed beds

20th International Symposium on Micro-Scale Bioseparations (MSB 2006), Amsterdam, Netherlands

Oral presentations at international meetings:

[1] <u>Ivo Nischang</u>, Katja Spannmann and Ulrich Tallarek

Key to analyte migration and retention in electrochromatography

20th International Symposium on Micro-Scale Bioseparations (MSB 2006), Amsterdam, Netherlands